NASA/CR—2002-211840

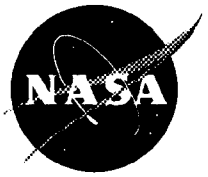

Research Reports—2001 NASA/ASEE Summer Faculty Fellowship Program

G. Karr, Editor
The University of Alabama in Huntsville, Huntsville, Alabama

J. Pruitt and S. Nash-Stevenson, Editors
Marshall Space Flight Center, Marshall Space Flight Center, Alabama

L.M. Freeman and C.L. Karr, Editors
The University of Alabama, Tuscaloosa, Alabama

Prepared for Marshall Space Flight Center
Under Contract NAG8–1786

July 2002

The NASA STI Program Office...in Profile

Since its founding, NASA has been dedicated to the advancement of aeronautics and space science. The NASA Scientific and Technical Information (STI) Program Office plays a key part in helping NASA maintain this important role.

The NASA STI Program Office is operated by Langley Research Center, the lead center for NASA's scientific and technical information. The NASA STI Program Office provides access to the NASA STI Database, the largest collection of aeronautical and space science STI in the world. The Program Office is also NASA's institutional mechanism for disseminating the results of its research and development activities. These results are published by NASA in the NASA STI Report Series, which includes the following report types:

- TECHNICAL PUBLICATION. Reports of completed research or a major significant phase of research that present the results of NASA programs and include extensive data or theoretical analysis. Includes compilations of significant scientific and technical data and information deemed to be of continuing reference value. NASA's counterpart of peer-reviewed formal professional papers but has less stringent limitations on manuscript length and extent of graphic presentations.

- TECHNICAL MEMORANDUM. Scientific and technical findings that are preliminary or of specialized interest, e.g., quick release reports, working papers, and bibliographies that contain minimal annotation. Does not contain extensive analysis.

- CONTRACTOR REPORT. Scientific and technical findings by NASA-sponsored contractors and grantees.

- CONFERENCE PUBLICATION. Collected papers from scientific and technical conferences, symposia, seminars, or other meetings sponsored or cosponsored by NASA.

- SPECIAL PUBLICATION. Scientific, technical, or historical information from NASA programs, projects, and mission, often concerned with subjects having substantial public interest.

- TECHNICAL TRANSLATION. English-language translations of foreign scientific and technical material pertinent to NASA's mission.

Specialized services that complement the STI Program Office's diverse offerings include creating custom thesauri, building customized databases, organizing and publishing research results...even providing videos.

For more information about the NASA STI Program Office, see the following:

- Access the NASA STI Program Home Page at ***http://www.sti.nasa.gov***

- E-mail your question via the Internet to help@sti.nasa.gov

- Fax your question to the NASA Access Help Desk at (301) 621–0134

- Telephone the NASA Access Help Desk at (301) 621–0390

- Write to:
  NASA Access Help Desk
  NASA Center for AeroSpace Information
  7121 Standard Drive
  Hanover, MD 21076–1320
  (301)621–0390

NASA/CR—2002–211840

Research Reports—2001 NASA/ASEE Summer Faculty Fellowship Program

G. Karr, Editor
The University of Alabama in Huntsville, Huntsville, Alabama

J. Pruitt and S. Nash-Stevenson, Editors
Marshall Space Flight Center, Marshall Space Flight Center, Alabama

L.M. Freeman and C.L. Karr, Editors
The University of Alabama, Tuscaloosa, Alabama

Prepared for Marshall Space Flight Center
Under Contract NAG8–1786

National Aeronautics and
Space Administration

Marshall Space Flight Center • MSFC, Alabama 35812

July 2002

Available from:

NASA Center for AeroSpace Information
7121 Standard Drive
Hanover, MD 21076–1320
(301) 621–0390

National Technical Information Service
5285 Port Royal Road
Springfield, VA 22161
(703) 487–4650

PREFACE

This document is a collection of technical reports on research conducted by the participants in the 2001 NASA/ASEE Summer Faculty Fellowship Program at Marshall Space Flight Center (MSFC). This was the thirty-seventh consecutive year the program has been conducted at MSFC. The 2001 program was administered by the University of Alabama in Huntsville (UAH), and the University of Alabama (UA) in cooperation with MSFC. The program was operated under the auspices of the American Society for Engineering Education (ASEE) with sponsorship and funding from the Office of External Relations, NASA Headquarters, Washington, DC. The MSFC program was one of ten such Aeronautics and Space Research Programs funded by NASA Headquarters in 2001. Similar programs were conducted at seven other NASA centers. The basic common objectives of the NASA/ASEE Summer Faculty Fellowship Program are:

a. To further the professional knowledge of qualified engineering and science faculty members;

b. To stimulate an exchange of ideas between participants and NASA;

c. To enrich and refresh the research and teaching activities of participants' institutions; and

d. To contribute to the research objectives of the NASA centers.

The MSFC Faculty Fellows spent 10 weeks (May 29 through August 3, 2001) working with NASA scientists and engineers on research of mutual interest to the university faculty member and the NASA colleague. The editors of this document were responsible for selecting appropriately qualified faculty to address some of the many problems of current interest to NASA/MSFC. A separate document reports on the administrative aspects of the 2001 program. This document contains the technical reports on research performed by the individual 2001 participants. The NASA/ASEE program is essentially a two-year program to allow in-depth research by the university faculty member. In some cases, a faculty member has developed a close working relationship with a particular NASA group that has provided funding beyond the two-year limit. The reports are arranged in alphabetical order.

TABLE OF CONTENTS

2001

NASA/ASEE SUMMER FACULTY FELLOWSHIP PROGRAM

MARSHALL SPACE FLIGHT CENTER
THE UNIVERSITY OF ALABAMA IN HUNTSVILLE

Microelectric Heterogeneous Hybrid Devices for Space Applications

Prepared By:	Mohammad A. Alim, Ph.D.
Academic Rank:	Associate Professor
Institution and Department:	Alabama A & M University Department of Electrical Engineering P.O. Box 297, Normal, Alabama 35762
NASA/MSFC Directorate:	Engineering
MSFC Colleague:	Mr. Cydale C. Smith Materials Process and Manufacturing Department ED 34

Introduction

The existing projects designated as SACA (Sample Ampoule Cartridge/Container Assembly) and QMI (Quench Module Insert) at NASA – MSFC involve development of high-temperature coating materials. A number of material systems need to be evaluated for this purpose. The requirement of these coating materials included high emissivity (approaching unity), sufficient physical strength, appropriate thermal conductivity to dissipate heat, and above all high temperature ($T \geq 2000^{o}C$) withstanding capability. Potential materials for applications considered were non-oxide based materials such as tungsten carbide, tantalum carbide, compounds of niobium, etc.

Effort was put to find the possibility of using niobium based proprietary material known as WC103. There exist some problems of this material to obtain a stable coating. Based on the information available through the SACA Team the possible characterization techniques utilized were evaluated. It is felt that the electrical aspect of the material system is not considered.

Usually each material system displays dangling bonds on its abrupt surfaces. These dangling bonds constitute surface charge density and gives rise to a property of the material that plays an important role in the adhesive behavior with another material's surface. Therefore, the surface property is crucial for both the substrate and the coating material. In general, *immittance spectroscopy* (IS) resolves this issue effectively. This is a proven advanced technique for characterizing a number of heterogeneous polycrystalline material systems [1-4]. For a non-Newtonian fluid system, when dried, the resulting surface charging issue is well understood by this technique. The use of this non-destructive tool/technique was recommended strongly to obtain the behavior and response of the surfaces as well as the coating materials.

Another aspect of the on-going and future work at NASA – MSFC is associated with the device systems that are related to heterogeneous hybrid device systems based on single-crystal and polycrystal materials for space applications. This effort is a gear toward miniaturization or further integration of the devices with decreased mass possessing identical existing functional capabilities. Activities in this direction include electrical components such as solid-state transformers, resistors, capacitors, inductors, etc., and electronic devices such as high-voltage diodes, transistors, thyristors, varistors, thermisters, etc.

The aforementioned devices are projected with single-crystal substrates on to polycrystal materials. Such a heterojunction may yield high-voltage handling capability based on the principles operating in surge protecting varistors [5] and high-temperature thermistors [6]. To obtain these junction devices vacuum coating unit can serve the purpose. Sintering technology is not ruled out for obtaining the polycrystalline compound semiconductors. Such materials can also be used as a substrate. With the utilization of these types of processing conditions polymer-inorganic based light composite magnetic materials can be evaluated.

Potential Solution to the Surface Charging Effect

A simple arrangement for characterization of a coating material is depicted in the Figure 1. This arrangement provides the effect of the interfacial region across the single interface in conjunction with the single surface characterization. Another simple arrangement is extracted from the double interface concept shown in Figure 2. There each interfacial region across the single interface can be characterized. In all arrangements utilization of the *immittance spectroscopy* is emphasized.

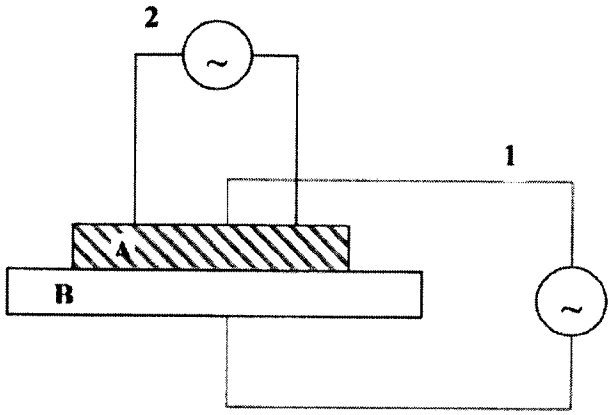

Figure 1: Arrangement of Single Surface-Interface Characterization.
1 → Single Interface Characterization (vertical set-up)
2 → Single Surface Characterization (horizontal set-up)
A → coating material
B → substrate

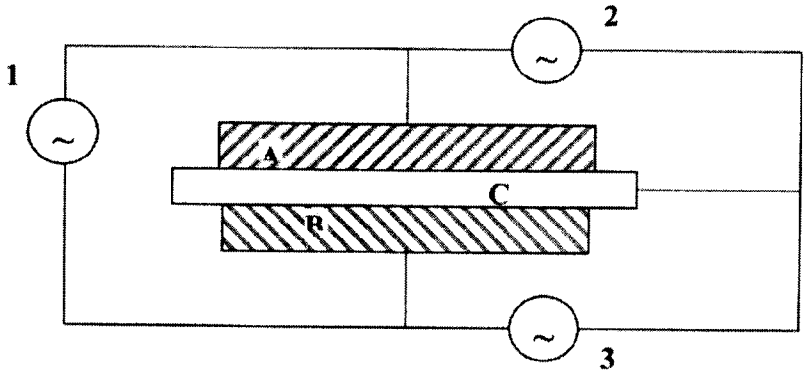

Figure 1: Arrangement of Double Surface-Interface Characterization.
1 → Double Interface Characterization (vertical set-up)
2 → Single Interface Characterization (vertical set-up)
3 → Single Interface Characterization (vertical set-up)
A → first coating material
B → first coating material
C → substrate

Experimental Approach

A series of experimental outlines have been discussed and documented in the Materials Processes and Manufacturing facility laboratory. These outlines provide a strong guideline as how to fabricate a coating or a junction device using either single-crystal or polycrystal substrates. The properties of the materials to be used for evaporation using a vacuum coating unit are also emphasized.

The electrical characterization of these coated systems and junction devices will be done utilizing an Impedance Analyzer having at least a frequency range extending over 6 orders in magnitude. For example an HP 4192A (or Agilent) Impedance Analyzer having measurement frequency range 5 Hz through 13 Hz is extremely desirable. The author has experienced with this instrument and expressed satisfaction in using it for such materials systems [1-6].

Recommendation of Procuring Instruments

NASA – MSFC needs to procure an Impedance Analyzer to accomplish the experiments suggested in this report. For this purpose necessary information on the instrumentation such as HP 4192A is provided to the NASA colleague as well as to the SACA Team members. In the near future additional Impedance Analyzer(s) may be needed to expand the frequency range data so that a broad window of interpretation becomes easy with precision.

Conclusions

The devices and material systems mentioned here are based on both single-crystal and polycrystal heterojunctions. The use of silicon as a single crystal is not ruled out. However, single-crystal compound semiconductors and oxide-based polycrystal compound semiconductors are highly recommended as these usually have large band gaps. Also such semiconductors are intrinsically either *n*- or *p*-type based on the type of non-stoichiometry. In this case additional doping may not be necessary. Usual material handbook will be consulted to select the materials. For example, ZnO is intrinsically n-type.

Acknowledgments

The author would like to thank NASA - SFFP (Summer Faculty Fellowship Program). Discussion with Mr. Cydale C. Smith including interactions with the Summer Co-op Students and participation with the SACA Team members are gratefully acknowledged.

References

[1] Alim, M. A. (1996), "Electrical Characterization of Engineering Materials," Active and Passive Electronic Components, Vol. 19, 139-169.

[2] Alim, M. A. (1996), "Immittance Data-Handling/Analyzing Criteria For Heterogeneous Systems," Materials Research Society Symposium Proceeding, Vol. 411, 13-23.

[3] Alim, M. A. (1996), "Phenomena Related To Concurrent Multiple Complex Plane Representations Of The Immittance Data," Materials Research Society Symposium Proceeding, Vol. 411, 113-125.

[4] Alim, M. A., et al. (1994), "Immittance Spectroscopy of Smart Components and Novel Devices," Active and Passive Electronic Components, Vol. 16, 153-170.

[5] Alim, M. A. (1989), "Admittance-Frequency Response in Zinc Oxide Varistor Ceramics," Journal of the American Ceramic Society, Vol. 72(1), 28-32.

[6] Patton, V. D., et al. (1995), "The AC Electrical Behavior of Polycrystalline Yttria," Journal of Applied Physics, Vol. 78(3), 1757-1762.

2001

NASA/ASEE SUMMER FACULTY FELLOWSHIP PROGRAM

MARSHALL SPACE FLIGHT CENTER
THE UNIVERSITY OF ALABAMA IN HUNTSVILLE

NUMERICAL SIMULATION OF FLOW FIELD WITHIN PARALLEL PLATE PLASTOMETER

Prepared By:	Basil N. Antar
Academic Rank:	Professor
Institution and Department:	The University of Tennessee Mechanical & Aerospace Engineering & Engineering Science
NASA/MSFC Directorate:	Science
MSFC Colleague:	Edwin Ethridge

Introduction

Parallel Plate Plastometer (PPP) is a device commonly used for measuring the viscosity of high polymers at low rates of shear in the range 10^4 to 10^9 poises. This device is being validated for use in measuring the viscosity of liquid glasses at high temperatures having similar ranges for the viscosity values. PPP instrument consists of two similar parallel plates, both in the range of 1 inch in diameter with the upper plate being movable while the lower one is kept stationary. Load is applied to the upper plate by means of a beam connected to shaft attached to the upper plate. The viscosity of the fluid is deduced from measuring the variation of the plate separation, h, as a function of time when a specified fixed load is applied on the beam. Operating plate speeds measured with the PPP is usually in the range of 10^{-3} cm/s or lower.

The flow field within the PPP can be simulated using the equations of motion of fluid flow for this configuration. With flow speeds in the range quoted above the flow field between the two plates is certainly incompressible and laminar. Such flows can be easily simulated using numerical modeling with computational fluid dynamics (CFD) codes. We present below the mathematical model used to simulate this flow field and also the solutions obtained for the flow using a commercially available finite element CFD code.

Mathematical Model of the PPP

As pointed out earlier since the flow is laminar and incompressible then the mathematical model appropriate for such a system comprises of the equations of motion for incompressible flow, the Navier-Stokes equations, in this case. These are the conservation of mass equation

$$\nabla \cdot \mathbf{v} = 0 \tag{1}$$

and the momentum equations:

$$\rho(\partial \mathbf{v}/\partial t + \mathbf{v}\cdot\nabla\mathbf{v}) = -\nabla p + \rho\mathbf{g} + \eta\nabla^2\mathbf{v} \tag{2}$$

where $\mathbf{v}$ is the fluid velocity vector field, ρ is the fluid density, p is the pressure within the fluid and η is the fluid viscosity. The flow fields as well as the pressure within the samples in PPP apparatus can be resolved by solving these equations subject to the appropriate boundary conditions.

Due to the circular cylindrical nature of the geometry of the samples used with the PPP, a cylindrical coordinate system (r, θ, z) is the most appropriate for use with the present configuration. Also, since the load is applied in the vertical direction making the upper plate movement to be also in that direction, axial symmetry can be used without any loss of generality. Under these conditions, equation (1) for axisymmetric flow in a cylindrical coordinate system becomes

$$\frac{1}{r}\frac{\partial}{\partial r}(rv_r)+\frac{\partial v_z}{\partial z}=0 \qquad (3)$$

v_r and v_z are the fluid velocity components in the r- and z-directions, respectively. While the momentum equations for the same geometry will take the following form for the two velocity components v_r and v_z

$$\rho\left(\frac{\partial v_r}{\partial t}+v_r\frac{\partial v_r}{\partial r}+v_z\frac{\partial v_r}{\partial z}\right)=-\frac{\partial p}{\partial r}+\eta\left[\frac{\partial^2 v_r}{\partial r^2}+\frac{\partial}{\partial r}\left(\frac{v_r}{r}\right)+\frac{\partial^2 v_r}{\partial z^2}\right] \qquad (4)$$

$$\rho\left(\frac{\partial v_z}{\partial t}+v_r\frac{\partial v_z}{\partial r}+v_z\frac{\partial v_z}{\partial z}\right)=-\frac{\partial p}{\partial z}+\rho g+\eta\left[\frac{\partial^2 v_z}{\partial r^2}+\frac{1}{r}\frac{\partial v_z}{\partial r}+\frac{\partial^2 v_z}{\partial z^2}\right] \qquad (5)$$

These equations must be solved subject to the appropriate boundary conditions. For physically accurate simulation of the operation of the PPP the top plate in this model will be made to move in the axial direction subject to a prescribed applied axial load, F_z Mathematically, this condition will take the following form:

$$F_z(r)=\tau_{zz} \quad \text{at} \quad z=h \qquad (6)$$

While the no-slip boundary condition should be used at the bottom plate, given by

$$v_r=v_z=0 \text{ at } z=0 \qquad (7)$$

Also, in order to model the true physics of the problem, the appropriate free surface conditions must be applied at the circumference of the sample, i.e.,

$$p_\infty-p=\frac{2\sigma}{R}-2\eta\frac{\partial v_r}{\partial r} \qquad (8)$$

where in the above σ is the surface tension and R is the radius of curvature of the axial free surface, p and p_∞, are the pressures in the liquid and the gas, respectively.

The flow field within the sample can be resolved by solving equations (3) - (5) together with the boundary conditions (6) - (8). This system comprises of highly non-linear, coupled partial differential equations for which an analytical solution is impossible and the only recourse for solving these equations is through numerical approximations, or Computational Fluid Dynamics, CFD. For this purpose a commercially available CFD code was utilized. In this case, a Finite Element Method (FEM) software, the FIDAP code was used.

When using a packaged CFD code, the first thing to do is to define the geometry of the configuration as well as the properties of the fluid being investigated. In this case the specific geometry had to be supplied to the code together with all of the thermodynamic coefficients appearing in problem (3) - (8). Specifically, the fluid is assumed to be ZIBLAN in the liquid state and whose properties are: the density, $\rho = 5.0$ g/cm^3, the viscosity, $\eta = 3 \times 10^7$ g/cm s, and surface tension $\sigma = 216$ dyne/cm. The initial geometry of the sample was that of right circular cylinder with a given initial diameter D and initial height h as shown in Figure 1 below.

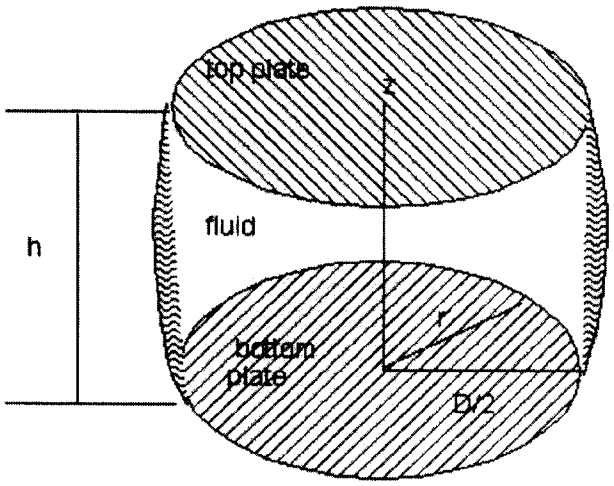

Figure 1. Sketch of the geometry used for the numerical simulation model.

The simulation effort was initiated by first using a simple geometry. The simulation effort was initiated by first using a simple geometry with a small aspect ratio D/h of the order of 2.0 inches which the sample height was half its diameter, i.e. h=5.0 cm and D=10 cm. Normally, samples used by PPP have diameters D of the order of 1.5 cm and height h of up to 0.4 cm but usually much smaller, making D/h of up 10. However, it is not advisable to use such high value for the aspect ratio until the code is fully validated. Note, that the important dimension in the numerical simulation is D/h and neither D nor h alone. In addition to the geometry being important for the numerical simulation effort specification of the loading characteristics of the top plate is another important factor. However, in order to facilitate the validation phase, another important factor. However, in order to facilitate the validation of the CFD code, the velocity of motion of the top plate towards the bottom one was used in place of loading the top plate. In other words, the boundary condition (6) was replaced for this phase of the analysis with the following boundary condition:

$$v_z = -V, \qquad v_r = 0, \qquad \text{at} \qquad z = h \tag{9}$$

Figure 2 shows the fluid region variation with time for a case in which the top plate velocity was .01 cm/s. The figure shows the plate separation at t = 10, 50, 100 and 130

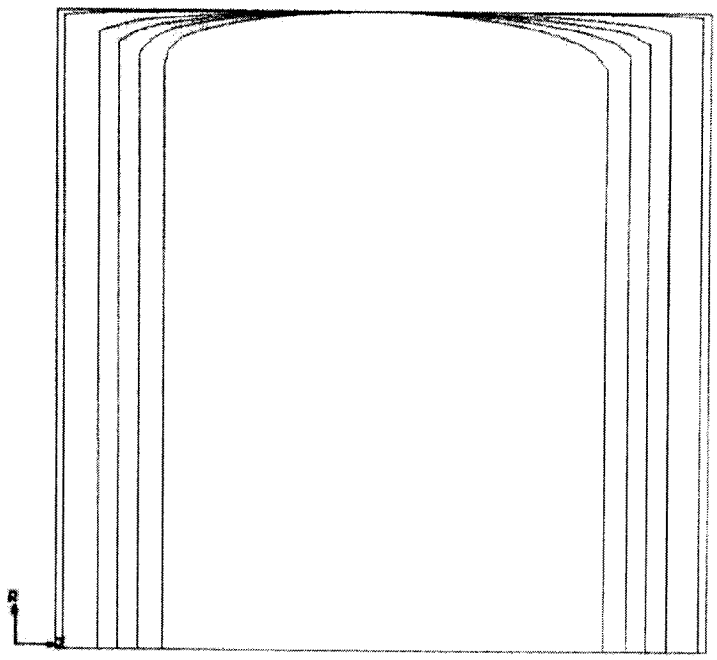

Figure 2. The time evolution of fluid geometry from t = 0 to t = 130 seconds.

seconds after the start of the simulation. Figure 3 shows the velocity field vectors at 4 times, while figure 4 shows the shear distribution within the fluid also at the corresponding times of figure 3.

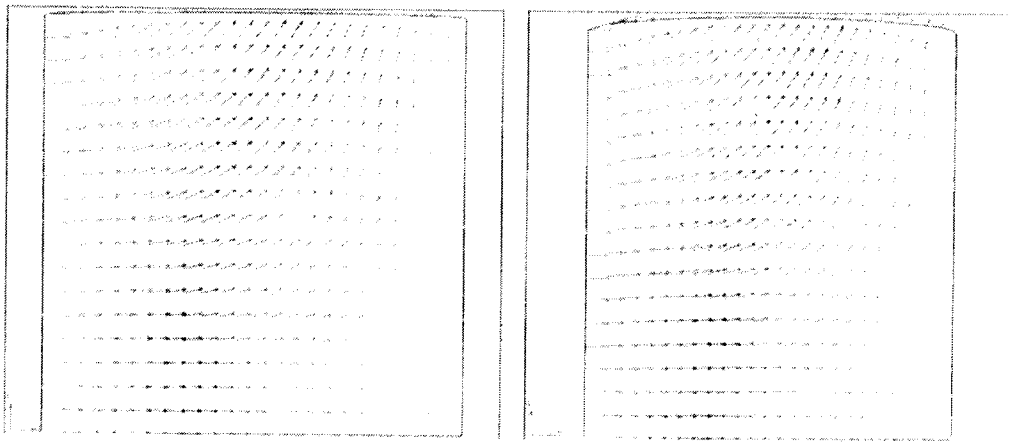

time = 10 seconds

time = 50 seconds

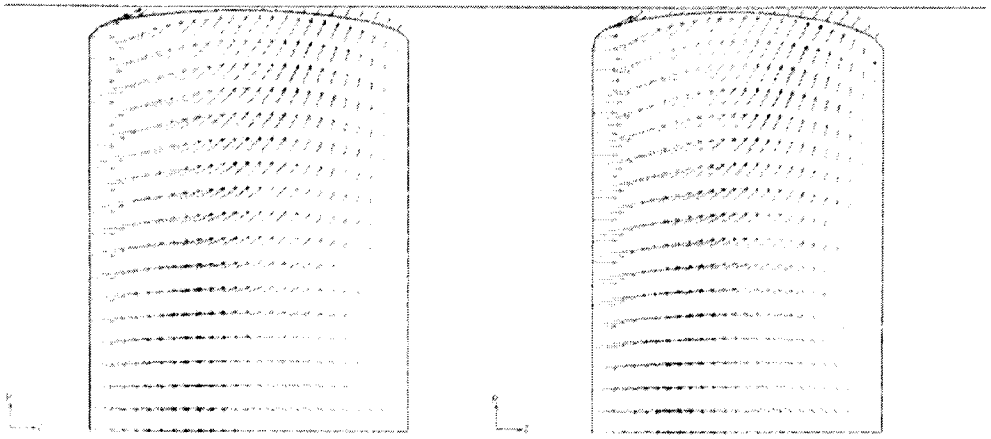

Figure 3. Fluid velocity vector field at 4 time intervals

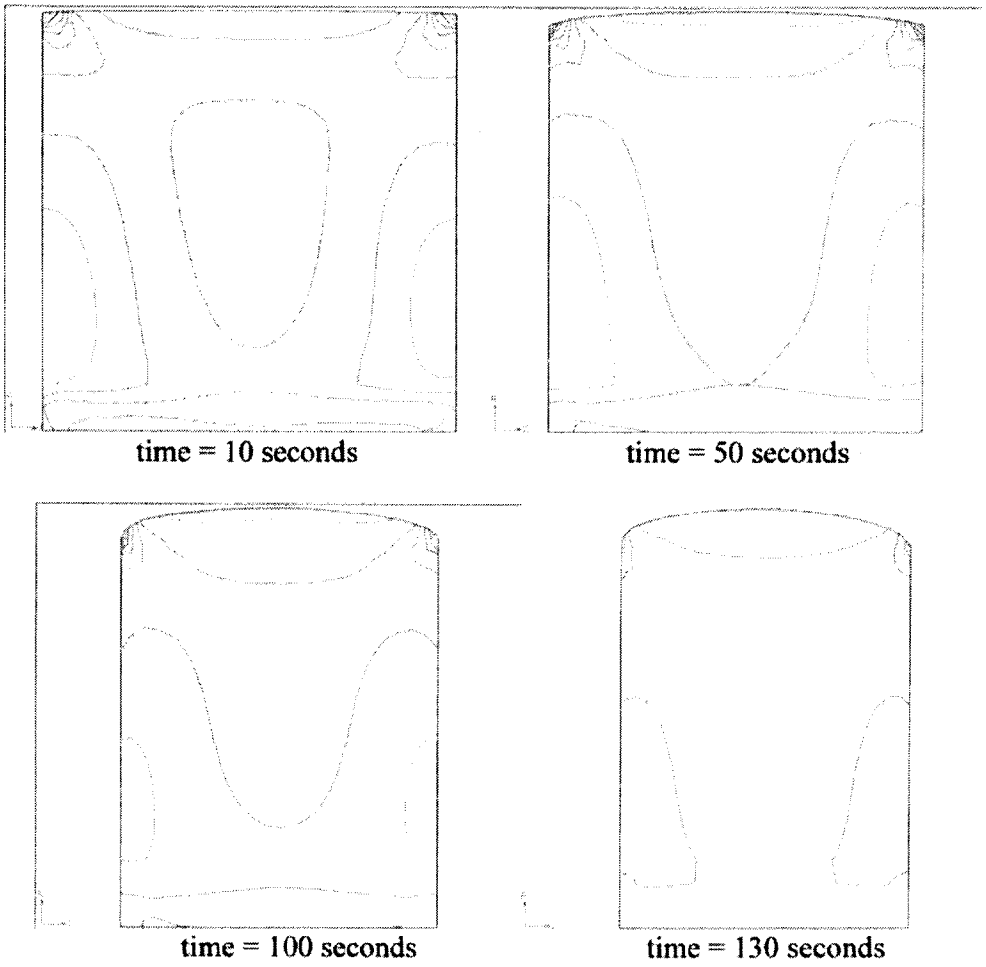

Figure 4. Contours of equal shear values at 4 time intervals.

2001

NASA/ASEE SUMMER FACULTY FELLOWSHIP PROGRAM

MARSHALL SPACE FLIGHT CENTER
THE UNIVERISTY OF ALABAMA IN HUNTSVILLE

CANCER RISK -ASSESSMENT OF RADIATION DAMAGE IN ATAXIA-TELANGIECTASIA HETEROZYGOUS HUMAN BREAST EPITHELIAL CELL CULTURES

Prepared By:	Lisa C. Applewhite
Academic Rank:	Assistant Professor
Institution and Department:	Spelman College Department of Biology
NASA/MSFC Directorate:	Science
MSFC Colleague:	Robert C. Richmond

Introduction

For most breast cancer cases, the genetic causes remain undefined. One such genetic determinant involves the mutation of the tumor suppressor gene, ataxia telangiectasia (ATM), as a mechanism of tumor promotion in the breast. The function of the ataxia telangiectasia (AT) gene involves cell cycle control, DNA damage recognition, and repair of DNA damage (Buchholz et al., 1999, Khanna 2000). AT carriers comprise up to 1% of the general population and their identification is of considerable interest in cancer epidemiology and radiation therapy (Djuzenova et al., 1999). Individuals that are heterozygotes (carriers) of ataxia telangiectasia (AT) have no clinical expression of AT but may be highly radiosensitive and predisposed to several forms of cancer. Irradiation of AT heterozygous cells can alter the functionality of the remaining ATM gene, thus resulting in a ATM protein titer to recognize and repair damaged DNA.

Ionizing radiation is cytotoxic to cells as a direct consequence of DNA damage (Araujo etal., 1999). Absorption of radiation by DNA bases can directly result in ionization of the nucleotides. An indirect effect of ionizing radiation is the reaction with the water molecules immediately surrounding the DNA, resulting in water radiolysis. The formation of primary free radicals by water radiolysis introduces oxidative damage to the genetic material. Thus, the damage induced by ionizing radiation results in free radical formation, double strand breaks, chromosomal aberrations, mutations, and neoplastic transformation.

During neoplasia, normal cellular development and functionality are significantly altered. However, current understanding of the initialization of tumor progression remains unclear. In order understand the mechanism(s) involved, AT heterozygous human mammary epithelial cell cultures were the selected model because of the noted radiation sensitivity of this cell type. NASA MSFC is investigating the mechanism(s) by which environmental stressors such as ionizing radiation can promote cancer in human cells.

This paper describes the study of the markers of cellular changes that are found during the onset of carcinogenesis. Several of the biological factors are markers of stress response, oncoprotein expression, and differentiation factors. Oxidative stress response agents such as heat shock proteins (HSPs) protect cells from oxidative stresses such as ionizing radiation (Baek et al., 2000). The onocoprotein HER-2/neu, a specific breast cancer marker, indicates early onset of cancer (Gullick, 1990). Additional structural and morphogenetic markers of differentiation were considered in order to determine initial cellular changes at the initial onset of cancer. As an additional consideration, all-*trans* retinoic acid (RA), a differentiation agent, was considered because of its known role in regulating normal differentiation and inhibiting tumor proliferation via specific nuclear receptors (Zhou et al., 1997; Mangiarotti et al., 1998; Van heusden et al., 1998).

This paper discusses study and results of the preliminary analyses of gamma irradiation of AT heterozygous human breast epithelial cells (WH). Comparisons are also made of the effects various RA concentrations post-irradiation.

Methodology

This study focused on identifying cellular changes in WH cell cultures as a result of oxidative stress resulting from gamma irradiation exposure.

WH cells were grown to confluence at pass 8 in T-25 confluent flasks and irradiated with varying doses of gamma irradiation, 30 RAD, 60 RAD, and 90 RAD. A non-irradiated control was also included of the same sample. Within 2 hours of irradiation, cells from each flask were seeded into a 96-well plate corresponding to each radiation dose. After adherence for 24 hours the cells were then treated with varying concentrations of all-*trans* retinoic acid (RA) at 10^{-7} M, 10-6 M, and 10-5 M, along with untreated controls (Figure 1).

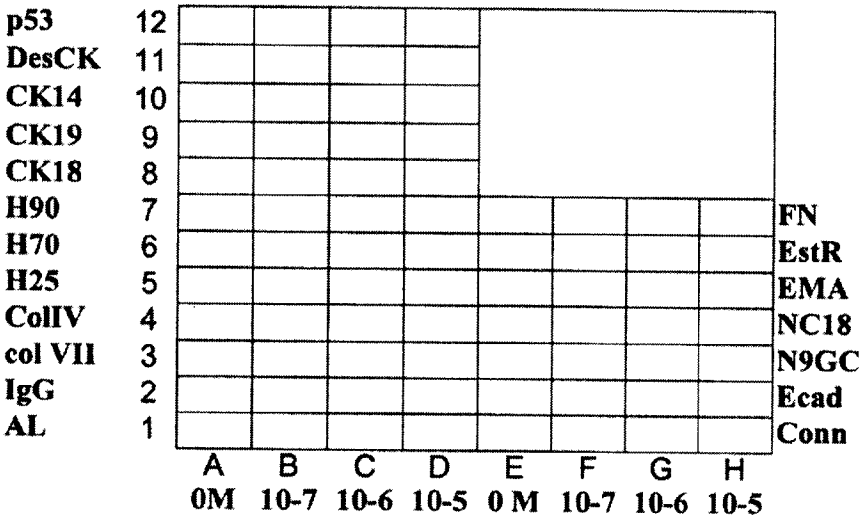

Figure 1: Template of 96-well plate for a single radiation dose sample.

Once the cells are grown to the appropriate phase of growth, they were fixed with methanol:acetone (1:1) and stored at -80 C until ready for antibody labeling and immunostaining. The primary antibodies utilized are indicated in Table 1 and abbreviated in Figure 1. Immunostaining was accomplished by HRP-conjugated secondary antibody labeling with Vector Laboratories ABC kit followed by staining with DAB reagent.

Table 1. Primary Antibodies grouped by function.

Differentiation		**Oncoproteins**	**Stress Response**	**Controls**
Desmocytokeratin (DesCK)	Connexin-43 (Conn)	Her-2/neu (NC18 and N9GC)	HSP 90	IgG -negative
Cytokeratin 14 (CK14)	Fibronectin (FN)		Hsp 70	FN - positive
Cytokeratin 19 (CK19)	Human Episialin (EMA)		Hsp 25	
Cytokeratin 18 (CK18)	Laminin (AL)		P53	
Collagen IV (Col IV)	E-Cadherin (Ecad)			
Collagen VII (Col VII)	Estrogen Receptor (EstR)			

Results and Discussion

The negative and positive immunostaining controls, IgG and fibronectin (FN) were established from previous studies in the lab at NASA MSFC. Our results were consistent with these controls, thus allowing qualitative assessment of the intensity and localization of the immunostain by DAB. Analysis of control plate, 30 RAD plate, 60 RAD plate, and 90 RAD plate fixed at early log phase at pass 9 (one passage post-irradiation passage of 8) indicated significant levels of staining. These specific wells were of cells primarily labeled with Fibronectin (FN), Collagen VII (Col VII), Cytokeratin 18 (CK18), and Cytokeratin 14 (CK14). No significant staining or non-specific staining was noted for the other antibodies/markers. This observation is especially pertinent for p53, which exhibits an immediate response within minutes of introduction of oxidative stress. Thus, indication of p53 upregulation is significantly diminished prior to fixation. The duration and mechanism of the other stress response markers, oncoproteins and differentiation factors are currently under further observation. Several more generations are needed before an observed effect of DNA damage is apparent through transformation.

Comparison of the effect of RA concentration on the level of immunostaining of FN, Col VII, revealed some concentration dependent changes in the plates of irradiated cells. However, CK14 staining by the non-irradiated controls indicated a RA dose-dependent response while all radiation experimentals maintained the same level of CK14 immunostaining.

These are preliminary results indicate that the WH cells are differentially derived from luminal epithelia, as indicated by CK18 staining, and basal cell epithelia, indicated by CK 14 staining. An abundance of FN is often associated with post-radiation fibrosis, but those levels are not yet determined in the cultures studied. Long term indicators of DNA damage would be determined through further observation of continued passage of irradiated cells and controls, flourescent immunostaining for quantification and localization, and analysis for chromosomal aberrations and cell cycle via flow cytometry.

Acknowledgements

I would like to thank Dr. Robert C. Richmond for an invigorating environment for challenging research and discussions, Mrs Karen Bors and Dr. Angela Cruz for technical support and expertise, Mr. Yong Kim for performing several demanding experiments and calculations. Finally, I wish to extend appreciation to the NASA MSFC Education Department and the SFFP office for the wonderful opportunity for research and collaborations.

References:

Baek, S.-H., et al. (2000), Role of Small Heat Shock k Protein HSP25 in Radioresistance and Glutathione-Redox Cycle. *Journal of Cellular Physiology* 183: 100-107.

Buchholz, T.A., Weil, M.M., Story, M.D., Strom, E.A., Brock, W.A., and McNeese, M.D. (1999) Tumor suppressor genes and breast cancer. *Radiation Oncology Investigations* 7(2): 55-65.

Djuzenova, C.S., Schnindler, D., Stopper, H., Hoehn, H., Flentje, M., and Oppitz, U. (1999) Identification of ataxia telangiectasia heterozygotes, a cancer-prone population, using the single-cell gel electrophoresis (Comet) assay. *Lab Investigations* 79(6): 699-705.

Gullick, W.J. (1990) The role of the epidermal growth factor receptor and the c-erB-2 protein in breast cancer. *International Journal of Cancer* 5: 55-61.

Khanna, K. K. (2000) Cancer risk and the ATM gene: A Continuing Debate. *Journal of the National Cancer Institute* 10: 795-802.

Mangiarotti, R., Danova, M., Alberici, R., and Pellicciari, C. (1998) All-*trans* retinoic acid (ATRA)-induced apoptosis is preceded by G1 arrest in human MCF-7 breast cancer cells. *British Journal of Cancer* 77: 186-191.

Van heusden, J. et al. (1998) All-*trans* retinoic acid metabolites significantly inhibit the proliferation of MCF-7 human breast cancer cells in vitro. *British Journal of Cancer 77: 26-32.*

Zhou, Q., Stetler-Stevenson, M., and Steeg, P. (1997) Inhibition of cyclin D expression in human breast carcinoma cells by retinoids *in vitro*. *Oncogene* 15: 107-115.

2001

NASA/ASEE SUMMER FACULTY FELLOWSHIP PROGRAM

MARSHALL SPACE FLIGHT CENTER
THE UNIVERSITY OF ALABAMA IN HUNTSVILLE

Viscosity Relaxation in Molten HgZnTe

Prepared By:	James K. Baird
Institution and Department	Department of Chemistry University of Alabama in Huntsville Huntsville, AL 35899
NASA/MSFC Directorate:	SD 40
MSFC Colleagues:	S. L. Lehoczky and Ching-Hua Su

Introduction

Because of its narrow electronic band-gap, HgZnTe solid solutions have been proposed as effective detectors for infrared radiation [1]. To produce the best single crystals of these materials for this application, knowledge of the phase diagram that governs the freezing of the liquid is essential [2]. Besides the phase diagram, however, some information concerning the thermophysical properties of the melt, such as viscosity, density, specific heat, and enthalpy of mixing, can also be useful [3,4]. Of these thermophysical properties, the viscosity, is perhaps of the most interest scientifically. Measurements using the oscillating cup method [5,6] have shown that the isothermal melt requires tens of hours of equilibration time before a steady value of the viscosity can be achieved [3]. Over this equilibration time, which depends upon temperature, the viscosity can increase by as much as a factor of two before reaching a steady state. We suggest that this relaxation phenomenon may be due to a slight polymerization of Te atoms in the melt.

The Group VI elements, S and Se, are famous for their many allomorphs [7]. Orthorhombic sulfur, which has the formula S_8, is the stable form at room temperature. This allomorph melts at 113 °C to form a yellow red liquid [8]. Above 159 °C, the viscosity of the liquid begins a rapid increase due to the conversion of S_8 rings into long chains, which may contain as many as 100,000 sulfur atoms [9]. Above 200 °C, the chains begin to break up, however, and the viscosity of sulfur returns to a normal value [10]. Polymeric selenium can be prepared in a similar fashion, and both polymeric sulfur and polymeric selenium appear to form chains by a free radical mechanism [8].

By contrast, the viscosity of liquid Te is more like that of normal liquids [11], and the reality of polymeric Te in the liquid state has been the subject of some debate. The existence of a two-fold coordinated chain structure in solid tellurium, on the other hand, is well documented [12]. Noting that the atomic coordination number of a Te atom in the melt lies between 2 and 3, Cabane and Friedel argued that the chain structure does not continue into the liquid [11]. Tsuzuki et. al., however, have recently studied the structure of the liquid near the freezing point using EXAFS and neutron inelastic scattering and report evidence for the existence of a two-fold coordinated chain structure consisting of long and short covalent bonds [13]. They propose that a strong correlation between individual chains can account for a coordination number larger than 2. Electronic structure calculations also support their observations by suggesting that the chain structure of the solid is preserved upon melting [12, 14].

To account for the time dependence of the viscosity in the HgZnTe melt, we propose that the liquid acts as a solvent that favors the formation of Te atom chains. We suggest that as the melt is cooled from a high temperature to the temperature for measurement of the viscosity, a free radical polymerization of Te atoms begins. As is the rule in the case of polymer solutions, the viscosity increases with the increasing average molecular weight of the dissolved polymer [15].

Several molecular weight averages can be defined in the case of polymer solutions [16]. Colligative property measurements, for example, are sensitive to the number average molecular weight, while light scattering measurements depend upon the weight average molecular weight. The viscosity depends upon still another average molecular weight that is, nevertheless, close in numerical value to the weight average.

To estimate this average molecular weight, we use a simple free radical polymerization mechanism, including a depolymerization step, to calculate the time dependence to the concentration of each Te polymer molecular weight fraction. From these molecular weight fractions, we compute the weight average molecular weight of the distribution. Using the semi-empirical relation between average molecular weight and viscosity, we obtain a formula for the time dependence of the viscosity of the melt.

Upon examining this formula, we find that the viscosity achieves a steady value when a balance is achieved between the rate of formation of the chains and the rate of their depolymerization into species which do not effect the viscosity. This formula is fitted to the experimental viscosity measurements [3] carried out at temperatures 790 °C and 810 °C, respectively, for the pseudo-binary HgZnTe melt with zinc mole fraction equal to 0.16. The comparison of the theory with experiment permits both the first order rate coefficient for Te chain depolymerization and the pseudo first order rate coefficient for Te atom chain formation to be evaluated as functions of temperature.

Theory

We let η_o be the Newtonian viscosity of the melt in the absence of Te atom chains. If c g cm^{-3} of Te polymer are created in the melt, the viscosity, η, is determined by the semi-empirical formula

$$\eta/\eta_o = 1 + K\langle M\rangle^a c \qquad (1)$$

where K is a constant, and "a" is an index that depends upon the shape of the dissolved macromolecules [15]. The value of "a" varies from ½ for a random coil [15] to 2 for a rigid rod [17]. For a polymer that is not monodisperse, $\langle M\rangle$ is the "viscosity average" molecular weight [18] defined by

$$\langle M\rangle^a = \frac{\sum_{i=1}^{\infty} c_i M_i^{1+a}}{\sum_{i=1}^{\infty} c_i M_i} \qquad (2)$$

In Eq.(2), M_i and c_i are the molar mass and mass concentration in mol cm^{-3} of the i-th molecular weight fraction, respectively.

The elements, sulfur and selenium, polymerize to form helical chains, a structure intermediate between the random coil and the rigid rod. Without *a priori* knowledge of the structure of our proposed tellurium atom chains, we assume for mathematical convenience that a = 1. Making this assumption and noting that

$$c = \sum_{i=1}^{\infty} c_i M_i \tag{3}$$

we can substitute Eq. (2) into Eq.(1) to obtain

$$\eta/\eta_o = 1 + K \sum_{i=1}^{\infty} c_i M_i^2 \tag{4}$$

Given a kinetic scheme for calculating the time dependence of the $\{c_i\}$, we can use Eq. (4) to evaluate the time dependence of the viscosity.

If M_1 is the atomic weight of a tellurium, the molar mass of a tellurium j-mer is $M_j = jM_1$. The lowest molecular weight polymer fraction is the dimer with j = 2; hence, Eq. (4) becomes

$$\eta/\eta_o = 1 + KM_1^2 \sum_{j=2}^{\infty} j^2 c_j(t) \tag{5}$$

The next step is to compute $c_j(t)$ as a function of time.

Let symbol, (1), represent a single Te atom, (2) represent a dimer of Te atoms, and (j) a j-mer. We propose the following simple kinetic scheme for the polymerization of tellurium atoms:

$$\begin{array}{lllll} (1) + (1) & \rightarrow (2) & \rightarrow & \text{inactive} \\ (1) + (2) & \rightarrow (3) & \rightarrow & \text{inactive} \\ g \quad g & \quad g & & g \\ g \quad g & \quad g & & g \\ g \quad g & \quad g & & g \\ (1) + (j-1) & \rightarrow (j) & \rightarrow & \text{inactive} \end{array} \tag{6}$$

The second-order rate coefficient for the dimerization of two Te atoms is k''. Since the mechanism assumes the stepwise addition of single Te atoms, the rate coefficient for the formation of each succeeding j-mer is also k''. Once formed, however, we assume that each j-mer can also disappear into a form, which is inactive, so far as the viscosity is concerned. The first-order rate coefficient for this inactivation is k'. Since the HgZnTe

melt is a pseudobinary formed from the compounds HgTe and ZnTe [2], inactivation may result by the pseudo first-order reaction of a Te j-mer with metal atoms to reform the compounds, or in the case of the higher j-mers, by a first order cyclization reaction to form Te rings. In any case, the essential role of the inactivation reaction is to prevent unbounded growth of the average molecular weight. To account for the time dependence of the viscosity, the average molecular weight should increase with time and approach a constant value asymptotically.

The concentration of tellurium (50 mole %) in the melt is so high that we can safely assume that little of the initial Te atom population is depleted as the j-mers form. For this reason, we can set $c_1(t) = c_1(0) = \text{constant}$. According to the kinetic scheme, the rate of formation of the dimer is thus the constant, $F = k''(c_1(0))^2$. The subsequent formation steps then become pseudo first-order with rate constant $k = k''c_1(0)$. Using this notation, the rate equations governing the reactions in Eqs.(6) are

$$\begin{aligned}
\frac{dc_2}{dt} &= F - (k+k')c_2 \\
\frac{dc_3}{dt} &= kc_2 - (k+k')c_3 \\
g &\qquad g \\
g &\qquad g \\
g &\qquad g \\
\frac{dc_j}{dt} &= kc_{j-1} - (k+k')c_j
\end{aligned} \tag{7}$$

We can reduce this system of differential equations to a system of algebraic equations by introducing Lapace transforms.

In the standard fashion [19] we define the Laplace transform, $\hat{c}_j(s)$, of the time function, $c_j(t)$, as

$$\hat{c}_j(s) = \int_0^\infty e^{st} c_j(t)\,dt \tag{8}$$

Because it is the quenching of the melt that produces the conditions satisfactory for polymerization, we can assume that there is no j-mer present initially, and $c_j(0) = 0$ for all $j \geq 2$. After Laplace transformation, the system of Eqs.(7) becomes

$$
\begin{aligned}
(s+\lambda)\hat{c}_2(s) &= F/s \\
(s+\lambda)\hat{c}_3(s) &= k\hat{c}_2(s) \\
g &\quad g \\
g &\quad g \\
g &\quad g \\
(s+\lambda)\hat{c}_j(s) &= k\hat{c}_{j-1}(s)
\end{aligned}
\tag{9}
$$

where we have defined

$$\lambda = k + k' \tag{10}$$

Eqs.(9) can be solved iteratively to obtain

$$
\begin{aligned}
\hat{c}_2(s) &= \frac{F}{s(s+\lambda)} \\
\hat{c}_3(s) &= \frac{kF}{s(s+\lambda)^2} \\
g &\quad g \\
g &\quad g \\
g &\quad g \\
\hat{c}_j(s) &= \frac{k^{j-2}F}{s(s+\lambda)^{j-1}}
\end{aligned}
\tag{11}
$$

Inverting these functions to the time domain [19], we find

$$c_j(t) = \frac{k^{j-2}F}{(j-2)!}\int_0^t d\tau\, \tau^{j-2}e^{-\lambda\tau}, \qquad j \geq 2 \tag{12}$$

For each value of j, the integral in Eq.(12) can be evaluated by parts. The results are summarized in Appendix A. A few examples of the functions that are obtained have been plotted in Figure 1.

Closed forms for the functions, $c_j(t)$, are not required to evaluate the sum on the right hand side of Eq.(5), however. After substituting Eqs.(12) into Eq.(5) and interchanging the integral and the sum, we obtain

$$\frac{\eta}{\eta_o} = 1 + KF\left[\int_0^t d\tau\, e^{-\lambda\tau}\sum_{j=2}^{\infty}\frac{j^2}{(j-2)!}(k\tau)^{j-2}\right] \tag{13}$$

The sum in Eq.(13) is evaluated in Appendix B. The result is

$$\frac{\eta}{\eta_o} = 1 + KF\int_0^t d\tau\left((k\tau)^2 + 5(k\tau) + 4\right)e^{-k't} \tag{14}$$

The elementary integral that remains in Eq.(14) can be evaluated by parts to obtain

$$\eta/\eta_o = 1 + \beta\left[\left(\alpha(2\alpha+5)+4\right) - \left(\alpha^2(k't)^2 + \alpha(2\alpha+5)(k't) + \alpha(2\alpha+5) + 4\right)e^{-k't}\right] \tag{15}$$

where we have set

$$\alpha = k/k' \tag{16}$$

and

$$\beta = FKM_i^2/k' \tag{17}$$

After defining

$$\gamma = 2\alpha^2 + 5\alpha + 4 \tag{18}$$

Eq.(15) can be cast in the form

$$(\eta/\eta_o - 1)/\beta\gamma = \left(1 - e^{-k't}\right) - (1/\gamma)\left(\alpha(2\alpha+5) + \alpha^2(k't)\right)(k't)e^{-k't} \tag{19}$$

According to Eq.(19), the viscosity relaxes with the specific rate, k', and reaches the limit $\eta_o(1+\beta\alpha)$ as t approaches infinity.

Discussion

Figures 2 and 3 show Eq.(19) plotted for comparison with the experimental data. In making this comparison, we began by equating the viscosity of the unpolymerized melt, η_o, to the earliest (which was also the lowest) viscosity value in the data set. The numerical values of α, β, γ, and k' then were adjusted so as to obtain the best fit of Eq.(19) to the time dependence of the data. The values of these parameters plus the derived parameter, k, are listed in Table 1.

At both temperatures, the fit of Eq.(19) to the data dictated a very small value for α. This is because the existing data points form a curve which is everywhere concave down, whereas Eq. (19) evaluated for substantial values of α is slightly concave up at early times. Additional early time viscosity data need to be collected to search for the presence of this kind of curvature.

Every molecular weight fraction, $c_j(t)$, contributes to the final value of the viscosity. This follows as a consequence of the term, $1 - \exp(-\lambda t)$, which approaches unity at long

times and which appears in each of Eqs.(A.2) – (A.4). As the time approaches infinity, dc_j/dt goes to zero, and the rate of formation of a j-mer is just balanced by the sum of its rate of deactivation and its rate of polymerization to form a (j + 1)-mer.

Since k is small, the values of k′and λ are nearly the same; hence, according to Eqs. (A.1)-(A.4), the ratio, $c_j(t)/c_2(t)$, becomes at long times equal to α^{j-2}. Because $\alpha << 1$, the steady state concentration of the j-mer relative to that of the dimer decreases rapidly with j.

According to Table 1, the value of k decreases with increasing temperature. Because k is only a *pseudo* first order rate constant, however, it need not increase with increasing temperature, as otherwise would be expected for the rate constant for an elementary reaction. Indeed, since k is the product of an elementary rate constant, k″, and the Te atom concentration, $c_1(0)$, k can display a negative effective activation energy if $c_1(0)$ decreases for some reason with increasing temperature. This might occur, for example, if simultaneously with polymerization, Te atoms were also involved in an endothermic equilibrium with Te atom rings. Ring structures are known, for example, in the case of sulfur and selenium [7]. Since Te is in Group VI, eight membered rings would be favored [20].

By contrast, k′ is the rate coefficient for an elementary reaction. If we assume that k′ satisfies the Arrhenius equation, $k' = A'\exp(-E'RT)$, we can use the value of the gas law constant, R, and the two values of k′ listed in the table to estimate the activation energy for destruction of a j-mer. We find E′= 442 kJ/mol. This value is somewhat larger than the double bond dissociation energy in gaseous Te [21]. Ignoring solvation effects, our estimate of E′ may imply that deactivation step in Eqs. (1) involves breaking of more than one bond joining Te atoms in the chain.

We note that the rotating cup method is directly sensitive to the kinematic viscosity, which is the ratio of the Newtonian viscosity to the mass density of the liquid [5, 6]. In analyzing the data, we have used the ratio of the measured *kinematic* viscosities to represent the ratio of the *Newtonian* viscosities, which is required to evaluate the left hand side of Eq.(19). In doing so, we are assuming that the density of the melt is unaffected by the slight polymerization of the Te atoms.

These provisos not withstanding, the viscosity is one of the most sensitive measures of polymer molecular weight, and its determination is an excepted standard method for following the kinetics of polymerizing systems [22]. Thus a kinetic explanation for the relaxation of viscosity in HgZnTe is not without plausibility.

Acknowledgements

This work was completed while J. K. Baird was a NASA/ASEE summer faculty fellow at the Marshall Space Flight Center. Y. W. Kim would like to thank the NASA EPSCoR program for support.

Appendix A

For the first few values of j, the integral in Eq.(12) can be evaluated by parts. The results are:

$$\frac{\lambda c_2(t)}{F} = 1 - e^{-\lambda t} \tag{A.1}$$

$$\frac{\lambda^2 c_3(t)}{kF} = \left(1 - e^{-\lambda t}\right) - (\lambda t)e^{-\lambda t} \tag{A.2}$$

$$\frac{\lambda^3 c_4(t)}{k^2 F} = \left(1 - e^{-\lambda t}\right) - \left(\frac{1}{2}(\lambda t) + 1\right)(\lambda t)e^{-\lambda t} \tag{A.3}$$

$$\frac{\lambda 4 c_5(t)}{k^5 F} = \left(1 - e^{-\lambda t}\right) - \left(\frac{1}{6}(\lambda t)^2 + \frac{1}{2}(\lambda t) + 1\right)(\lambda t)e^{-\lambda t} \tag{A.4}$$

Appendix B

After expansion of the factor $(p+2)^2$, the integral in Eq.(13) becomes

$$\int_0^1 d\tau\, e^{-\lambda\tau} \sum_{p=0}^{\infty} (p+2)^2 \frac{(k\tau)^p}{p!} = \int_0^1 d\tau\, e^{-\lambda\tau} \left[\sum_{p=0}^{\infty} \frac{p^2 (k\tau)^p}{p!} + 4\sum_{p=0}^{\infty} \frac{p(k\tau)^p}{p!} + 4\sum_{p=0}^{\infty} \frac{(k\tau)^p}{p!} \right] \tag{B.1}$$

The third sum in Eq.(B.1) can be evaluated by recognizing the series expansion for the exponential function.

$$\sum_{p=0}^{\infty} \frac{(k\tau)^p}{p!} = e^{k\tau} \tag{B.2}$$

The second sum in Eq. (B.2) can be evaluated by recognizing the exponential function and its first derivative. The computation is:

$$\sum_{p=0}^{\infty} \frac{p(k\tau)^p}{p!} = (k\tau)\sum_{p=0}^{\infty} \frac{p(k\tau)^{p-1}}{p!} = (k\tau)\frac{\partial}{\partial(k\tau)} e^{k\tau} = (k\tau)e^{k\tau} \tag{B.3}$$

Finally the first sum in Eq.(B.3) can be evaluated by recognizing the exponential function and its first two derivatives. The computation is:

$$\sum_{p=0}^{\infty}\frac{p^2(k\tau)^p}{p!}=\sum_{p=0}^{\infty}\frac{p(p-1)(k\tau)^p}{p!}+\sum_{p=0}^{\infty}\frac{p(k\tau)^p}{p!}$$
$$=(k\tau)^2\frac{\partial^2}{\partial(k\tau)^2}e^{k\tau}+(k\tau)\frac{\partial}{\partial(k\tau)}e^{k\tau} \qquad (B.4)$$
$$=(k\tau)^2e^{k\tau}+(k\tau)e^{k\tau}$$

After substitution of Eqs.(B.2) – (B.3) into Eq.(B.1), we obtain the final result,

$$\int_0^t d\tau\, e^{-\lambda\tau}\sum_{p=0}^{\infty}(p+2)^2\frac{(k\tau)^p}{p!}=\int_0^t d\tau\left((k\tau)^2+5(k\tau)+4\right)e^{-k'\tau} \qquad (B.5)$$

where we have used $\lambda = k + k'$.

References

[1] Petty, M. C. And Juhasz, J. (1976) *J. Phys.* D **9**, 1605.

[2] Yu, T.-C. And Brebrick, R. F. (1992). *J. of Phase Equilibria* **13**, 476.

[3] Mazuruk, K., Su, Ching-Hua, Sha Yi-Gao and Lehoczky, S. L. (1996). *J. Appl. Phys.* **79**, 9080.

[4] Su, Ching-Hua, Sha, Yi-Gao and Lehoczky, S. L. (1996). *J. Appl. Phys.* **80**, 137.

[5] Thresh, H. R. (1962). *Trans. ASME* **55**, 790.

[6] Kestin, J. and Newell, G. F. (1957). *J. Appl. Math. Phys.* **8**, 433.

[7] Thorne, P. C. L. and Roberts, E. R. (1949). Inorganic Chemistry (Interscience Publishers, New York), pp. 126-132.

[8] Allcock, H. R. and Lampe, F. W. (1990). Contemporary Polymer Chemistry (Prentice-Hall, Inc., Englewood Cliffs, NJ), pp.215-217.

[9] Zallen, R. (1983). Physics of Amorphous Semiconductors (John Wiley, New York), p. 94.

[10] Tobolsky, A. V. and MacKnight, W. J. (1965) Polymeric Sulfur and Related Polymers (Interscience, New York), pp. 1-2.

[11] Cabane, B. and Friedel, J. (1971). *J. de Physique* **32**, 73.

[12] Yamaguchi, T., Ohtani, H. and Yonezawa, F. (1999). *J. Non-Cryst. Solids* **250-252**, 437.

[13] Tsuzuki, T., Makato, Y. and Endo, H. (1995). *J. Phys. Soc. Jpn.* **64**, 485.

[14] Bichara, C., Raty, J.-Y. and Gaspard, J.-P. (1996), *Phys. Rev.* **B** 53, 206.

[15] Alberty, R. A. (1987) Physical Chemistry, 7th Ed. (John Wiley, New York), pp.813-816.

[16] Ref. 8, Chapt. 14.

[17] Alfrey, T. (1948). Mechanical Behavior of High Polymers (Interscience, New York), p.466.

[18] Ref. 8, p. 388.

[19] Abramowitz, M. and Stegun, I. (1972). Handbook of Mathematical Functions, NBS Aplied Mathematics Series No. 55 (U. S. Government Printing Office, Washington, DC), pp. 1020 and 1022.

[20] Mingos, D. M. P. and Wales, D. J. (1990) Introduction to Cluster Chemistry (Prentice Hall, Englewood Cliffs, NJ) p. 73.

[21] Weast, R. C. and Lide, D. R. (1989/90). CRC Handbook of Chemistry and Physics, 70th Ed. (CRC Press, Boca Raton, FL), p. F-200.

[22] Peebles, L. H., (1971). Molecular Weight Distributions in Polymers. (Interscience, New York), p. 38

Table 1. Parameter values resulting from fitting Eq. (19) to HgZnTe viscosity data as shown in Figures 2 and 3. The value of k was calculated using Eq. (16). The Zn mole fraction in the pseudo-binary melt was 0.16.

T(K)	$\alpha\left(10^{-4}\right)$	β	$(\gamma-4)\left(10^{-4}\right)$	$k\left(10^{-6}h^{-1}\right)$	$k'\left(10^{-2}h^{-1}\right)$
1063	1.6	0.40	8.2	4.6	2.9
1083	0.10	0.078	0.5	0.73	7.3

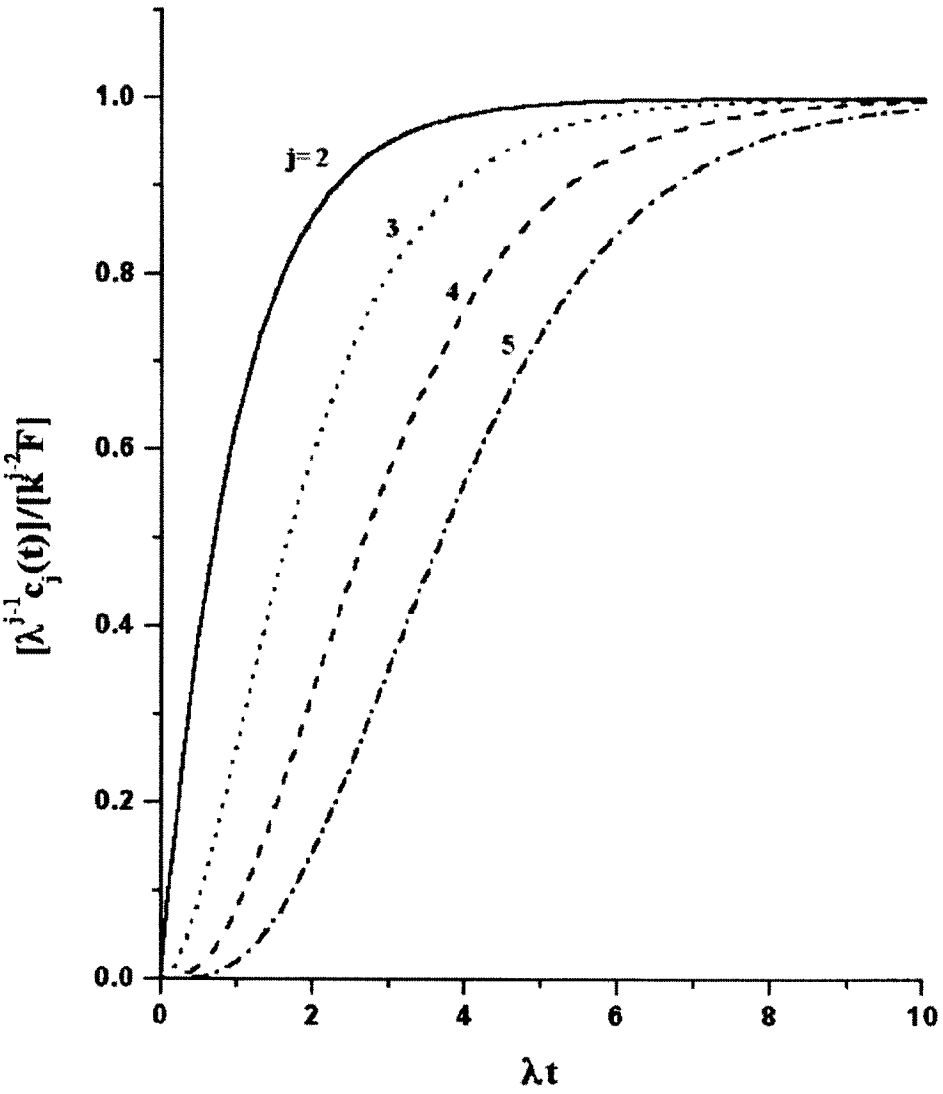

Figure 1. Plots of the functions defined by Eqs. (A.1)-(A.4).

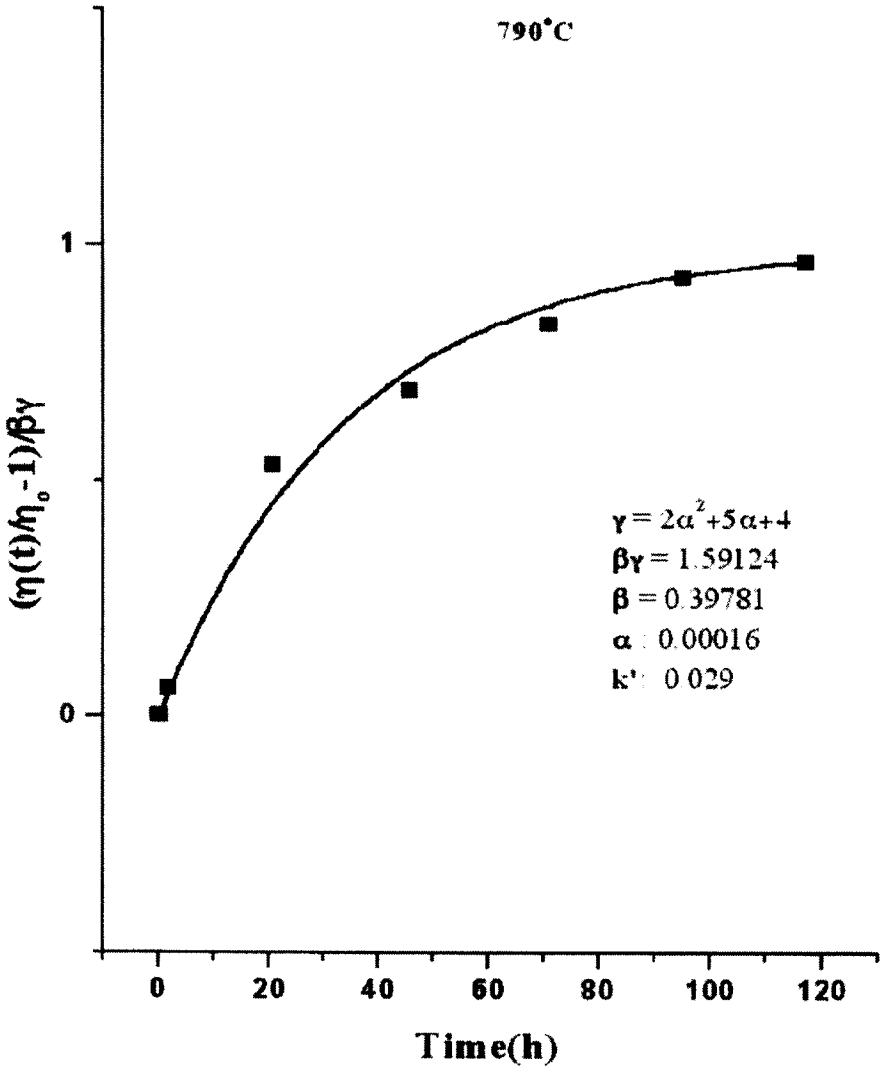

Figure 2. Curve fit of the function defined by Eq. (19) to the experimentally observed time dependence of the viscosity of molten HgZnTe at 790 °C .

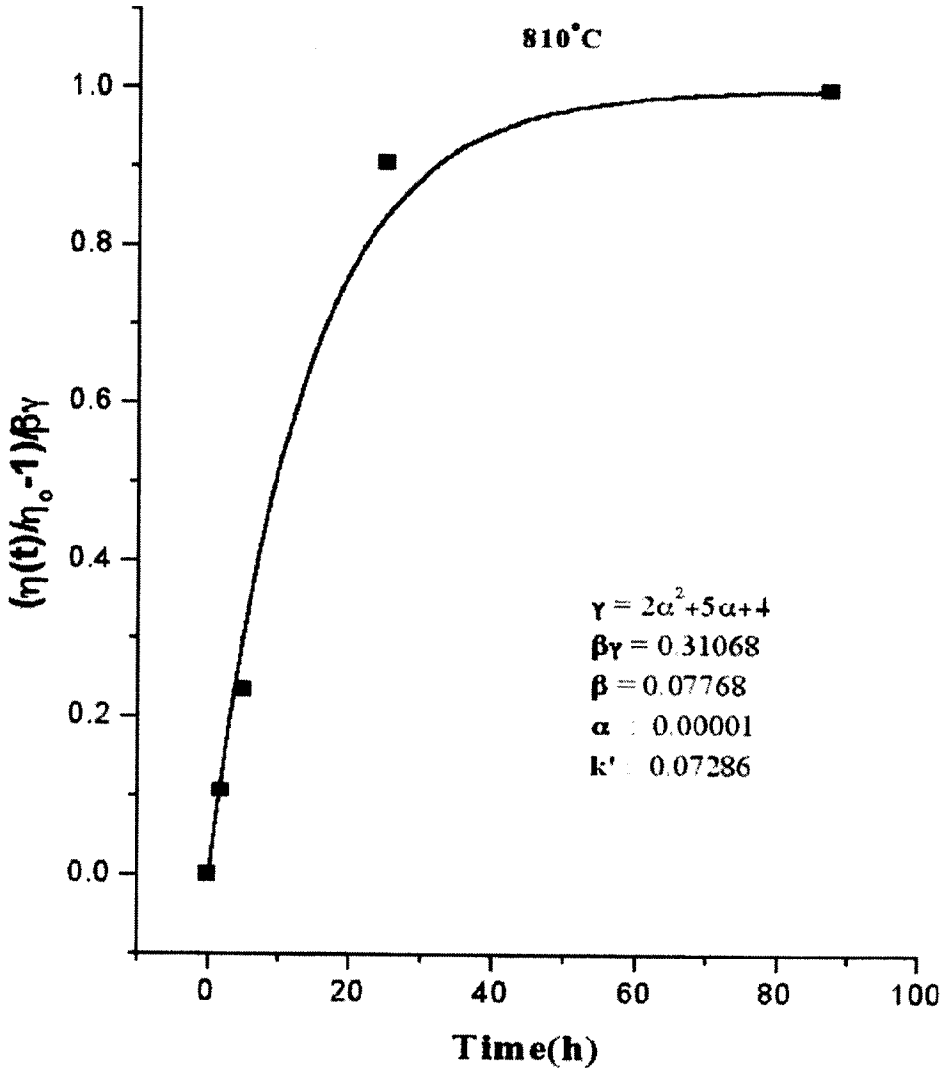

Figure 3. Curve fit of the function defined by Eq. (19) to the experimentally observed time dependence of the viscosity of molten Hg Zn Te at 810 °C.

2001

NASA/ASEE SUMMER FACULTY FELLOWSHIP PROGRAM
THE UNIVERSITY OF ALABAMA IN HUNTSVILLE

ADVANCED COMPUTING TECHNOLOGIES FOR ROCKET ENGINE PROPULSION SYSTEMS: OBJECT-ORIENTED DESIGN WITH C++

Prepared By:	Gete Bekele
Academic Rank:	Assistant Professor
Institution and Department:	Oakwood College Mathematics and Computer Science Department
NASA/MSFC Directorate:	Engineering
MSFC Colleague:	Dr. Luis Trevino Flight Software Group ED 14

Introduction

Science concerns itself with the discovery of basic principles, laws, and relationships. On the other hand, engineering deals with the practical application of science to develop useful artifacts. Software engineering attempts to combine sound engineering principles of analysis, design, management, testing with scientific concepts of computing in the production of reliable and cost-effective computer software [1].

The process of software development involves elements of great complexity, depending the project's size, purpose, and the number of people involved in development. According to Grady Booch, a noted author in the area of object-oriented development, software complexity is an essential property. He states that, the complexity is due to the problem domain, the difficulty of managing the development process and the problem of characterizing the behavior of a system. Generally, these complexities could be inescapable. This is mainly due to conflicting requirements, performance issues, cost and survivability and reliability, which will finally affect the outcome of the project in question [2]. Examples of such complex systems are the requirements for an electronic system of a multi-engine aircraft, a cellular phone switching system or an autonomous robot.

Booch further states that, during development, planned or not, large software systems tend to evolve over time, a condition that is often labeled as software maintenance. To be more precise, it is maintenance when we correct errors; it is evolution when we respond to changing requirements; it is preservation when we continue to use extraordinary means to keep an ancient and decaying piece of software in operation. Unfortunately, reality suggests that an inordinate percentage of software development resources are spent on software preservation.

Software developers have always followed certain methods of devising solutions to problems. For a long time, a popular approach that has been used from the early days of computing was top-down design. Recently, Object-Oriented Design (OOD) has become the approach of choice by many software developers [1]. Whatever approach or method of design has been taken, the major concern is on the software quality. Today, quality is measured by readability, robustness, verifiability, validity, simplicity, modifiability, reusability, compatibility, efficiency, and ease of use, portability, and integrity. A maximum efficiency may be required in some applications dealing with real-time systems that are mission critical.

Purpose:
To explore the use of advanced computer technologies with an emphasis on object-oriented design to be applied in the development of a software for a rocket engine to improve vehicle safety and reliability. The actual focus is on phase 1 of this project, smart start sequence module (Appendix 2).

Objectives:
1. To use current sound software engineering practices, object-orientation
2. To improve on software development time, maintenance, execution and management
3. To provide an alternate design choice for control, implementation, and performance

Requirements:
In order to implement the above stated objectives, the following knowledge areas or understanding were required.
1. Rocket engine propulsion system
2. Software engineering for embedded flight software system
3. Object-oriented technology and design

Methodology:
In order to meet the above stated objectives the following methods were employed:
1. Reviewed existing literature on rocket engine propulsion system
2. Researched Object Oriented Technology (OOT)
3. Researched current Object-Oriented (OOD) tools for best software engineering practice
4. Analyzed the schematic engine diagram and developed requirements database, i.e., terminology to be applied to the design (Appendix 1)
5. Determined the method and the Modeling Language to be used for design
6. Applied the selected design tool to rocket engine smart start sequence model
7. Surveyed current MSFC's software development practices (Appendix 3)

Why Object-Oriented Technology (OOT)?
Before the advent of object-oriented technology, there were various ways of software development approaches, from no method to some kind of methods that have not satisfied the needs of development. As time goes on, each of the methods were gradually improved to provide better technologies. Currently, OOT has become the choice of software development mainly for larger systems. Older methods are still in use by many.

In the 1960s's there was no development methods. Developers built small and relatively simpler applications and using simpler programming languages such as Assembly, FORTRAN or COBOL based on their individual creativity. This led to what is known as spaghetti code and GOTO statements that were difficult to maintain. In the 1970's, some developers came up with methods of development that used functions as a building block. That was accepted as a much better way, especially for modular programming in addition to structured analysis and design. However, this method provided no data management capacity. Though structure analysis and design was successfully applied, it led to larger maintenance and continuous change. In some

cases rebuilding the applications was necessary. This problem created a need for other software development methods [4].

In the 1980's, Peter Chen the developer of entity-relationship diagram and Ed Codd the designer of relational database responded to the need. They introduced a new way of developing software based on an entity as a building block. This discovery gave a new methodology, especially in data modeling for business applications. However, this method did not satisfy system requirements related to functions as well as capturing dynamic behavior of systems. It also lacked exception handling mechanism and declarative semantics or rules. As a result of these gradual development, the object-oriented method came into existence.

According to Lee (2001), the object-oriented technology is the only method that provides software developers with a method that supports all views of a system. With this method, developers are able to manage the complexities inherent in software development. OOT views, the application as a dynamic network of collaborating objects [7] which helps developers to view the problem in more meaningful manner. Overall, one can manage more aspects of the problem domain and can produce more flexible and maintainable software, which was difficult to do in previous methods.

Object-Oriented Programming Languages (OOPL)

There are a variety of languages including Simula-67, SmallTalk, Eiffel, Ada, Object-Pascal and C++. However, based on the definition of object-orientation, special OOT classification has been assigned like, object-based, class-based, object-oriented, advanced and leading-edge programming languages. Based on this classification, Ada is an object-based language, which means it uses encapsulation and objects, but does not support a class mechanism, inheritance relationships, dynamic behavior and rules.

Grady Booch defined object-oriented programming (OOP) as a method of implementation in which programs are organized as a cooperative collection of objects, each of which represents an instance of some class, and whose classes are all members of a hierarchy of classes united via inheritance relationships [2]. There are three important parts of the above definition:

- OOP uses objects, not algorithms as its building block
- Each object is an instance of a class
- The classes are related to one another through inheritance

Under this definition, only Smalltalk, Object Pascal, C++ and Eiffel are object-oriented. He said that a program may appear OO, but if any of the above elements are missing, it is not.

All object-oriented languages are known to be descended from Simula, which was derived from Algol, a procedural language. Originally, this language was a used in modeling industrial and scientific applications. This introduced an approach to software design based on modeling the direct representation of real world objects in a program [6]. Since then, the above listed languages were introduced as part the object oriented technology.

The C++ programming language was designed to build on the strength of C that it can support data abstraction. Its object-oriented characteristics was taken from Simula and Smalltalk [10]. Due to this, C++ was categorized as a hybrid OOL, while Smalltalk and Eiffel are recognized pure OOLs.

The argument is that, in a pure OO, the power of OOT is not compromised and the programmer has only to master a single paradigm.

According Hares et. al (1994), once the concept of object-oriented development is understood, any general programming language may be used as an object-oriented language, with a varying degree of success [5]. But, he admits that, where there is no built-in language support, it is very difficult. However, Grady Booch, does not accept such a compromise and says, " ...one can fake OOP in a non-OOP languages such as Pascal, COBOL or Assembly, but it is horribly ungainly to do so". Also, Bjarne Stroustrup, the designer of C++ supports Booch's idea by saying, "if the term 'object-oriented language means anything, it must mean a language that has the mechanism that supports the object-oriented style of programming. A language does not support a technique if it takes exceptional effort or skill to write such programs".

Languages	**Style**	**Applications Examples**
Procedure oriented	Algorithms	Best suited for designing computation-intensive operations
Object-oriented	Classes and objects	**Best suited to the broadest set of applications**
Logic oriented	Goals, often expressed in predicate calculus	
Rule-oriented	If-then rules	Best for designing knowledge base
Constraint-oriented	Invariant relationships	

Table 1: Five main kinds of programming styles

Based on table 1, Grady Booch concluded that the object model has proven to be a unifying concept, not only in programming, but also in the design of user interfaces, databases, and even computer architectures [2]. Overall, Object oriented analysis and design is an evolutionary development, not a revolutionary one. It builds upon the proven programming practices of the past than breaking away from it.

Why C++

C++ has all the OO features and a resemblance to the C programming language which makes it easily adoptable by many. According to Seed [10], the author of an OOP in C++, major features C++ include:

- A superset of the C language
- Strong type checking than C
- Support for data abstraction and OO programming
- Classes and abstract classes that encapsulate data and functions which operate on a class' data defining a given structure and behavior
- Inheritance and multiple inheritance, enabling the creation of hierarchies of classes

- Support for run-time polymorphism via virtual functions, allowing a class in an arbitrary inheritance hierarchy to redefine its parent's member functions
- Overloading. Overloading functions and member functions allow a function with the same name but with a different member type of arguments, or both, and return type
- Support for the creation of parameterized types, generics or templates and generic functions
- Exception handling or error handling techniques
- Run-time type information (RTTI) to obtain run-time identification of types and expressions
- Namespaces to solve the problem of a single global namespace or scope

Object Management Group

The Object Management Group (OMG) is the leading worldwide organization dedicated to producing a framework and specifications for commercially available object environments. It is dedicated to maximize the portability, reusability, and interoperability of software [11]. Within the OMG, the Object Analysis and Design Special Interest Group is created with a mission to advance the technology and create awareness of object analysis and design as well as encourage the development of applications that exploit the Object Management Architecture. This group surveyed the available methods that were used in object analysis and design and came up with the methods listed in table 2. According to this group, each style of programming has it own conceptual framework. Each style requires a mindset, a different way of thinking about the problem it has to handle. For all things object-oriented, the conceptual framework is the *object model.* There are four major elements of the object model:

- Abstraction
- Encapsulation
- Modularity
- Hierarchy
- And there are three minor elements which are:
- Typing
- Concurrency
- Persistence

Grady Booch states that, "one may program in a language such as Smalltalk, Object-Pascal, C++, Eiffel, or Ada, but the design is going to smell like a FORTRAN, Pascal, or C. However, without a conceptual framework, one may have missed out or otherwise abused the expressive power of the object-oriented language he is using for implementation. More importantly, the complexity of the problem at hand is no likely to have been mastered."

Short name	Method name	Supplier
Booch	Booch Method of Object-Oriented	Rational

	Analysis and Design	
CCM	Class-Centered Modeling	CASElode Consulting
Coad, Yourdon, and Nicola	OOA, OOD, 00P	Object International, Inc.
Demeter	Demeter	Northeastern University, Boston
Fresco	Fresco	Object Engineering
Fusion	Fusion	Hewlett-Packard
Graham/SOMA	Semantic Object Modeling Approach	BIS Information Sys.
IE\O	Information Engineering with Objects	Texas Instruments
MTD	Marketing to Design	ICL
OBA	Object Behavior Analysis	ParcPlace Systems
Objectory	Objectory	Objective Systems SF AB
OGROUP	OGROUP	Olivetti
OOIE	Object-Oriented Information Engineering	James Martin and Co., Intellicorp
OORAM	Object Oriented Role Analysis and Modeling	TASKON A/S
OSMOSYS	OSMOSYS	Winter Partners
Rumbaugh	Object-Oriented Modeling and	Rumbaugh, GE.
SE/OT	Systems Engineering for Object Technology	LBMS
Shlaer/Mellor	Object-Oriented Systems Analysis	Project Technology, Inc.
SSADM	SSADM	CCTA
Wirfs-Brock	Responsibifity-Driven Design	R. Wirfs-Brock
Z++	Z++ Method	Lloyds Register

Source: Object Analysis and Design methods, Andrew T. F. Huff, 1994.

Table 2: Object Analysis and Design Methods

OOD and Unified Modeling Language (UML)

Object-oriented design is a method of design encompassing the process of object oriented decomposition and a notation for depicting both logical and physical as well as static and dynamic models of a system under design. There are two parts of the above definition:

1. OOD leads to object-oriented decomposition, logical breakdown
2. Uses different notations to express different models of the logical (classes & Objects) and physical design of the system (module & process architecture).

The support for object-oriented decomposition is what makes OOD quite different from structured design. The former uses classes and object abstractions to logically structure systems, while the later uses algorithmic abstractions. Object-oriented Analysis (OOA) is a method of analysis that examines requirements from the perspective of classes and objects found in the vocabulary of the problem domain. The products of object-oriented analysis serve as a model from which we may start an object-oriented design. The products of object-oriented design can be used as a blueprint for completely implementing a system using object-oriented programming methods [2].

The OO modeling languages listed in table 2 appeared between mid 1970s and 1980s as methodologies. This gave large-scale developers to experiment with the various methods

developing complex systems. Soon, many discovered the strength and weakness of each methodology. Among these the most notable methods were, Booch's method, Jacobson's OOSE (OO Software Engineering) and Rumbaugh's OMT (object-modeling technology). Booch's method was found to be expressive during design and construction phase, OOSE provided an excellent support to capture requirements and high level design while OMT was found to be useful for analysis and data-intensive information system [9]. Finally, Booch, Rumbaugh and Jacobson agreed to merge their methods to form the Unified Modeling Language. For this reason, they are known as the three amigos, in the OO world.

Since the mid 1990s the UML has emerged as the industry standard for modeling [11] and is being used in the development of a variety of software systems. More recently the OMG has promoted the development of model driven architectures that use UML to specify enterprise applications throughout the software lifecycle. Large corporations such as McDonald Douglas, Intergraph and others use UML in visualizing, specifying and documenting the artifacts of their software intensive systems, covering from the conceptual stage to final development [9]. Overall, the final goal of the UML is established to be:

- To model systems, from system to executables using OOT
- To address the issue of scale inherent in complex, mission critical systems
- To create modeling language usable both by humans and machines

UML uses the following types of diagrams to describe the strategic and tactical analysis in design decisions that must be made when creating an object-oriented system.

A Class Diagram: shows a set of classes, interfaces and collaborations and their relationships these are the most common diagram used in OO systems.

A Use Case Diagram: shows a set of use case and actors (a special kind of class) and their relationships. Use case diagrams address the static view of the system. As well as in organizing and modeling the behavior of a system.

Sequence and Collaboration Diagrams: are kind of interaction diagrams. An interaction diagram shows between object relationships and the messages that may be dispatched among the objects.

State Transition Diagram: shows a state machine, consisting of state transitions, events and activities.

An Activity diagram: is a special kind of diagram that shows the flow of activities within a system. They are especially important in modeling the function of a system and emphasize the flow of control among objects.

A component Diagram: shows the organizations and dependencies among a set of components. This also addresses the static implementation view of a system.

A Deployment Diagram: shows the run-time processing nodes and the components that live on them. Deployment diagrams are related to component diagrams. The node typically encloses one or more components.

Deliverables: Results

Based on the process of OOA and OOD discussed in the previous sections and the application of UML the following results were presented as partial deliverables of the project. These include: the requirements analysis text for the smart sequence module of MC-1 engine, a class diagram (figure 1), a use case diagram (figure 2), a component diagram (figure 3) and a reverse engineered class diagram from C++ code (figure 4) and a C++ code of the engine class diagram (figure 5). As part of documenting the design process, a variety of reports were generated indifferent of formats as shown in figures 5 through 7. The rest of the UML diagrams such as, sequence, activity, state transition diagrams could not be completed due to time constraint.

Requirements analysis text

A. Initiate LOX Flow to TCA
   1. Open Main Oxidizer Valve (MOV)
   2. Are the MOV Switches disqualified?
      a. If yes then continue to wait 0.5 seconds then continue to Open MFVP
      b. If no then start 0.5 second timer then continue to has timer expired?
         1a) if Yes then continue to MFPV
         1b) if No then does switches indicate valve is open
            2a) If yes then continue to MFPV
            2b) If no then return to timer step (a)

B. Initiate Spin-Start
   1) Open Main Fuel Purge Valve (MFPV) / Open SV09
   2) Begin 1.0 timer
   3) Has Timer Expired
      a) if yes then Proceed to shut down
      b) if no then Is Fuel Purge pr above min, Is GG Pc Above min, and Is Fuel Pump Ds Pr above min?
         1a) If yes then continue to Open IFV
         1b) If no then return to timer step (2)

C. Initiate Triethenal aluminum and Triethenal boron flow to TCA
   1) Open Ignition Fuel Valve (IFV)
   2) Begin .5 second timer
      a) If timer expires then proceed to shut down
      b) If timer does not expire then is MCC Pc above Min
         1a) If yes then continue to fire igniter
         1b) If no then return to timer step (2)

D. First Initiate fuel Flow To TCA
   1) Open the Main Fuel Valve (MFV)
   2) Then Begin .5 second Timer

a) If Timer expires Proceed to Shut Down (S/D)
b) If Timer does not Expire Proceed with MCC PC

3) Is Main Combustion Chamber (MCC) and Pressure Chamber (PC) above Min?
   a) If yes, continue to close Oxidizer Bleed Valve (OBV)
   b) If no, go back to step 2 (.5 second Timer).

E. Terminate LOX Bleed

1) Close OBV
2) Are OBV Switches Disqualified
   a) If yes wait .1 sec and continue to Initiate Fuel Flow to GG
   b) If No then begin .1 sec timer
      1a) Has timer expired?
         2a) If yes then continue to Initiate Fuel Flow to GG
         2b) If no, do switches indicate valve is closed?
            3a) If yes then continue to to Initiate Fuel Flow to GG
            3b) If no return to step 1a (has timer expired).

F. Initiate fuel Flow to Gas Generator (GG)

1) Open Gas Generator Fuel Valve (GGFV)
2) Begin 0.2 Timer
   a) If timer expires then proceed to Shut Down
   b) If timer Doesn't expire then continue to GGFV
3) Is GGFV Ds Pr above Min?
   a) if yes then continue to open MOV valve.
   b) If no return to timer step (2)

G. Initiate LOX Flow to GG / Terminate Spin-Start Flow

1) Fire Igniter /Close GLPV,MFPV, and SV09

H. Verify Ramp to M/S

1) Wait .2 seconds
2) Begin ramp0 up timer (1.1)
3) Has timer expired
   a) if yes then initiate M/S Phase
   b) if No then is GG Pc below min and is MCC Pc below Min
      1a) If yes then initiate Shut down,
      1b) If no then return to timer step (3)

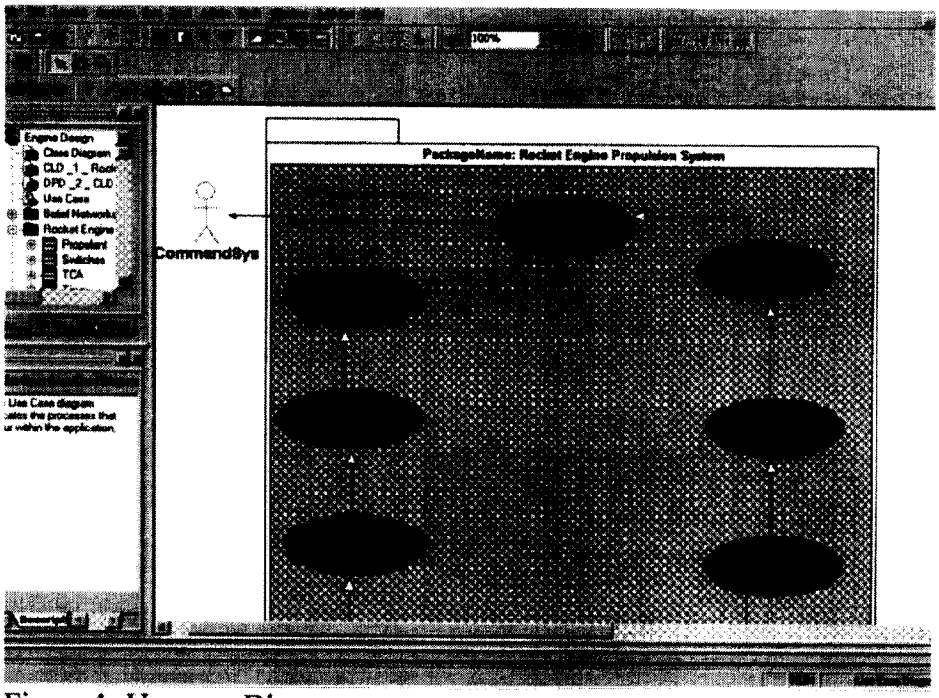

Figure 1: Use case Diagram

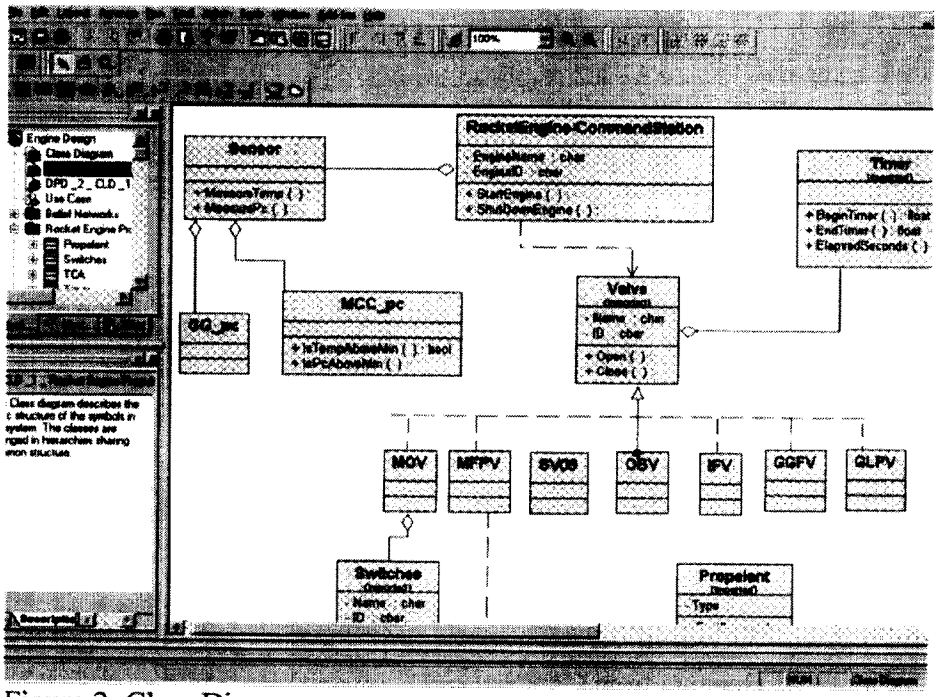

Figure 2: Class Diagram

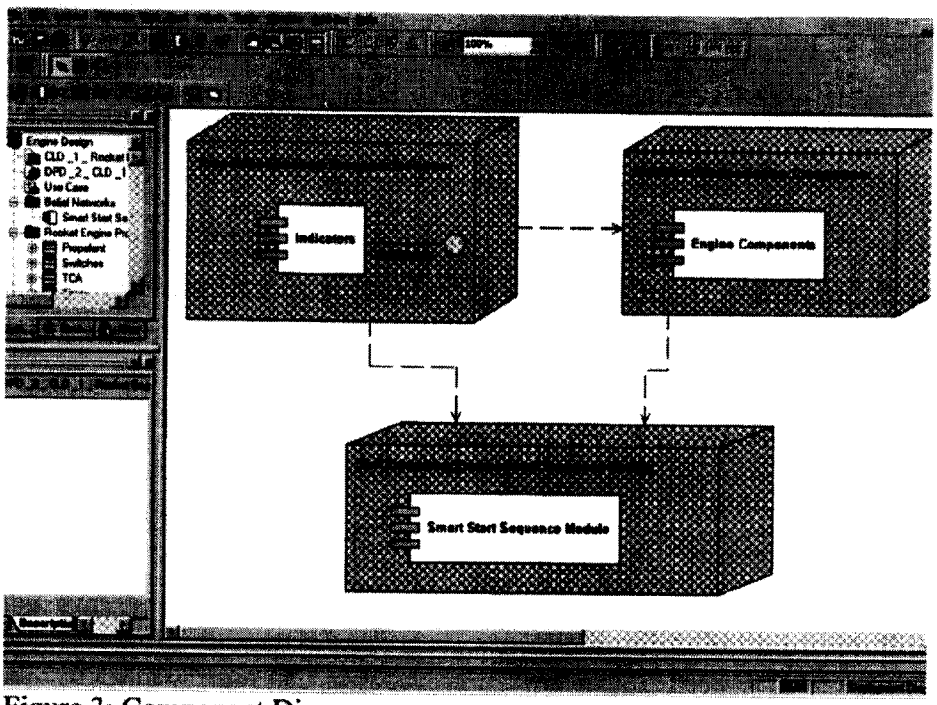

Figure 3: Component Diagram

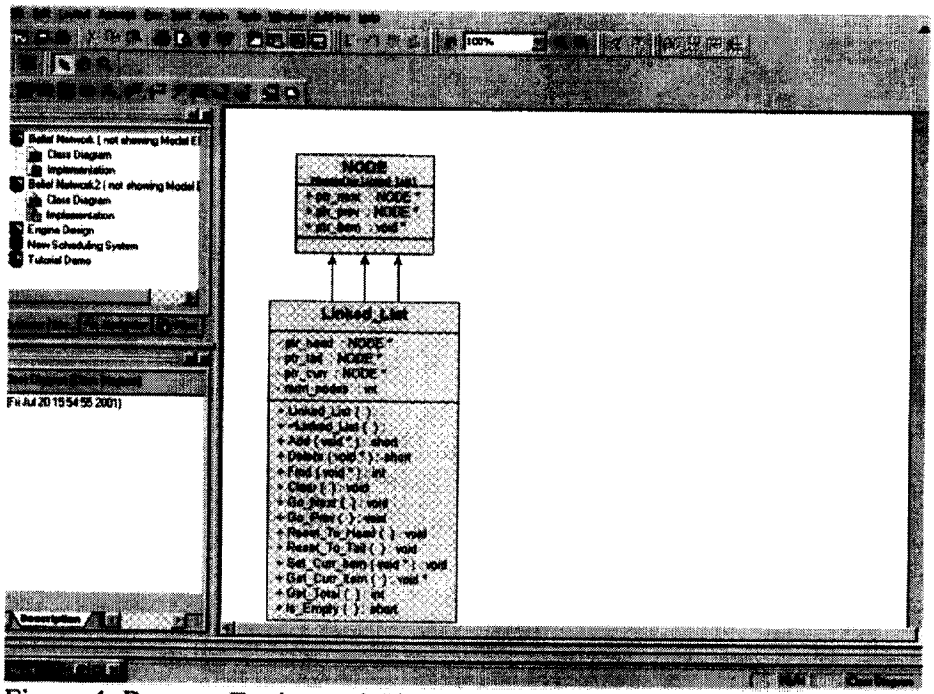

Figure 4: Reverse Engineered Class Diagram from C++ Source Code

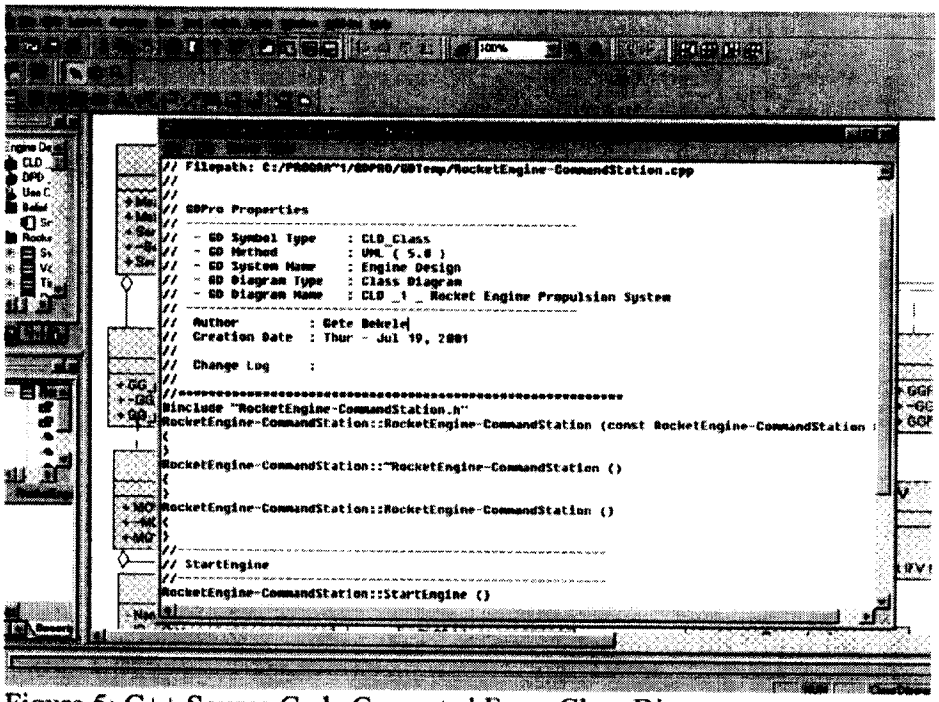

Figure 5: C++ Source Code Generated From Class Diagram

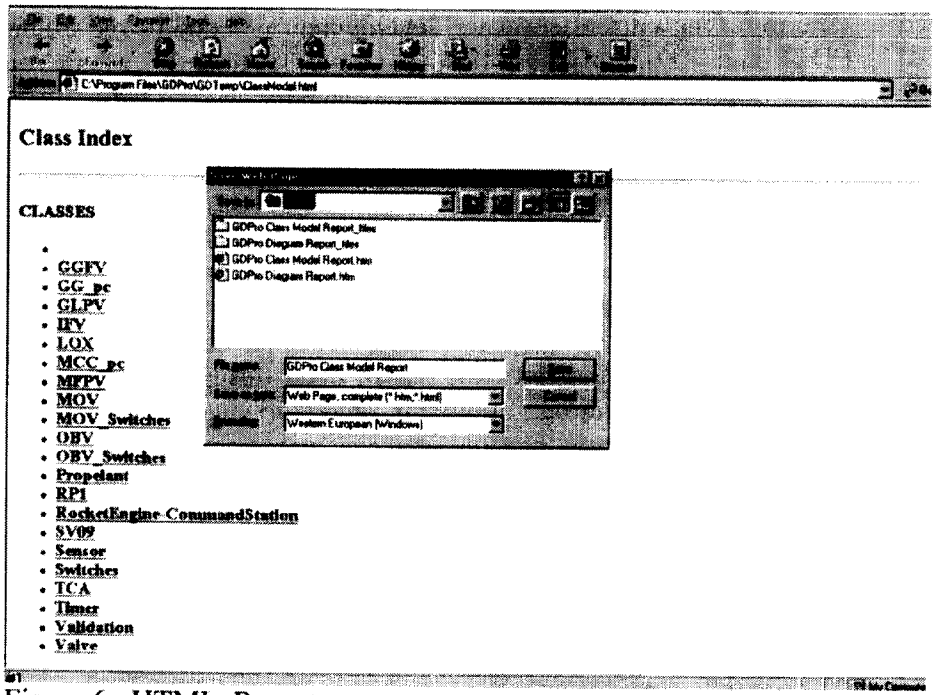

Figure 6: HTML Report

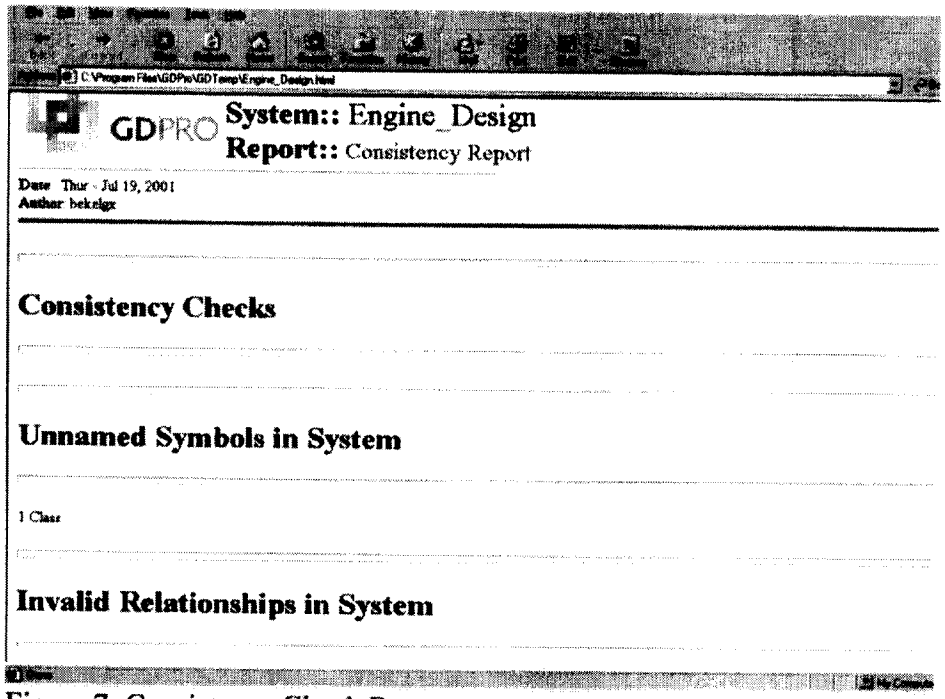

Figure 7: Consistency Check Report

Current Practices at MSFC

A survey was conducted to determine the current software development practice of the Flight Software Group of Ed13, ED14 and ED19 of the MSFC. Out of a total of 44 survey questionnaire distributed, only 22 were completed and returned (Appendix 3). The survey data was analyzed using SPSS, the Statistical packages for social Sciences.

According to this survey, 56.5% of the respondents were software designers and developers, 26.1% testers and 17.1% other professionals. When they were asked the type of programming language they use, 65.2% said C, 4.3% C++ and 12.9% of them a combination of Ada, C, and C++ (Table 3). Among these respondents, about 78.3% of them indicated that their group practices software design, but none indicated knowledge of neither UML nor have training in it (Table 4). Though UML is not adopted, 56.5 indicated the use of other design tools, but not GDPro or Rational Rose which are specific design tools for object-oriented development, generating C++ or Java source code to be used to produce the final executable or application.

Responsibility	Language Practiced

	C	C++	C & C++	Ada	Java	Combined	Total
Software Design & Development	**10** **66.7**	**1** **100.0**	**1** **50**		1 100.0	1 100.0	**13** **56.5%**
Software Testing	**3** **20.0**					2	**6** **26.1%**
Other	**2** **13.3**		**1** **50.0**	1 100.0			**4** **17.4%**
Total	**15** **65.2%**	**1** **4.3%**	**2** **8.6%**	**1** **4.3%**	**1** **4.3**	**3** **12.9%**	**23** **100%**

Table 3: Language Practice by Professional Responsibility

Design Practices	**Professional Responsibility**						
	Design & Development		**Testing**		**Other**		**TOTAL**
	Yes	**No**	**Yes**	**No**	**Yes**	**No**	
Design	**9** **69.2 %**	**3** **23.1**	**5** **83.3**		**4** **100**		**18** **78.3**
UML	**1** 7.7	**12** **92.3 %**		**2** **33.3%**		**4** **100.0**	**1** **4.3**
Tools **GDPro** **Other**	**2** **15.4** **5** **38.5**						**13** **56.5%**
UML Training **NO**							**23** **100.0**
Applied **No** **No answer**							**9** **39.1** **14** **60.9**
Benefit **No** **No answer**							**4** **17.4** **19** **82.6**

OMG **Yes** **No**	**3** **23.1**	**10** **76.9**		**6** **100.0**		**4** **100.0**	 **3 (13.0)** **20** **(87.0)**

Table 4: Design Practice by Professional Responsibility

Recommendations

The survey indicated that only 4.3% of the respondents use pure an OO such as C++, while 12.9% use combinations. There are a number of advantages in adopting the OOT such as, reduced maintenance and complexity, object reuse, timeliness, improved quality and reliability of software developed. According to this survey, the C programming language being the predominantly used language, transition to C++ should not be very difficulty.

With a move to C++, it is advisable to use UML in requirements analysis, design and all phases of development of complex software systems that are developed in house. The Rational suite [8], which includes all the needed tools, every aspect of development is available in house, but limited to one user on a laptop. Probably, upgrading this product to a multi user version may serve the needs of development teams. GDPro, a multi-user system from Embarcadero Technology may serve the same purpose for the fraction of the upgrade price for Rational suite. Transition to programming languages that fully support OOT seem to be more useful for MSFC with the purchase of a UML application that the whole team can access from a central server is invaluable investment for the success of software developed in house.

Summary & Conclusion

Object-Oriented technology is the best approach today for the development of complex systems. Since its inception, developers have tried to reap its benefits as well as build upon it for further improvement. As a result, not only powerful OO languages such as C++ have been developed, but also an expressive modeling language like the UML, that is useful from inception to final development stage of complex systems. Its ability to re-engineer existing codes into UML and generate source code and database from design has made it a preferred choice in the software industry.

Appendix 1: MC-1 Engine Schematic Diagram

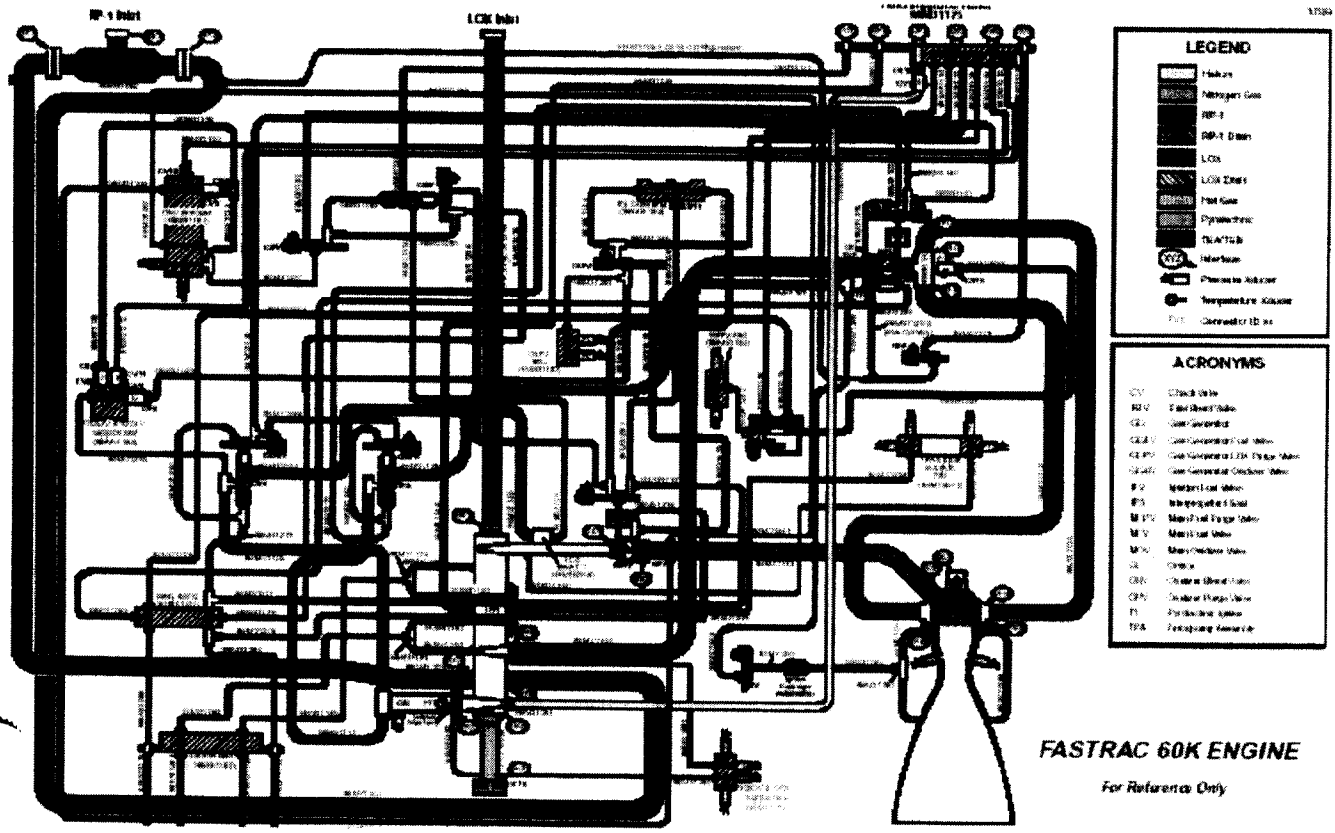

Appendix 2: Smart Start Sequence Model of MC-1 Engine

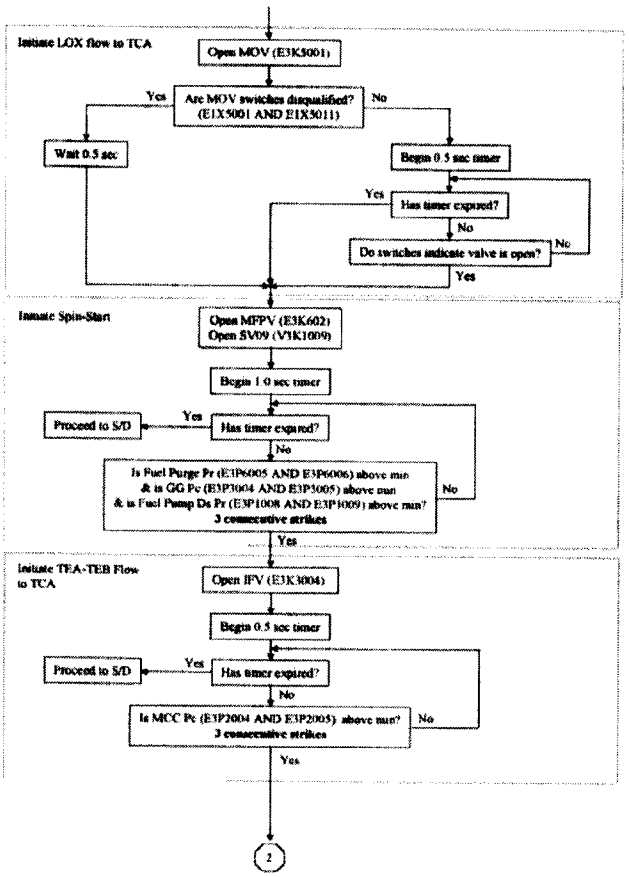

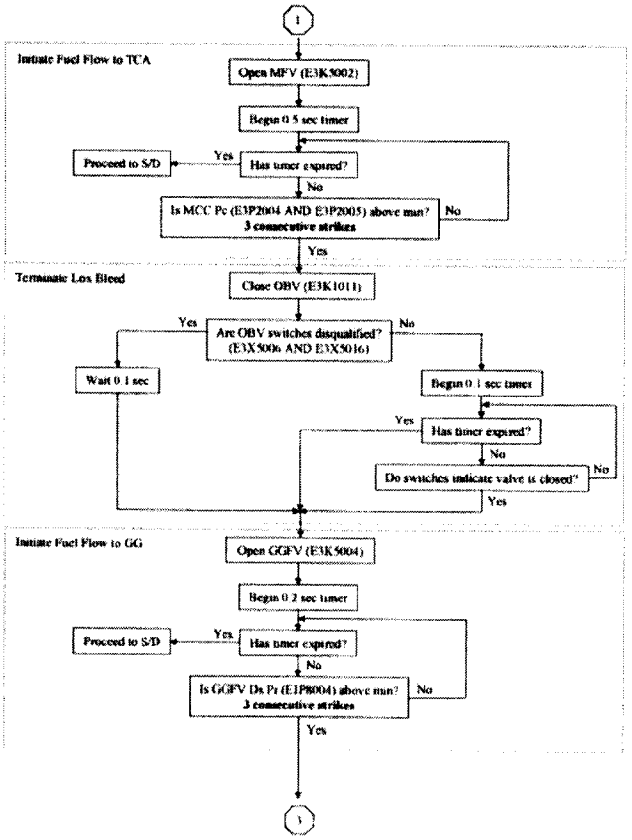
1
Initiate Fuel Flow to TCA
Open MFV (E3K3002)
Begin 0.5 sec timer
Proceed to S/D
Yes
Has timer expired?
No
Is MCC Pc (E3P2004 AND E3P2005) above min?
3 consecutive strikes
No
Yes
Terminate Lox Bleed
Close OBV (E3K1011)
Yes
Are OBV switches disqualified?
(E3X5006 AND E3X5016)
No
Wait 0.1 sec
Begin 0.1 sec timer
Yes
Has timer expired?
No
Do switches indicate valve is closed?
No
Yes
Initiate Fuel Flow to GG
Open GGFV (E3K5004)
Begin 0.2 sec timer
Proceed to S/D
Yes
Has timer expired?
No
Is GGFV Ds Pr (E3P8004) above min?
3 consecutive strikes
No
Yes
1

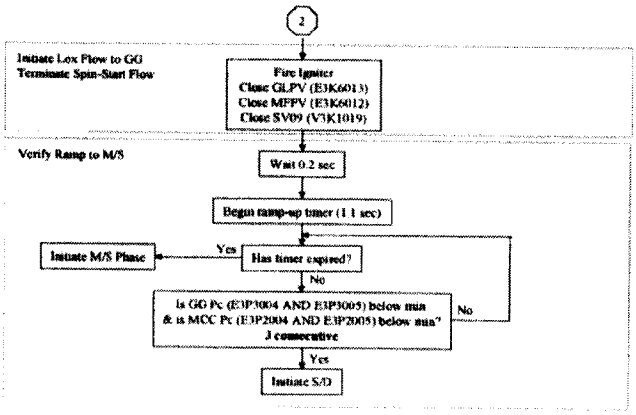
2
Initiate Lox Flow to GG
Terminate Spin-Start Flow
Fire Igniter
Close GLPV (E3K6013)
Close MFPV (E3K6012)
Close SV09 (V3K1019)
Verify Ramp to M/S
Wait 0.2 sec
Begin ramp-up timer (1.1 sec)
Initiate M/S Phase
Yes
Has timer expired?
No
Is GG Pc (E3P3004 AND E3P3005) below min
& is MCC Pc (E3P2004 AND E3P2005) below min*
3 consecutive
No
Yes
Initiate S/D

Appendix 3: Survey Questionnaire

1. My professional responsibility is
   a. Software design & development [ ]
   b. Software requirement & analysis [ ]
   c. Software system integration [ ]
   d. Software testing [ ]
   e. Other (Specify) _____ [ ]
2. The programming language I or my group use is
   a. ADA [ ]
   b. C [ ]
   c. C++ [ ]
   d. Java [ ]
   e. Other (Specify) _____ [ ]
3. My group or department practices software design as part of the software development process
   a. Yes [ ]
   b. No [ ]
4. If answered yes, the software design tool I or my group use is
   a. Rational Rose [ ]
   b. GDPro [ ]
   c. Other (Specify) _____ [ ]
5. Do you or your group use UML, the Unified Modeling Language for software design?
   a. Yes [ ]
   b. No [ ]
   c. Other (Specify) _____ [ ]
6. Are you trained with UML?
   a. Yes [ ]
   b. No [ ]
7. If yes, have you applied it since the training?
   a. Yes [ ]
   b. No [ ]
8. If yes, have you seen any benefit from using it?
   a. Yes [ ]
   b. No [ ]
9. Are you familiar with the Object Management Group?
   a. Yes [ ]
   b. No [ ]
10. My Group code at MSFC is _____ and Team Name _____

Acknowledgments

I would like to express my special thanks to Dr. Luis Trevino, Project PI for providing me with the opportunity to participate in the project. Project team members, Mr. Terry Brown, Co-PI; Mr. William Skipworth, Developer and Mr. Eric Ordonez, Student Intern, for their cooperation and support. I would also like to extend my thanks to Mr. Tim Crumbley, Flight Software Group Leader and Mrs. Valerie Parker for facilitating my stay during the 10-week period. My special thanks also goes to Drs. Karr and Jeanelle Bland for a well-coordinated Summer Faculty Program.

References

[1] Tremblay, Jean-Paul and Grant A. Cheston (2001), Data Structures and Software Development in an Object-Oriented Domain, Eiffel ed., Bertrand Meyer Series.

[2] Booch, Grady (1994), Object-Oriented Analysis and Design with Applications, 2n ed., Addison-Wesley, Santa Clara, California.

[3] Awad, Maher, et al. (1996), Object-Oriented Technology for Real-Time systems, Prentice-Hall.

[4] Lee, Richard C. and William M., Tepfenhart (2001), UML and C++: A Practical Guide to Object-Oriented Development, 2nd ed., Prentice-Hall, New Jersey.

[5] Bruce Powel Douglass (1999), Real-Time UML: Developing Efficient Object Objects for embedded Systems, Addison-Wesley, Object Technology series.

[6] Firesmith, Donald G. (1992), Object-Oriented Requirements Analysis and a Logical Design: A software Engineering Approach, ?

[7] Hares, John S. (1994), Object Orientation: Technology, Techniques, Management and Migration, Wiley Professional Computing.

[8] Booch, Grady, Jacobson and Rumbaugh (1999), The Rational Unified Process: an Introduction, Addison-Wesley, 1999.

[9] Booch, Grady, James Rumbaugh and Ivar Jacobson (1999), The Unified Modeling User Guide Addison-Wesley.

[10] Seed, Graham (1996), An Introduction to Object Oriented Programming in C++ with Applications in computer Graphics, Springer Inc.

[11] Hutt, Andrew T.F. (1994), Object Analysis and Design: Description of Methods, A Wiely-QED Publications, John Wiley & Sons, Inc.

2001

NASA/ASEE SUMMER FACULTY FELLOWSHIP PROGRAM

MARSHALL SPACE FLIGHT CENTER
THE UNIVERSITY OF ALABAMA IN HUNTSVILLE

SMALL OBJECTS IN LOW-EARTH ORBIT INTERSECTING GROUND-BASED LASER RADAR OPERATIONAL ENVELOPES

Prepared By:	Dr. Dona V. Boccio
Academic Rank:	Professor
Institution and Department:	Queensborough Community College The City University of New York Mathematics and Computer Science Department
NASA/MSFC Directorate:	Flight Projects
MSFC Colleague:	Dr. Jonathan Campbell

Introduction

NASA/Marshall Space Flight Center, in collaboration with the Air Force Research Laboratory/Directed Energy Directorate, is considering a series of experiments to demonstrate small object tracking capability. One such experiment involves a micro-satellite, about 25 cm in diameter, which will be deployed from a Space Shuttle Hitchhiker canister or from an Air Force vehicle. The High Performance CO_2 Ladar Surveillance Sensor (HI-CLASS) and the Advanced Electro-Optics System (AEOS) will be used to detect the micro-satellite.

The goal of this paper is to determine the number of times per day that a micro-satellite orbiting at a known altitude and inclination will be visible to the laser radar, and the length of time that the micro-satellite will be visible on each pass.

Methodology

Initially, we assume that the micro-satellite is released at time t_0 directly over the laser radar and continues on the ascending portion of its orbit. As the micro-satellite continues in its orbit, the laser radar moves eastward, rotating through 360° every 24 hours (see Figure 1). The beam of the laser radar illuminates a conical region extending from the surface of the earth into space (Figure 2). The "target region" is the intersection of this cone with a sphere, centered at the center of the earth, at the altitude h of the orbit.

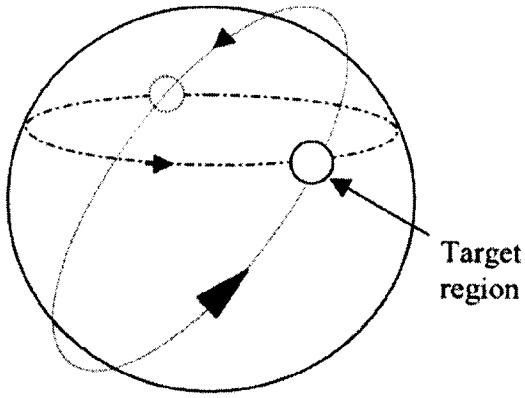

Figure 1: Orbit of micro-satellite and path of laser

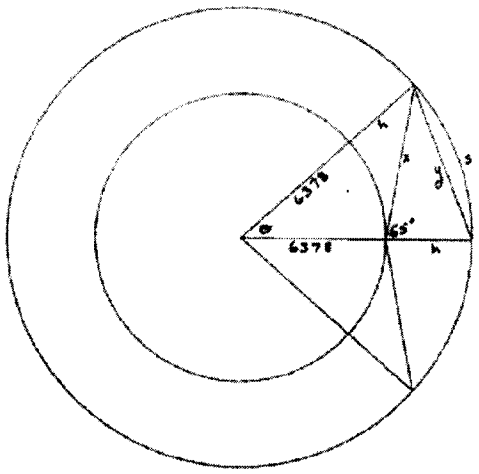

Figure 2: Target Region

Let λ = latitude of the laser radar, i = inclination of the orbit. To illustrate our results, we will use a typical Shuttle orbit with a 51.6° inclination and roughly circular 400 km orbit. For λ, we use 21° N, the latitude of the HICLASS/AEOS system.

For an object in circular orbit, velocity is given by $v = \sqrt{(GM/r)}$ where G = universal gravitational constant, M = mass of earth, GM = 398601.2 km^3/s^2, and r = radius of orbit = radius of earth + altitude of orbit = (6378+ h) km. The period of the orbit is $2\pi r / v = 2\pi\left(\sqrt{r}\right)^3 / \sqrt{GM}$. For an object at 400 km, the orbital period is 1.542625 hrs and velocity is 7.668643 km/s.

To calculate the size of the target region, we determine its central angle and arc length (see Figure 2).

$$x = 6378\cos 115^\circ + \sqrt{(6378\cos 115^\circ)^2 - 6378^2 + (6378+h)^2} \tag{1}$$

$$\theta = \sin^{-1}\left(\frac{x\sin 115^\circ}{6378+h}\right); \qquad y = \sqrt{x^2 + h^2 - 2xh\cos 65^\circ}\ ; \qquad s = (6378+h)\theta \tag{2}$$

Note that θ is half the central angle, and that y can be used as an approximation for s. For an altitude of 400 km and 65° zenith angle of the laser radar, $\theta = 6.47^\circ$.

Next we determine the times when the micro-satellite will cross 21 N° latitude. A successful intercept will occur if the laser is within ±6.47° or 180° ± 6.47° from its initial position at time t_0. The micro-satellite will cross 21° N latitude on the ascending portion of its orbit every 1.542625 hrs, i.e., every period. To calculate the time from t_0 when it crosses 21° N latitude on the descending portion of its orbit, we first determine the angle ϕ in the plane of the orbit, with vertex at the center of the earth, between the points of intersection of the orbit with the latitude circle of the laser radar (see Figure 3).

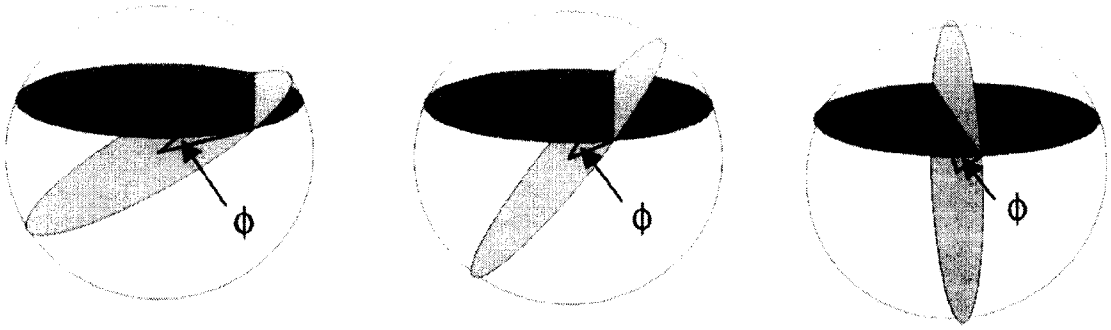

Figure 3: Angle ϕ for several values of orbital inclination

A formula for ϕ can be written as:

$$\phi = 2\cos^{-1}\left(\frac{\sin\lambda}{\sin i}\right) \tag{3}$$

For an orbital inclination i of 51.6°, $\phi = 125.5764°$. Therefore the micro-satellite crosses 21° N latitude after 1 period $\times \phi/360°$, or about 0.538104 hrs. It will cross 21° N latitude every 1 period thereafter.

To determine the angle through which the laser radar has moved by the times at which the micro-satellite crosses 21° N, we multiply these times by the rotational rate of the laser radar, 15° per hour. Taking these angles modulo 360° gives the angle from the initial position of the laser radar. We test these values against the radius of the cone of illumination of the laser radar to determine whether or not a successful intercept has occurred.

When a success is found, Figure 4 is used to determine the distance the micro-satellite moves while in the target region.

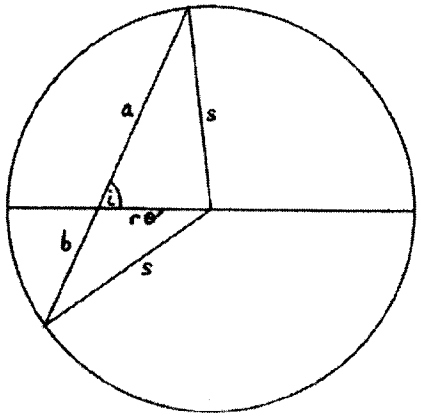

Figure 4: Distance across target region

The total distance across the disk is given by:

$$a+b=2\sqrt{(r\theta'\cos i)^2-(r\theta')^2+s^2} \tag{4}$$

where θ' is the angle between the initial position and current position of the laser radar.

The time the micro-satellite is visible to the laser radar is then (a+b)/v.

Results and Discussion

For a 400 km orbit, it was found that the micro-satellite will be visible to the laser radar 34 times in the first 30 days after release, or an average of 1.13 times per day. The average time that the micro-satellite will be visible on any given pass is 177.7 s, and the maximum time for 1 pass is 199.8 s. Table 1 gives a comparison of these results for orbital altitudes ranging from 200 km to 600 km.

Table 1: Comparison of Results for Various Altitudes

Altitude (km)	No. of intercepts in 30 days	Average time per intercept (s)	Max time per intercept (s)
200	19	90.8	103.5
300	25	134.9	152.3
400	34	177.7	199.8
500	40	218.0	246.3
600	49	260.7	291.9

Conclusions

The results of this preliminary study indicate that a micro-satellite in LEO will be visible to the HICLASS/AEOS laser radar approximately once per day, for an average of several minutes per pass. Further research needs to be performed to extend these conclusions to arbitrary release time and position of the micro-satellite.

Acknowledgements

The author wishes to thank Dr. Jonathan Campbell for his invaluable assistance with this project, and Mr. Mark Gerry and Dr. Michael Pangia for graphical support.

References

[1] Chobotov,V.A. (1991), *Orbital Mechanics*, AIAA Education Series, Washington, DC.

[2] Prussing, J.E. and Conway, B.A. (1993), *Orbital Mechanics*, Oxford Press, New York.

2001

SUMMER FACULTY FELLOWSHIP PROGRAM

MARSHALL SPACE FLIGHT CENTER
UNIVERSITY OF ALABAMA IN HUNTSVILLE

DISTRIBUTED I/O CONTROL SYSTEM IMPLEMENTATION FOR THE 1238 OPTICAL WITNESS SAMPLE THERMOELECTRIC QUARTZ CRYSTAL MICROBALANCE THERMAL VACUUM BAKEOUT CHAMBER

Prepared By:	Randy K. Buchanan
Academic Rank:	Associate Professor
Institution and Department:	Kansas State University Engineering Technology Department
NASA/MSFC Directorate:	Engineering
MSFC Colleague:	Andy Finchum

Overview

The 1238 Thermal Vacuum Bakeout Chamber (Fig. 1) is used to test materials to determine if they meet space program contamination requirements. The system was previously manual in its operation, in that there was no supervisory control system and therefore, no means for automated operation. Marshall Space Flight Center (MSFC) requested that its operation be automated. The subsequent process implemented involved a hybrid scenario that included existing hardware, a distributed input and output (I/0) system and a graphical user interface (GUI).

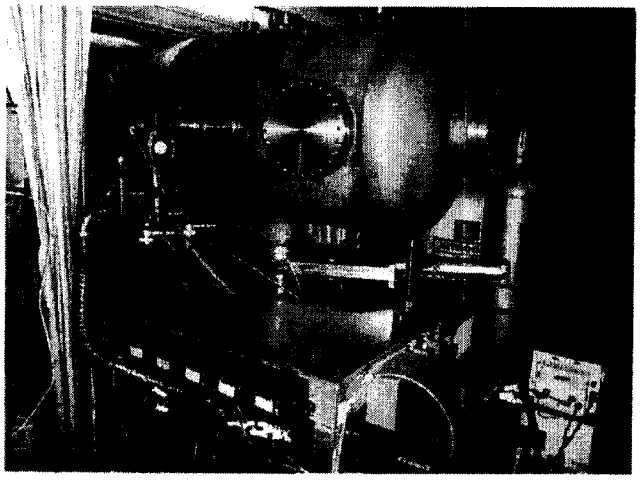

Fig. 1. 1238 Chamber

Principle of Operation

The 1238 Thermal Vacuum Bakeout Chamber is a thermal vacuum chamber with specialized hardware to enable the measurement of contamination. An optical witness sample (OWS), is placed near a Thermoelectric Quartz Crystal Microbalance (TQCM). The OWS is a mirror that collects contamination during the process and its change in reflectivity is ultimately measured. The TQCM uses two quartz crystals, and measures the difference in resonate frequency relative to the amount of contaminants deposited on the crystal exposed to the chamber. The more contaminants that are present within the chamber, the lower the frequency of the oscillation of the TQCM crystal. Therefore, by using the difference of the two frequencies, a higher frequency output versus time occurs per the relationship *dHz/dt*. (ref. 6) When the change of frequency varies one hertz within 36 hours, the OWS is chilled to a desired setpoint and held in the chilled state within a vacuum for a 24-hour period. Once the 24-hour period has elapsed, the chamber is returned to within 5°C of room temperature, and power is terminated before repressurization. The chamber is restored to atmospheric pressure via the introduction of filtered air, missile-grade air, or gaseous nitrogen.

Fig. 2. Control Rack

The system has six thermocouples located within the interior of the chamber that measure the temperature of the deck and the sample. Two thermocouple pressure gauges are used to measure rough chamber pressure and turbo pump backpressure. The cooling system consists of a liquid cooler used to control the temperature of the OWS and the quartz crystal housing. The roughing pump provides vacuum for the chamber down to 500 millitorr, and a turbo pump provides secondary pumping down to 10^{-6} torr. (ref. 2) A control rack (Fig. 2), located next to the chamber, houses the controller for the pressure gauges, the TQCM controller, and a computer that provides the system GUI.

Distributed I/O

In distributed I/O systems, processing for control applications is distributed throughout the I/O configuration, rather than consolidated in a central CPU. Often, several processors in parallel perform local logic processing and a central controller provides coordination among the various processors. I/O interfaces are placed near the actual devices and connected over a bus structure. (ref. 1)

The control hardware and software used to implement distributed I/O for the 1238 chamber included FieldPoint and Lookout, both products of National Instruments. One option within the selected platform was the use of Object Linking and Embedding (OLE) for Process Control (OPC), an industry standard connectivity interface that is based on Distributed Component Object Model (DCOM). The OPC specification is a non-proprietary technical specification that defines a set of standard interfaces. The application of the OPC standard interface makes possible the interoperability between different automation devices, platforms, and systems, business/office applications, as well as multi-vendor networking. (ref. 5)

"OPC promises what, up to now, has been virtually unachievable - to provide multi-vendor plug-and-play components that manufacturing customers and system integrators can easily integrate into enterprise-wide automation and business systems." (ref. 3) Overall, OPC removes barriers between traditionally proprietary systems. By providing a standard interface to the OPC/COM objects, OPC client applications are allowed to exchange data and control commands in a generic way. (ref. 3)

Chamber Automation

Previously, all 1238 chamber operations other than the TQCM process were manual. Implementation of an automated control system was initiated to improve the operation of the chamber and to increase the dependability, accuracy, and repeatability of results. The implementation of a control system afforded the ability to automate standard operating procedures.

FieldPoint distributed I/O modules were installed in addition to a dedicated computer and the FieldPoint and Lookout software. The TQCM hardware and software were also upgraded. Other hardware changes were implemented to accommodate the new control system, such as the addition of automated valves.

To enable accurate control over the temperature of infrared quartz heating lamps used for heating and circulation bath temperatures, Proportional Integral Derivative (PID) functions available within the software were utilized. The PID algorithm used may be stated as

$$u(t) = K_c\left(e + \frac{1}{T_i}\int_0 e\,dt + T_d\frac{de}{dt}\right) \text{ (ref 4)},$$

where K is proportional gain, e is the error, and T and t are time. Note that the integral and derivative components of the equation are affected by the proportional gain. Values ultimately used for this algorithm were derived from heating and cooling systems characterization tests, as well as other required parameters.

All operable devices were made to be individually controllable by the user through the GUI. An automated sequence was then created that assured a rigid sequential procedure when activated. Included in the automated sequence were system initialization, obtaining rough and high vacuum, activating and controlling the temperature of the heating lamps and circulation baths for the OWS and TQCM heat sink structure, controlled repressurization, and other functions.

Graphical User Interface

The GUI provides a means of allowing the operator to fully control and observe system functions. The Lookout GUI interface developed (Fig. 3) provides for full manual or automated control and the ability to monitor all measured variables and adjust system parameters. The automated sequence includes operator notification and interaction throughout the process. Access to automatic data logging features has also been made available through the GUI.

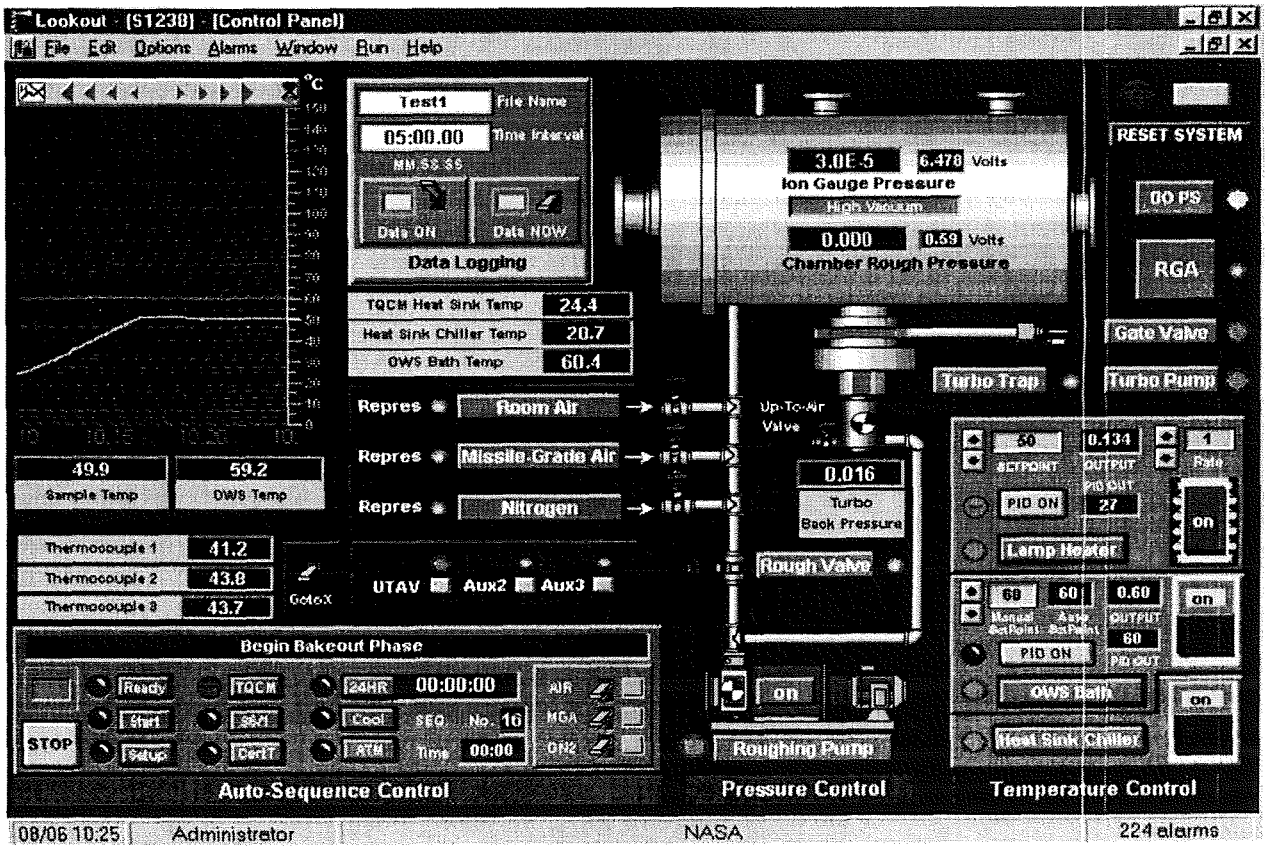

Fig. 3. Lookout Graphical User Interface

Conclusions

Distributed I/O typically provides for low wiring costs and small physical space requirements, as well as promising easier installation, setup, and programming for the average user. Relevant to this application, wiring costs and space requirements were not an issue. As far as ease of installation and setup, some aspects of the FieldPoint/Lookout setup were user-friendly. However, many of the details of setup and configuration were not included in any documentation provided with the related products, nor were they available via the Internet.

When attempting to program Lookout to develop the GUI, similar problems were encountered. Many industry standard intuitive approaches to programming standard functions were either labeled unconventionally, difficult to implement, or simply not available. In an attempt to cater to the lay user, programming that is usually mundane was made difficult. To exacerbate the situation, few example applications were available for examination and/or comparison. The manufacturer claims "National Instruments Lookout, the easiest to use HMI/SCADA software on the market, is a Web-enabled software system that delivers unparalleled power and ease of use for demanding manufacturing and process control applications.". In attempting to oversimplify the software, they accomplished making it difficult (in the sense that it is unconventional) to use. Therefore, this outstanding claim is suspect in its validity.

The OPC capability of the system proved to be desirable. Traditionally, each software or application developer was required to write a custom interface, or server/driver, to exchange data with hardware field devices. OPC can be created once and then easily reused by other control applications regardless of other proprietary differences. By utilizing the OPC features of FieldPoint and Lookout, the system is ready to be networked, if so desired.

After implementing the distributed I/O control system and customizing the GUI for desired operation, the operation of the 1238 Chamber was greatly enhanced. Not only are simple operations such as valve and pump control automatically actuated, but all device actuation is performed precisely the same way, under the exact same conditions every time. A complete display of all process variables (such as temperature, pressure, time, etc.) is provided for the benefit of the user. Also, continuous or on-demand data logging can be achieved at the user's discretion. Initial tests indicate that the 1238 Chamber should now provide greater reliability and ease of operation for future contamination testing for Marshall Space Flight Center.

References

[1] GE-Fanuc. PLC. Product Information. Retrieved July 24, 2001 from World Wide Web: http://www.gefanuc.com/PLC/515001.html

[2] Marshall Space Flight Center. Standard Operating Procedure. MSFC-SPEC-1238. Marshall Space Flight Center, AL.

[3] National Instruments. *Product Information.* Retrieved July 24, 2001 from World Wide Web: http://www.ni.com/opc/why_opc.htm

[4] National Instruments. *Product Information.* Retrieved July 24, 2001 from World Wide Web: http://digital.ni.com/manuals.nsf/web_productcurrent

[5] OPC Foundation. *Product Information.* Retrieved July 24, 2001 from World Wide Web: http://www.opcfoundation.org/

[6] QCM Research. MK20 Thermoelectric Quartz Crystal Microbalance Operations Manual. QCM Research; Laguna Beach, CA. 1996.

2001

NASA/ASEE SUMMER FACULTY FELLOWSHIP PROGRAM

MARSHALL SPACE FLIGHT CENTER
THE UNIVERSITY OF ALABAMA IN HUNTSVILLE

MOLECULAR PROBE FLUORESCENCE MONITORING OF POLYMERIZATION

Prepared By:	Patrick Bunton
Academic Rank:	Professor
Institution and Department:	William Jewell College Department of Physics
NASA/MSFC Directorate:	Science
MSFC Colleague:	Helen Cole

Introduction

This project investigated the feasibility of using fluorescence spectroscopy to determine viscosity of polymer/monomer in support of *Transient Interfacial Phenomena in Miscible Polymer Systems (TIPMPS).* TIPMPS – P.I. Dr. John Pojman of the University of Southern Mississippi -- will attempt to measure gradient induced flow at a miscible interface during and/or after in-flight polymerization of dodecyl acrylate (lauryl acrylate). Concentration and temperature gradients will be intentionally introduced during polymerization and the resultant fluid flow determined by Particle Imaging Velocimetry (PIV). This report describes an investigation of the feasibility of using fluorescence of a probe molecule to monitor viscosity and/or concentration during and after polymerization. The probe used was pyrene which has been shown to be sensitive to its local environment in methyl methacrylate.[1]

Experiment

An imaging spectrometer equipped with an imaging CCD array (Acton Research 300i) was used to monitor fluorescence from a molecular probe in dodecyl acrylate and poly(dodecyl acrylate) during UV irradiation at 365nm. Illumination at 365nm was provided by an EFOS Lite, light guide, appropriate filters and collimation optics. Note that use of the filter supplied by EFOS alone is not sufficient since its transmission overlaps the pyrene emission. A Schott UG-11 filter was added to the illumination optics to cleanly separate the UV excitation light from the pyrene fluorescence. Spectra are corrected for grating and CCD efficiencies. A power meter (Ophir Nova) was used both to monitor source power as well absorption by the monomer and polymer. Molecular pyrene emission and pyrene excimer emission were monitored over the wavelength range from 350 nm to 750nm (or subregion thereof). Fluorescence spectra were obtained and ratio of molecular-to-excimer emission of pyrene was determined as a function of (1) polymer concentration and (2) temperature from 30°C to ≈100°C. Heating was accomplished with a circulating heating bath in conjunction with constant temperature quartz fluorometer cuvettes (NSG Precision Cells, Type 54FL Water Jacketed Cell). Silicone oil was used instead of water as the thermal transfer fluid. Measurements showed that the silicone oil did not absorb at the 365 nm excitation wavelength nor does it fluoresce. It's only effect seems to be a positive one in that it provides a degree of index matching and actually increases the light through the cell. Differing concentrations were produced by elevated-temperature mixing of polymer and monomer using a magnetic stirring hotplate.

Results

Room temperature fluorescence spectra of dodecyl acrylate and poly(dodecyl acrylate) are shown in figure 1. Both spectra exhibit essentially three features:

1. A broad pyrene excimer fluorescence centered somewhere between 450nm and 500nm. This fluorescence appears more as a tail in the polymer emission.
2. Molcecular pyene emission at about 392 nm. Other pyrene lines are in the vicinity and may or may not be resolved.
3. UV light from the EFOS lamp at 365nm.

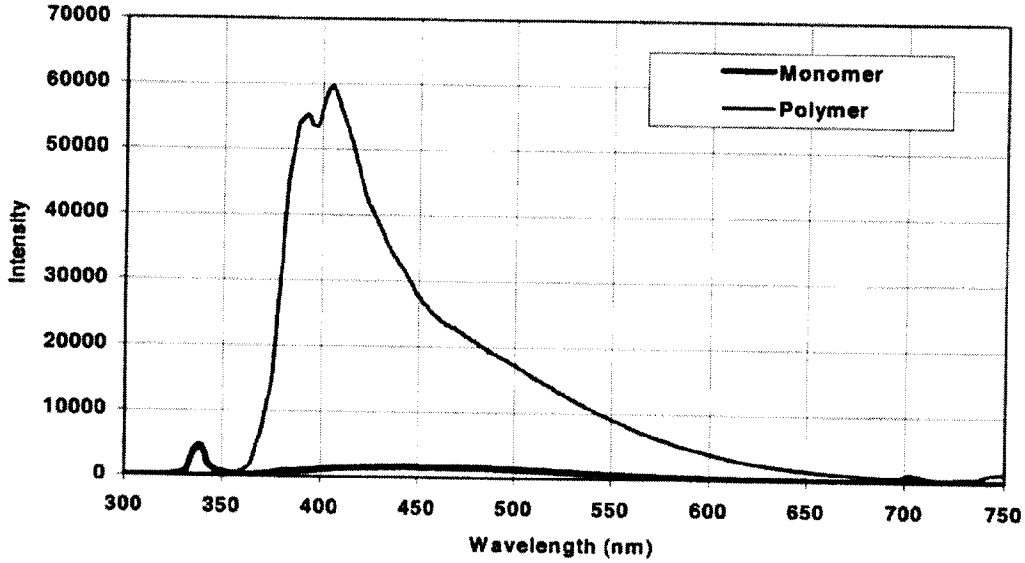

Figure 1: Fluorescence of Dedecyl Acrylate and Poly(Dodecyl Acrylate) containing 10^{-7} mole/liter of pyrene. Excitation at 365 nm. The structure near and past 700 nm is second order reflection from the grating.

Clearly the monomer emission is less intense as a whole. Further, the excimer emission is more clearly pronounced in the monomer data. It is not completely clear if this is excimer emission or a background fluorescence from another source such as the inhibitor or initiator.

Emission spectra were obtained as a function of temperature from room temperature to about 100°C for 365 nm irradiation of monomer, 25% polymer, 50% polymer, 75% polymer and 100% polymer. A much more pronounced decrease in fluorescence as with increasing temperature is evident. Similar data were obtained for other concentrations. Since we had observed a dose-dependence to the emission, the excitation source was shuttered off between observations – except for the monomer where the irradiation was continuous. The lamp itself was not turned off to maintain a more stable output. The data obtained were used to study the ratio of molecular to excimer fluorescence as well as the pyrene molecular fluorescence alone.

As mentioned in the introduction, previous work in methyl methacylate and poly(methyl methacrylate)[1] has shown that the ration of pyrene to excimer emission is sensitive to the "local viscosity"[1] of the pyrene. Ratios of molecular to excimer pyrene fluorescence were obtained for pyrene in dodecyl acrylate and poly(dodecyl acrylate). While the ratio data (not shown) are somewhat preliminary, initial indications are that the ratio technique would not be an appropriate monitor of polymerization of dodecyl acrylate. These may be due to background fluorescence due to the inhibitor or initiator. However, the fluorescence intensity of pyrene molecular emission by itself shows significant promise of being a monitor of polymerization. Figure 2 shows a plot of fluorescence intensity from various concentrations of poly(dodecyl acrylate)

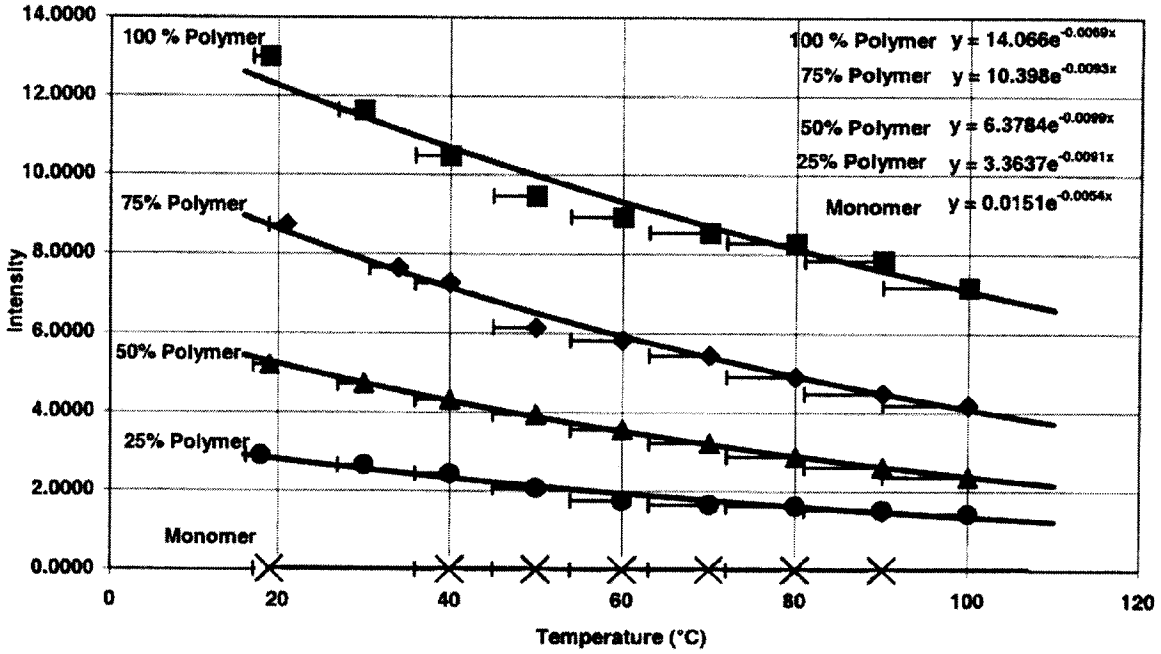

Figure 2: Temperature and concentration dependence of 393 nm emission during 365 nm excitation of 10^{-7} mole/liter of pyrene in dodecyl acrylate and poly(dodecyl acrylate). The curves through the data points are exponential fits.

containing 10^{-7} mole/liter of pyrene. Provided the temperature is known separately, indications are that the pyrene emission at 393 nm would be an indication of degree of polymerization at any temperature. All data shown except for the monomer were obtained at an exciatation power density of approximately 3mW/cm^2. Temperature was monitored by the digital readout on the silicone bath. A check at high temperature showed the sample to be about 12° C lower in temperature; hence, 10% horizontal error bars to the left are used for the temperature. Correction still remains to be made for difference in intensity due to the Beer's law absorption of the 365 nm light across the cell. However, preliminary indications are that this does not significantly alter the trends. The spectrometer slit was generally viewing the center of the cell. Note the similarity in the argument to the exponential fits for the 25%, 50%, and 75% data. The polymer also fits the same trend if only the first five data points are used. This needs to be checked further. It certainly seems that a characteristic exponential behavior is of the intensity is indicated with differing amplitudes for different concentrations.

While results to date are quite encouraging, certainly significant issues remain. Significant power is absorbed from the 365 nm excitation source in passing through the polymer. Far less power is absorbed in the monomer. Such a correspondingly large absorption coefficient in the polymer would lead to a concentration gradient during polymerization. The source of this large absorption coefficient is most likely the initiator or the inhibitor. Another concern is that 365nm irradiation exciting fluorescence can cause additional polymerization. Consequently, use of 365 nm light to excite the pyrene fluorescent probe may also lead to a gradient. Fortunately, the pyrene probe fluorescence is very efficient so it may be possible to keep light levels sufficiently

low as not to affect the experiment. Also, the use of other fluorescent probes that respond to a different excitation wavelength than that used for the polymerization might be useful.

Conclusion

Early results indicate that the ratio of pyrene to excimer fluorescence emission for a pyrene probe in dodcyl acrylate and poly(dodecyl acrylate) may be inadequate as a monitor of polymer concentration (*i.e.* conversion) during and following polymerization. However, the simpler task of monitoring the pyrene emission is showing great promise that it could serve as such a monitor of concentration during polymerization. Some issues that remain include (1) the large absorption coefficient for the pyrenated polymer at 365nm likely due to too much initiator or initiator, (2) refinement of the temperature monitoring and other details, (3) determination if another probe would be more appropriate, (4) calibration for other molecular weights, and (5) clarifying that excimer emission is being observed and separating excimer emission from other fluorescence.

Acknowledgments

Thanks to Mr. Blair Unger for his careful data collection and insightful interpretation. We gratefully acknowledge Dr. John Pojman and Mr. William Ainsworth of the University of Southern Mississippi for providing samples for this investigation. We thank Dr. Steve Paley of Marshall Space Flight Center for significant help as well.

References

[1] "Pyrene as a Fluorescent Probe for Monitoring Polymerization Rates," O. Valdes-Aguilera, C.P. Pathak, and D.C. Neckers, Macromolecules 23 (1990) 689-692.

2001

NASA/ASEE SUMMER FACULTY FELLOWSHIP PROGRAM

MARSHALL SPACE FLIGHT CENTER
THE UNIVERSITY OF ALABAMA IN HUNTSVILLE

DYNAMIC ANALYSIS OF CAPTURE DEVICES FOR MOMENTUM EXCHANGE WITH TETHERS

Prepared by:	Stephen Canfield
Academic Rank:	Assistant Professor
Institution and Department:	Tennessee Technological University Department of Mechanical Engineering
NASA/MSFC Directorate:	Transportation
MSFC Colleague:	Ken Welzyn

Introduction

One of the significant challenges in developing a momentum-exchange/electrodynamic reboost tether system is in the analysis and design of the capture device and its effects on the overall dynamics of the system. The goal of this work is to develop appropriate tether momentum exchange models that can simulate and evaluate the requirements of such a system, and be used to create specifications on the design of a capture device. This report briefly describes dynamic model development, simulation of the momentum exchange process, evaluation of dynamic effects of errors in the momentum exchange process, and the development of guidelines in selecting dynamic properties in the design of a capture device.

Tether Momentum Exchange Model Development

The dynamics of a flexible tether in space flight are evaluated using a finite element model formulation of the continuous flexible system. This dynamic model will provide a time response of the flexible system throughout the momentum exchange process. This dynamic model departs from many of the current lumped-mass or beaded models proposed. These models have been shown to be generally accurate in tether flight simulation, and may have advantages in modeling tether deployment and retrieval. However, the continuous, flexible nature of the tether system and the ability to refine element types to accurately reflect the various components of the momentum exchange system make a finite element formulation a significant and robust modeling approach for the MX process.

In the finite element model, the continuous tether system is modeled as a collection of elements, each of which represent discrete components of the tether, as shown in Fig. 1. Then, approximate solutions to the governing PDE are made for each element with consistent and continuous boundary conditions applied. The designer can select the degree of complexity on approximate solutions for each element, with higher order shape functions providing more accurate solutions.

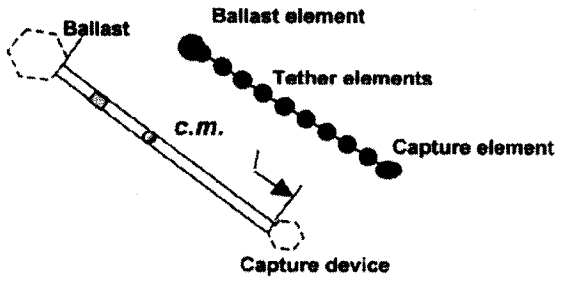

Figure 1: Tether and FEM schematic

As shown in Fig. 1, the tether system can include tether elements, ballast elements, and capture elements. Models for each of these elements are constructed, and then a composite model of the system is formed through appropriate combination of the individual elements, including local element transformations and nodal connectivity to result in a system model as:

$$\mathbf{M}\ddot{\mathbf{x}} + \mathbf{C}\dot{\mathbf{x}} + \mathbf{K}\left(\mathbf{x} - \mathbf{x}_{rigid}\right) = \mathbf{F} \qquad \text{Eq. 1}$$

where $\mathbf{x}$ is the vector of nodal positions, $(\mathbf{x} - \mathbf{x}_{rigid})$ a vector of nodal displacements (displacement from rigid body motion), $\mathbf{M}$, $\mathbf{C}$, and $\mathbf{K}$ the global mass, damping and stiffness matrices, and $\mathbf{F}$

the force vector. Matrices **M**, **C**, and **K** are of size ($n\ d$ x $n\ d$) where n is the number of nodes and d the number of degrees of freedom for each node. These matrices are composed as appropriate combinations of elemental mass, damping and stiffness matrices for each individual elements, with appropriate coordinate transformations provided. Eq. 1 then provides a second order differential equation in the nodal positions of the tether system, and as such can be solved to determine nodal positions in time. From these nodal solutions and the element shape matrices, the total time response of the flexible tether system can be examined in time using appropriate adaptive time step integration routines. The remainder of this report describes the results from the analysis of the momentum exchange process, with the goal of creating guidelines for capture device development and providing requirements on tether flight accuracy.

Analysis of Tether Capture and Release of Payload:

Using the FEA tether model derived above, the capture process is modeled as follows. The tether simulation is started and proceeds for a period of time sufficient to allow initial condition transients to die out. Similarly, the payload is released and simulated in its proper orbit. Initial conditions of both the tether and payload are selected to result in a rendezvous precise in space and time. The momentum process begins when the payload enters the capture region of the tether and continues through the carry and release process. For the general case, the capture occurs when the tether is at perigee and the tether is aligned with the local vertical, the capture end pointing toward earth. The tether than carries the payload through a predetermined angle (e.g., 135 deg.) and releases the payload, with both the payload and tether assuming a new trajectory. The simulation process records the data from the tether model including tether tension, rotation rate, center of mass, and velocity. These results provide essential information in predicting momentum exchange performance under ideal conditions, setting the bounds on required tether propagation accuracy, and in providing design guidelines for design of the capture device. Results from analysis in each of these areas follow. These results are based on tether and payload sizes published by Hoyt, 2000, as shown in Table 1.

Table 1: Tether and Payload Parameters

Constants		Tether Facility Orbit	
μ	3.986E+14	Perigee (m)	6,785,136.00
Payload Mass (kg)	1000	Apogee (m)	14,823,136.00
Capture Mass (kg)	250	Time for one orbit (s)	11,176.25
Ballast Mass (kg)	11000	SMA	10,804,136.00
Tether Length (m)	80000	e	0.371987172
Cross Sect Area (m^2)	1.9635E-05	Perigee Velocity (m/s)	8977.690593
ρ (kg/m)	970	Apogee Velocity (m/s)	4109.444293
Payload orbit		ω of tether fac. (rad/s)	-0.013881192
Orbit Radius (m)	6694275.739		
Vp (m/s)	7716.44186		
Time for one orbit (s)	5450.876936		

Results From an Error-Free Momentum Exchange Simulation

The first momentum exchange analysis will demonstrate simulation of tether and payload rendezvous, capture, carry and release, under ideal conditions. Here, ideal conditions imply that there is no error in position or velocity of either the tether or payload. At the point of rendezvous, both the capture device and payload have the same position and velocity. The tether produces and instantaneous application of acceleration on the payload in the direction of the tether, resulting in increase in tether tension with much smaller effects on transverse vibrations.

The results from this ideal capture are shown in figs. 2-3, giving the time history of the tether tension and showing the shift in tether center of mass orbits.

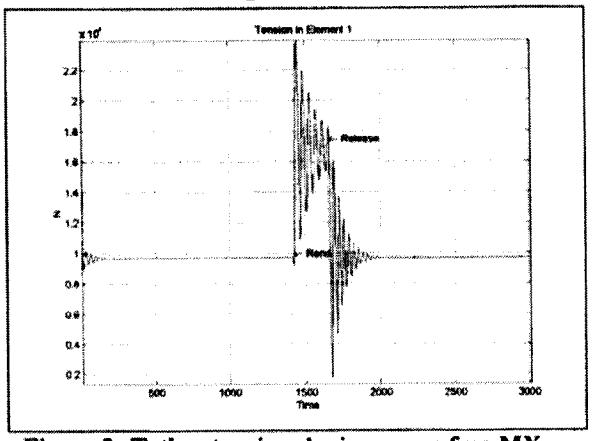

Figure 2: Tether tension during error-free MX

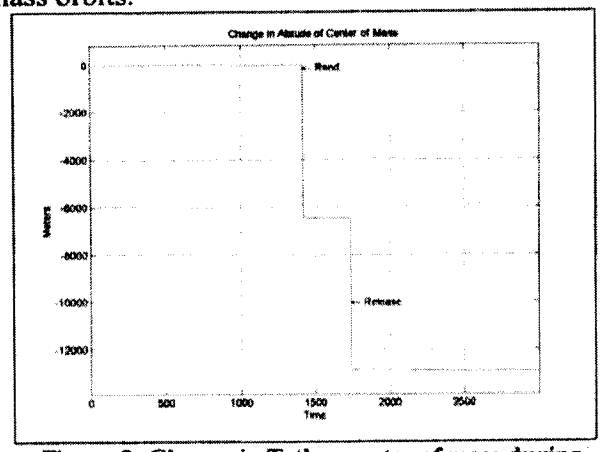

Figure 3: Change in Tether center of mass during

From the error free momentum exchange case several results are noted. First, general effects on the tether orbit correspond to those published in the current literature (Hoyt, 2000, Bangham et al, 1998). However, the tether orbit is also affected by elastic material change during the capture and release process. The tension undergoes a significant increase during both capture and release. Finally, the tether rotation rate is largely unchanged during this error-free capture, again matching the results shown in current literature.

Analysis of Error Effects on Momentum Exchange

An analysis is conducted using the momentum exchange simulation tool to investigate the effects of various errors during the rendezvous process. The results of this analysis will be used to provide requirements on tether and payload state accuracy, using both current and future predicted state of the are materials. Figs 4-5 below demonstrate the effects of velocity error in the payload or tether rotation rate, and angular position error of the tether leading or trailing nadir. In each case, tether tension as a function of the error is demonstrated.

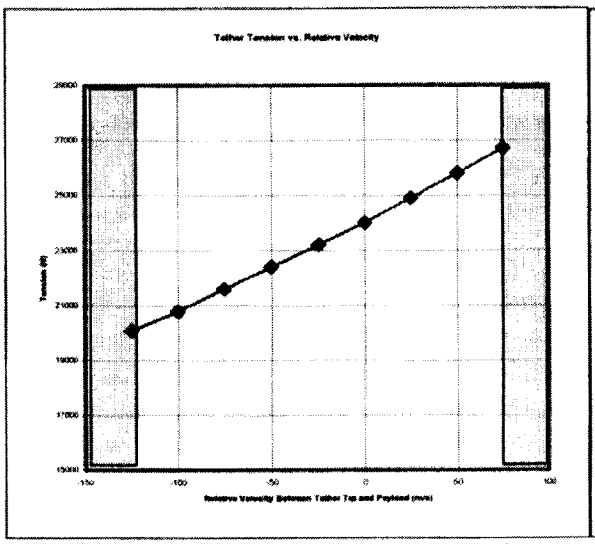

Figure 4: Tether Tension Vs. Velocity Error

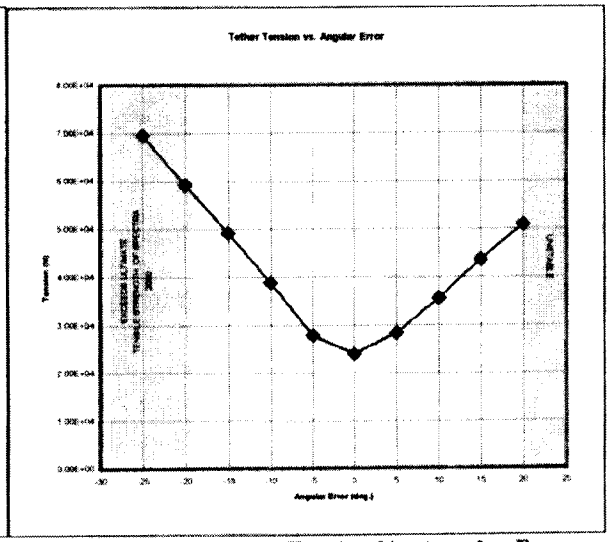

Figure 5: Tether Tension Vs. Angular Error

From this error analysis, the effects of each type of error are clearly demonstrated. An increase in each type of error results in an increase in the detrimental dynamic effects on the tether, even causing the tether simulation to go unstable. From this analysis, criteria on the accuracy required for both the tether and the payload are identified at the point at which the tether exceeds its maximum tensile strength or goes unstable.

Design Guidelines for a Capture Mechanism

A final dynamic analysis is performed to create a design guide for the parameters governing the capture mechanism dynamics. In particular, the overall capture mechanism mass, stiffness and damping properties are considered, with results showing their effects on tether tension. The goal is to design the capture mechanism to minimize the dynamic effects on the overall tether while providing for efficient and effective momentum exchange. The analysis is performed with results shown in Figs. 6-7. Figure 6 demonstrates the relation between capture device stiffness and maximum tether tension under ideal momentum exchange, while fig. 7 shows the effects of damping in the capture device.

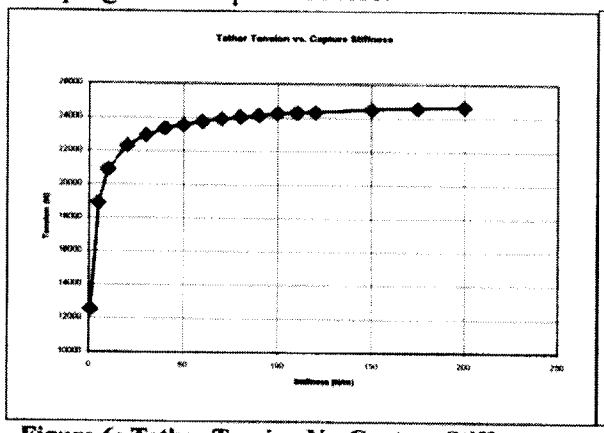

Figure 6: Tether Tension Vs. Capture Stiffness

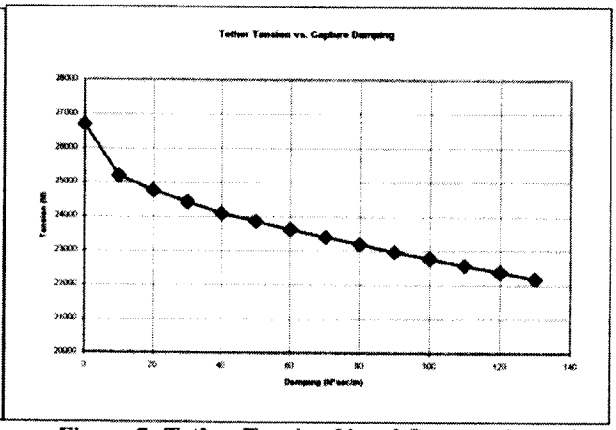

Figure 7: Tether Tension Vs. of Capture Damping

Summary

The momentum exchange process has been modeled using a FEA approach, with the basic processes verified against current literature. This report presents an analysis of the dynamic effects of error as well as guidelines for the design of a specific capture mechanism. Based on these dynamic considerations, targets on capture mechanism parameters are a low stiffness and a higher viscous damping.

Acknowledgements

The author would like to thank Kirk Sorensen, Ken Welzyn and Randy Baggett for their technical advice and support with this project.

Bibliography

Hoyt, R., 2000, "Design and Simulation of a Tether Boost Facility for LEO to GTO Transport," AIAA Paper 2000-3866, *36th AIAA/ASME/SAE/ASEE JPC* Huntsville, AL.

Bangham, M., Lorenzini, E., and Vestal, L., 1998, "Tether Transportation System Study," *NASA/TP-1998-206959*.

2001

NASA/ASEE SUMMER FACULTY FELLOWSHIP PROGRAM

MARSHALL SPACE FLIGHT CENTER
THE UNIVERSITY OF ALABAMA IN HUNTSVILLE

SEMICLASSICAL CALCULATION OF REACTION RATE CONSTANTS FOR HOMOLYTICAL DISSOCIATIONS

Prepared By:	Beatriz H. Cardelino
Academic Rank:	Associate Professor
Institution and Department:	Spelman College Chemistry Department
NASA/MSFC Directorate:	Science and Engineering
MSFC Colleague:	Craig E. Moore

Introduction

There is growing interest in extending organometallic chemical vapor deposition (OMCVD) to III-V materials that exhibit large thermal decomposition at their optimum growth temperature, such as indium nitride[2]. The group III nitrides are candidate materials for light-emitting diodes and semiconductor lasers operating into the blue and ultraviolet regions[1]. To overcome decomposition of the deposited compound, the reaction must be conducted at high pressures, which causes problems of uniformity. Microgravity may provide the venue for maintaining conditions of laminar flow under high pressure[3].

Since the selection of optimized parameters becomes crucial when performing experiments in microgravity, efforts are presently geared to the development of computational OMCVD models that will couple the reactor fluid dynamics with its chemical kinetics[6,7]. In the present study, we developed a method to calculate reaction rate constants for the homolytic dissociation of III-V compounds for modeling OMCVD. The method is validated by comparing calculations with experimental reaction rate constants.

Method

According to transition state theory, a unimolecular rate constant k_{uni} may be defined by:

$$k_{uni} = \frac{k_\infty}{1 + \frac{k_\infty}{k_1 P}}[A] \qquad [1]$$

where k_∞ is the value of the rate constant at high pressures and k_1 is a bimolecular rate constant, first order in pressure. The calculation of k_∞ for homolytic dissociation is based on the RRKM[14] theory (equation 2). The method assumes the existence of a critical configuration $A^\#$.

$$k_\infty = L\frac{k_B T}{h}\frac{Q^\#}{Q^{UM}}\exp\left\{-\frac{E^\# - E^{UM}}{k_B T}\right\} = L\frac{k_B T}{h}\exp\left\{-\frac{G^\# - G^{UM}}{k_B T}\right\} \qquad [2]$$

L is the degeneracy of the reaction path; k_B, Boltzmann constant; T, temperature in Kelvin; h, Plank constant; E, the electronic energies; Q, the molecular partition function; and G, the Gibbs free energy, defined as $E - k_B T \ln Q$.

The k_1 value was estimated in two ways. In the L-H approach[9,13], k_1 is based on collision theory (see equation 3). In the Troe approach[16], k_1 is based on the RRKM theory (see equation 4).

$$k_1 = \frac{z_1}{(s-1)!}\left(\frac{E^\# - E^{UM}}{k_B T}\right)^{s-1}\exp\left\{-\frac{E^\# - E^{UM}}{k_B T}\right\}F_e \qquad [3]$$

$$k_1' = z_1'\,\rho\,\frac{1}{Q_v}\exp\left\{-\frac{(E^\# - ZPE^\#) - (E^{UM} - ZPE^{UM})}{k_B T}\right\}F_e' F_{anh} F_{rot} F_{rot\,int} \qquad [4]$$

where z_1 and z'_1 are collision parameters; s, internal degrees of freedom of the reactant; the F terms, correction factors for temperature, anharmonicity, molecular and internal rotations; ρ, harmonic oscillator density of states, Q_v, vibrational partition function; and ZPE, zero-point energy corrections.

The total partition function Q is assumed to be the product of electronic, vibrational, rotational, internal rotational and translational contributions. Two modes of calculations were performed: Mode V, eliminated the vibrational contribution along the reaction path associated with the bond dissociation; and Mode T, eliminated the translational contribution along the reaction path. For Mode V, the vibrational partition function for the critical configuration involved one less vibrational mode than the partition function for the unperturbed molecule. For Mode T, the vibrational corresponding to the bond that breaks was treated similarly as the other vibrational modes that become annihilated, but the translational partition function of the critical configuration included the contribution from just two directions. Since the translational partition function is the only partition function that depends on pressure, and one of the translational modes did not cancel out, k_∞ for Mode T was never pressure independent. A real-gas correction was incorporated, using a compressibility factor obtained from a virial correction.

The critical configuration corresponds to the maximum point of the Gibbs free energy change. A novel procedure for selecting the critical configuration was developed. The terms for the Gibbs free energy calculations were obtained from statistical thermodynamic calculations on the unperturbed molecule and dissociated products, and classically derived electronic energies and vibrational frequencies on intermediate structures, as follows:

$$E^I = E^{UM} + E_D\left\{1-\exp\left[-\pi\nu_0^{UM}\left(\frac{2\mu}{E_D}\right)^{1/2}(R^I - R_o^{UM})\right]\right\}^2 \qquad [5]$$

$$\nu_i^I = \nu_i^{UM}\exp\left\{-\pi\nu_0^{UM}\left(\frac{2\mu}{E_D}\right)^{1/2}(R^I - R_0^{UM})\right\} \qquad [6]$$

where E_D is the dissociation energy, μ, the reduced mass between the products, ν vibrational frequencies, R bond distances, UM the unperturbed molecule, I the intermediate structure, 0 properties of the bond that dissociates.

Results and discussion

The method was validated by comparing the calculations with experimental data on the rate constants for methyl dissociation of three metal-alkyl compounds [$Al(CH_3)_3$, $Ga(CH_3)_3$, $In(CH_3)_3$] and for hydrogen dissociation of three group V hydrides [NH_3, PH_3, AsH_3]. These calculations were compared with the corresponding experimentally obtained rate constants. Table 1 compares the k_{uni} values predicted in this paper with published values, as a fraction of the former over the latter. These fractions are calculated at the lower and higher ends of the temperature range. The factors shown in the table should be evaluated against the uncertainty of the experimental measurements. For example, Jacko and Price[11] reports the value for a methyl dissociation from $Ga(CH_3)_3$ with uncertainties that result in factors as large as 1,585 and as small as 1,244.

In all cases, the predicted k_∞ were larger than the reported values. Except for the ideal-gas calculations of the group V trihydrides, Mode T calculations were considerably smaller than Mode V calculations, as much as 185 times. Thus, the predicted k_∞ values from Mode T were

closer to the published values. For the Group III molecules, the Troe approach and the ideal-gas approximation gave better agreements with experimental results, but the other treatments also gave reasonable values. Within this group, In and Al reactions gave the best results. The requirement for real gas approximation is very noticeable for the Group V molecules, which have high critical pressures. Within Mode T, the four combinations of L-H/Troe approach, and ideal/real gas approximation, gave reasonaly good agreement with experimental values for the Group V molecules. In summary, the results of Mode T calculations, with real gas correction for Group V molecules, seem in very good agreement with experimental values.

Conclusions

Reliable values of reaction rate constants for the homolytic dissociation of a methyl group in trimethyl-group III compounds and of a hydrogen atom in group-V hydrides were obtained using a semiclassical approach based on statistical thermodynamics data obtained from quantum mechanical calculations, and on the RRKM theory. Comparison between calculations involving elimination of a vibration mode or a translation mode along the reaction pathway showed that the latter consistently gave the best values when compared to experimental data. Inclusion of real-gas effects were extremely necessary for predicting reaction rates for a hydrogen dissociation of group V trihydrides.

Acknowledgments

The author would like to thank Dr. Craig E. Moore and Dr. Donald O. Frazier for providing a stimulating work environment and many hours of fruitful discussions.

References

[1] Ambacher, O.; Brandt, M. S.; Dimitrov, R.; Metzger, T.; Stutzmann, M.; Fischer, R. A.; Miehr, A.; Bergmaier, A.; Dollinger; G.;J. Vacuum Science Technology B **1996**, *14*, 3532.

[2] Bachmann, K.J.; Cardelino, B. H.; Moore, C. E.; Cardelino, C. A.; Sukidi, N.; McCall, S.; in "In Situ Process Diagnostics and Modeling"; A. Ochello, et al. editors; Materials Research Society Symposium Proceedings **1999**, *59*, 569

[3] Bachman, K. J.; Kepler, G. M.; SPIE **1997**, *3123*, 64.

[5] Buchan, N. I.; Jasinski, J. M.; J. Crystal Growth **1990**, *106*, 227.

[6] Cardelino, B. H.; Moore, C. E.; Cardelino, C. A.; Frazier, D. O.; Bachmann, K. J.; J. Phys. Chem. A, **2001**, *105*, 849..

[7] Cardelino, C. A.; Moore, C. E.; Cardelino, B. H.; Zhou, N.; Lowry, S.; Krishnan, A.; Frazier, D. O.; Bachmann, K. J.; SPIE **1999**, *3625*, 447.

[8] Gardiner Jr., W. C.; Troe, J.; in "Combustion Chemistry"; W. C. Gardiner Jr., editor; Springer, New York, **1984**

[9] Hinshelwood, C.N.; Proc. Roy. Soc. (A) **1927**, *113*, 230.

[10] Holzrichter, K; Wagner, H. Gg.; 18th International Symposium Combustion; Combustion Institute; Pittsburgh, **1981**.

[11] Jacko, M. G.; Price, S. J. W.; Can. J. Chem. **1963**, *41*, 1560.

[12] Jacko, M. G.; Price, S. J. W.; Can. J. Chem, **1964**, *42*, 1198.

[13] Lindemann, F. A.; Trans. Faraday Soc. **1922**, *17*. 598.

[14] Marcus, R.A.; J.Chem. Phys **1952**, *20*, 359

[15] Smith, G. P.; Patrick, R.; Intern. J. Chem. Kinetics **1983**, *15*, 167.

[16] Troe, J.; J. Chem. Phys., **1977**, *66*, 4750; Troe, J.; J. Chem. Phys., **1977**, *66*, 4758.

Table 1: Comparison between experimental and predicted reaction rate constant at low and high temperature (LT and HT, respectively).

Reaction; Approach	$\frac{k^{calc}}{k^{exp}}$ at LT		$\frac{k^{calc}}{k^{exp}}$ at HT		T range (K)	Ref.
	Mode V	Mode T	Mode V	Mode T		
$In(CH_3)_3 \rightarrow In(CH_3)_2+CH_3$					550-650	12 & 15
L-H; ideal	67	7	188	17		
L-H;real	66	20	184	45		
Troe; ideal	195	13	170	6		
Troe; real	163	12	165	20		
$Ga(CH_3)_3 \rightarrow Ga(CH_3)_2+CH_3$					750-850	11 & 15
L-H; ideal	1,900	142	2,900	166		
L-H; real	1,900	199	2,800	224		
Troe; ideal	1,200	52	192	8		
Troe; real	1,200	307	194	204		
$Al(CH_3)_3 \rightarrow Al(CH_3)_2+CH_3$					850-950	5
L-H; ideal	172	14	252	18		
L-H; real	212	30	309	39		
Troe; ideal	128	8	25	1		
Troe; real	122	30	25	23		
$AsH_3 \rightarrow AsH_2 + H$					850-950	5
L-H; ideal	2,000	1×10^5	1,600	9×10^4		
L-H; real	2,000	13	1,600	11		
Troe; ideal	1,500	7×10^4	1,300	5×10^4		
Troe; real	1,500	14	1,300	12		
$PH_3 \rightarrow PH_2 + H$					850-950	5
L-H; ideal	3,300	1×10^5	2,700	1×10^5		
L-H; real	3,000	21	2,400	17		
Troe; ideal	2,100	2×10^5	1,700	1×10^5		
Troe; real	2,100	22	1,700	18		
$NH_3 \rightarrow NH_2 + H$					2,350-2,450	10
L-H; ideal	1,300	1×10^4	1,200	1×10^4		
L-H; real	1,300	7	1,200	7		
Troe; ideal	1,100	1×10^4	1,000	1×10^4		
Troe; real	1,100	7	1,000	6		

2001

NASA/ASEE SUMMER FACULTY FELLOWSHIP PROGRAM

MARSHALL SPACE FLIGHT CENTER
THE UNIVERSITY OF ALABAMA IN HUNTSVILLE

Directionally Sensitive Silicon Radiation Sensor (VCELL)[1]

Prepared By:	Koy B. Cook
Academic Rank:	Associate Professor
Institution and Department: Department of Electrical Engineering	Alabama A&M University
NASA/MSFC Directorate:	Engineering (ED-12)
MSFC Colleagues:	Mike Watson/WT Powers

Introduction

Sensors are a mission critical element in many NASA programs and require some very unique properties such as small size, low power, high reliability, low weight.[2,3] Low cost sensors offer the possibility of technology transfer to the public domain for commercial applications One sensor application that is important to many NASA programs is the ability to point at a radiation source, such as the sun. Such sensors may be an integral part of the guidance and control systems in space platforms and in remote exploratory vehicles. A sensor or sensor system that "points" at a radiation source is called naturally a " pointer". A sensor which points at the sun is called a sun pointer. Sun/solar pointing is also important for ground-based systems such as solar arrays. These systems are not required to be small and light weight. However, if a sensor with a sun pointing capability was developed that is very small, rugged, lightweight and at the same time low cost, it certainly could be used in existing and perhaps many new ground based applications.

The objective of the VCELL research is to develop a new and very unique silicon based directionally sensitive radiation sensor which can be fabricated using conventional monolithic IC technologies and which will meet the above requirements. The proposed sensor is a novel silicon chip that is directionally sensitive to incident radiation, providing azimuth and elevation information on the incident radiation. The resulting sensor chip will be appropriate for integration into a silicon IC or useful in a hybrid structure to be interfaced with a standard IEEE 1451 bus interface IC to create an Intelligent Sensor.

It is presently estimated that it will require about three man-years of effort to complete the VCELL research and development. This includes the optical, electrical, mechanical and silicon fabrication and testing as well as computer simulations and theoretical analysis and modeling including testing in simulated space environments.

This report summarizes the sensor research completed this summer as part of the Summer Faculty Fellowship Program. The primary effort was focused on activity necessary to fabricate prototype sensors.

Fabrication activities included the design and development of a sensor fabrication process, the development of deposition and diffusion processes using the Thermco furnaces and solid sources, the development of preferential silicon etching processes, ordering necessary process supplies and chemicals, fabrication and tooling of necessary hardware items to support the required silicon process equipment in place in bldg. 4487 and bldg. 7804.

Fabrication Activity and Results

The process to design the VCELL structure followed from theory and simulations accomplished by Dr. Cook previously (unpublished). The theory and simulations result in a process sequence requiring five photolithographic masks as shown in Figure 1. The CAD design was accomplished using GenCadd 6.1.5. The results of the CAD layout of

the VCELL test IC chip are shown in Figure 2. In Figure 2, all five photomask layers are shown.

Mask #1 – Boron Diffusion
Mask #2 – Silicon Etch
Mask #3 – Phosphorus Diffusion
Mask #4 – Contact Etch
Mask #5 – Metallization Pattern Etch

Figure 1 - The VCELL Process by Photolithographic Mask Layer

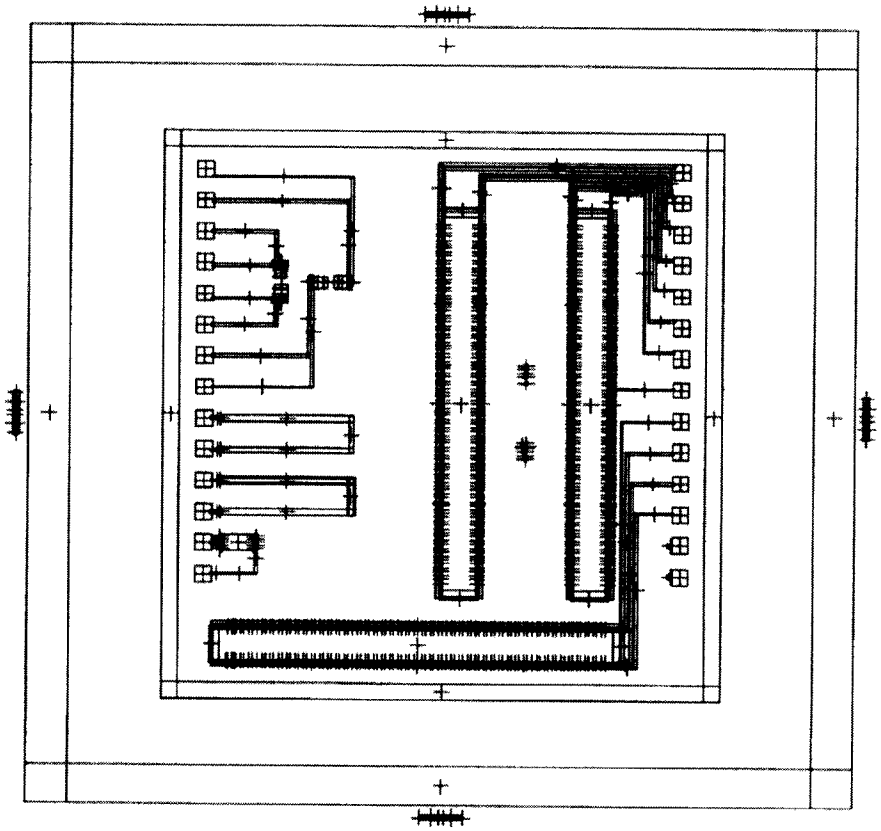

Figure #2 – The VCELL Test Chip CAD Layout

The VCELL test chip is 6.6 mm by 7.1 mm and requires a 28 pin package. The test chip contains three VCELL detectors, two of which are orthogonal, providing the required X and Y axis information to compute the azimuth and elevation of incoming radiation. The third VCELL detector is parallel and identical to the first. The test chip also includes devices to monitor the silicon wafer processing.

All photolithographic processing was accomplished in the Joint AMCOM/NASA Integrated Devices Laboratory located in Building 7804. Chemical processing, doping and diffusions and etching was done in the NASA/ MSFC silicon wafer doping and diffusion lab located in Building 4487 MSFC.

Conclusions

Significant progress has been made toward the completion and testing of the first VCELL test chip. With the first topological/CAD designs complete and working photolithographic masks available, fabrication including process development was accomplished through mask level #2, including the silicon preferential etching process. A photograph of an "in process" VCELL chip is shown in Figure #3. This photograph shows the surface topology for a wafer processed through mask level #2.

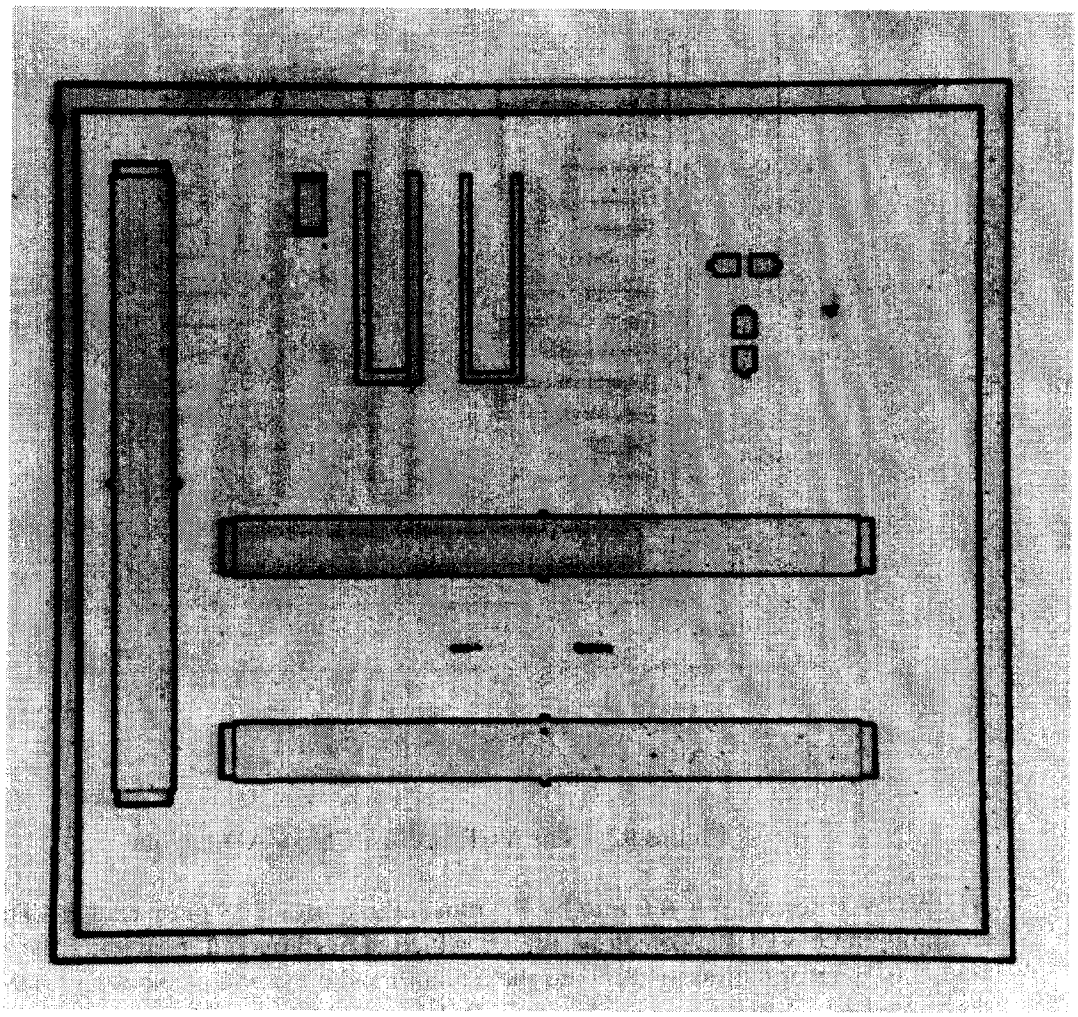

Figure #3 – The VCELL Test Chip (showing chip processed through mask #2)

Acknowledgments

This work would not have been possible without the support of both the NASA/MSFC Summer Faculty Fellowship program and key NASA and AMCOM personnel who assisted with the research. I am grateful to Mr. Patrick McManus and Mr. W.T. Powers for allowing me to work with the Advanced Sensors Team (ED-12) this summer and for supporting this research. In addition, I am very grateful to Mr. David Burns for his assistance with the chemistry and to Dr. Paul Ashley for his support and use of his lab facilities.

References

1. Dr. Koy B. Cook first conceived the VCELL acronym and the sensor concept in 1996 to describe the silicon structure used in the radiation-pointing sensor.

2. Commerce Business Daily, August 12, 1997 PSA #1907 NASA Goddard Space flight Center, Code 217, Greenbelt, Md. "*SUN SENSOR MINIATURIZATION*" study. Contact was: Otilia I Rodriguez-Alvarez, Technical Officer, oir712@rs710.gsfc.nasa.gov.

3. Commerce Business Daily, September 9, 1997, R&D Contracting Directorate, WPAFB, OH. Sensor Technologies Integration Lab Program, "*SENSOR TECHNOLOGY DEVELOPMENT*", Contact was: Alan Struckman, WL/AAKR, (937) 255-2902.

2001

NASA/ASEE SUMMER FACULTY FELLOWSHIP PROGRAM

MARSHALL SPACE FLIGHT CENTER
SOUTHERN UNIVERSITY
BATON ROUGE, LOUISIANA

INVESTIGATION OF FRICTION STIR WELLDING AND LASER ENGINEERED NET SHAPING OF METAL MATRIX COMPOSITE MATERIALS

Prepared By:	Ravinder M. Diwan, Ph.D.
Academic Rank:	Professor
Institution and Department:	Southern University Department of Mechanical Engineering
NASA/MSFC Directorate:	Engineering
MSFC Colleague:	Dr. Sandeep Shah

INTRODUCTION

The improvement in weld quality by the friction stir welding (FSW) process invented by TWI of Cambridge, England, patented in 1991, has prompted investigation of this process for advanced structural materials including Al metal matrix composite (Al-MMC) materials. Such materials can have high specific stiffness and other potential beneficial properties for the extreme environments in space. Developments of discontinuous reinforced Al-MMCs have found potential space applications and future for such applications is quite promising. The space industry has recognized advantages of the FSW process over conventional welding processes such as, the absence of a melt zone, reduced distortion, elimination of the need for shielding gases, and ease of automation. The process has been well proven for aluminum alloys, and work is being carried out for ferrous materials, magnesium alloys and copper alloys. Development work in the FSW welding process for joining of Al-MMCs is relatively recent and some of this and related work can be found in referenced research publications. [1-6]. NASA engineers have undertaken to spear head this research development work for FSW process investigation of Al-MMCs. Some of the reported related work [7] has pointed out the difficulty in fusion welding of particulate reinforced MMCs where liquid Al will react with SiC to precipitate aluminum carbide (Al_4C_3). Advantages of no such reaction and no need for joint preparation for the FSW process is anticipated in the welding of Al-MMCs. The FSW process has been best described as a combination of extrusion and forging of metals. This is carried out as the pin tool rotates and is slowly plunged into the bond line of the joint as the pin tool's shoulder is in intimate contact with the work piece. The material is friction-stirred into a quality weld.

Al-MMCs, 4 in x 12 in plates of 0.25 in. (6.35mm) thickness, procured from MMCC, Inc. were butt welded using FSW process at MSFC NASA using prior set of operating conditions. Details of welding history, pin tool performance and weld quality were investigated. The MMC weld plates included MMC plates with 40 vol. % and 55 vol. % SiC, (17 μ+ 3 μ), 3 DP+ sintered + a 0.25 in. layer of ceramic edge of 5%, 20% and 30% Al_2O_3 saffil edges that were friction stir welded. Two friction stir weld pin tools of Ferro-Tic and Stellite composition and selected designs were investigated. Weld quality was evaluated using radiography and standard metallography techniques. Mechanical behavior of these plate materials upon friction stir welding of these plates is to be analyzed with increasing volume fraction of ceramic particles in the composites. Pin tool wear is reviewed and recommendations for further work are included. Such studies are essential if Al-MMCs are to find their wide spread use in space applications.

The FSW processes are seen to give best results with stellite pin tools in the present experimental work. Ferro-Tic tool shoulders are seen to exhibit fracture easily due to its low ductility during installation. In general, Ferro-Tic material appeared more brittle than Stellite. 55 vol.% SiC plate could not be welded with either Ferro-Tic or Stellite pin tools. There were some defects found in radiography that were generated in welds. However more investigation of this with metallography or structure correlation is needed on the cause of the defects. Based on the study, for comparison of pin tool wear behavior and performance, it is recommended that analyses be made with other monolithic Ferro-Tic pin tools, and these be related to Stellite pin tools and T 15 similar pin tools designs. Long welds are to be also analyzed in the continuation of the study.

Another aspect in the fabrication of the MMCs centered around the use of the laser engineered net shaping (LENS) processing of selected Narloy-Z composites. Such an approach has been earlier studied for fabrication of 316 stainless steels, and Inconel 718 MMCs. Research in this processing technique promises to yield results for applications such as for next generation optical systems and other space applications. In the present study, attempts were made to fabricate straight cylindrical specimens using LENS process of Narloy-Z and Narloy-Z with 20 vol.% Al_2O_3 MMCs using the direct metal deposition Optomec LENS-750 system. Experiments have yielded some success in fabrication of Narloy-Z. However, Narloy-Z composite fabrication has not been possible due to bead like structure and agglomeration of specimens. This could be due to difficulty of process conditions, power requirements, and or need for coating of Al_2O_3 particles or better mixing process conditions. This preliminary experience is similar with that in case of Incolonel 718 composites, which has earlier shown particulate segregation and porosity in the structures. More work is needed to accomplish composite deposition and control of structure. This is highly recommended as the 316 stainless steel LENS deposited materials have shown definite improvement in their properties in addition to the possible economic advantages of the process.

EXPERIMENTAL

Five categories of the selected Al-MMCs, 4 in x 12 in plates of 0.25 in. (6.35mm) thickness with 40 vol. % SiC and 55 vol. % SiC, (17μ+3μ), 3DP+sintered + 0.25 in. layer with ceramic edge of 5%, 20% and 30% Al_2O_3 saffil edges were friction stir welded. All welds were single pass butt welded in comparative similar conditions as previously used for counterpart materials. Tool designs used earlier for Ferro-Tic and Stellite pin tools were utilized in this study as shown in Fig.2. Earlier studies had shown high wear of H-13 pin tools, which were not used in this study. The FSW process was performed using the MSFC vertical weld tool friction stir weld system in the Productivity Enhancement Complex as shown in Fig. 1. The welded panels were radiographed and examined and the section including the weld regions and related weld zones were then cut at selected locations for macroscopic and microscopic analyses and the second long edges were again welded. Details of welding history, pin tool performance and weld quality investigated in this study are reported separately in a tabular form. The second welds were earmarked for weld properties evaluation at room temperature and cryogenic temperature and for determining joint efficiency. Tool wear was quantified using micrometer, and profile measurements.

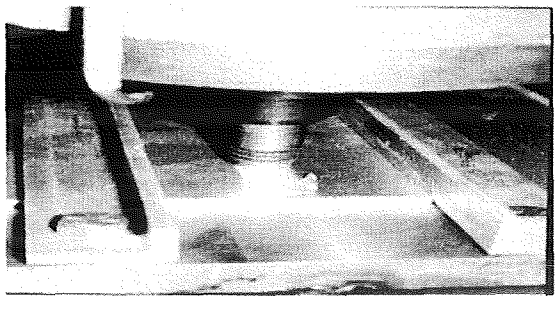

Fig.1 Photograph showing FSW in action.

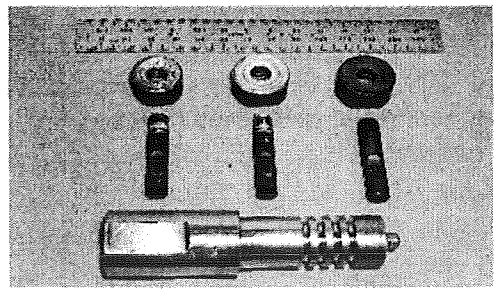

Fig. 2 Pin tool design of Ferro-Tic and Stellite Pins.

The typical empirical weld parameters used in this FSW study are based on prior similar studies as shown in Table 1.

Table 1. Empirical Parameters for FSW of Al-MMCs

FSW Parameters	Value	Description
Travel Speed	3.25-3.5 ipm	Inch-per-minute horizontal speed
Rotating Spindle Speed	550-750 rpm	Rotating speed of the pin tool
Lead Angle	2.5 deg	Pin tool's tilting angle from vertical plane
Plunge Depth	0.010-.015 in.	Shoulder length plunges below crown side
Penetration ligament	0.01- 0.02 in.	Distance between tip of pin and backing anvil

The typical empirical LENS processing conditions utilized in this study for Optomec system are as shown in Table 2

Table2. LENS Naroloy-Z Processing Conditions

Laser Power (A)	Head Speed (in/min)	Feeder Speed (rpm)	Step Layer Thickness (in.)
35-45	30-50	60-70	0.01

The Narloy-Z powder used was with Ag 3.0 wt%, Zr 0.5 wt%, Balance Cu. The Narloy-Z powder was mixed with 20 vol. % Al_2O_3 in a laboratory rotary mixer. The LENS deposition was carried out in the Optomec system under argon atmosphere using selected processing conditions. The material specimen microstructures were examined in longitudinal and transverse sections. More work is recommended in the development of the Narloy-Z composites.

RESULTS AND DISCUSSION

Five categories of Al-MMC functionally graded materials (FGMs) with 5%, 20%, 30% Al_2O_3 saffil edges, and without saffil edges with 40% and 55% SiC were welded for their FSW feasibility. Two pin tools were used for comparison purposes. The weld panels were photographed after the FSW weld process and evaluated by radiography. Large optical macroscans were then made of the weld regions of selected weld category specimens to cover the general overall regions in the FSWs. A representative view of welds in category1 and category 3 materials is shown in Fig. 3.

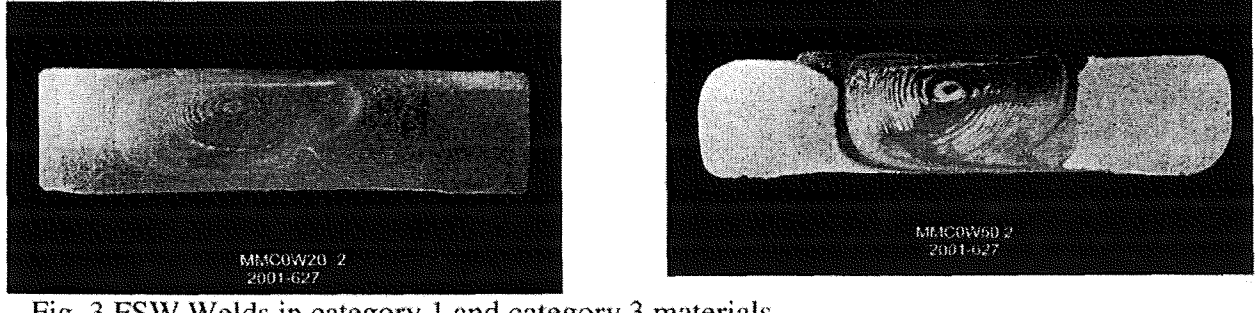

Fig. 3 FSW Welds in category 1 and category 3 materials.

The FSW welds showed a typical weld metal and stir zone structure as evidenced by the typical onion type structure in the center, enclosed by surrounding HAZ, and the unaffected parent metal structure. The composite base plate with saffil edges show in the weld structures the gradient and interactions of the Al_2O_3 and the SiC particulates in category 1-3 materials, and the variation of SiC particulates in the materials with out the saffil edges. FSW microstructures of typical category 3 and category 4 materials are shown in Fig. 4. In this, the Al_2O_3 particles appear as lighter elongated particles and the SiC as the angular, darker particulates. The microhardness data for this typical category 1 material gave values of about 140-150 VHN for the parent metal

and in transition range about 69.4 VHN and in the weld region about 87.5 VHN. Similar trend in variation was seen in category 2 material. However, the values are not uniform and depend upon the indentor location whether on the Al_2O_3 particles or on the SiC. Much more data will be needed for a detailed analysis for each condition of the FSW welds.

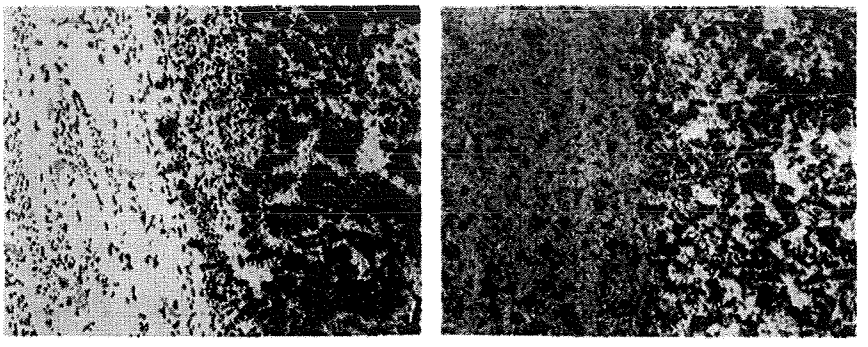

Fig. 4 FSW weld microstructure of category 3 and category 4 materials.

FSW in the welding panels of welding of FGM Al-MMCs categories 1-3 materials using Ferro-Tic and Stellite pins has been accomplished in some cases with lack of consolidation and possible worm holes. Quality improvements are possible with control and modification of weld parameters based on experience and lots of data generated by this study. In some cases, flash has been accumulated possibly due to too hot a weld. In some cases, material push through problems are seen at the back side due to weld plates mismatch and soft saffil constituents being plastically pushed out. In case of use with Ferro-Tic pin tools, more push through is observed. Flat Ferro-Tic pins provide deeper penetration compared to the use of Stellite pin tools. Continuing mechanical property evaluations are to be carried out and the work is in progress. Higher spindle speed and lower travel speed should provide higher weld temperatures in operation, and further parameter control and using load control or position control during the FSW process based on these studies should help in further formulation of FSW operating conditions. Category 4 and 5 Al-MMCs without the saffil edges at present time appear to be difficult to weld which is due to 40% and 55 vol.% of SiC in the MMCs. Such high concentrations make the material difficult to weld. The welded plate specimens and all data are available for fine tuning of weld conditions and further research in this direction. The pin tool history has indicated that Ferro-Tic tools provided weld lengths of about 11.5 inches, and about 21.5 inches weld lengths, and that the Stellite pin tool provided a weld length of about 54 inches in our evaluations. Relatively, Stellite pin tools appear to be more durable in the FSW welding process. Pin material properties and design both of course would be affecting their performance. The continuation of the FSW study will look into monolithic tool design and it is recommended to study the Ferro-Tic, Stellite and T 15 tool material pin tools for comparative study along with the study of long 4 feet welds of Al-MMCs.

The LENS process has provided some success in the deposition of Narloy-Z. The microstructure indicated some porosity, and more work is needed. Analysis of previous work has indicated similar difficulties with Inconel 718 and Inconel 718 MMCs with 20% Al_2O_3. However, in the trials with Narloy-Z, a sample about 2 ½ inch long with rough surface has been currently deposited. However, there is difficulty in the processing due to high reflectivity and low absorption in case of these materials. A macrogarph of the longitudinal section of the LENS cast Narloy-Z specimen and a micrograph of the cross section near the top edge of the specimen is

shown in Fig. 5. Results indicate segregation and lack of consolidation or porosity in the structure. More work is recommended.

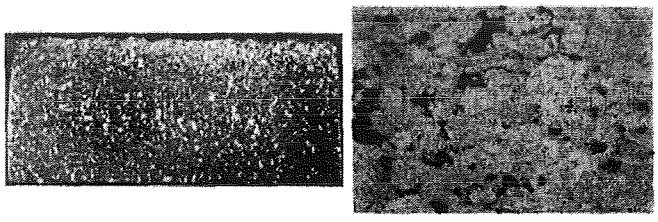

Fig. 5 LENS Narloy-Z longitudinal macrosection and a transverse microsection.

CONCLUSIONS

The FSW and LENS processes have been evaluated and investigated in this research. Problems encountered have been discussed. The processes hold special promise to applications for MMC materials. The work has yielded progress and is to be continued in relation to the results and recommendations of this work.

ACKNOWLEDGMENTS

The author expresses his appreciation and thanks to Dr. Sandeep Shah and Dr. Biliyar N. Bhat, MSFC Research Colleagues for their support and encouragement during this research. Thanks are also expressed to several associated personnel; Mr. Robert Carter for FSW work and to Mr. Ken Cooper and Mr. Robert Minor for LENS processing, Mr. Jeff Ding for FSW test planning, Mr. Jonathan Lee for discussions related to prior FSW work, Mr. Pat Salvail and Mr. Robert Bond for FSW specimens and test planning, and to Mr. Steve Cato, Mr. Greg Steele and Mr. Mike Gant for performing metallography related work.

REFERENCES

[1] C. J. Dawes : Development of the New Friction Stir Technique for Welding Aluminum-Phase III Final Report, TWI, Compiled by C.J. Dawes, April, 1997.
[2] S. Rawal, Metal-Matrix Composites for Space Applications, Journal of Metals, vol.53, No. 4, 2001.
[3] M. Schwartz: Joining of Composite Materials, ASM International, 1994.
[4] TWI, Proceedings of the 1st Friction Stir Welding Symposium, Thousand Oaks, CA, June 1999.
[5] TWI, Proceedings of the 2nd Friction Stir Welding Symposium, Gothenburg, Sweden, June 2000.
[6] W.L. Stellwag Jr. and T.J. Lienert, "Friction Stir Welding of Aluminum Metal-Matrix Composites", AEROMAT Conference, June 2001.
[7] J. A. Lee, R. W. Carter, and J. Ding: Friction Stir Welding for Aluminum Metal Matrix Composites (MMC's), NASA/TM – 1999-209876.
[8] W. Hofmeister, M. Wert, J. Smugeresky, J. A. Philliber, M. Griffith and M. Ensz, "Investigating Solidification with the Laser Engineered Net Shaping (LENS™) Process", Journal of Metals, vol.51, No. 7, 1999.
[9] D.R. Herling, G.J. Grant and W.H. Hunt, Jr., "Low-Cost Metal Matrix Composites, Advanced Materials & Processes", July 2001.

2001

NASA/ASEE SUMMER FACULTY FELLOWSHIP PROGRAM

MARSHALL SPACE FLIGHT CENTER
THE UNIVERSITY OF ALABAMA IN HUNTSVILLE

HUMAN MOTION TRACKING AND GLOVE-BASED USER INTERFACES FOR VIRTUAL ENVIRONMENTS IN ANVIL

Prepared By:	Joseph D. Dumas II, Ph.D.
Academic Rank:	Associate Professor
Institution and Department:	University of Tennessee at Chattanooga College of Engineering and Computer Science
NASA/MSFC Directorate:	Engineering
MSFC Colleague:	George Hamilton

Introduction

The Army/NASA Virtual Innovations Laboratory (ANVIL) at Marshall Space Flight Center provides an environment where engineers and other personnel can investigate novel applications of computer simulation and Virtual Reality (VR) technologies. Among the many hardware and software resources in ANVIL are several high-performance Silicon Graphics computer systems and a number of commercial software packages, such as Division MockUp by Parametric Technology Corporation (PTC) and Jack by Unigraphics Solutions, Inc. These hardware and software platforms are used in conjunction with various VR peripheral I/O devices, CAD models, etc. to support the objectives of the MSFC Engineering Systems Department/Systems Engineering Support Group (ED42) by studying engineering designs, chiefly from the standpoint of human factors and ergonomics.

One of the more time-consuming tasks facing ANVIL personnel involves the testing and evaluation of peripheral I/O devices and the integration of new devices with existing hardware and software platforms. Another important challenge is the development of innovative user interfaces to allow efficient, intuitive interaction between simulation users and the virtual environments they are investigating. As part of his Summer Faculty Fellowship, the author was tasked with verifying the operation of some recently acquired peripheral interface devices and developing new, easy-to-use interfaces that could be used with existing VR hardware and software to better support ANVIL projects.

Ascension MotionStar Testing, Integration and Troubleshooting

One of the most useful human motion tracking devices in ANVIL is the MotionStar six-degree-of-freedom spatial tracking system by Ascension Technology Corporation (see Figure 1). Based on the DC magnetic field technology used in the original Flock of Birds tracker, the MotionStar is able to track the position and orientation in space of a large number of sensors simultaneously. Some software packages, such as Jack, have a built-in interface to the Flock of Birds/MotionStar trackers, while others, such as Division MockUp, allow the end user to create software drivers for use with this and other devices.

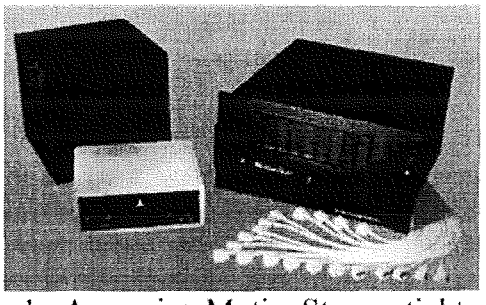

Figure 1: Ascension MotionStar spatial tracker.

During the previous summer's fellowship period, the author developed and tested a software driver that allowed ANVIL's MotionStar system with six sensors to be used as an input device with Division MockUp 6.0.2. Jack 2.2i's Flock of Birds/MotionStar support was used with the Motion Capture Toolkit to evaluate whole-body human motion capture (see Figure 2) using a female subject. While somewhat realistic motion capture was possible with sensors on the head, torso,

hands, and feet only, it was concluded that at least four additional sensors were needed to attach to the knees and elbows. By measuring the position and orientation of these joints instead of allowing them to be estimated by the software, motion capture of sufficient accuracy for ANVIL projects would be possible.

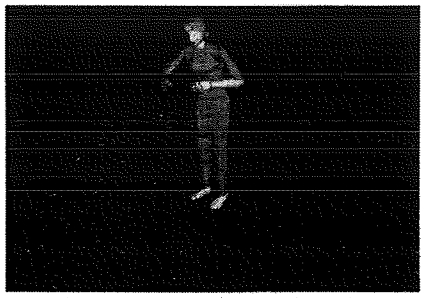

Figure 2: Motion capture in Jack using MotionStar.

During the intervening year, ANVIL was able to acquire four additional sensors and sensor interface cards for the MotionStar. One of the author's first tasks was to install and test the new hardware in the system. Due to hardware and software problems, this required more time than had been anticipated. Once all programming issues had been addressed, intermittent hardware problems remained. Eventually, these problems were traced to a single sensor interface card, which had to be returned to the manufacturer for replacement. After the replacement hardware was received, the complete MotionStar system was tested and found to be fully operational.

The additional sensors purchased for the MotionStar system prompted the author to develop an enhanced version of the software driver developed for Division MockUp during the previous summer. The original version could only work with the existing six sensors and communication speed was limited to 38,400 baud due to the environment in which the code was compiled. The new version allows the user to specify any number of sensors (up to 29) communicating via any desired serial ports at any baud rate supported by the Silicon Graphics host machine.

Perhaps the most important potential use for the MotionStar tracking system, as far as ANVIL objectives are concerned, is in conjunction with human factors/ergonomics software packages such as Jack. In particular, there is often a need to position and/or move simulated human figures in the virtual world in ways which mimic as closely as possible the postures and motions of human subjects in the real world. Traditional computer input devices such as keyboards and mice are not well suited to this task; the process can be time-consuming and the simulated actions often appear artificial. One way to improve this situation is to use a "human figure input device" such as the Monkey 2 (made by Digital Image Design, Inc.) to pose the simulated figure. This device, however, is very expensive and must be posed and moved by hand; it does not provide real-time performance or capture actual human motion. Fortunately, those are areas in which the MotionStar excels; so perhaps the best way to "puppet" virtual humans is to use it to track and capture the movements of a real human user. With this in mind, the author tested the ten-sensor MotionStar system with Jack 2.3's Flock of Birds tracking module and found it to operate reliably. Unfortunately, the temporary license obtained the previous summer for the Jack Motion Capture Toolkit, an add-on feature which had proven essential for motion capture studies using Jack, had expired and the author was unable to further evaluate the system by performing motion capture using human subjects during the term of his fellowship.

Object Selection and Navigation Using the Fakespace Pinch Glove System

Besides the obvious, nearly constant use of the visual sense to interact with one's surroundings, perhaps the most important interface between a person and the real or virtual world is the use of one's hands to interact with objects. A number of devices have been developed to allow users to manually manipulate items in virtual environment simulations. Most of these devices have taken the form of gloves (for example the VPL DataGlove and the Virtual Technologies CyberGlove) which sense the degree of bending of the user's fingers, allowing the computer to recognize certain meaningful gestures made by the user. This usually requires that the glove(s) be calibrated to the geometry of each different user's hand. Other devices, such as the Pinch gloves made by Fakespace Labs (see Figure 3), detect only contacts (touches) between fingers. This approach avoids the need for time-consuming calibration at the expense of limiting the types of gestures that can be distinguished. The position and orientation of the hands, which is normally tracked using a 6DOF system such as the MotionStar or Polhemus Fastrak, may or may not be part of the definition of the various gestures.

Figure 3: Fakespace Pinch gloves with Polhemus Fastrak sensors.

The versatility and ease of use of the Fakespace Pinch gloves, plus the ability (not shared by ANVIL's other glove systems) to use both hands simultaneously, makes them a very desirable user interface device for a number of projects. However, few of the software platforms used in ANVIL come with support for the Pinch gloves, and where they are supported, the gestures recognized and functions supported are not necessarily those desired. For example, the Pinch driver supplied with Division MockUp treats the Pinch glove set as a single device rather than as one device connected to each hand, making some types of interactions impossible. Thus, the author was tasked with writing new input device drivers to better support the use of the Pinch gloves. A module was developed for use with Division MockUp that allows the user to make twelve different gestures, each assignable to a different action in the virtual world, with each hand. (Some of the gestures involve using both hands, but all involve the use of the thumb and/or index finger of one hand and not the other, and so are defined as being dominated by that hand.) The ability to make a large number of gestures with each hand allows the user to grasp and manipulate objects with either or both hands and also issue a variety of commands to the program without having to remove the gloves or use the keyboard or mouse.

Another important task in a real or virtual environment is navigation. In order to touch and/or pick up objects, one must be able to move to the physical vicinity of those objects. Position trackers such as the Fastrak or MotionStar can readily be used to track the position of the hand(s) relative to the body, but there is still the need to be able to move the body as a whole within the

virtual world, the dimensions of which may be considerably greater than the range of the position tracker. Most software packages allow the user's body position to be "flown" by using keyboard or mouse commands, but this is awkward and detracts from the "immersive" experience desired for the user. One often-used alternative is the use of a joystick-type control(s) for navigation; however, this complicates the user interface and may (unless separate joysticks are used) introduce coupling between translational and rotational movements. To avoid these problems, it was desired to develop a glove-based interface that would allow for navigation as well as object interaction.

At the suggestion of his NASA colleague, the author developed a software driver for a unique navigation and interaction device dubbed the "Pinchigator" which uses the Fakespace Pinch gloves to perform the combined functions of grasping or "pinching" objects and navigating through the virtual world (as well as issuing other commands to the software). This input device driver was evaluated in conjunction with a model of the International Space Station that had been imported from CAD drawings (see Figure 4).

Figure 4: Using the "Pinchigator" to explore a model of the International Space Station.

Object selection using the Pinchigator is done in the same manner as with the basic Pinch glove driver, by maneuvering either virtual hand to be in contact with an object and making a pinching gesture with the thumb touching the index finger. Navigation is accomplished using a different gesture: thumb touching both the index and middle fingers of the same hand. Any time this gesture is being made with one hand, movements of that hand in the x, y, and/or z directions are mapped to corresponding movements of the user's virtual body, giving the user the illusion of pulling or pushing himself through space. When the navigation gesture is made with both hands at the same time, relative motions of the hands are mapped to yaw, pitch, and/or roll rotations of the virtual body, producing a "steering" effect. Thus, the user can navigate freely in three dimensions without using any other input devices or ever having to remove the gloves. Additional gestures are defined which increase or decrease the sensitivity of the navigational controls (allowing movements to be better scaled to the size and proximity of objects in the virtual world) and which issue other commands defined by the Division MockUp software package. A number of users, both VR-experienced and novices, have tried this interface and found it to be easy to use and intuitive in "feel."

Summary and Recommendations

As part of the 2001 Summer Faculty Fellowship Program, the author was able to install, configure, and troubleshoot additional sensors ordered for the MotionStar tracking system to support human motion capture and other VR tracking needs. Due to the lack of a license for a particular software module (Jack's Motion Capture Toolkit) motion capture with these additional sensors could not be tested, but the hardware and other needed software are in place to allow motion capture as soon as the requisite license is obtained. Permanent licensing of the Motion Capture Toolkit is recommended as a significant improvement over using keyboard and mouse commands to position virtual human figures and as a less expensive alternative to the purchase of a human figure input device such as a Monkey 2.

Another major activity supported by the author's Fellowship was the development of software drivers to support the use of Fakespace Pinch gloves for interaction with virtual objects and navigation through the virtual world. The Pinch glove driver allows the user to make up to twelve different gestures with each hand, where each can be assigned to a different action. The "Pinchigator" driver combines the ability to make a pinching (grasping) gesture to select objects, three other gestures that may be mapped to desired software commands, and another navigational gesture that can be used to translate or rotate the user's virtual body in the simulated environment. Six additional gestures are supported for varying the sensitivity of the translation and orientation commands. This software module allows the Pinch gloves to function as a very natural and intuitive interface between the user and the VR simulation. The successful integration of all of these devices and drivers has added significant capability to the ANVIL laboratory at MSFC and should significantly enhance the ability of ANVIL personnel to develop and use VR simulations in support of departmental objectives.

2001

NASA/ASEE SUMMER FACULTY FELLOWSHIP PROGRAM

MARSHALL SPACE FLIGHT CENTER
THE UNIVERSITY OF ALABAMA IN HUNTSVILLE

SECOND GENERATION REUSABLE LAUNCH VEHICLE DEVELOPMENT AND GLOBAL COMPETITIVENESS OF U.S. SPACE TRANSPORTATION INDUSTRY: CRITICAL SUCCESS FACTORS ASSESSMENT

Prepared By:	Chris I. Enyinda
Academic Rank:	Associate Professor
Institution and Department:	Alabama A & M University Department of Management and Marketing
NASA/Directorate:	Systems Management Office
MSFC Colleague:	Eric Shaw

Introduction

In response to the unrelenting call in both public and private sectors fora to reduce the high cost associated with space transportation, many innovative partially or fully RLV designs (X-34-37) were initiated. This call is directed at all levels of space missions including scientific, military, and commercial and all aspects of the missions such as nonrecurring development, manufacture, launch, and operations (Wertz, 2000). According to Wertz (2000), for over thirty years, the cost of space access have remained exceedingly high. For example, London (1996, 1994), Wertz (1996), and Hammond (1999) have discussed in details the reasons for the skyrocket launch costs.

The consensus in the popular press is that to decrease the current astronomical cost of access to space, more safer, reliable, and economically viable SGRLVs must be developed. This current skyrocket cost of space launch poses a major constraint to broadening and expanding U.S. economic activities into LEO. As a result, affecting global competitiveness of U.S. CST industry. Foreign firms control greater share of the launch market once dominated by U.S. For example, in the mid 1980s U.S. service providers had approximately 100% of the commercial space launch market revenues, but today U.S. has less than 50% of that market (Graham, 2001). Further, because of the growth potential in the international launch market, countries such as Brazil, India, Japan, and Israel are gearing up to enter the global launch market with their own commercial space launch vehicles. Considering this fact, NASA and U.S. space launch industry cannot afford to lag behind. Therefore developing SGRLVs will immeasurably improve the U.S' space transportation capabilities by helping the U.S. to regain the global commercial space markets while supporting the transportation capabilities of NASA's space missions.

Because space represents an important commercial frontier for U.S. to explore and exploit for economic, political, social, and security purposes it, has become more crucial than ever before to change the era of discovery and exploration of near space into an era of economic exploitation in the 21st century (Richardson, 1991). The economic effect of a reliable, robust, and the future competitive edge of the U.S. space launch industry cannot be overstated. The full economic potential of this new frontier can be achieved by developing economically viable RLVs. To address this concern, NASA's Marshall Flight Center through its space launch initiative (SLI) is taking the lead responsibility to develop the SGRLV that is billed for flight in 2010. In addition, high rates of launch traffic that will result from SGRLVs will lead to further major reductions in the cost of space transportation and the expansion of human activities to LEO (Collins and Ashford, 1986). Overall, developing the SGRLVs will provide an affordable commercial space transportation that will assure the competitiveness of the U.S. commercial space transportation industry in the 21st century.

The difficulty commercial space launch systems are facing is obtaining financing needed in the capital markets because of the dollar amounts and the risk involved (Scottoline and Coleman, 1999). Access to key financial markets is necessary for commercial space ventures. However, public sector programs in the form of tax incentives and credits, as well as loan guarantees are not yet available. The purpose of this paper is to stimulate discussion and assess the critical success factors germane for RLVs development and U.S. global competitiveness.

Critical Success Factors for SGRLVs and U.S. Competitiveness

Developing a business climate that encourages and supports private sector investment in the next generation space transportation systems development cannot be overemphasized. Some of the critical success factors that can have significant impact on SGRLV development and recapturing U.S. competitiveness in the global launch market include government incentive schemes and the proposed U.S. Space Development Bank (USSDB).

Government Incentive Schemes

There is much that U.S. government can do to stimulate private sector investment in developing SGRLVs. There is a need for the government to stimulate domestic private investment with specific guidelines aimed toward economic goals. The government may expect investors to create local employment, stimulate growth and development of local industry as a requirement for certain concessions. Thus, the intent of some assistance from the government is to encourage investment by helping to minimize and shift some of the risks that are known to be associated with space activities. Incentive schemes government can use to promote investment in SGRLVs include fiscal, financial, and nonfinancial incentives.

Fiscal Incentives: Represent specific tax measures designed to serve as an attraction to the domestic investor. These tax measures typically consist of special depreciation allowances, tax credits or rebates, special deductions for capital expenditures, tax holiday or zero gee-zero tax, and other reductions of the tax burden on the investor (Shaw, Hamaker, and Prince 1998, Sponable, 2000). Tax holiday that can be offered to investors can take a form of a reduction in normal corporate taxes or their elimination. This reduction can be for a specified period of time, which is estimated as the average time needed to establish efficient and competitive operations. Also, a tax reduction or relief can help in further development of space launch programs.

Financial Incentives: Granting of private investors financial incentives if they are willing to invest in the space program. This incentive can be in the form of loans, loan guarantees, among others. It can also offer low-interest loans and grant loans to firms wishing to increase their investments in space programs. It may also guarantee the loans that a firm takes from financial institutions.

Nonfinancial Incentives: The government can offer nonfinancial incentives such as advance purchase agreements, cooperative R&D, indemnification, policy stability, regulatory streamlining, and predictable certification to investors (Sponable, 2000).

Proposed USSDB

An alternative solution to the shortfall of venture capital for RLV industry is supporting and creating the proposed USSDB. Such a bank can bridge the shortfall in venture capital while at the same time allowing the market to select winners and losers (Matula, 200).

Implications and Conclusions

For many years, space community has been calling for much better and cheaper access to LEO, thus suggesting more reliable and economically viable space transportation launch vehicles. The RLV technology program is driven by the need to lower the cost of access to space in order to encourage the creation and delivery of new space activities that will eventually improve U.S. economic competitiveness. Although it is widely believe in the space launch community that RLVs are the future access to space, a purely private enterprise will not be able to develop and operate such a system with only private funds through conventional investment rules (Kaplan, 1999). Therefore, some form of government support is necessary to create and achieve a successful RLV program.

The fundamental benefit of RLVs is that they cannot be discarded every time they are used. Thus, amortizing the cost over multiple flights. Reducing the launch cost to a factor of 5 to 10 near term can result to an increase in the market size, thus leading to lower costs of space access in the offing. The effect of this action will encourage an increase in demand and in turn offer the opportunity for RLVs to become economically viable (Wertz, 200). The development of SGRLV would enable U.S. space launch industry to 1) become less dependent on the federal government for its continued survival and profitability and 2) partially rely on commercial industry to maintain its technical experience base in essential areas (Hammond, 1999). Also, Safer, more reliable and affordable access to space will enable the realization of new markets including space tourism, space business parks, pharmaceuticals and materials R&D labs, space manufacturing, sub-orbital fast-package delivery, solar space power, satellite internet content delivery, state or commercially-owned spaceports, among others. Therefore, to secure the future existence of the space industry and new entrepreneurial know-how in the high tech industry, U.S must be the first to the launch market with SGRLVs that is significantly safer, reliable, and cheaper than the current manned first RLV systems.

The U.S. commercial launch industry is under constant pressure of being dwarfed or even eliminated by foreign competition. Without an appropriate cost-cutting innovativeness by the government and industry in this endeavor, future commercial space boosters may be made in foreign countries. U.S. space launch manufacturers seeking low-cost space access could be held captive to foreign launch providers. Also, if the U.S. commercial space launch industry continues to erode, the government may face difficulties in placing future government payloads into orbit. This could eventually force the government to either subsidize the U.S. launch industry, or to rely on foreign government launch payloads, including those critical to U.S. national security. Also, failure of the U.S. commercial launch industry would mean loss of a national technical and defense base, millions of dollars in commercial revenue, and numerous jobs (London, 1996). It is therefore important that government and industry invest in this nation's future by working together to drastically curtail the cost of space launch by developing SGRLVs.

References

[1] Collins, P. and Ashford, D. (1988). "Potential Economic Implications of the Development of Space Tourism." Ada Astronautica, Vol. 17 (4), 421-431.

[2] Graham, J. B. (2001). "2nd Generation RLV: Program Goals and Acquisition Strategy." Space Technology and Applications International Forum, Jan 01, 1-7.

[3] Hammond, W. (1999). Space Transportation: A Systems Approach to Analysis and Design. Reston, VA: AIAA.

[4] Kaplan, M. H. (1999). "Are RLVs Economically Viable?" Launchspace, Vol. 4, No. 5, Oct. 1, 26-27.

[5] London, III, J. R. (1996). Reducing Launch Cost (Ch. 4) in J.R. Wertz and W. J. Larson (eds.), Reducing Space Mission Cost. Torrance, CA and Dordrecht, The Netherlands: Microcosm Press and Kluwer Academic Publishers.

[6] London, III, J. R. (1994). LEO on the Cheap-Methods for Achieving Drastic Reductions in Space Launch Costs. Maxwell Air Force Base, AL: Air University Press.

[7] Matula, T. L. (2000). "Bridging the RLV Financing Gap with a Space Development." Space 2000; Proceedings of Space 2000: The 7th International Conference and Exposition on Engineering, Construction, Operations, and Business in Space, Albuquerque, NM, Feb. 27-Mar. 2, 2000, 7-12.

[8] NASA Facts, MSFC. (2001). "The Space Launch Initiative: Technology to Pioneer the Space Frontier." June

[9] Richardson, R. C. (1991). "Prospect for Inexpensive Space Transportation." (http:/www.spacefuture.com/archive/prospect_for_inexpensive_space_transportation.shtml).

[10] Scottoline, S. and Coleman, R. (1999). "Effectiveness of Loan Guarantees versus Tax Incentives for Space Launch Ventures." Space Technology, Sep. 28-30.

[11] Shaw, E., Hamaker, J. and Prince, F. (1998). "Benefits of Government Incentives for Reusable Launch Vehicle Development." Paper IAA-98-IAA.1.2.01, 49th International Astronautical Congress, Sept. 28-Oct. 2, Melbourne, Australia, 1-11.

[12] Sponable, J. D. (2000). "Opening the Spaceways." Space Technology and Applications International Forum, 17th Symposium on Space Nuclear Power and Propulsion, Albuquerque, NM, January, 1150-55.

[13] Wertz, J. R. (2000). "Economic Model of Reusable Vs. Expendable Launch Vehicles." International Astronautics Congress, Rio de Janeiro, Brazil, Oct. 2-6, 1-15.

2001

NASA/ASEE SUMMER FACULTY FELLOWSHIP PROGRAM

MARSHALL SPACE FLIGHT CENTER
THE UNIVERSITY OF ALABAMA IN HUNTSVILLE

COMPOUNDED MICROSPHERES IN PHOTONICS: POTENTIAL BIOSENSOR AND BANDGAP APPLICATIONS

Report Not Available

Prepared By:	**Kirk A. Fuller**
Academic Rank:	**Adjunct Assistant Research Professor**
Institution and Department:	**The University of Alabama in Huntsville Earth Systems Science Center**
NASA/MSFC Directorate:	**Materials Science**
MSFC Colleague:	**David D. Smith**

2001

NASA/ASEE SUMMER FACULTY FELLOWSHIP PROGRAM

MARSHALL SPACE FLIGHT CENTER
THE UNIVERSITY OF ALABAMA IN HUNTSVILLE

ISO 9000 AND/OR SYSTEMS ENGINEERING CAPABILITY MATURITY MODEL?

Prepared By:	**Sampson E. Gholston**
Academic Rank:	**Assistant Professor**
Institution and Department:	**The University of Alabama in Huntsville Industrial & Systems Engineering & Engineering Management**
NASA/MSFC Directorate:	**Systems Management Office (VS10)**
MSFC Colleague:	**Gerry Flanagan**

Introduction

For businesses and organizations to remain competitive today they must have processes and systems in place that will allow them to first identify customer needs and then develop products/processes that will meet or exceed the customers needs and expectations. Customer needs, once identified, are normally stated as requirements. Designers can then develop products/processes that will meet these requirements. Several functions, such as quality management and systems engineering management are used to assist product development teams in the development process. Both functions exist in all organizations and both have a similar objective, which is to ensure that developed processes will meet customer requirements. Are efforts in these organizations being duplicated? Are both functions needed by organizations? What are the similarities and differences between the functions listed above?

ISO 9000 is an international standard of goods and services. It sets broad requirements for the assurance of quality and for management's involvement. It requires organizations to document the processes and to follow these documented processes. ISO 9000 gives customers assurance that the suppliers have control of the process for product development.

Systems engineering can broadly be defined as a discipline that seeks to ensure that all requirements for a system are satisfied throughout the life of the system by preserving their interrelationship. The key activities of systems engineering include requirements analysis, functional analysis/allocation, design synthesis and verification, and system analysis and control (Blanchard, B. S., 1998). The systems engineering process, when followed properly, will lead to higher quality products, lower cost products, and shorter development cycles (Martin, 2000). The System Engineering Capability Maturity Model (SE-CMM) will allow companies to measure their system engineering capability and continuously improve those capabilities.

ISO 9000 and SE-CMM seem to have a similar objective, which is to document the organization's processes and certify to potential customers the capability of a supplier to control the processes that determine the quality of the product or services being produced. The remaining sections of this report examine the differences and similarities between ISO 9000 and SE-CMM and makes recommendations for implementation.

ISO 9001:

NASA is ISO 9001 certified, which includes a quality systems model for quality assurance in design, development, production, installation, and servicing (Goetsch and Davis, 2000). This certification helps NASA achieve its policy, which is "to provide quality products and services to our customers". This policy states that NASA is committed to pursuing excellence and continuous improvement, maintaining high quality, safety, and reliability standards, and retaining high-quality employees. The ISO 9001 documentation sets the standards and guidelines for NASA to have an effective quality system.

Under ISO 9000 each employee should:

- Know MFSC's Quality Policy.
- Know their job responsibilities.
- Know where quality policies and procedures are located.
- Know where work instructions are located.
- Know how to handle nonconforming products and services.
- Know their job qualifications.
- Understand the overall quality system.

Unfortunately, ISO 9001 set the minimum requirements necessary for an effective quality system. It is left up to the organization to define their quality system and determine how they want to do business. Some organizations view quality system registration as a requirement to do business, not an opportunity to improve their processes. As a result organizations are mislead to only target minimum requirements. The correct approach is for these organizations to use ISO certification as an opportunity to document and improve their processes. To really benefit from ISO certification, organizations must be aggressive. They must identify the most effective way for them to do business.

Systems Engineering Capability Maturity Model

The SE-CMM describes the essential elements of an organization's systems engineering process that must exist to ensure good systems engineering. It also provides a reference for comparing actual systems engineering practices against the essential elements of systems engineering. The process areas are shown in the following table.

Engineering		Project		Organization	
PA01	Analyze Candidate Solutions	PA08	Ensure Quality	PA18	Coordinate with Suppliers
PA02	Derive and Allocate Requirements	PA09	Manage Configurations	PA13	Define Organization's SE Process
PA03	Evolve System Architecture	PA10	Manage Risk	PA14	Improve Organization's SE Process
PA04	Integrate Disciplines	PA11	Monitor and Control Technical Risk	PA15	Manage Product Line Evolution
PA05	Integrate System	PA12	Plan Technical Effort	PA16	Manage SE Support Environment
PA06	Understand Customer Needs and Expectations			PA17	Provide Ongoing Knowledge and Skills
PA07	Verify and Validate System				

Table 1. Process areas for systems engineering capability maturity model.

The SE-CMM has a continuous improvement loop built in. Each organization is certified based on a scale of 0 to 5. The objective is to reach level 5. A model is shown below. Notice that an organization that is level 5 certified is continuously improving its processes and has a repeatable product development system.

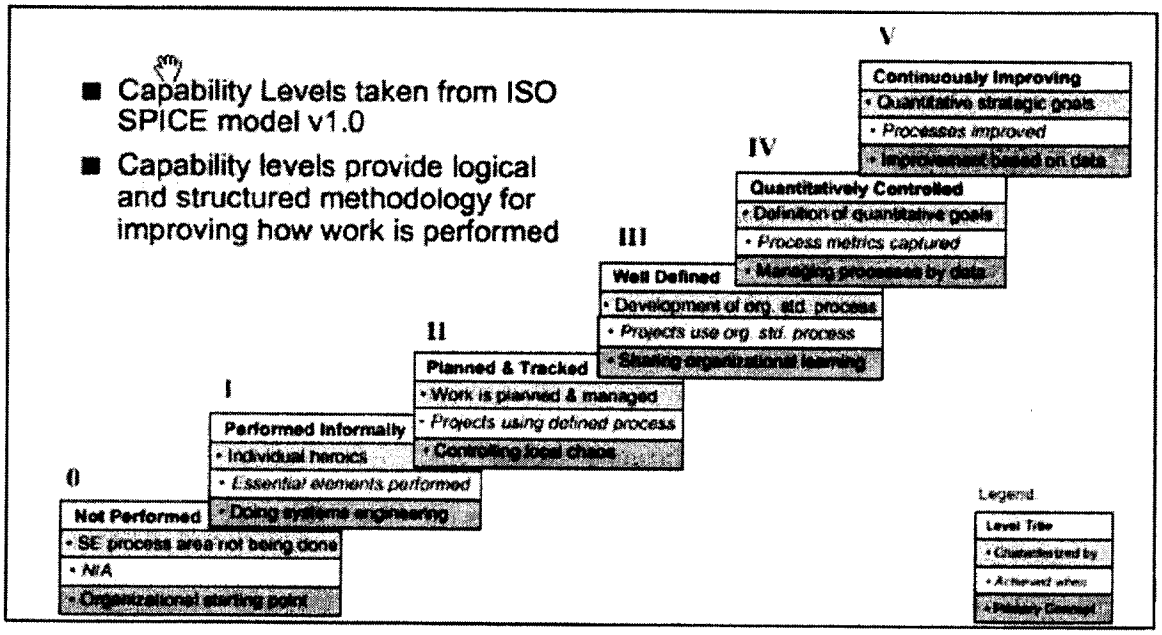

Figure 1. Level of systems engineering maturity.

Conclusions and Recommendations

Both ISO 9000 and the SE-CMM have a similar objective, which is to standardize the product development process. This allows organizations to control the process that is used to develop systems and products. Quality problems can usually be traced back to problems with the process that was used in development. Organizations must determine which system to implement when there are no contractual requirements.

ISO 9000 establishes the minimum requirements for a quality system. Thus, unless an organization is aggressive in implementing ISO 9000 and go above and beyond the minimum requirements, they will see little improvement from its implementation. SE-CMM is a more detailed system that guides the organization through the essential elements of a product development system. It also has a built in continuous improvement element.

MSFC already has ISO 9001 certification. By comparing the two systems, ISO 9001 misses more of the key elements of SE-CMM, than SE-CMM misses of ISO 9001. This would suggest that organizations should seek to implement a SE-CMM, rather than ISO 9001. However, organizations with ISO 9001 would meet the requirements for SE-CMM level 1.

It is recommended that MSFC combine the SE-CMM and ISO 9001 efforts at the Center. Take the spirit of both and roll it into the ISO 9001 certification. Or, build off the ISO 9001 documentation to implement a SE-CMM. Two systems would be counterproductive. Folding both under one umbrella would increase the chances of improving the product developing process. The ultimate goal of both is to make the product development process one of high quality that is better, faster, and cheaper. This goal should be a catalyst in determining which system is better for NASA.

Acknowledgements

The author is thankful to Gerry Flanagan, Steve Newton and Pam Takada of NASA Marshall Space Flight Center for facilitating this research. He is also thankful to Austin Boyd for extending his time and effort in showing the benchmark data from SAIC and generously proving data for this study. The author has also benefited from fruitful discussions with personnel in the Systems Management Office. This research was funded by the NASA-ASEE Summer Faculty Program's Contract *#NAG8-1786.*

References

[1] Blanchard, B. S., System Engineering Management, Second Edition, John Wiley & Sons, Inc. (1998).

[2] Goetsch, D. L. and Davis, S. B., Quality Management: Introduction to Total Quality Management for Production, Processing, and Services. Prentice Hall, Columbus, Ohio, 2000.

[3] Martin, J. N., Systems Engineering GuideBook: A Process for Developing Systems and Products, CRC Press (2000).

Bibliography

[1] Considine, V., System Engineering in Strategic Management Planning (Digest No:1997/141), IEE Half-Day Colloquium, Leatherhead, UK (Mar. 3, 1997), pp.2/1-2/4.

[2] Hoyle, D., ISO 9000 Quality Systems Handbook, Butterworth-Heinemann Ltd. (1994).

[3] Juran, J. M. and Gryna, F. M., Juran's Quality Control Handbook, Fourth Edition, McGraw-Hill, Inc. (1988).

[4] Kerzner, H., Project Management A systems Approach to Planning, Scheduling, and Controlling, John Wiley & Sons, Inc. (1998).

[5] Sage, A. P. and Rouse, W. B. (Editors), Handbook of Systems Engineering and Management, John Wiley & Sons, Inc. (1999).

2001

NASA/ASEE SUMMER FACULTY FELLOWSHIP PROGRAM

MARSHALL SPACE FLIGHT CENTER
THE UNIVERSITY OF ALABAMA IN HUNTSVILLE

ION MILLING OF SAPPHIRE

Prepared By:	Don A. Gregory
Academic Rank:	Professor
Institution and Department:	The University of Alabama in Huntsville, Department of Physics
NASA/MSFC Directorate:	Science
MSFC Colleague:	Kenneth A. Herren

Introduction

The ion figuring system at the Marshall Space Flight Center has been successfully used for at least three previous investigations into the ion milling of metals. The research was directed toward improving the surface quality of X-ray directing optics. These studies were performed on surfaces that were already hand polished to an excellent surface quality and were intended to remove the residual unwanted figure left by those techniques. The ion milling was typically carried out on test surfaces or mandrels that were several centimeters in width and length. The good thermal conductivity of the metal samples allowed the ion beam to be directed onto the sample for an indefinite period of time. This is not true of sapphire or most electrical insulators and problems have arisen in recent attempts to ion mill thin samples of sapphire. The failure and fracture of the material was likely due to thermal stresses and the relatively low thermal conductivity of sapphire (compared to most metals). These assumed stresses actually provided the key as to how they might be monitored. A thermal gradient in the sapphire sample will induce an effective index of refraction change and because of the shape constraint and the crystal structure and simple thermal expansion, this index change will be nonuniform across the sample. In all but simple cubic crystal structures, this leads to a spatially nonuniform optical retardance induced on any polarized optical beam traversing the sample, and it is this retardance that can be monitored using standard polarimetric procedures.

Stress Induced Birefringence

The term birefringence refers to the existence of two indices of refraction within one material. This is simple to understand with a non-cubic crystal structure. The atomic forces that hold the crystal together are proportional to the distance between the atoms or ions and in a non-cubic material these distances are different in orthogonal directions. Thus the forces present are different. This leads to a difference in the electrical conductivity in the two directions (a difference in dielectric constant) that is proportional to the index of refraction of the material. An even simpler explanation involves the proportionality of the index of refraction to density as in the Lorentz- Lorenz model [1]. The density of atoms or ions is different in orthogonal directions in the simple non cubic material model. If the index of refraction is different in orthogonal directions then that means that the speed of light in the material is different depending on which direction it is traveling. The birefringence is thus defined as the difference in these indices of refraction. The index of refraction is defined as the ratio of the speed of light in a vacuum to the speed of light in the material. This number is ordinarily purely real and greater than one for common optical materials. Polarized light has a definite orientation of its electric field vector and for illustration purposes assume that the light is linearly polarized. This means that the electric field vector does not rotate as the field progresses in space. The magnitude of the electric field vector does of course change in space and time as a simple sinusoid. The electric field vector as any other vector can be decomposed into components in a suitable basis. For a suitably chosen direction of the electric field vector this means that the components will have values in the two index of refraction directions. This means that one component of the vector will travel faster than the other, leading to a phase difference in the two components. The exiting beam will no longer be a simple

linearly polarized field and will behave very differently when analyzed by a simple polarizer. The phase retardance is the product of the magnitude of the wave vector, the thickness of the material, and the difference in the indices of refraction.

In more realistic materials the explanation is much more difficult but the observed effect is very similar. Suppose now that stress is applied to the material. On a microscopic scale this means that the atoms or ions have been forced closer together in some regions and separated more in others. This effect causes the same changes to the index of refraction as described with the simple non-cubic model just discussed. The incident linearly polarized light experiences many different indices of refraction thus leading to a nonuniform retardance over the sample which can be observed using a polarizer. These stresses are always present in any real material but it is the change in these stresses that are of concern. Additional stresses can be induced by many methods but it is the stresses induced by the thermal transport of energy from the ion source that are of interest in this investigation.

Experimental Arrangement

The experimental arrangement employed as much of the existing equipment as possible. This included the Kaufman type ion source (3 cm.) and the vacuum chamber equipped with two glass window ports [2]. These ports proved invaluable in introducing the Helium Neon laser beam to probe the transparent sample. A sketch of the optical system is shown in Figure 1. The laser beam was expanded and collimated using a microscope objective and pinhole arrangement. The beam was then expanded using a simple spherical lens to a diameter of about 1.5 cm. The beam was then directed by a mirror through a linear polarizer and finally into the vacuum chamber through one of the windows. The beam then passed through the sample that was held without stress in a metal mount. A mirror then directed the beam through the exit glass port and through a second polarizer and to the ccd camera. Various filters were used to control the intensity detected by the camera to avoid saturation.

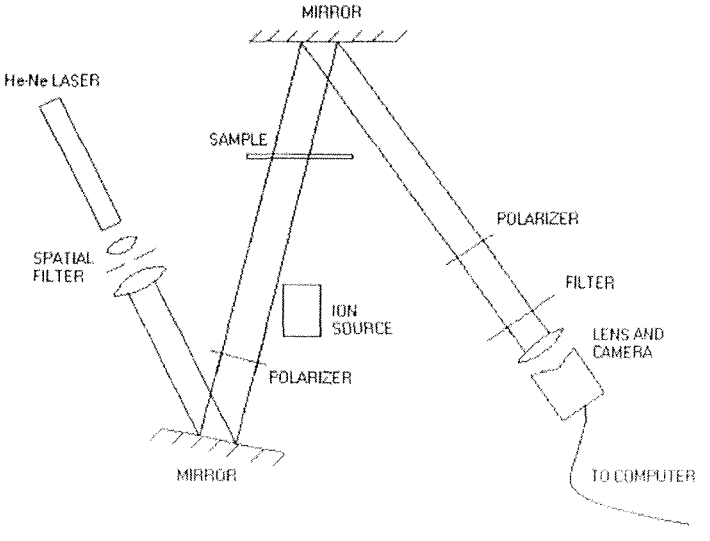

Figure 1: Sketch of optical system

A photograph of the chamber containing the ion source is shown in Figure 2. The source of the ions is argon gas. The energy of the ion beam is about 1000ev. The ions pass near a charge-neutralizing filament as they leave the source to avoid charging the target material. The entire ion system is a commercially available unit from IonTech [TM]. The starting parameters for the ion source were: discharge voltage 55 volts, discharge current .88amps, beam voltage 1000 volts, beam current 60 mA, acceleration voltage 200 volts, and acceleration current 1 mA. All of these parameters are variable and control the intensity of the beam and its shape. Other researchers have determined that these settings will produce a reasonably Gaussian beam at a distance of 2-3 inches from the source [3].

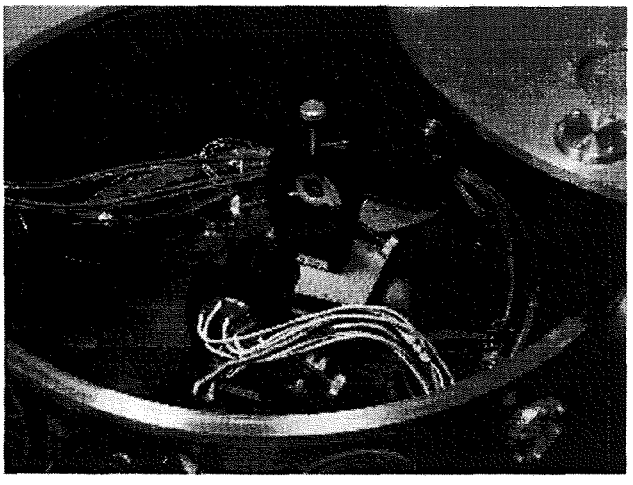

Figure 2: Chamber containing ion source

Experimental Results

The initial experiments were performed with glass microscope slides as the target. Previous attempts by others demonstrated the difficulty in ion milling sapphire, so it was decided to begin with a less expensive transparent optical material to gain experience and to determine if the stress induced birefringence could be observed at all. The slides were typical microscope cover glasses and 1 mm thick. The polarizers were oriented such that a minimum amount of laser light reached the camera. The source itself is an intense source of white light due to the neutralizing filament so a red filter was employed to insure that the camera would only detect the red laser light. If the ion bombardment of the glass slide did indeed heat it, then the thermally induced stresses should cause the birefringence of the slide to change and some of the laser light would pass through the analyzer polarizer. Figures 3a-3e show the images captured by the camera as the ion beam was turned on for about 30 seconds. It is possible to see the metal mount holding the slide in the pictures. The camera is actually focused on the plane of the slide using a bit of tape placed on the slide before the experiment begins. The red light seen in the first figure is from the laser and represents the leakage light that was not blocked by the

analyzer polarizer. In Figure 3b the beam has been on for about 15 seconds and it is obvious that more of the light is passing through the analyzer, which indicates that the stresses induced in the slide are indeed changing the birefringence of the glass. Figure 3c was taken at 30 seconds exposure and shows even more light passing through the analyzer. The beam was then turned off and the final two figures show the sample cooling down and eventually returning to the original state after about 2 minutes. This series of experiments demonstrated the central objective of the initial part of the research. The ion beam did induce stresses in the material that could be monitored using polarized light as the probe. The goal then is to use this fact to monitor the stress in sapphire so that ion milling could proceed without fracturing the sample.

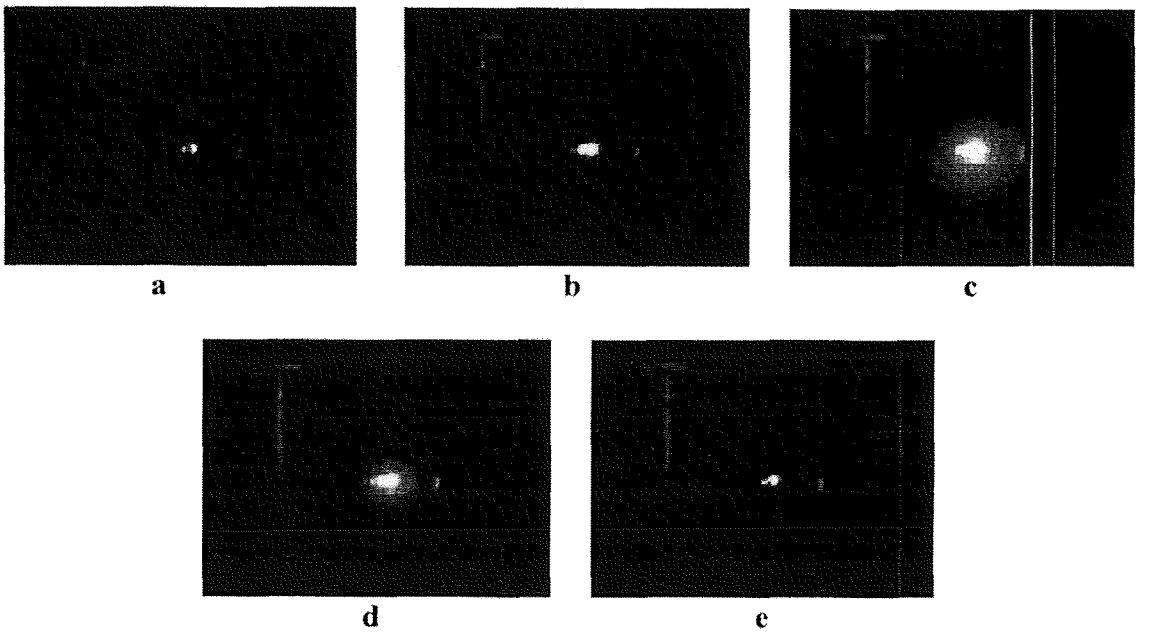

Figure 3a-3e: Images taken by camera as ion beam was turned on for 30 seconds

The glass samples were also analyzed after the experiment to determine if any ion milling of the surface had occurred during the experiment. These observations were done using a standard microscope and an interferometer. Figure 4 is an interferogram of the microscope slide. One half of the slide for this experiment was covered with aluminum foil as a reference. The interferogram clearly shows where the slide was covered. Figure 5 is a profile of the surface taken with the WYKO and shows clear evidence that about one-half wave of surface has been removed. The total time of the exposure was about 4 minutes.

The next step was to replace the glass plate with a very thin (0.25 mm) sapphire sample. The sample was mounted in a specially prepared holder that allowed only half of the sample to be exposed to the ion beam. The holder was aluminum, the half-mask was steel and the sapphire was held in the mount without pressure. Figure 6 shows that ion milling

of the surface was successful and that about 140 nanometers of material was removed. The sample showed no cracking and could have been exposed longer. The total exposure was approximately 3 minutes, which was comprised of two 90 second exposures.

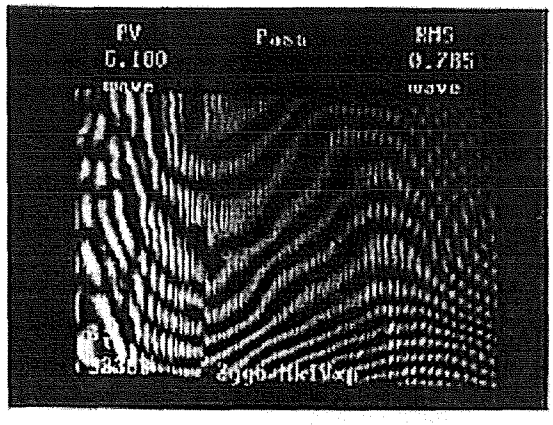

Figure 4: Interferogram of ion milled microscope slide

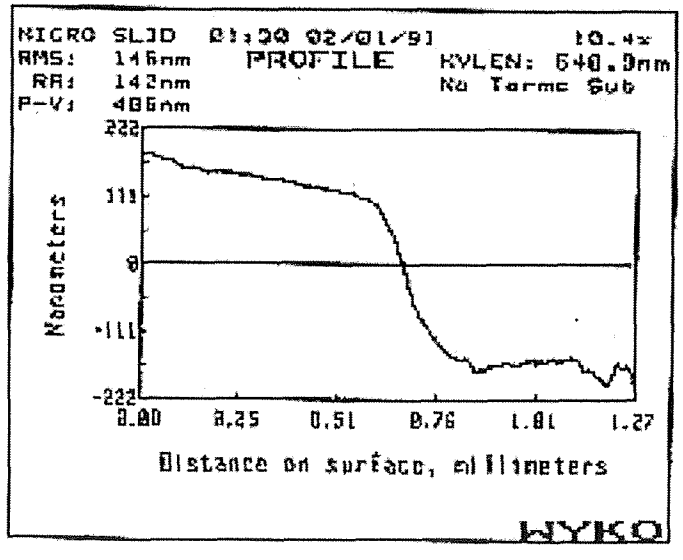

Figure 5: Surface profile of ion milled microscope slide

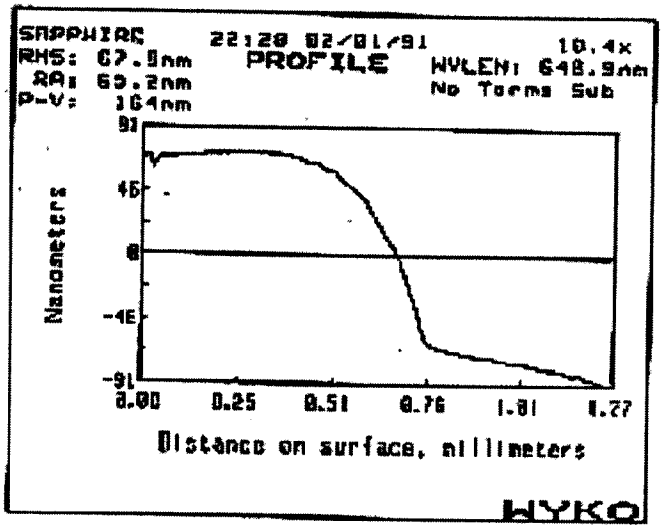

Figure 6: Surface profile of ion milled thin Sapphire sample

Conclusions

The goals of this preliminary research were to determine if ion milling of transparent optical materials could be done, and to determine if the thermal energy produced by the ion milling process was sufficient to produce stress induced birefringence. This optically measurable effect would then be used as a monitor of the sample. Early experiments with glass showed this to be the case and that the amount of birefringence induced was easily observed using a standard ccd camera. The same procedure was then employed for a thin Sapphire sample. The stresses produced less optical phase retardance, as expected, due to the extreme thinness of the single sample examined, however the increase in transmission through the analyzer was still easily observed. The sample was also in reasonably good thermal contact with the metal mount. Ion milling was effective for both type samples examined in this research, without causing either to crack. Surface scans of both type samples showed that ion milling can be an effective method for removing small amounts of material without serious damage.

References

[1] Hecht, E. and Zajac, A., *Optics,* Addison- Wesley, Menlo Park, CA, 1975, p.86

[2] Mooney, James, *Ion Figuring of Non-Planar X- ray Optics*, MS Thesis, The University of Alabama in Huntsville, Department of Physics, 2000

[3] Cantey, T., *Ion Figuring of X-ray Mirror Mandrels*, MS Thesis, The University of Alabama in Huntsville, Department of Physics, 1997

2001

NASA/ASEE SUMMER FACULTY FELLOWSHIP PROGRAM

MARSHALL SPACE FLIGHT CENTER
THE UNIVERSITY OF ALABAMA – HUNTSVILLE

MAGNETIZED TARGET FUSION

Prepared By:	Steven T Griffin
Academic Rank:	Associate Professor
Institution and Department:	The University of Memphis Electrical and Computer Engineering Department
NASA/MSFC Directorate:	Transportation
MSFC Colleague:	Francis Thio

Introduction - MTF

Magnetized target fusion (MTF) is under consideration as a means of building a low mass, high specific impulse, and high thrust propulsion system for interplanetary travel. This unique combination is the result of the generation of a high temperature plasma by the nuclear fusion process. This plasma can then be deflected by magnetic fields to provide thrust. Fusion is initiated by a small fraction of the energy generated in the magnetic coils due to the plasma's compression of the magnetic field. The power gain from a fusion reaction is such that inefficiencies due to thermal neutrons and coil losses can be overcome. Since the fusion reaction products are directly used for propulsion and the power to initiate the reaction is directly obtained from the thrust generation, no massive power supply for energy conversion is required. The result should be a low engine mass, high specific impulse and high thrust system. The key is to successfully initiate fusion as a proof-of-principle for this application.

Currently MSFC is implementing MTF proof-of-principle experiments. This involves many technical details and ancillary investigations. Of these, selected pertinent issues include the properties, orientation and timing of the plasma guns and the convergence and interface development of the "pusher" plasma. Computer simulations of the target plasma's behavior under compression and the convergence and mixing of the gun plasma are under investigation. This work is to focus on the gun characterization and development as it relates to plasma initiation and repeatability.

Trigatron and Plasma Gun Initiation

The basic plasma gun is a cylindrically symmetric coaxial line. An inner conductor is charged positive by several kilovolts with respect to the outer conductor. The space between is filled with gas at 10 millitorr of pressure or gas is puffed in via the gas puffing valves. Trigatrons are fired generating significant local ionization initiating a vacuum arc breakdown [4,5] at the breech of the gun between the two coaxial components. The resulting high current flow through a low inductance circuit produces a strong magnetic field circulating around the central anode. The resulting Lorentz Force on the arc region produces acceleration down the tube towards the gun muzzle. Rapid heating of the ion and neutral population ahead of the plasma produces a hypersonic shock wave out the gun. This wave collects and pushes the background gas out the muzzle. The basic gun configuration has been tested and verified as a precursor to a twelve gun MTF configuration test.

A significant factor in the performance of the twelve-gun configuration is the consistency and reliability of the arc initiation in the breech of the plasma gun. Variable delays in plasma formation in the gun breech could result in timing problems in the twelve-gun configuration. In particular the firing jitter [3] of a plasma gun needs, at a minimum, to be known and repeatable. Further the maximum tolerable timing errors in the arrival of a sector's pusher plasma may require that the jitter be reduced. In turn, the plasma formation time in the gun breech needs to be controlled and is heavily dependent on behavior of the plasma initiating triggers (trigatrons).

Both the gun and trigatron behavior depend in turn on the driver circuit and electronics. The driver circuit and breech plasma interact heavily with device rise time and plasma formation

delay dominated by the total stray inductance including circuit as well as plasma internal inductance. In an idealized configuration, planned circuit inductance should dominate the residual circuit inductance and plasma inductance thereby creating a consistent plasma initiation sequence and low jitter. In particular dependence on plasma inductance [1] should be avoided because of its dependence on minority gas constituents, cathode surface morphology, etc. Variation in these parameters from gun to gun could result in excessive variation in the gun-to-gun firing delays - delays that it would be difficult to repeat due to variation in gun histories.

To investigate this, an experiment is planned as a series of phases designed to isolate dominant effects within the gun. Phase one will concentrate on the repeatability of the hydrogen thyratron based trigatron pulse generator and trigatron. Phase two will concentrate on the delays associated with the plasma formation in the main gap of the gun. For this reporting period, phase one was completed and the apparatus for phase two constructed. The data generated for phase one is too voluminous to be reported under this format and will be published elsewhere. Anticipated phase two data will also be reported under other cover. A description of the apparatus, a sample of the results and implications are detailed below.

Phase I Apparatus

The phase one experimental apparatus is shown in figure one. A vacuum system demonstrating a base pressure of 8×10^{-6} Torr was constructed from a Turbomolecular pump with the usual gauges, fixtures and valves. An experimental apparatus was built on top of this as shown in figure one. A three inch acrylic spacer was placed between two 304 stainless plates. Though optical paths are available for laser interferometer measurement of the ion density. Additional optical access is available for determination of temperature, time imagery and spectroscopy. A laser interferometer [2] was partially constructed but was not completed when data recording requirements delayed its progress. Gas feed and vacuum ports were installed and covered with stainless steel mesh to block stray discharge paths. A leak valve / pressure regulator based helium flow system was implemented. A standard MTF trigatron was installed in the upper plate in the same manner as the actual guns. An electrical interface for the trigatron was designed with a measured inductance of 9 nHy. Unshielded trigatron wires exhibit an inductance of 500 nHy. The trigatron alone is approximately 20 nHy.

The phase I apparatus uses extensive low inductance RF shielding [6] resulting in a device constructed form the same material as the actual gun but with the total inductance reduced to 250 nHy and the RF shielding improved by more than 40 dB. All of the apparatus was extensively shielded from RF and ground loop interference [7]. The vacuum apparatus and supporting instrumentation is contained in point grounded aluminum boxes. Tektronix digital storage oscilloscopes (Model TDS3052) are used for primary data collection and are shielded by floating aluminum enclosures. All instrumentation and vacuum system components are isolated from building power by battery powered UPS. Preliminary characterization of the vacuum system established a procedure for controlling the chamber pressure to ± 0.1 mTorr precisions at 10 mTorr. Pressure accuracy is approximately $\pm$ 0.2 mTorr. Non-helium partial pressure should be less than 1 part per thousand.

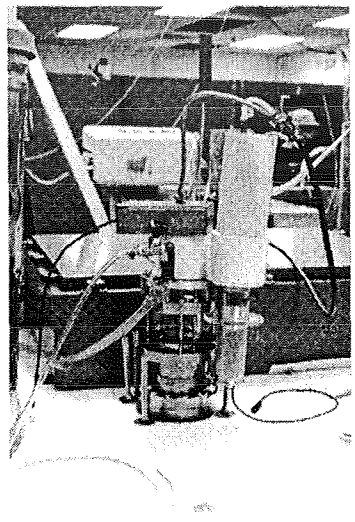

Fig. 1: Phase one experimental apparatus

Results and Discussion

Various data sets were taken with the phase I apparatus. These results will be reported under other cover. As an example of the results, consider figures two and three below. These are plots versus time of the Trigaton voltage and current. These curves were obtained from a modified Pearson Coil and NorthStar 10,000:1 voltage probe. Of interest here are the delay times from a fiber optical timing mark designated time zero. The curves below were signal processed and converted through MathCAD. These programs were written for this effort to remove all detected signals above the upper cutoff frequencies of the probes and some digital artifacts associated with the 5G Sa/sec oscilloscopes used to record the data.

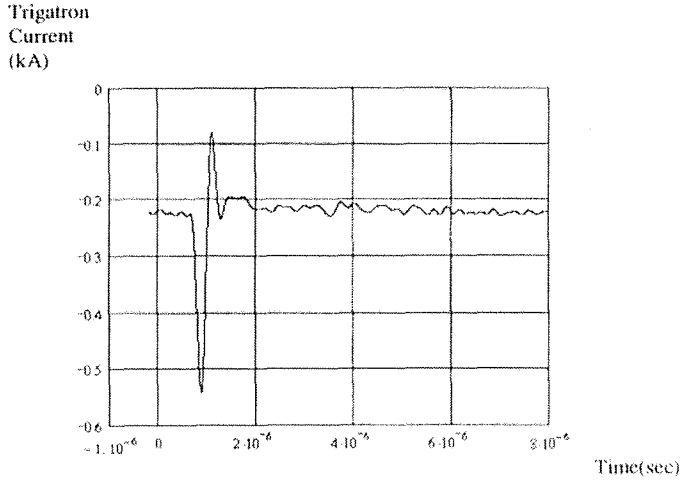

Fig. 2: Current versus time in a trigatron

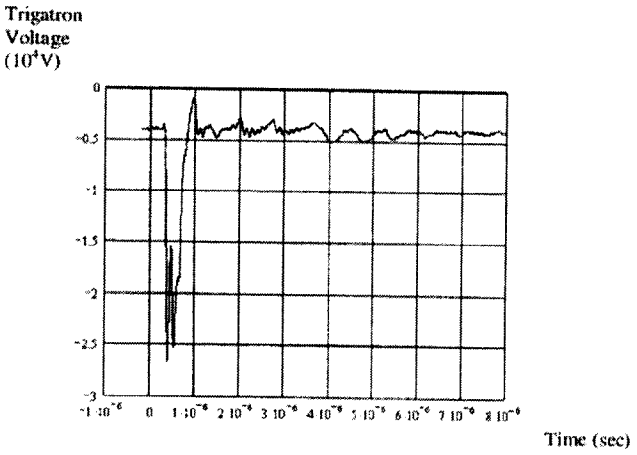

Fig. 3: Voltage versus time in a trigatron

Conclusions and Subsequent Work

Several conclusions can be drawn from the results to date. (1) Repeatable and accurate voltage and current measurements can be made despite the operating environment. Improvements in Pierson coil shielding and low inductance current path control has substantially reduced sensor noise. (2) The discharge performance changes when background pressure is at least three orders of magnitude below run pressure. Discharge emission is consistent with highly energetic helium and breakdown voltage is consistent with pure helium. (3) Long path breakdown occurs at this pressure regime. This is verified by stored images demonstrating initial breakdown at distances equivalent to the trigatron to far side inner wall of the outer gun sleeve. The voltage breakdown performance is also comparable to the plasma gun history. (4) Breakdown trigatron pulser and trigatron performance is repeatable and consistent. Detailed support for each claim is available upon request.

A phase two apparatus was constructed and is shown diagrammatically in figure four. This is the same basic apparatus as phase one with the addition of an intermediate grid element one inch below the upper plate. This grid is constructed of 304 SS plate and is connected to a capacitor charged to the anode voltage in the original gun. The intention is to simulate the environment at the gun breech and determine the breakdown characteristics, delays and jitter. The external capacitor is connected by a low inductance technique to simulate gun anode behavior for at least the first fraction of a microsecond. The grid is placed at the same distance as the gun anode from the trigatron and contains 144 holes. Initially the holes will not be obscured to allow discharge penetration to simulate the trigatron plasma's ability to access the longer distances to the far side of the gun coaxial geometry. Though this is not exactly the same geometry as the gun breech it approximates its distance, pressure, transparency and gas environment. The geometry difference is incorporated to allow optical diagnostics of the apparatus.

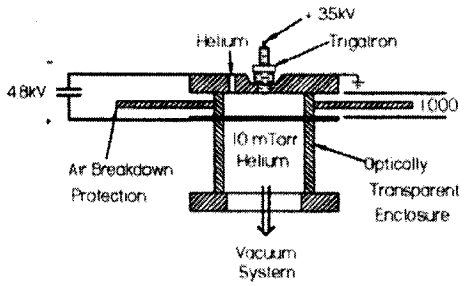

Fig. 4: Phase two experimental apparatus

Acknowledgements

The author would like to thank Francis Thio, Richard Eskridge, James W. Smith, Adam Martin, Jeff Richeson, Stacey Anacker, Rafael Martinez , Emily Hall, Steve Leckenby, Doug Davenport, Richard Potvin, Roger Harper, Jason Cassibry, Jim Martin, Chris Dobson, Jeanelle Bland, Susan Dunnavant, Tony Robertson and Gerry Karr for their assistance during the summer.

References

Complete list available upon request.

[1] Boxman, R.L., Sanders, D.M., Martin, P.J., and Lafferty, J.M. (1995), *Handbook of Vacuum Arc Science and Technology*, Noyes Publications, Park Ridge NJ, pp. 625 – 699.

[2] Huddlestone, R.H. (1965), *Plasma Diagnostic Techniques*, Academic Press, New York, pp. 460 – 464.

[3] Kuffel, E. and Abdullah, M. (1970), *High-Voltage Engineering*, Pergamon Press, New York, pp. 30 – 67.

[4] Lafferty, J.M. (1980), *Vacuum Arcs Theory and Application*, John Wiley and Sons, New York, pp. 107 – 168.

[5] Latham, R.V. (1981), *High Voltage Vacuum Insulation: The Physical Basis*, Academic Press, New York, 53 – 81, 117 - 139.

[6] Pozar, D.M. (1998), *Microwave Engineering*, 2nd ed, John Wiley and Sons, New York, pp. 59 – 65.

[7] Waters, W.E. (1983), *Electrical Induction from Distant Current Surges*, Prentice-Hall, Englewood, NJ.

2001

NASA/ASEE SUMMER FACULTY FELLOWSHIP PROGRAM

MARSHALL SPACE FLIGHT CENTER
THE UNIVERSITY OF ALABAMA IN HUNTSVILLE

AN INVESTIGATION INTO THE POTENTIAL APPLICATION OF WAVELETS TO MODAL TESTING AND ANALYSIS

Prepared By:	A. Fort Gwinn, Jr
Academic Rank:	Associate Professor
Institution and Department:	Lipscomb University Physics and Engineering Dept
NASA/MSFC Directorate:	Engineering
MSFC Colleague:	Kathy Kappus

Introduction

The analysis of transient data of the type found in vibrating mechanical systems has been greatly improved through the use of modern techniques such as Fourier analysis. This is especially true when considered in conjunction with the development of the so-called Fast Fourier Transform algorithm by Cooley and the tremendous strides in computational power of the last several decades. The usefulness of the discrete Fourier Transform is its ability to transform sampled data from the "time-domain" to the "frequency domain," thereby allowing the analyst to decompose a signal into its frequency content.

More recent developments have led to the wavelet transform. The strength of wavelet analysis is its ability to maintain both time and frequency information, thus making it an attractive candidate for the analysis of non-stationary signals. This report is an overview of wavelet theory and the potential use of the wavelet transform as an alternative to Fourier analysis in modal identification.

Fourier Transform

Figure 1 show two input signals and their corresponding frequency response functions (FRFs) that result from the Fourier analysis of each signal. The input signal, shown in figure 1a, is a stationary signal composed of two lightly damped sine waves that are both present from t=0 to t=3.12 seconds. As can be seen from the corresponding FRF (shown in the lower part of figure 1(a) the frequency of each sine wave is revealed to be 80 hz and 128 hz respectively.

Figure 1(b) also contains the 80 hz and 128 hz frequency components as shown in the accompanying FRF. However, it is non-stationary since the signal changes abruptly from a pure 80 hz signal to a pure 128 hz signal at time, t=1.515 seconds

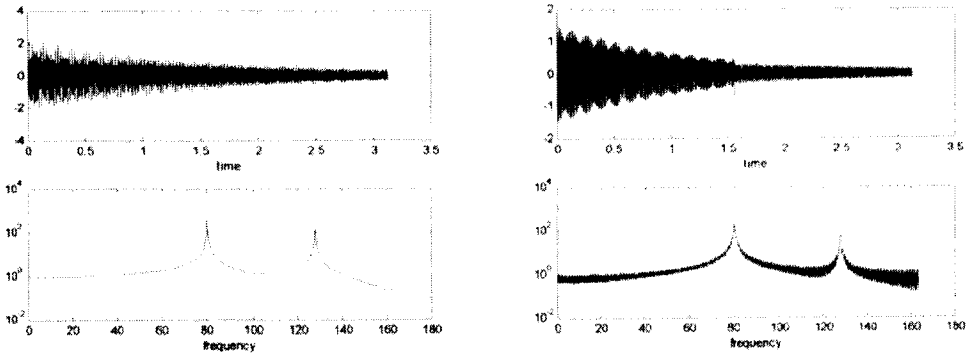

(a) Stationary Signal **(b) Non-Stationary Signal**

Figure 1, Two Example Signals with 80hz and 128 hz Signal Content

As can be seen in Figure 1(b), while the two frequencies can be identified from the FRF, the only indication that there is also a time-dependency present in the data is the apparent "noise" that shows up in the trace.

Wavelet Transform

During the late 80's and early 90's, research began to develop methods of preserving the time dimension of a signal. Among the methods that were developed was the wavelet transform. The wavelet transform is similar to the Fourier transform in that it is the superposition of an infinite series of basis functions. However, unlike Fourier transforms, the wavelet basis functions are of varying dilation (scale) and translation defined by Chui [1] to be

$$f(t) = \sum_{j,k=-\infty}^{\infty} c_{j,k}\psi_{j,k}(t) \tag{1}$$

where $\psi_{j,k}$ is the wavelet function and the wavelet coefficients, $c_{j,k}$, are

$$c_{j,k} = \int_{-\infty}^{\infty} f(t)\psi_{j,k}(t)dt\,. \tag{2}$$

Using Daubechies' [2] notation, we can define the wavelet function to be:

$$\psi_{j,k}(t) = a^{\frac{-j}{2}}\psi(a^{-j}t - k\tau) \quad \text{for a} > 1 \tag{3}$$

where τ represents the sample time interval and the indices j and k represent the dilation and translation increments respectively. Note that the CWT is continuous in the sense that the dilation of the basis wavelet may be continuously variable.

Choosing a = 2 (i.e. a dyadic scale), leads to an efficient implementation algorithm called the discrete wavelet transform (DWT) which results in the corresponding wavelet series

$$f(t) = a_0 + \sum_{j=0}^{\infty}\sum_{k=0}^{2^j-1} a_{2^j+k}\psi(2^j t - k) \tag{4}$$

In this form, it is said that the transform consists of the summation over j "levels," where each level contains 2^j wavelets spaced $\frac{1}{2^j}$ apart [4,5]. Furthermore, the DWT can be shown to be equivalent to multi-resolution analysis using quadrature mirror filtering resulting in a DWT algorithm that is considerably faster than the CWT in an economy of operations reminiscent of Cooley's FFT.

Wavelets Applications

Although wavelet analysis is relatively new, it has already found commercial application. One of the most successful applications of wavelet analysis is in the area of image processing. A significant amount of data compression can be achieved by using a two-dimensional DWT as a filter to preserve only the minimum amount of details necessary

to reconstruct an image. A second area where wavelet analysis has gained some popularity is in the area of "health monitoring" of machinery. Since the wavelet transform preserves the temporal dimension of the signal, it is possible to identify atypical transient events that are precursors of impending mechanical failure. Other areas of industrial use, such as acoustics, have begun to capitalize on the strengths of wavelet analysis also.

Example CWT Signal Decomposition

An undamped version of the example signal of figure 1 was analyzed using a complex Morlett wavelet transform subroutine that was written this summer using MATLAB®. The resulting data is plotted in terms of time, frequency, and magnitude in Figure 2 below.

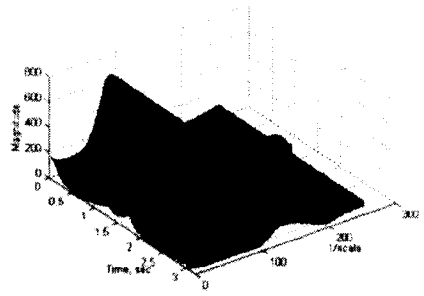

Figure 2, Complex Morlett Wavelet Transform

This illustrates one of the more important characteristics of wavelet transforms. That is, high frequency components have poor frequency resolution and good time resolution, while low frequency components have good frequency resolution and poor time resolution.

Example DWT Signal Decomposition using the Wavelet Toolbox

In 1996, MathWorks, Inc introduced a "Wavelet Toolbox" for their MATLAB® software. Although the current version of this toolbox is not written with complex signal analysis in mind, it is still an instructive tool for demonstrating the use of the wavelet in the field of health monitoring. Here the chosen example signal is the one used by Kimble [3]. This signal consists of one pure 80 hz signal, one 128 hz signal with a 10 hz amplitude modulation, and two Gaussian spikes that represent anomalies that might occur in a piece of rotating equipment. The resulting FRF using Fourier analysis is shown in Figure 3. Note that Fourier analysis divides the 128 hz signal into two peaks spaced at ±10 hz on either side of the center frequency and there is no indication of the Gaussian spikes. When the same input signal is subjected to a 10 level DWT analysis using a 4 coefficient Daubechies wavelet, the Gaussian spikes are clearly visible in levels 3 through 7.

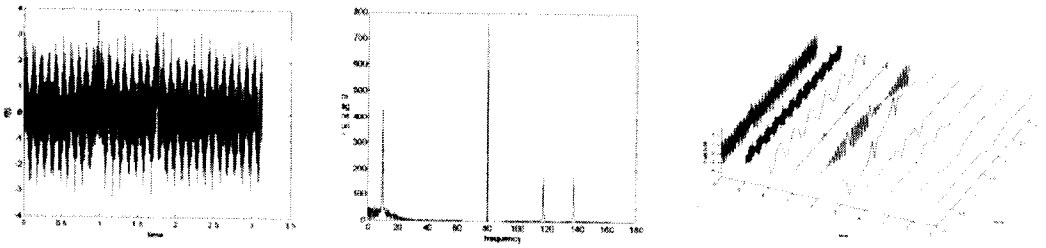

(a) Input Signal **(b) Fourier Transform** **(c) Discrete Wavelet Transform**

Figure 3, Input Signal, Fourier Transform, and 10 level DB4 DWT

Future Research

Although wavelets have not found wide commercial application in the field of modal analysis, there is still a considerable amount of interest among researchers in this new tool. In particular, there has been some promising work in areas such as wavelet-based FRFs, IRFs, and system identification [6], as well as the development of wavelet-based tools for characterizing the inherent non-linearity of a system [7].

Acknowledgments

The author would like to thank Ms. Kathy Kappus and the entire Modal and Control Dynamics Team for providing the opportunity and guidance for this research.

References

[1] Chui, C. K., An Introduction to Wavelets, Academic Press, San Diego, CA, 1992.

[2] Daubechies, I., Ten Lectures on Wavelets, Society of Industrial and Applied Mathematics (SIAM), Philadelphia, PA, 1992.

[3] Kimble, K. R., Tibbals, T. F., "Spectral Analysis Techniques Using Wavelets as an Alternative to Fourier Analysis for Transient Dynamic Data," AEDC-TR-94-17, January 1995.

[4] Newland, D.E. "Wavelet Analysis of Vibration, Part 1: Theory," Transactions of the ASME Journal of Vibration and Acoustics, Vol 116, October 1994, ASME, pp 409-416.

[5] Newland, D.E. "Wavelet Analysis of Vibration, Part 2: Wavelet Maps," Transactions of the ASME Journal of Vibration and Acoustics, Vol 116, October 1994, ASME, pp 417-425.

[6]Ruzzene, M., Fasana, A., Garibaldi, L., and Piombo, B. "Natural Frequencies and Dampings Identification Using Wavelet Tansform: Application to Real Data," Mechanical Systems and Signal Processing, Vol 11, No. 2, pp 207-218, 1997.

[7] Staszewski, W.J. , Chance, J.E., "Identification of Nonlinear Systems Using Wavelets – Experimental Study," IMAC XV International Modal Analysis Conference, 1997.

2001

NASA/ASEE SUMMER FACULTY FELLOWSHIP PROGRAM

MARSHALL SPACE FLIGHT CENTER
THE UNIVERSITY OF ALABAMA IN HUNTSVILLE

ANALYTICAL MODAL ANALYSIS FOR THIN-FILM FLAT LENSES

Prepared By:	Hamid R. Hamidzadeh
Academic Rank:	Professor
Institution and Department:	South Dakota State University Mechanical Engineering Department
NASA/MSFC Directorate:	Engineering
MSFC Colleague:	Michael Tinker

Introduction

Due to strong potential applications and more demanding requirements imposed upon thin-film structures for space deployable, there has been increasing research and development activities during recent years in the field of vibration analysis of these types of structures. Moreover, interests in employing these structural components have received renewed emphasis in recent years within NASA and the Air Force. This is due to their inherent lightweight, low packaging and launch volume, and relative simplicity of deployment. Among the potential mission concepts for which these structural elements are included, one can mention solar sails, space solar power generation systems, solar thermal propulsion vehicles, large space telescopes, and inflatable communication antennas.

This paper presents analytical procedures to determine vibration and physical characteristics of thin film lenses with circular and elliptical shapes membranes considered in design of a solar concentrator. In general, three methods are used to obtain approximate solutions of Helmholtz boundary value problems. One method requires that solution satisfy the differential equation exactly and the boundary condition approximately. Another method demands a solution that satisfies the boundary conditions exactly and the governing equations approximately. The third method sees a solution that satisfies both the governing equation and boundary conditions approximately. Extensive reviews of vibrations of membrane and plates are provided by Leissa (1965) and Mazumdar (1982). Figure 1 illustrates a solar concentrator assembly in a test facility with lens and thin-film struts.

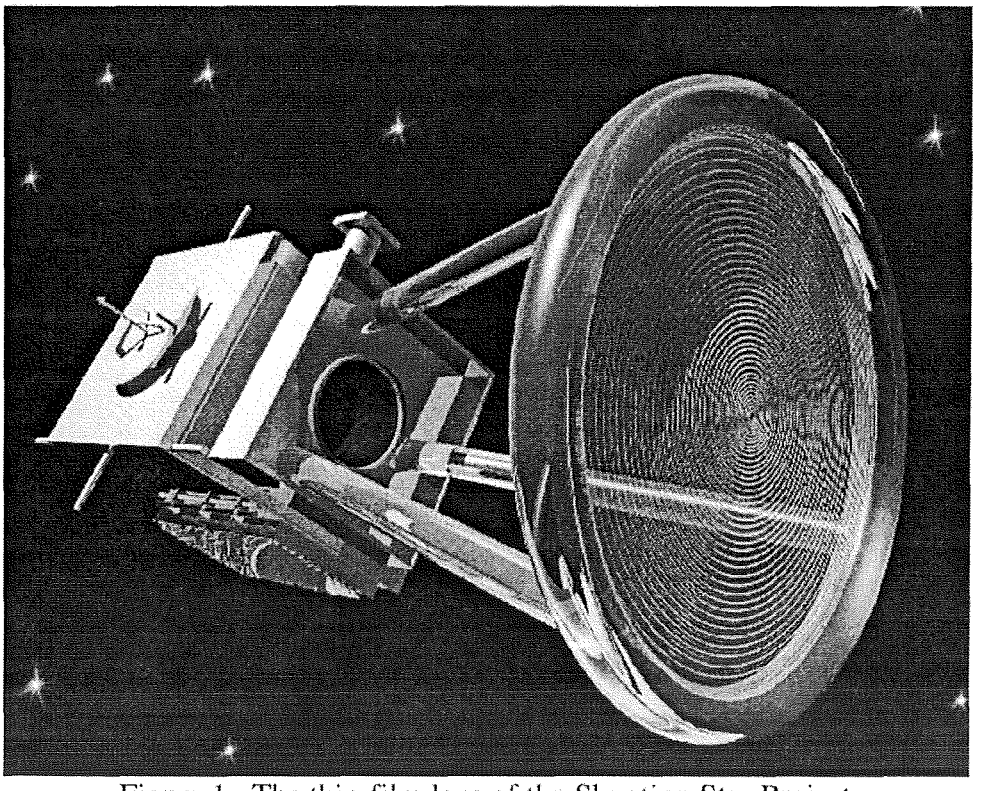

Figure 1. The thin-film lens of the Shooting Star Project

Vibrations Analysis of Circular Thin-Film Clamped Lens

Free vibration of a thin film circular lens made of CP1 supported by an aluminum ring is considered. Two different analytical models based on pre-strained membrane and plate theory are developed and the results are compared with experimental modal analysis. Comparing the results of experiment and membrane theory provides estimation for the pre-strain in the film. CP1 material and physical properties are: Film Thickness of 0.0005 in, Film Diameter of 17.5 in, Mass density of 0.0001341 lb s^2 /in^4 , Poisson's ratio of 0.34, and modulus of elasticity of 300000 psi. The mathematical model for transverse free vibration of the membrane as shown by Soedel (1993) can be represented by the following Helmholtz equation.

$$\nabla^2 w - \frac{\rho h}{N}\ddot{w} = 0 \tag{1}$$

Where ρ is the mass density, h is the film thickness, and N is the radial uniform boundary tension per unit length. Assuming harmonic vibration, the modal displacement function in polar coordinate can be written as:

$$w_n(r,\theta,t) = W_n(r)\cos n(\theta - \alpha)e^{i\omega t} \tag{2}$$

The solutions to $W_n(r)$ for each value of the integer n are two linearly independent solutions of Bessel's equation. However, since W_n is always a finite value for $r \leq 0$ and is zero at the boundary of $r = a$, therefore the frequency equation can be given by

$$J_n(\lambda a) = 0 \tag{3}$$

where $\lambda^2 = \frac{\rho h \omega^2}{N}$

The above equation is the frequency equation and has infinite number of roots for each value of n. few of these roots are listed in the Table I. The natural frequencies of the membrane are given by

$$\omega_{mn} = \frac{(\lambda a)_{mn}}{a}\sqrt{\frac{N}{\rho h}} \tag{4}$$

Table I. Values for $(\lambda a)_{mn}$

	n			
m	0	1	2	3
0	2.404	5.520	8.654	11.792
1	3.832	7.016	10.173	13.323
2	5.135	8.417	11.620	14.796
3	6.379	9.760	13.017	16.224

Table II. Experimental Modal Information

Frequency - Hz	Loss factor
53.3	1.680-002
185.9	1.298e-002
356.0	0.072e-002

Integers m and n represent number of nodal circles and nodal diameter for each mode respectively. Radial Tension force along a unit length of the membrane in terms of uniform pre-strain can be presented by the following equation $N = Eh\varepsilon_0/(1-\nu)$. Where ε_0 is the value of radial pre-strain. Considering that zeros of the first Bessel functions for non-negative orders are always real, it can be concluded that for linear viscoelastic material the modal loss factor for each mode is the same as the material loss factor. Computed natural frequencies for first sixteen modes for different values of strains are computed and are presented in Figure 2. The results illustrate as the pre- strain increases natural frequencies for all modes increase too. Theses results are compared with those obtained from Finite Element analysis for the fundamental

modes. The comparison establishes an excellent agreement between analytical and Finite Element results.

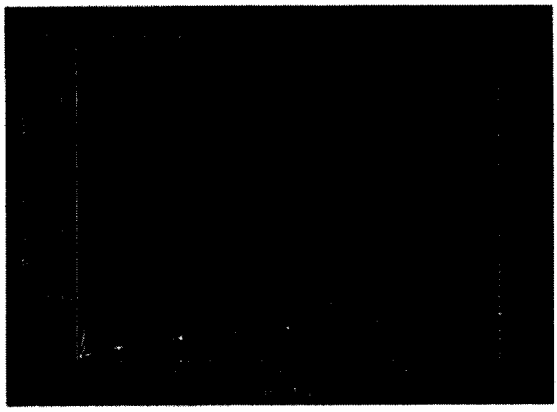

Figure 2. Natural frequencies versus pre-strain

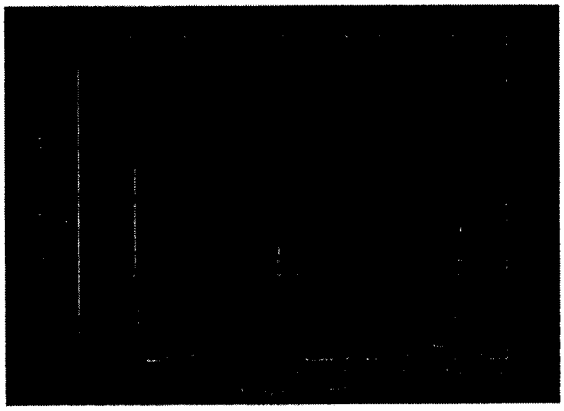

Figure 3. Experimental receptance response

Experimental Modal Analysis for a Circular Membrane

Experimental modal analysis was also conducted on CP1 membranes with the same geometry and properties. The tests were performed using miniature impulse hammer for excitation while laser vibrometer was used to measure the response of the membrane. Frequency responses for excitation and response measurement at center and half way along the radius were determined. For the case of driving and measuring points to be at the center, the receptance versus frequencies is plotted in Figure 3. Using Half power point technique natural frequencies and modal loss factors for the three major peaks shown in figure 3 are tabulated in Table II. Natural frequencies for fifteen different modes for several pre-strain values were computed and were compared with those obtained experimental with measured point being halfway along the radius. Figure 4 shows that the comparison established good agreement between analytical results for pre-strain of 0.0004 and the experimental data. This comparison can be used to estimate the amount of pre-strain and consequently the radial tension per unit length of the circular membrane.

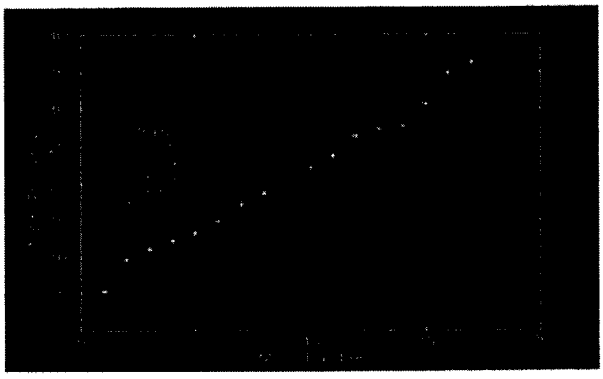

Figure 4. Natural frequencies for different pre-strains

Free Vibration of Clamped Thin Film Elliptical Membrane

Free vibration of a thin film elliptical n XXI-4 ıade of CP1 supported at its boundary is considered. An analytical model is developed and a solution based on Mathieu functions in elliptical coordinate is provided. In the analysis following material properties for CP1 material are assumed. Film Thickness of t = 0.0005 in, Film major diameter of a = 226 in, Film minor diameter b= 164.08 in, Mass density of ρ = 0.0001341 lb s^2 /in^4, Poisson's ratio of ν = 0.34, Modulus of elasticity of E = 300000 psi. The mathematical model for transverse free vibration of the membrane can be represented by the following Helmholtz equation

$$\nabla^2 w - \frac{\rho h}{N}\ddot{w} = 0 \tag{5}$$

Where ρ is the mass density, h is the film thickness, and N is the radial uniform boundary tension per unit length. Assuming harmonic vibration, the modal displacement function in polar coordinate can be written as:

$$w(x, y, t) = W(x, y)e^{i\omega t} \tag{6}$$

transforming from Cartesian to elliptical coordinates on may write:

$$x + i\,y = h\cosh(\zeta + i\,\eta) \tag{7}$$

Transforming the Laplacian operator from Cartesian to the elliptical coordinate after extensive simplifications the equation of motion will be simplified by introducing a separable solution of $W(\zeta, \eta) = \Psi(\zeta)\,\phi(\eta)$ in elliptical coordinate. Further simplification results in getting two ordinary differential equations called Mathieu and modified Mathieu equations (McLachlan (1947)).

$$\frac{d^2\phi}{d\eta^2} + (a - 2k^2\cos 2\eta)\phi = 0 \quad \text{and} \quad \frac{d^2\psi}{d\zeta^2} - (a - 2k^2\cosh 2\zeta)\psi = 0 \tag{8}$$

After satisfying all the required boundary conditions, solution of $w(\zeta, \eta)$ which closely satisfy the above conditions is:

$$w(\zeta,\eta) = \sum_{m=0}^{\infty} C_m Ce_m(\zeta, q)ce_m(\eta, q)\cos(\omega_m t + \gamma) + \sum_{m=0}^{\infty} S_m Se_m(\zeta, q)se_m(\eta, q)\cos(\bar{\omega}_m t + \bar{\gamma}) \tag{9}$$

Where $C_m, S_m, \gamma_m, and\ \bar{\gamma}_m$ are arbitrary constant determined from the initial conditions, $\omega_m and\ \bar{\omega}_m$ are natural frequencies of the mth mode. Each individual solution in the above equation for m = 0, 1, 2, ... corresponds to a different modes of vibration. Where, q has its appropriate value. Considering the above conditions we must have

$$Ce_m(\zeta_0, q) = 0 \ \ for\ m = 0,1,2,... \ and \ \ Se_m(\zeta_0, q) = 0 \ \ for\ m = 1,2,... \tag{10}$$

The value of ζ_0 is fixed, so we need those positive values of q, say $q_{m,r}, \bar{q}_{m,r}$ for which for which the above two functions vanish. These may be regarded as the positive parametric zeros of the functions. There is an infinity of zeros for each m. Hence for Ce_m if r = p, there are (p-1) nodal ellipses within the clamping rings, and likewise for Se_m , but their location differ. Natural frequencies are related to $q_{m,r}, \bar{q}_{m,r}$. For $0 \le q, 1 \le m$, the functions ce_m (η,q), se_m (η,q) have zeros in η. Hence w vanishes also if η satisfies the respective equations

$$f_{m,r} = \frac{1}{\pi h}\sqrt{\frac{Nq_{m,r}}{\rho t}} \quad and \quad \bar{f}_{m,r} = \frac{1}{\pi h}\sqrt{\frac{N\bar{q}_{m,r}}{\rho t}} \tag{11}$$

$$ce_m(\eta, q_{m,r}) = 0 \, and \, se_m(\eta, \bar{q}_{m,r}) = 0 \tag{12}$$

Now $ce_m(\eta, q_{m,r})$ *and* $se_m(\eta, \bar{q}_{m,r})$ each have m zeros in $0 \le \eta < \pi$, so for a given m each function rise to m nodal hyperbolas. Therefore, these roots define a series of confocal nodal hyperbolas. In this analysis, approximate functions for Computation of Ce_m , Se_m , ce_m , and se_m given by McLachlan (1954) are adopted. Of course, the accuracy of the numerical values of natural frequencies is entirely depends on the accuracy of these functions. For the given elliptical membrane with major and minor diameters of 226 in and 164.08 in respectively we have h = 155.41 in and the eccentricity of the ellipse is $e = h/a = 0.6877$. since cosh $(\zeta_0) =$ 1/e, therefore is $\zeta_0 = 0.9203$. first roots of $Ce_m(\zeta_0, q)=0$ and $Se_m(\zeta_0, q)=0$ for m = 0, 1, and 2 are computed to be

$q_{01} = 0.9967$, $q_{11} = 2.0506$, q_{11} = is complex, $q_{21} = 3.2729$, and $q_{21} = 3.9323$

Considering pre-strain of $\varepsilon_0 = 0.03\%$ value of pre-tension force per length of membrane will be calculated to be N = 0.06818 lb/in.

Using equation (11) estimated natural frequencies in Hz for the elliptical membrane are obtained to be:

$f_{01} = 4.1238$, $f_{11} = 5.9150$, $\bar{f}_{11} = 7.044$, $f_{21} = 7.4728$, and $\bar{f}_{21} = 8.1911$

Conclusion

The following conclusions are drawn from the present study:

1. Analytical models for solutions of linear free vibrations of circular and elliptical membranes are developed.
2. The solutions provide the natural frequencies and mode shapes for these clamped membranes. Excellent comparison, between the analytical and experimental results, concludes that the linear model is adequate for the required analysis.
3. Analysis has demonstrated that experimental results for natural frequencies can be used to determine the radial tension force within the membrane.
4. Pre-stress due to the tension in the membrane has a marked effect on the flexural vibrations of both types of membranes.

References

[1] Leissa, A. W., "Vibration of plates," *NASA SP-288,* 1969.

[2] Mazumdar, J., "A review of approximate methods for determining the vibrational modes of membranes," Shock and Vibration Digest, Vol. 14, pp. 11-17, 1982.

[3] McLachlan, N. W, "Vibrational problems in elliptical coordinates," Quart. Appl. Math., 1947

[4] McLachlan, N. W, "Theory and application of Mathieu functions," Dover publishing Company, 1954.

[5] Soedel, W., "Vibrations of shells and plates," 2nd Edition, Marcel Dekker, 1993.

2001

NASA/ASEE SUMMER FACULTY FELLOWSHIP PROGRAM

MARSHALL SPACE FLIGHT CENTER
THE UNIVERSITY OF ALABAMA IN HUNTSVILLE

Plasma Interaction with International Space Station High Voltage Solar Arrays

Prepared By:	John W. Heard
Academic Rank:	Assistant Professor
Institution and Department:	Clarion University of Pennsylvania Physics Department
NASA/MSFC Directorate:	Engineering
MSFC Colleague:	Todd Schneider

Introduction

The International Space Station (ISS) is presently being assembled in low-earth orbit (LEO) [5] operating high voltage solar arrays (-160 V max, -140 V typical with respect to the ambient atmosphere). At the station's present altitude, there exists substantial ambient plasma that can interact with the solar arrays. The biasing of an object to an electric potential immersed in plasma creates a plasma "sheath" or non-equilibrium plasma around the object to mask out the electric fields [2]. A positively biased object can collect electrons from the plasma sheath and the sheath will draw a current from the surrounding plasma. This parasitic current can enter the solar cells and effectively "short out" the potential across the cells, reducing the power that can be generated by the panels.

Predictions of collected current based on previous high voltage experiments (SAMPIE, PASP+) were on the order of amperes of current. However, present measurements of parasitic current are on the order of several milliamperes, and the current collection mainly occurs during an "eclipse exit" event, i.e., when the space station comes out of darkness. This collection also has a time scale, $\tau \sim$ 1000 s, that is much slower than any known plasma interaction time scales. The reason for the discrepancy between predictions and present electron collection is not understood and is under investigation by the PCU "Tiger" team. This paper will examine the potential structure within and around the solar arrays, and the possible causes and reasons for the electron collection of the array.

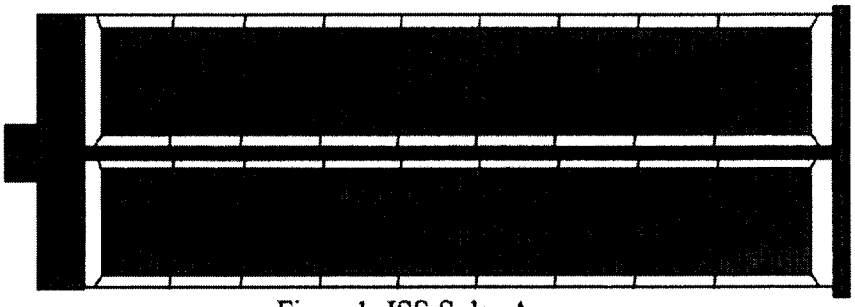

Figure1: ISS Solar Array.

Solar Array Description

Figure 1 shows a diagram of the ISS high voltage solar arrays. It consists of two blankets suspended on wire to a support structure mounted on a gambol to rotate the array so the solar radiation illuminates the array perpendicular to the array surface. Each blanket has 41 solar cell strings attached parallel to side power conduits. Each string consists of 400 solar cells arranged in series illustrated in Figure 2. Each gray solar cell in the diagram is an 8.0 cm by 8.0 cm square of 8 mil thick silicon (bulk resistivity $\rho = 4.13 \times 10^4$ Ω m, dielectric constant $\kappa = 11.7$). When illuminated, each solar cell has a work function potential of 0.40 volts with a resistance of ~1312 Ω. Therefore, each string will contribute 122 mA at 160 Volts, and each wing will contribute 1.6 kW of power.

The individual solar cells are attached to a flexible Kapton sheet ($\kappa = 3.9$) and protected by cerium-doped cover glass ($\kappa = 7.0$) that extends over the cell edges. The cross-section view of the solar cell placement is shown in Figure 3. There is a 39 mil gap (1 mil =

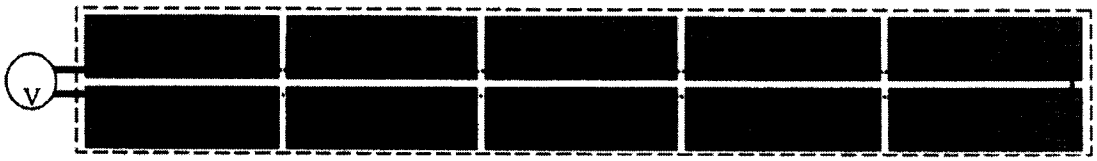

Figure 2: ISS Solar Cell String Arrangement.

2.54×10^{-5} m) separating the solar cells, and the attachment of the cells to the glass and Kapton uses different silicone adhesives (κ= 2.7 and 2.5, respectively). The gap and other side of this structure is immersed in plasma of electron density, n_e= 1×10^{12} electrons/m^3, and electron temperature, T_e= 0.1 eV.

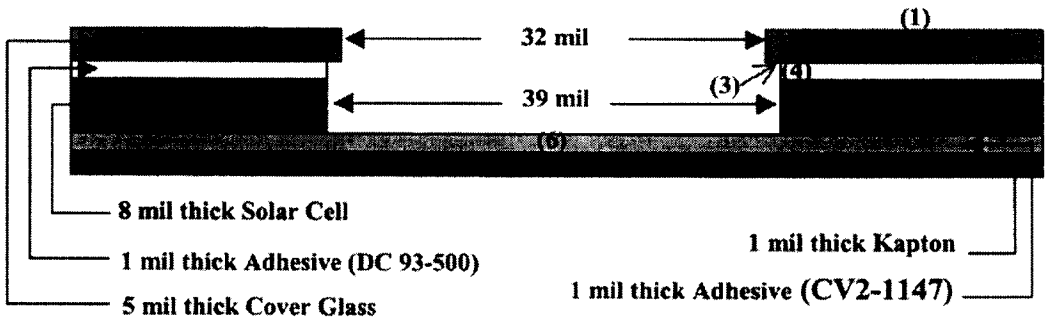

Figure 3: Solar Cell Cross-section Emphasizing gap geometry.

Potential Field Modeling

Mapping the electric potential structure in the gap and vicinity will allow calculations of collected electron current. It is extremely difficult to calculate Poisson's equation, $\nabla^2\phi = \rho/\varepsilon_0$, in the presence of dielectric materials. The dielectric surfaces will affect the field structure of the gap, and involves coupled partial differential equations. The surface boundary conditions at the plasma will try to charge to the plasma floating potential, ϕ_f, i.e., the potential at which an object would collect as many ions as electrons and have no net current to the surface. Fighting this effect is another named "snap-over," and this occurs due to secondary electron emission due to energetic electrons impacting a surface and liberating more electrons than entering the surface. If these electrons do not return to the surface, the surface will acquire a more positive charge. Also current conduction along the surface can also occur, so the plasma surface charging evolves in time as well as spatially varying.

Instead of solving the differential equations as continuous functions, the approximate, steady-state solution at discrete points can be found by using an initial solution guess at each point and "relaxing" these solutions until it approaches the true solution [1]. The relaxation method linearizes the partial derivatives in the equations to numerical approximations of adjacent solutions. Solving these linearized equations produces an iterative form,

$$\phi_{n+1}(x,y) = \frac{\phi_n(x+\Delta,y)+\phi_n(x-\Delta,y)+\phi_n(x,y+\Delta)+\phi_n(x,y-\Delta)-\rho_n(x,y)\Delta^2/\varepsilon_0}{4}, \quad (1)$$

which converges toward the exact solution asymptotically. The mesh grid step size for this model, Δ= 0.5 mil, is identical for both the vertical and horizontal directions.

The boundary conditions for a horizontal surface is a combination of the discontinuity of the perpendicular displacement field, $\hat{n} \bullet \left(\vec{D}_2 - \vec{D}_1\right) = \sigma_{\text{free}}$, and parallel electric field continuity, $\hat{n} \times \left(\vec{E}_2 - \vec{E}_1\right) = 0$ (assuming no surface currents) for linear isotropic homogeneous dielectrics, $\vec{D} = \kappa \varepsilon_0 \vec{E}$ [3]. Linearizing the equations and solving for the potential on the surface yields,

$$\phi_{n+1}(x,y) = \frac{\phi_n(x+\Delta,y) + \phi_n(x-\Delta,y) + \kappa(x,y+\Delta)\phi_n(x,y+\Delta) + \kappa(x,y-\Delta)\phi_n(x,y-\Delta) - \sigma_{\text{free}}(x,y)\Delta/\varepsilon_0}{2 + \kappa(x,y+\Delta) + \kappa(x,y-\Delta)}, \quad (2)$$

and there is a similar equation for vertical surfaces.

As shown on Figure 3, there are 7 surfaces in the grid exposed to the plasma: (1) the cover plate top, (2) the cover plate side, (3) the cover plate bottom, (4) the adhesive "creep," (5) The solar cell side, (6) the treated silicone on the gap bottom, and (7) the solar array bottom. For surfaces (1), (6), and (7), they have an almost clear path to plasma and should charge close to ϕ_f, so these surfaces were held at this potential. Surface (5) was held at cell potential, V_C= 140 V, to maximize the field for electron collection. Surfaces (2), (3), and (4) were allowed to relax to solution values, and all interior surfaces relax utilizing equation (2) with $\sigma_{\text{free}} = 0$.

One caveat of this method is that the linearization process does not converge with the nonlinear response of the plasma charge density. Therefore, the gap solution is calculated with $\rho = 0$. This is a first approximation and worse case to maximize the positive potential in the gap. Another caveat of the relaxation method is the solution convergence criterion. The iterative loop was performed until the difference in successive iterations produced a maximum change in the mesh of less that 0.01 V. This is a very small number, and required over one thousand iterations to converge, but with electron temperatures and space potentials on the order of 0.1 V, the seemingly small value is acceptable.

The modeling code was written in Mathematica 4.0 [6] using an augmented relaxation algorithm. The grid size was determined by the floating potential sheath calculation [2] to be 128 by 1300 in horizontal and vertical direction, respectively. The edge boundary conditions on the horizontal edge are set to the sheath potential, V_s= -T_e/2, and the vertical edge is set by reflexive condition, $\phi(x-\Delta, y) = \phi(x+\Delta, y)$, and this is placed into equations (1) and (2).

Modeling Results

Preliminary modeling results from Figure 4 show that the potential at the gap entrance is substantially lower than the cell voltage. The potential "saddle" at the gap entrance is between 10-20 V depending on V_C and the potential on surface (7). This shows the entire cell potential doesn't leak out of the gap and attract a large amount of current. The

ballooning of the potential as it expands out of the gap enhances the current collection by focussing electrons entering the sheath into the gap.

Further developments are planned to enhance the modeling approach with a linearized plasma "Poisson solver" kernel, time dependent evolution of the surface charge density, and numerical floating potential calculation due to the object moving through the plasma [4].

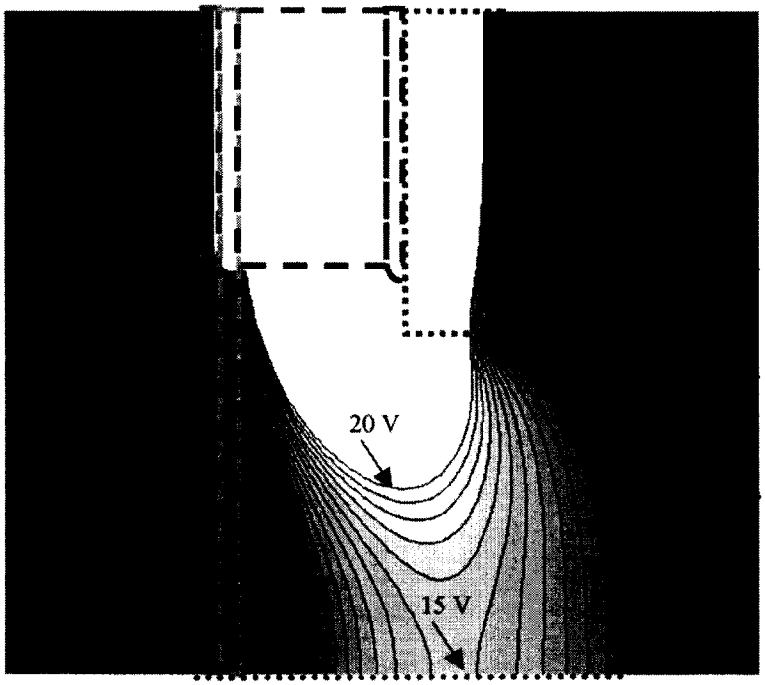

Figure 4: Gap Potential Relaxation Result.

Acknowledgments

The Author would like to thank Todd Schneider, Ralph Carruth, and other members of the Tiger team for allowing me to collaborate in the research and calculations.

References

[1] Chapra, S. C., Canale, R. P., Numerical Methods for Engineers, 2nd Ed., McGraw-Hill, New York, 1988.

[2] Hutchinson, I. H., *Principles of Plasma Diagnostics*, Cambridge University Press, New York, 1987.

[3] Jackson, J. D., Classical Electrodynamics, 2nd Ed., John Wiley, New York, 1975.

[4] Katz, I., *et al*, private communication.

[5] Vaughn, J. A., *et al.* "Electrical Breakdown Currents on Large Spacecraft in Low Earth Orbit," Journal of Spacecraft and Rockets, Vol.31, No. 1, pp. 54-59, 1994.

[6] Wolfram, S., *Mathematica*, 4th Ed., Cambridge University Press, New York, 1999.

2001

NASA/ASEE SUMMER FACULTY FELLOWSHIP PROGRAM

MARSHALL SPACE FLIGHT CENTER
THE UNIVERSITY OF ALABAMA IN HUNTSVILLE

"Processes and Procedures of the Higher Education Programs at Marshall Space Flight Center"

Prepared By:	Pamala D. Heard
Academic Rank:	Assistant Professor
Institution and Department:	Langston University Department of Mathematics
NASA/MSFC Directorate:	Customer & Employee Relations
MSFC Colleague:	Dr. Shelia Nash-Stevenson

Introduction

The purpose of my research was to investigate the policies, processes, procedures and timelines for the higher education programs at Marshall Space Flight Center. The three higher education programs that comprised this research included: the Graduate Student Researchers Program (GSRP), the National Research Council/Resident Research Associateships Program (NRC/RRA) and the Summer Faculty Fellowship Program (SFFP). The GSRP award fellowships each year to promising U.S. graduate students whose research interest coincides with NASA's mission. Fellowships are awarded for one year and are renewable for up to three years to competitively selected students. Each year, the award provides students the opportunity to spend a period in residence at a NASA center using that installation's unique facilities. This program is renewable for three years, students must reapply. The National Research Council conducts the Resident Research Associateships Program (NRC/RRA), a national competition to identify outstanding recent postdoctoral scientists and engineers and experience senior scientists and engineers, for tenure as guest researchers at NASA centers. The Resident Research Associateship Program provides an opportunity for recipients of doctoral degrees to concentrate their research in association with NASA personnel, often as a culmination to formal career preparation. The program also affords established scientists and engineers an opportunity for research without any interruptions and distracting assignments generated from permanent career positions. All opportunities for research at NASA Centers are open to citizens of the U.S. and to legal permanent residents. The Summer Faculty Fellowship Program (SFFP) is conducted each summer. NASA awards research fellowships to university faculty through the NASA/American Society for Engineering Education. The program is designed to promote an exchange of ideas between university faculties, NASA scientists and engineers. Selected participants in fields of science, engineering, math, and other disciplines spend approximately 10 weeks working with their professional peers on research projects at NASA facilities. Workshops and seminars further enrich the experience. This program is only for U.S. citizens.

The Education Programs Department is part of a policy that involves the educational community and support endeavors designed to inspire students, create learning opportunities, and enlighten inquisitive minds. These efforts are directed toward ensuring the continued availability of scientists/engineers and the preservation of our leadership in aerospace science and technology. The Education Program Department consist of five teams-the Education Alliances, Higher Education, Pre-College, Educational Technology and the Office of Manager teams. The Educational Alliances team is responsible for using NASA's unique assets to support all types of learning by collaborating with non-profit educational organizations and business partners. The Educational Technology team is responsible for design, development, implementation and evaluation of products and services that employ technology to enhance the educational process for formal and informal education and lifelong learning. The Precollege Education team is responsible for supporting K-12 teachers and engaging students through the use of NASA's inspiring missions, unique facilities, and specialized workforce. The Higher Education team is responsible for involving the higher education community in NASA research and technology activities. Its mission, from a programs perspective, is to support America's faculty and to inspire domestic students through experiences, internships and exposure to NASA's mission in science, mathematics, engineering, and technology. This is accomplished by serving as a learning laboratory for experiments with new approaches and practices in the design and delivery

of both formal and informal learning initiatives. The Higher Education program wants to create learning opportunities, enlighten, inspire inquisitive minds and enhance the communication capabilities of the educational community.

This research project is a road map to help review, evaluate current programs, leverage resources, provide unique incentives and evaluate for quality, impact and effectiveness. Efforts must be exhausted to update and discontinue old processes and focus current services to meeting the stakeholder's needs. Do we value our customers? If so, we must embrace meaningful change, learn from successes and mistakes. Challenging and competitive goals must be set. We need to properly plan, fund and staff the program and communicate our intentions clear and concise. A streamline process and procedure must also be developed to function at a higher level for the higher education program with synergy from other programs. This research is designed to focus on the deadline, the process needed to work with our customers (participants, universities, mentors and our directorates/offices). Each program must be individually examined and a determination made in relationship to how we can improve service to customers in a timely manner. Inquiries, from inside and outside customers, must be addressed and efforts exhausted to meet projected deadlines and goals.

Research Approach

The research approach selected for this project required an investigation into existing policies, processes, procedures and timelines. Programs and related benefits were thoroughly examined to determine quality of operation. Next, problems that may hinder and/or hamper growth were explored. These restraints dictated a strategy that would lead to successful programming.

Microsoft Project was used to examine tasks related to existing programs and those been considered for implementation. My research indicated that personnel awareness is vital for successful program operation, transition and the timeline required to meet and/or exceed customer's needs. If Higher Education is to become a more effective communicator of benefactor needs its staff must monitor tasks, examine policies and interact with targeted organizations and groups. Higher Education could also better communicate needs of mentors, departments and directorates by not breaking the connection of communication. This is accomplished by constant interaction with program coordinators. This effort will increase the possibility of higher-order program function and increase the likelihood of success. Sure, the programs are functioning but improvement is needed if continued progress and productivity is to be realized.

Results and Discussion

The three Higher Education Programs, GSRP, NRC/RRA and SFFP that comprised my research have been in operation for a plethora of years at the Marshall Space Flight Center. Processes have been altered and/or changed but the basic fiber remains intact. A one-year examination of program operation/s and associated tasks revealed the following: GSRP possesses more than 600 tasks, NRC-more than 600 tasks and SFFP-more than 70 tasks. These tasks serve as the major connection responsible for effective program operation. Some key milestones for these programs are the GSRP- the application process, closeouts, EDCATS and the GSRP Research Booklet. For the NRC/RRA, its milestones are funding process, new NRC, the NRC research booklet and

the October, February and June reviews. The SFFP milestones are funding, final report, application process, Education Point-of Contact for each Directorate and Tasks Descriptions. These milestones are key to the success of the program. These milestones, if objectives are met, will produce successful program performance.

My research dictated the need for an Education Point-Of-Contact for each Directorate. Within the Higher Education spectrum, this key ingredient is needed to better communicate with our internal customers. If we have an Education Point-Of-Contact from each directorate, then we can communicate our needs, policies, processes and timelines so both can meet the common and agreed upon goals of the programs. For example, if we have the same point-contact for each directorate for each higher education program, they can better understand the Education Programs Department functions and better communicate needs and expectations outlined by mentors/advisors. First, the University Affairs Officer needs to meet with each directorate/office to secure an Education Point-of-Contact to represent the directorate/office on behalf of the entire Education Program Department. This is key so we can continue the communication link that is needed in a plethora of areas. Each partner involved in an endeavor would be allowed to represent his/her area of expertise and share vital information necessary for successful completion of a project. We will also have the opportunity to partner more with other programs and explore additional areas of interest within education. A two-way linkage of communication is desperately needed! Monthly meetings with advisors/mentors are necessary for the purpose of recruitment and briefing efforts related to revised programs. This communication linkage fosters an environment that is responsive to timelines and the understanding of successful program operation, a possible reality that could also reduce the amount of paperwork generated by projects. After the directorates/offices have selected the Education Point-of-Contact, timelines, processes and program procedures, information can be relayed from management to the labs, and advisors/mentors.

Another Element of all higher education processes is EDCATS – the evaluation tools for all education programs. Sure, participant completion of necessary paperwork is vital but effort must also be exhausted to analyze data necessary to improve and promote customer feedback. Probably, no the most important issue for the existence of the entire program is *funding*. After the funding is secured, it must be appropriated in a timely manner. This is essential if program function and goal achievement is a priority. The next key issue revolves around task/research descriptions for higher education programs. Each program has a requirement that dictates task/research descriptions that participants are required to implement. This process promotes a year round link of communication and discussion of tasks. I staunchly recommend the development of a database that host tasks/research descriptions for all programs. The database would also serve as the collection-point for all necessary additions/changes to the research task and program descriptions. This strategic information collection method would also serve as a reference tool for the publication of manuals, booklets and websites. In addition, Higher Education would set a timeline for updates and additions to be complete each year, for higher education programs. It would also be essential that all programs have the same deadlines for entry into the research tasks description.

Another recommendation that would better serve focused efforts would be the selection of coordinators for each higher education program currently in operation at Marshall Space Flight Center. This personnel implementation would increase the program operation and performance. The delegation of tasks would also increase the ability to monitor the need for program shifts and or modifications. Whenever personnel are strained, the customers experience a lack of continuity in our efforts to deliver a message/s; this creates problems that are internally induced but preventable.

Another recommendation would result in an adopted team approach to recruiting during program promotion efforts. Whenever one Education Department program is promoted, all programs should be promoted, especially higher education! This method of outreach offers and exposes the customer to a variety of related programs. Whenever organizations recruit, a conscious effort must be made by higher education to promote its programs because it has limited funds budgeted for travel. We must network with Human Resources, Minority University and Co-op Programs when they recruit. We must ask for their support through the distribution of higher education brochures and announcements. Cross training is also needed among members of the higher education team; each individual must know what their co-workers program/s entails. This effort will result in a more productive and viable communication with customers. They will also sense and appreciate the balance of understanding among team members.

Again, communication links among team members, department, and directorates/office must continue to improve. The programs must be promoted and advertised in a manner that sends a message of clarity to our customers. We must never waver in our efforts to meet timelines and understand processes that promote a productive level of effectiveness. Yes, I am confident that if we understand, communicate and implement our tasks, all program processes and procedures will adhere to established deadlines. Finally, if the concept of team is enforced each coordinator/manager will develop processes for successful and productive implementation.

Acknowledgment

I would like to thank Shelia Nash-Stevenson, Jim Pruitt, and the Higher Education Team for their support in my endeavors.

2001

NASA/ASEE SUMMER FACULTY FELLOWSHIP PROGRAM

MARSHALL SPACE FLIGHT CENTER
THE UNIVERSITY OF ALABAMA IN HUNTSVILLE

IMPLEMENTING A WORKFORCE DEVLOPMENT PIPELINE

Prepared By:	Billy Hix
Academic Rank:	Professor
Institution and Department:	Motlow College Business Information Systems
NASA/MSFC Directorate:	CD
MSFC Colleague:	Jim Pruitt

A Proposal for Developing a Workforce Development Pipeline within MSFC

Through science, technology, mathematics, and engineering, our nation continues to lead the world in the development and utilization of new technologies. Whether related to our health, to the environment, or to our production of material goods, science, mathematics, engineering, and technology are integral and essential parts of daily life for virtually everyone in the United States and around the globe. However, the understanding of science, mathematics, engineering, and technology by most Americans is inadequate for full participation in this increasingly technological world. This reflects the level of education in these areas most Americans have received. To have a competent workforce for the future, we must assist education in developing students for future jobs.

Marshall Space Flight Center is in a unique position to provide pro-active support in the area of workforce development. The world's latest technological revolution, of which we have only seen the beginning, is different than any of the past. Prior technological revolutions had a characteristic gradual onset. Our most recent transformation of comparable magnitude was the Industrial Revolution. In that transformational era, the education of the workforce had time to adjust to the new demands of an industrial society. The current revolution outpaces our capacity to implement change and our educational institutions struggle to prepare for this reformation.

Research shows that the number of highly trained scientist and engineers has continued a steady decline during the 1990's. Furthermore, at the high school level, almost 40% of the total high school graduates are seeking technical skills in preparation of entering the workforce directly. The decrease of students in technology and science programs, along with the lack of viable vocational programs, haunts educators and businesses alike. However, MSFC has the opportunity to become a leading edge model of workforce development by offering a unified program of apprenticeships, workshops, and educational initiatives. These programs will be designed to encourage young people of all backgrounds to pursue the fields of technology and science, to assist research opportunities, and to support teachers in the systemic changes that they are facing. The emphasis of our program based on grade levels will be:

Elementary Level ---------- Exposure to the workforce
Middle School ----------Examine the workforce
High School and beyond ---------- Instruct the workforce

It is proposed that MSFC create a well-integrated Workforce Development Pipeline Program. The program will act to integrate the many and varied programs offered across MSFC directorates and offices. It will offer a clear path of programs for students throughout middle school, high school, technical training, and college and universities. The end result would consist of technicians, bachelors degrees, masters degrees, and PhDs in science and engineering fields entering the nation's workforce, with a focus on NASA's future personnel needs.

Never before in our nation's history have our youth been in such great need of vision for the future. Our country is in need of being able to produce a well-trained workforce. NASA is capable of assisting in both areas. Our workforce development program will work with students and educators to support our nation's future employees. Educator and author T. O. Davenport, in his book, Human Capital, points out that it is "of extreme importance to get the students out of the classroom and into the field to deal with problems. They will make mistakes, but they will learn faster and better than they would in the classroom." Davenport's words strike a familiar note from the apprenticeship days. By working alongside a professional, the apprentice learned the skills by attaching meaning to observation, emulating the work, and applying any lessons presented formally or informally. This is one of the best ways to deliver the tacit knowledge that NASA and other employers seek.

Goals of the MSFC Workforce Development Program

- To increase the exposure for young people in the areas of science and engineering, starting at the middle school level with educational/workforce preparation programs.
- To prepare students for initial and continued employment in technology related careers and to assist students in making educational and career decisions
- To assist students in developing decision-making, communication, problem-solving, leadership, and citizenship skills
- To ensure that NASA has access to a highly skilled and creative workforce for the 21st century
- To strengthen NASA's commitment to educational excellence and university research
- To assist colleges and universities in the critical need to increase the nation's undergraduate and graduate science, engineering, mathematics, and technology graduates, especially among under represented groups.
- To provide developmental programs for educators and to help bridge the gap between working engineers and scientist and educators in the MSFC region.

Workforce development Vision and Design

NASA has a long tradition of supporting education. In a recent article in *Ad Astra*, a publication for the National Space Society, Dr. George O'Neal stated that of all of the programs at NASA, the education programs stand out as examples of excellence. However, the education, workforce preparation, and economic development structures that have served in the past are in need of change. A system that develops students to the

highest possible levels of knowledge and skill necessary to excel in the workplace must be implemented. This should be the vision of this program.

The development of the workforce development pipeline will be addressed in two areas. First will be the short-term proposals addressing what can be done at this current time to strengthen the impact of students entering the science and technology fields. In addition, long-term programs must address the longer process of preparing students from an early age to the period that they make successful employees.

Curriculum will also follow guidelines developed by federal and state government. Existing courses that are used within the workforce development pipeline program should include the following workforce development strategies.

- Hands-on approaches
- Cooperative learning
- Inquiry method of learning
- Integration of academic skills
- Development of communication and presentation skills

Commonalities among all course offerings within the workforce development program should include:

- Development of critical and creative thinking
- Improvement of communication skills
- Enhancement of problem solving skills
- Development of better leadership/citizenship skills
- Provision of information regarding career information and planning
- Provision of examples representing the impact of technology on the student's future

Each activity experienced by the student should act as a building block to assist him in the selection of other programs offered as well as the development of an individual career development plan.

Proof of Need

In 1998 there were 1,184,406 students receiving a B.S. degree in the United States. Five percent of that figure majored in engineering. Less than one percent of the total majored in Aerospace engineering. The numbers will have an impact on the future pool of employees for NASA.

In the entire state of Alabama, during the school term of 1999, there were 661 electrical, civil, and mechanical engineer graduates. During the month of May 2001, there were over 250 job openings for electrical, civil and mechanical engineers by companies listed on Monster.com for the Huntsville area.

The University of Tennessee governing board is considering closing their Space Institute in Tullahoma, Tennessee due to the impact of low enrolment. In 1980, there were over 1100 students in undergraduate and graduate studies at the school. Today, there are less than 200 students enrolled in regular school programs.

Findings from the Third International Mathematics and Science Study (TIMSS)(1994-1996) showed that students from the United States excel in their early educational experience in science. U.S. fourth graders scored second in the 26 countries being assessed with only Korea scoring higher. However, by the twelfth grade, U.S. students could only outperform students from 2 countries. Scores from the math section of the assessment are almost identical.

These facts can support the assertion that efforts by the education community in the past 10-20 years in the area of science and engineering have not yielded a positive outcome. There is additional proof that the method that we use to educate our young people in the area of engineering and technology is not working.

In the book, How People Learn, by John Bransford and Ann Brown, the authors state that students must be engaged at an early age in knowledge centered or hands-on centered learning. Any efforts beyond middle school years will have a lesser effect in producing long-term impact on student outcomes in regard to careers.

In the following reports: From Analysis to Action: Undergraduate Education in Science, Mathematics, Engineering, and Technology (1996a) and Shaping the Future: New Expectations for Education in Science, Mathematics, Engineering, and Technology (1998) from the National Science Foundation Advisory Committee, point to the need for change. The authors highlight the need for restructuring the current program of courses and programs. They propose that immediate attention must be given to the areas of science/technology education. They feel the current method of education in the area of science and engineering is failing to provide the needed workforce for the 21st century.

The Boyer Commission's report entitled Reinventing Undergraduate Education: A Blueprint for America's Research Universities (1998) states that education should provide diverse opportunities for all students to study science, mathematics, engineering, and technology as practiced by scientists and engineers as early in their academic careers as possible.

During the period of 1992-1998, there has been a general decline in graduate students enrolled in the areas of science and engineering. There is a severe decline in the area of mathematics, mechanical, aerospace, and petroleum engineering. The low enrolments in these areas will take considerable effort to reverse.

Percent of change in the number of graduate students in Science and Engineering
(Table 1)

Field	1992	1993	1994	1995	1996	1997	1998	% Change 1992-98
Overall Total	430,635	435,869	431,233	422,533	415,258	407,656	404,903	-5.98%
Sciences, Total	312,632	319,035	318,240	315,360	312,069	306,586	304,934	-2.46%
Physical	35,348	35,318	34,449	33,388	32,324	31,078	30,571	-13.51%
Earth	15,333	15,731	15,968	15,722	15,185	14,565	14,259	-7.00%
Computer	36,325	36,213	34,158	33,458	34,626	35,991	38,027	4.69%
Mathematical	20,355	20,000	19,579	18,509	18,015	16,729	16,488	-19.00%
Agricultural	11,841	11,988	12,273	12,450	12,009	11,893	11,877	0.30%
Biological	54,180	56,458	58,152	58,775	58,170	57,140	57,124	5.43%
Psychology	53,484	54,557	54,554	53,641	53,122	53,126	52,577	-1.70%
Social	85,766	88,770	89,107	89,417	88,618	86,064	84,031	-2.02%
Engineering, Total	118,003	116,834	112,993	107,173	103,189	101,070	99,969	-15.28%
Chemical	7,397	7,516	7,608	7,424	7,373	7,247	7,060	-4.56%
Civil	19,572	19,583	19,925	19,218	18,528	17,156	16,481	-15.79%
Electrical	36,428	35,290	33,020	30,721	29,702	30,548	31,129	-14.55%
Industrial/manufacturing	13,525	13,596	13,661	13,143	12,399	11,736	10,995	-18.71%
Mechanical	18,637	18,477	17,761	16,363	15,509	15,045	14,696	-21.15%
Metallurgical	5,512	5,363	5,191	4,920	4,713	4,649	4,644	-15.75%
Aerospace	4,036	3,940	3,715	3,343	3,208	3,083	3,137	-22.27%
Biomedical	2,537	2,675	2,750	2,732	2,732	2,847	2,905	14.51%
Petroleum	737	725	624	610	562	561	571	-22.52%
Other	10,359	10,394	9,362	9,309	9,025	8,759	8,922	-13.87%

Source: Directorate for Social, Behavioral, and Economic Sciences, National Science Foundation 1/11/01

During the past decade, enrollment of minorities has shown an overall increase. Much of this credit can be giving to the actions taken as recommended by The Task Force on Women, Minorities, and the Handicapped in Science and Technology in 1989. This report, commissioned by the U.S. Congress, shows that change can take place within the educational community.

Graduate enrollment in science and engineering, by citizenship and race/ethnicity: (Table 2)

Citizenship and Race/Ethnic	1992	1993	1994	1995	1996	1997	1998	% Change 1992-98
Total	430,635	435,869	431,233	422,533	415,258	407,656	404,903	-5.34%
U.S. citizens	321,171	330,148	329,073	323,993	317,101	308,665	302,875	-3.89%
Black	15,445	17,116	17,610	18,282	19,068	19,346	19,654	25.26%
American Indian/Alaskan Native	1,243	1,309	1,382	1,516	1,538	1,600	1,607	28.72%
Asian/Pacific Islander	21,751	24,059	26,475	25,904	25,928	26,007	26,709	19.57%
Hispanic	12,246	13,381	13,277	14,111	14,568	14,980	15,476	22.33%
White, non-Hispanic	253,425	256,840	255,701	245,893	238,062	228,018	220,689	-10.03%
Other or Unknown	17,061	17,443	14,628	18,287	17,937	18,714	18,740	9.69%
Non-U.S. citizens	109,464	105,721	102,160	98,540	98,157	98,991	102,028	-9.57%

Source: Directorate for Social, Behavioral, and Economic Sciences, National Science Foundation 1/11/01

By reviewing the following data representing Bachelor's degrees conferred by degree-granting institutions by discipline, one can see the trends in the area of science and technology.

(Table 3) **Number of Bachelor's degrees given by major**

Discipline division	1970-71	1980-81	1990-91	1995-96	1997-98	% of Change
Total	839,730	935,140	1,094,538	1,164,792	1,184,406	41.05%
Agriculture	12,672	21,886	13,124	21,431	23,284	83.74%
Architecture	5,570	9,455	9,781	8,352	7,652	37.38%
Area, ethnic studies	2,582	2,887	4,884	5,786	6,153	138.30%
Biological sciences	35,743	43,216	39,530	60,994	65,868	84.28%
Business	14,729	198,983	249,311	227,102	233,119	103.19%
Communications	10,324	29,428	51,650	47,320	49,385	378.35%
Communications tech	478	1,854	1,123	683	729	52.51%
Computer sciences	2,388	15,121	25,083	24,098	26,852	1024.46%
Education	176,307	108,074	110,807	105,509	105,968	-39.90%
Engineering	44,898	63,287	61,531	62,114	59,910	33.44%
Engineering-related technologies	5,148	11,713	17,119	15,323	14,000	171.95%
English language	64,342	32,254	51,841	50,698	49,708	-22.74%
Foreign languages	20,536	11,273	13,133	13,952	14,451	-29.63%
Health professions	25,226	63,649	59,070	84,036	84,379	234.49%
Home economics	11,167	18,370	14,892	15,803	17,296	54.88%
Law and legal studies	545	776	1,758	2,052	2,017	270.09%
Liberal arts and sciences,	7,481	21,643	30,526	33,997	33,202	343.82%
Library science	1,013	375	90	58	73	-92.79%
Mathematics	24,937	11,433	15,310	13,143	12,328	-50.56%
Interdisciplinary studies	6,286	12,848	17,561	26,515	26,163	316.21%
Parks and recreation	1,621	5,729	4,315	13,983	16,781	935.23%
Philosophy and religion	8,146	6,776	7,315	7,388	8,207	0.75%
Physical sciences	21,412	23,952	16,344	19,647	19,416	-9.32%
Psychology	38,187	41,068	58,655	73,291	73,972	93.71%
Public administration	5,466	16,707	14,350	19,849	20,408	273.36%
R.O.T.C. and military	357	42	183	7	3	-99.16%
Social sciences	155,324	100,513	125,107	126,479	125,040	-19.50%
Theological studies	3,744	5,841	4,813	5,358	5,903	57.67%
Visual and performing arts	30,394	40,479	42,186	49,296	52,077	71.34%
Not classified by field of study	0	0	13,258	1,756	1,373	

Source: U.S. Department of Education, National Center for Education Statistics, Higher Education General Information Survey (HEGIS), "Degrees and Other Formal Awards Conferred" surveys, and Integrated Postsecondary Education Data System (IPEDS)

Much of this mandate for change must be focused on students long before they arrive at college. Students at the high school level must be aware of the impact of decisions early in their education regarding career choices. An effort to reach students early will result in more students viewing science and technology careers as exciting and enjoyable. To often, students are being taught by teachers who have little or no background in these areas, causing the students to choose other paths. In addition, students have very few opportunities to view professionals in their work environment.

During the years 1994-96, the National Center for Education Statistics (NCES) expanded its role in collecting international data by serving as the national research center for the International Association for the Evaluation of Educational Achievement Reading Literacy Study. NCES has provided funding for international research studies comparing mathematics and science education. One of those studies was the Third International Mathematics and Science Study (TIMSS). TIMSS was the largest, most comprehensive comparative study of education that has ever been undertaken, testing a half million students. The study was designed to focus on students at different stages in school: midway through elementary school (3rd or 4th grade in most countries), midway through lower secondary school (7th or 8th grade in most countries), and at the end of upper secondary school. Their findings were released in 1998. This study was a call to arms for many groups and is used as one of the major data points in the effort to develop better school to work programs and to evaluate the manner in which science and math are integrated into the school curriculum.

In the 1994-96 TIMSS assessment in mathematics, U.S. 4th-graders scored above the international average of the 26 countries that participated. Fourth-graders performed below students in 7 countries, not significantly different from students in 6 countries, and above students in 12 countries. U.S. 4th-graders scored below Japan, not significantly different from Canada, and above England. U.S. 8th-graders scored below the international average of the 41 countries that were tested. In mathematics, U.S. 8th-graders scored below their counterparts in 20 countries, including top performer Singapore, but not significantly different from England and Germany. U.S. 12th-graders performed below the international average, and among the lowest of the 21 TIMSS countries on the assessment of mathematics general knowledge. U.S. students were outperformed by those in 14 countries, outperformed students in 2 countries, and were not significantly different from those in 4 countries.

U.S. 4th-graders performed above the international average of the 26 countries assessing fourth grade students in science. Only Korea scored above the U.S., with U.S. 4th-graders outperforming 19 other countries, including England and Canada. The remaining countries' scores, including Japan's, were not significantly different from those of U.S.

fourth grade students. U.S. 8th-graders compared more favorably with other countries in science than in mathematics, scoring above the international average of 41 countries. U.S. 8th grade students scored below their peers in nine countries, not significantly different from 16 countries, including Canada, England, and Germany, and outperformed students in 15 nations. U.S. 12th-graders performed below the international average and among the lowest scoring of the 21 TIMSS countries on the assessment of general science knowledge. U.S. students were outperformed by students in 11 countries, outperformed students in 2 countries, and did not score significantly different from students in 7 countries.

Table 5

Average **fourth grade** science scores by content areas

Country	Overall science scores	Earth science	Life science	Physical science	Ranking
Korea	74	72	76	75	1
United States	66	64	71	60	2
Australia	66	61	72	63	3
Japan	70	66	73	70	4
Netherlands	67	61	73	65	5
Canada	64	62	68	61	6
Czech Republic	65	64	71	62	7
England	63	61	68	60	8
Ireland	61	60	66	57	9
Austria	66	62	72	64	10
New Zealand	60	57	66	57	11
Slovenia	64	64	68	61	12
Norway	60	60	67	55	13
Scotland	60	58	65	57	14
Singapore	64	58	70	64	15
Israel	57	51	61	55	16
Hong Kong	62	61	68	60	17
Hungary	62	62	66	59	18
Thailand	49	48	52	46	19
Iceland	55	55	60	52	20
Latvia	56	57	60	54	21
Greece	54	52	61	49	22
Cyprus	51	48	55	50	23
Portugal	50	50	54	49	24
Iran, Islamic Republic	40	38	44	40	25
Kuwait	39	36	45	37	26

Source: Third International Mathematics and Science Study (TIMSS)

(Table 6)

Average **eighth grade** science scores by content areas						
	Average percent correct by content area					
Country	Overall science scores	Earth science	Life science	Physics	Chemistry	Ranking
1	2	3	4	5	6	
International average	56	55	59	55	51	
Singapore	70	65	72	69	69	1
Japan	65	61	71	67	61	2
Korea	66	63	70	65	63	3
Czech Republic	64	63	69	64	60	4
Netherlands	62	61	67	63	52	5
Austria	61	62	65	62	58	6
England	61	59	64	62	55	7
Belgium	60	62	64	61	51	8
Slovak Republic	59	60	60	61	57	9
Slovenia	62	64	65	61	56	10
Australia	60	57	63	60	54	11
Bulgaria	62	58	64	60	65	12
Hungary	61	60	65	60	60	13
Canada	59	58	62	59	52	14
Hong Kong	58	54	61	58	55	15
New Zealand	58	56	60	58	53	16
Switzerland	56	58	59	58	50	17
Germany	58	57	63	57	54	18
Israel	57	55	61	57	53	19
Norway	58	61	61	57	49	20
Russian Federation	58	58	62	57	57	21
Scotland	55	52	57	57	51	22
Sweden	59	62	63	57	56	23
Ireland	58	61	60	56	54	24
United States	58	58	63	56	53	25
Spain	56	57	58	55	51	26
France	54	55	56	54	47	27
Thailand	57	56	66	54	43	28
Denmark	51	49	56	53	41	29
Greece	52	49	54	53	51	30
Iceland	52	50	58	53	42	31
Latvia	50	48	53	51	48	32
Lithuania	49	46	52	51	48	33
Romania	50	49	55	49	46	34

Iran, Islamic Republic	47	45	49	48	52	35
Portugal	50	50	53	48	50	36
Cyprus	47	46	49	46	45	37
Kuwait	43	43	45	43	40	38
Colombia	39	37	44	37	32	39
South Africa	27	26	27	27	26	40

Source: Third International Mathematics and Science Study (TIMSS)

(Table 7)

Average science scores, at the end of secondary school	
	Average score in science
	Science
Country	Overall
Sweden	559
Netherlands	558
Japan	556
Singapore	554
Iceland	549
Norway	544
Canada	532
New Zealand	529
Australia	527
Switzerland	523
Austria	520
Slovenia	517
Denmark	509
Germany	497
Czech Republic	487
France	487
Russian Federation	481
Italy	480
Hungary	475
Lithuania	471
United States	470
Cyprus	448
South Africa	349

Source: Third International Mathematics and Science Study (TIMSS)

Challenges to be addressed by the Workforce Development Pipeline Program

Placing students in the pipeline
Students and parents alike must be informed of the pipeline program and must be able to understand it purpose. This will be done via a web site with information regarding all of the programs and how they interact with each other.

Expand workforce opportunities by partnering with outside organizations
It is impossible for MSFC/NASA to stand alone in this endeavor. Part of the administrative directive of this program will be to partner with other organizations that have the same concerns of developing tomorrow's workforce.

Using technology to foster communication between programs
It is important that information from one program is available to other programs. Based on research and interviews with management and staff at MSFC, it is apparent that there is very little information passed from one program to another. This information could be used to better recruit and inform students from one program to the next.

Bridging the gap between education and the workforce
Teachers have a lot to learn from scientists and engineers; and scientists and engineers, if they are to be really helpful, have a lot to learn from teachers. But teachers, scientists and engineers come from two divergent cultures. This divergence can inhibit the initiation of contacts between teachers and professionals. Teachers often have poor communications media available to them and are often intimidated by scientists/engineers, so that teacher-initiated contacts are rare. And scientists/engineers, who live in a different world in which education is a minor concern, are unlikely to have initiating ideas or other motivations to support the work of teachers. This situation also inhibits on-going communication, both psychologically and technologically, and that can undermine long-term relationships.

Evaluation of programs
Within many education programs offered by NASA, the number of people involved is of major emphasis and is used for the primary basis for evaluating the effectiveness of a program. However, for programs within the Workforce development pipeline, the goal for effective outcomes will be aimed at producing a deep impact on a smaller number of students. New methods, based on student knowledge outcomes should be devised to document the value and impact of the program. To scientists/engineers, the measures of success of a project are usually the discoveries, publications, grants and prizes that arise from the work. To educators, the objective measures of success are far less clear, so program assessments need to be undertaken by an outside assessment team with knowledge of evaluating educational programs.

Training of scientists/engineers
Scientists/engineers know a great deal about their subject matter, but often little about education and the education culture in general. All participants need meaningful and

useful training before participating within a program. How much training will depend on the project in which they will be involved.

Training of Teachers
Making an effort to reach students without reaching teachers is only marginally effective. Programs must involve teachers in developing excitement for the sciences and technologies.

Implementation

This paper will present a formalized method of how educators and students can matriculate and be supported within the MSFC workforce development pipeline to provide better educational opportunities and employee base for the future. A special emphasis must be placed on how this program would be advertised as a whole, appearing as a seamless entity to the public. This pipeline should not be directorate or department centric, even though components may lie within various directorates/departments. Initial implementation would utilize existing programs and be integrated into a larger program to contain a complete set of workforce development program elements. The study will also consider partnering with existing organizations that are active in the development of workforce programs.

Implementation Step 1

A road map for the MSFC workforce development pipeline:

Review of Current Programs

There should be a review of current MSFC programs that would determine which will be included in the workforce development pipeline program. Guidelines that each program should follow are:

- Programs should be work-site based, or hands-on in school based.
- Programs should be based upon the apprentice method of training and education.
- Each program should involve the integration of science, math, and technology.
- Programs should help develop teamwork skills.
- Each program should help students develop problem-solving skills in a hands-on environment.
- Students should be allowed to develop creative ways of solving problems.
- Programs should develop presentation and communication skills.

Point of Contact

MSFC will need to develop a POC position for the workforce development pipeline program. This person will supervise the development of the needed web presence. In addition, this position will work to design the data tools to create a system to allow data from different programs to be shared. As the program grows, partnering with other agencies will become increasingly important.

The POC will take the current offering at MSFC and develop a sequence of workforce development programs that will integrate unique NASA experiences into these programs. To be able to supply students and parents alike with the needed data, an information system will be put into place. Individuals should be able to quickly understand what programs are available to them and how programs flow into each other

Web Presence

To the public, NASA/MSFC should present a uniform and concise view of all of the programs that are involved in the workforce development. Currently, all of the programs that fall under this "virtual umbrella" are listed on several websites at Marshall. There must be a web site representing the workforce development pipeline that will provide comprehensive and easily understood information and be presented in such a manner that it is easy to make informed choices among programs.

Web Content

Web Content, Level 1:
To make the offering of the workforce development pipeline easier to understand, consider the difficulties encountered each fall by colleges. Students enter school and with little hands-on direction are able to navigate the series of classes offered by the college to obtain a degree. Much of this content is delivered in the format of a college catalog. A web site should be created that would follow the same concept. It will ask an individual for their grade level and then bring up the page that would have appropriate programs data. Each program should be hyperlinked to learn more information. Within the content of each program, it should list the skill set that will be taught. Also, each program should reference other programs that are similar nature but in the next higher educational level. A check box should be provided to have information about any program be emailed to the student. Each page regarding a program should be clear about for whom the program is intended and the skills and educational goals that will be met by participating in this program. The web page should also ask if the person would like to be emailed information about other programs that would match that particular grade level.

Web Content, Level 2:

After the development of the initial web page, the following additions should be considered. One would be a workforce job profile for selected jobs at MSFC. A new job would be highlighted each month talking about the skills and education requirements for this position. Another section could be the "ask an employee" section. This could be treated like an off-line chat. Within this section, information could be given about who is going to be the target of the questions and questions could be collected, selected, and then answered at a designated date. This would be done approximately bi-monthly. One of the reasons to go to such trouble is to encourage members of the educational community to visiting the workforce development page often. The workforce development pipeline should be able to impact our educational community throughout the year by keeping young people exposed to workforce possibilities.

In addition, there should be a check for students who have already participated within one of the pipeline programs. The web page should then query in which program they have already participated and suggest another program based on educational level.

Within the content of each program description, there should be links to other programs within the same educational level and programs that are related at the next educational level. No matter which page is being viewed on the web site, it should include a clear view of the current educational level for which it is intended, a listing of what programs are offered at this level, and a listing of other programs available after participation.

Information flow between programs

At the most basic level, a program should be able to take information from a previous program and utilize the data. This information should be available to help support the flow of students within programs. During one interview with a manager, the difficulty of recruiting minority co-op students was noted. An example of this data passing would be information from SHARP being passed on to the co-op officer at the university level. This could be done with the existing data tools at MSFC. The EDCATS database could be use to support this endeavor with minor modifications. Output from EDCATS may be easily copied via Microsoft Explorer into an appropriate Microsoft Access database.

Some of the difficulty with the passing of data is based on the culture of the programs. Many are treated as an end to themselves. However, it is important for all programs to see themselves as one piece of a large puzzle to provide future workforce needs. Once the data is available and some reporting tools are used to make it easy to generate reports, management will find it easy to integrate the data from all the programs. The Education Programs Department has laid initial groundwork with other programs by collaborating with other CaER and EOO programs toward a comprehensive summer student seminar series.

Skill / Education assessment for general positions at MSFC

One of the steps involved in almost every workforce development program is to define skills/goals needed for employment in an organization. This process also helps in determining some of the curriculum in the programs offered to young people. This process will give the students a clear set of goals to pursue.

In addition, a skill profile of entry-level applicants should be developed. Each directorate should select a small number of generic positions that will be filled in the future with current students. Documentation should be completed with a list of the skills needed by a future employee, the education level that must be obtained, and a list of the skills that can be introduced or acquired within our workforce development pipeline programs. These positions should be wide ranging in education levels and skills needed. This process is needed to assure that programs are meeting the needs of workplace. In addition, this process will help students learn about what skills are expected within jobs at the center. The data could also be published for school professionals on the web site. School faculty members can use documents like this to help students set personal goals. Within some programs, it will be necessary to revamp or revise the content to match a skills needed database.

Step 2

Develop a workforce development pipeline program CD for the middle school and early high school

Research shows that the greatest impact on the future career path of students must be addressed at the middle school level. To assist in exposing middle grade students to the career paths supported in the workforce development pipeline program, a CD for school distribution should be created. The content should be an opening with a menu of the different careers that one could select. Each career choice should be linked to information about the career and then video (stored on the CD) that would interview an actual employee and show footage of some of the activities of that position. Also, it should have Internet links to the workforce development pipeline page.

Outside entities involved in workforce development pipeline

At the end of step two, the POC should have linkages and collaborations from outside organizations.

Audit by outside review committee to examine the Pipeline program.

An outside team of experts needs to conduct an educational review of the activities from step 1. This will help direct the effort of new projects and assist in the improvement of current programs.

Step 3

Development of the Von Braun Scholars program

With the implementation of the workforce development pipeline, to better serve students and to further the impact on students entering science and technology fields, the Von Braun Scholars School will be created. This is a program that selects the best and brightest in science, technology, and engineering.

Development of MSFC Star teacher program

Research shows that it is as important to develop programs for teachers as it is for students in the areas of science and technology. The current NASA teacher programs need to be reviewed by a team of MSFC personnel and educators to determine if they are as efficient as NASA wants them to be at instructing teachers. All programs offered should be developed with the goal of integrating the support of workforce skills of students.

The teacher programs should be divided into three types. Type 1 and 2 programs would be longer and more inclusive programs and would only be offered during the summer. Type 3 programs would be shorter in nature.

Type 1 Teacher program (Middle school– High school)
Teachers will be involved in an immersion class in an area of MSFC expertise. The objective of each class should be how to teach a science or engineering topic. The Star teacher program should work to involve teachers with intense hands-on lessons that would inspire the teachers to return the information to the classroom. The program would be offered during the summer and begin with a general meeting on a Sunday night and finish at the end of the day on Thursday.

Type 2 Teacher program (Elementary – Middle School)
Teachers involved in this program should see more of a broad spectrum of what NASA has to offer. Classes should revolve around a theme, but time will be given to view a wide variety of NASA educational materials. Themes should change during the year to reflect current happenings or NASA interest.

Type 3 Teacher workshops

After meetings with members of ED, TD and SD directorates and meeting with the Assistant to the Director for Space Optics, it is apparent that each of the different directorates has a desire to showcase their knowledge and expertise to the educational community. With some teamwork from the education programs office, many are ready to conduct short sessions. These sessions could cover topics ranging from Microgravity to the Science of Optics. In an effort to reach a new audience, it is suggested that a different approach be taken on offering these classes to educators. Research from the education department at Tennessee Tech suggest that teachers are more receptive and retain more information by participating in short immersion classes. It is suggested that a series of classes be offered from Friday evenings through Sunday. These classes should be designed so they can be carried off site and conducted at schools in our six state service area.

Development of a plan to implement the Workforce Pipeline program to all NASA centers

After the implementation of the Workforce Pipeline program at MSFC, it should be offered to all NASA Centers.

Long Range Planning

Development of the TOS program (Tracking of Students)
The TOS system should be developed to create a record of students that have participated in the program. This record should reflect student information and the content of the program. Think of this as a transcript that the student could request. Much of the needed data is already in edcats. This will also present the opportunity to better standardize what is asked in EDCATS between the different programs. In addition, it would also be a way for the other programs in other CaER organizations to input their data on activities.

2001

NASA/ASEE SUMMER FACULTY FELLOWSHIP PROGRAM

MARSHALL SPACE FLIGHT CENTER
THE UNIVERSITY OF ALABAMA

Micro-Mechanical Modeling of Ductile Fracture in Welded Aluminum-Lithium Alloys

Prepared by:	Ahmed Ibrahim
Academic Rank:	Associate Professor
Institution and Department:	SUNY at Farmingdale Mechanical Engineering Department
NASA/MDFC Directorate:	Materials Processes and Manufacturing
MSFC Colleague:	Douglas N. Wells

Introduction

Figure 1 illustrates a simplified view of the conditions ahead of a macroscopic crack front in a ferritic steel containing different size inclusions. Void growth occurs over a relatively narrow band of thickness D [1]. Material outside this region experiences negligible void growth. This layer of damaged material ahead of the growing crack defines the process zone for ductile fracture. Within a finite element framework, a single layer of uniform, fixed-sized cells, having total thickness D, along the crack plane exemplify this scheme into a computational model (Figure 2).

The computation model consists of a cavity with initial volume specified by the fraction f_0, i.e. the void volume relative to the cell volume. Thus, cell size D and initial porosity f_0 defines the key parameters in this model. The choice of cell size requires:

1) D must be representative of the large inclusion spacing
2) Predicted R-curves scale almost proportionally with D for fixed f_0
3) mapping of one finite element per cell must provide adequate resolution of the stress-strain fields in the active layer and the adjacent material

For the ferritic steels studied thus far [3] with this model, calibrated cell sizes range from 50-200 μm with f_0 in the 0,0001 –0.004 range. This range of values for D and f_0 satisfies issues (1) and (3).

This Computation model employ the Gurson and Tvergaard constitutive model for porous plastic materials to describe the progressive damage of cells due to the growth of pre-existing voids. The model derives from a rigid-plastic limit analysis of a solid having a volume fraction (f) of voids approximated by a homogenous spherical body containing a spherical void. The yield surface and flow potential, g, is given by

$$\left[\frac{\sigma_e}{\bar{\sigma}}\right] + 2q_1 f \cosh\left[\frac{3q_2\sigma_m}{2\bar{\sigma}}\right] - \left[1 + q_3 f^2\right] = 0 \qquad (1)$$

Where σ_e denotes the mises equivalent (macroscopic) stress, σ_m is the macroscopic mean stress, $\bar{\sigma}$ denotes the flow stress for the matrix material of the cell and f is the current void fraction. Factors, q_1, q_2 and q_3, introduced by Tvergaard improve the model predictions.

Notch Tensile Specimen

Figure 3 shows the notch tensile specimen. This is 0.312" diameter specimen with 0.008 in. radius in the notch region. The middle part of the specimen is made of Al 4043 Weld and the rest is Al 2195. Fracture Surface of tensile-test revealed that: Ductile Fracture occurred by microvoid initiation, growth and coalescence. Figure 4 shows a small region in the high triaxility region of Al 4043 weld notch specimen tested at RT illustrates the distribution of various sizes of pores that develop during deformation.

Finite Element Model

The model was created using Patran. The 3-D analysis was performed by WARP-3D, a 3–D Dynamic Nonlinear Fracture Analysis code developed by the University of Illinois. Figure 5 shows the Axi-symmetric finite element model constructed for 3-D analyses of the specimen. Symmetry conditions enable analyses using one-half, 3-D model. The 3-D model has approximately 2320 elements and 3736 nodes. The model is set up with Gurson elements for the lower row of 0.001 in. size elements. The transformation matrix is for a 1-degree rotation about the axis of revolution. This was accomplished by sweeping the a 2-D model of 4-node elements in Patran about the Y-axis.

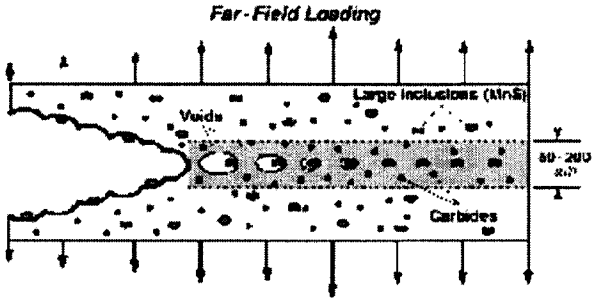

Figure 1: Microstructure for Ferritic Steels

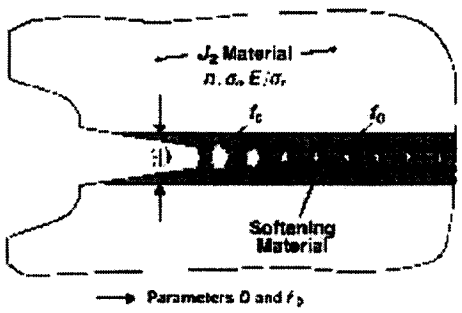

Figure 2: Computational Cell Model

Conclusions

This study describes a 3-D computational framework to model stable extension of a macroscopic crack under mode I conditions in ductile metals. Material separation occurs through a local fracture mechanism based on the growth and coalescence of microvoids dispersed in the material. The Gurson-Tvergaard plasticity model for void materials describes the eventual loss of material stress capacity under sustained loading. Fixed-sized computational cell elements defined on a thin layer adjacent to the crack plane provide an implicit length scale for continuum damage model. Outside this layer, the material remains undamaged by void growth, consistent with metallurgical observations. The key micro-mechanics parameters are D, the thickness of cell layer, and f_0, the initial cell porosity.

Acknowledgments

The author would like to thank Mr. Douglas Wells for the extraordinary support that he has provided during this work, Mr. Gerry Green for mechanical testing, Mr. J. Wright for analysis of Data, and Mr. Jiff Clounch for graphics support.

1. Gullerud, A., Dodds, R. ``Simulation of Ductile Crack Growth Using Computational Cells: Numerical Aspects," submitted for publication in *Engineering Fracture Mechanics,* April 1999.

2. Gullerud, A. and Dodds, R. ``3-D Modelig of Ductile Crack Growth in Thin Sheet Metals: Computational Aspects and Validation," *Engineering Fracture Mechanics,* Vol. 63, pp. 347-374, 1999.

3. Ruggieri, C. and Dodds, R. ``Numerical Modelig of Ductile Crack Growth in 3-D Using computational cell elements," *International Journal of Fracture,* Vol. 82, pp. 67-95, 1996

4. Dodds, R. H., Tang, M., and Anderson, T.L. ``Effects of Prior Ductile Tearing on Cleavage Fracture Toughness in the Transition Region," *Constraint Effects in Fracture Theory and Applications: Second Volume, ASTM STP 1244,* M. Kirk and A. Bakker (Eds.) American Society for Testing and Materials, Philadelphia, pp. 100-133, 1995.;

5. Dodds, R. H., Shih, C. F., and Anderson, T. L. ``Continuum and Micro-Mechanics Treatment of Constraint in Fracture," *International Journal of Fracture*, Vol. 64, pp. 101-133, 1993

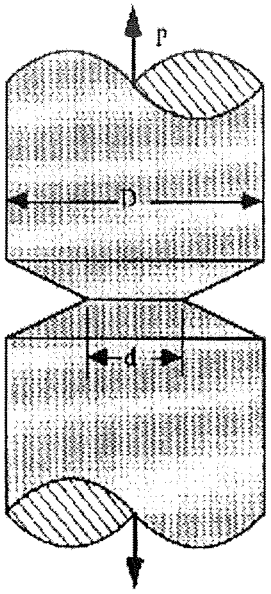

Figure 3: Notch Tensile Specimen

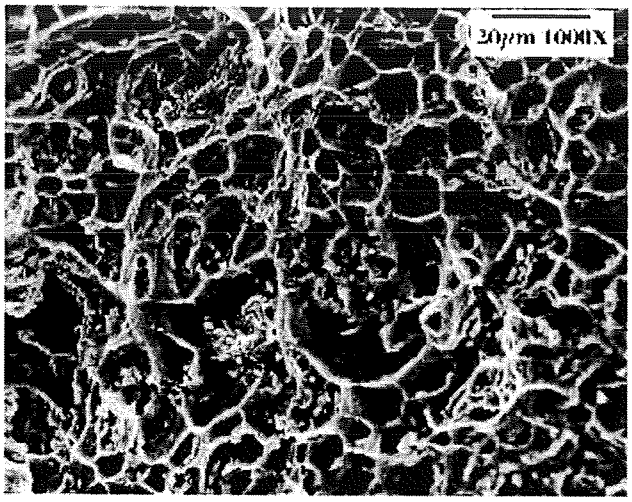

Figure 4: Microstructure of the Fracture Surface of Al 4043 Weld

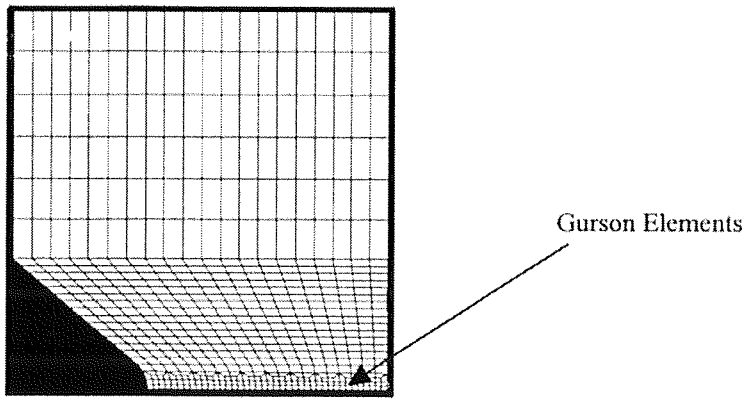

Figure 5: The Axi-Symmetric Finite Element Model

2001

NASA/ASEE SUMMER FACULTY FELLOWSHIP PROGRAM

MARSHALL SPACE FLIGHT CENTER
THE UNIVERSITY OF ALABAMA IN HUNTSVILLE

Synthesis Of Colloidal Silica Nanocomposites For Photonics Applications

Report Not Available

Prepared By	Njeri T. Karangu
Academic Rank:	Assistant Professor
Institution and Department:	Spelman College Department of Chemistry
NASA/MSFC:	
Office:	Biological and Physical Science
Department:	Science and Applications
MSFC Colleagues:	Mark Steve Paley, Ph.D David D. Smith, Ph.D.

2001

NASA/ASEE SUMMER FACULTY FELLOWSHIP PROGRAM

MARSHALL SPACE FLIGHT CENTER
THE UNIVERSITY OF ALABAMA IN HUNTSVILLE

AN ATOMISTIC SIMULATION OF CRACK PROPAGATION IN A NICKEL SINGLE CRYSTAL

Prepared BY:	Majid Karimi
Academic Rank:	Associate Professor
Institution and Department:	Indiana University of Pennsylvania Physics Department
NASA/MSFC Directorate:	Engineering
MSFC Colleague:	Gregory Swanson

Introduction

Crack and dislocation propagations are two major mechanisms of failure in metals and their alloys. Understanding these two mechanisms of failures is important in the development of new materials with high strength and toughness. The macroscopic properties of materials can often be determined through the underlying microscopic processes. In particular, this could become clear when we realize that in a brittle crack propagation it is the bonds between atoms that are broken. It is therefore clear that a complete understanding of properties of crack near the crack tip is directly linked to a detailed understanding of materials from an atomistic standpoint. On the other hand, regions far away from the crack are not atomically very important [1,2]. Finite element technique has provided valuable information about properties of the crack, specially, further away from the crack. Despite advantages of atomistic computer simulation, it has only received attention in the last decade or so. This is in part due to the fact that this type of simulation is computationally intensive. With the advent of more advanced computers and more optimized codes it is now possible to track the dynamics of crack propagation from an atomistic standpoint.

The main objective of this paper is to determine mechanisms of crack propagation in a nickel single crystal. Motivation for selecting nickel as a case study is because we believe that its physical properties are very close to that of nickel-base supper alloy. We are directed in identifying some generic trends that would lead a single crystalline material to failure. We believe that the results obtained here would be of interest to the experimentalists in guiding them to a more optimized experimental strategy. The dynamic crack propagation experiments are very difficult to do. We are partially motivated to fill the gap by generating the simulation results in lieu of the experimental ones for the cases where experiment can not be done or when the data is not available.

Methodology

The atomistic simulation technique that is employed in this study is based on the classical molecular dynamics (MD) method. Input to any MD simulation is a lattice file which contains positions and velocities of all the atoms in the system. In the MD simulation, Newton's equations of motion are integrated to determine the phase space trajectories of all atoms in the system using a force function which is derived from an interatomic potential E_{pot}.The Newton second law when applied to atom i has the following form,

$$f_i = m_i a_i = m_i \frac{dv_i}{dt} = m_i \frac{d^2 r_i}{dt^2}, \qquad (1a)$$

$$f_i = -\frac{\partial E_{pot}}{\partial x_i}, \qquad (1b)$$

where E_{pot} is calculated from the EAM technique [3]. Numerical solution of equation 1 for all the atoms in the system would lead to 3N values for the positions and 3N values for the velocities of all N atoms at each time step dt. In order to calculate $r_i(t)$ and $v_i(t)$ as a function of

t=n*dt, where n is the number of time steps, one requires 3N values for the initial positions $r_i(0)$ and 3N values for the initial velocities $v_i(0)$ of all the particles in the system at time zero. For the initial positions of the atoms we considered their values from their ideal fcc single crystalline sites. To each atom in the system, we just assigned zero initial velocity.

The main equations of the EAM technique is summarized below,

$$E_i = F_i(\rho_i) + \frac{1}{2}\sum_{j \neq i} \varphi_{ij}(r_{ij}), \qquad (2a)$$

$$E_{pot} = \sum_i E_i , \qquad (2b)$$

where E_i is the energy of atom i, ρ_i is the electronic charge density at site i, F_i is the embedding energy of atom i, and φ_{ij} is the pair potential function between atoms i and j. ρ_i is approximated as the superposition of atomic charge densities of atoms neighbor to atom I at the location of atom i. The EAM functions employed here are the one that were recently developed by Mishin et.al. [4]. The Mishin EAM functions of Ni, Al, and NiAl alloy are superior to the previous EAM functions for those materials due to the fact that they are fitted to the more richer data base using a new fitting scheme. In fact, the reliability of any MD results is directly related to the reliability of the interatomic potential that is employed by it. For the present application, it is critical that the potential reproduces the elastic constants as well as surface energies accurately.

Critical values of energy density G and applied stress-intensity K are calculated using the following formulas[5],

$$G = \frac{1}{2} E' W \varepsilon^2 , \qquad (3a)$$

$$K = \varepsilon E' \sqrt{\frac{W}{2}} , \qquad (3b)$$

where for a plane strain the Young modulus $E'=E/(1-\nu^2)$, ε is the tensile strain in mode I, and dimension W is shown on the strip geometry in figure 1. For an anisotropic material E and ν are obtained from the elastic constants through the following relations [6],

$$h=2*C_{44}-+C_{12}-C_{44},\ E=C_{12}-(1/5)h,\ \mu=C_{44}-(1/5)h,\ \nu=E/(2(E+\mu)). \qquad (4)$$

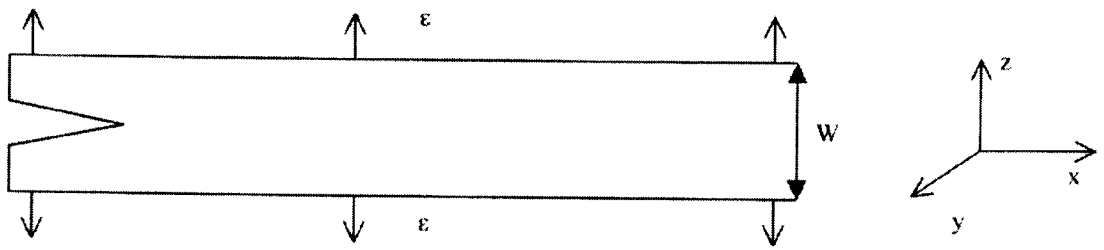

Figure 1. Schematic of the sample with crack

Results and Discussion

In order to check the reliability of the EAM potential of nickel employed here, elastic constants C_{11}, C_{12}, C_{44}, bulk modulus B, lattice constant a, cohesive energy E_c, and surface energies γ_{110}, γ_{100}, γ_{111} are calculated and compared with their corresponding experimental values .Some of our calculated values are as follows; C_{11}=247Gpa, C_{12}=148Gpa, C_{44}=125Gpa, B=181Gpa, cohesive energy E_c=4.45eV, and lattice constant a_0=3.52A. All the quantities calculated here are exactly equal to their corresponding experimental values except for the surface energies. Unfortunately, accurate experimental values of the surface energies γ_{110}, γ_{100}, γ_{111} are not reported in the literature. Most of the currently available experimental values of the surface energies are averages over various faces of the single crystal. From the theoretical studies it is predicted that $\gamma_{110} > \gamma_{100} > \gamma_{111}$. This trend is corroborated by the potential employed here.

All of our MD runs were performed at a constant temperature of T=0.001 K and all the samples were roughly of size 50x13x120 A^3 (about 8000 atoms), and periodic along the thin axis (y-axis). In the table below, critical values of G_c,K_c, and ε_c for the crack to propagate, twice the surface energy of the crack 2γ, and failure mode of the material are summarized.

TABLE I. Critical energy density G_c, critical applied stress-intensity K_c, critical strain ε_c,twice the surface energy 2γ, and failure modes for the crack propagation of different crack systems [6].

Crack systems	G_C (J/m^2)	K_C ($MPa\sqrt{m}$)	ε_c	2γ(J/m^2)	failure mode
(001)[100]	6.74	9.24	0.095	3.76	Stable regime: opening on (100)
(100)[011]	6.05	8.75	0.090	3.76	Stable regime: opening on (100)
$(1\bar{1}0)[110]^{(a)}$	5.46	0.798	0.082	4.10	Stable regime: opening on $(1\bar{1}0)$
$(1\bar{1}0)[110]^{(b)}$	7.55	0. 978	0.070	4.10	Stable regime: opening on $(1\bar{1}0)$
$(111)[2\bar{1}\bar{1}]$	<5	<0.6	0.04	3.26	Emitting an edge partial dislocation
$(111)[10\bar{1}]$	<5	<0.6	0.04	3.26	Emitting an edge partial dislocation

(a), (b). Calculations in parts (b) and (a) are similar except that in part (b) value of W is twice as the one in part (a) This was done to check the convergence of G and K formulas with the size of the system.

Summary and Future Extension

Our results can be summarized as follows:

(1) Crystallographic surfaces of a crack as well as direction of propagation of a crack are two very important factors that will dictate the failure mechanism of a material.

(2) The data presented in Table I show that among the crack systems studied here three are brittle and two are ductile

(3) Crack propagation in mode I does not follow G or K criteria.

(4) Values of G and K depend on the size of the sample and to reduce or eliminate this size effect the sample size should be increased to have about 80000 atoms.

Possible future extension of this project:

(1) Extending this work to larger systems

(2) Extending this work to include a mixed mode (I and II).

(3) Extending this work to higher temperatures.

(4) Extending this work to Ni_3Al alloy.

(5) Calculate critical values of G and K for the propagation of dislocation.

(6) Calculate the velocity of a crack as a function of time and G.

Acknowledgments

The author would like to thank: Dr. Gregory Swanson for providing a stimulating, professional, and friendly work environment, Mr. Doug Fox and Mr. Jeff Rayburn for computer related questions, and Mrs. Renee Wilson and Mrs. Leigh Ann Perkins for helping me when I needed something.

References

[1] Gumbsch, P., Zhou, S. J., and Holian, B. L. (1997), Physical Rev. B55, 3445-3455.
[2] Abraham, F.F., et.al. (1998), Modelling Simul. Mater. Sci. Eng. 6, 639-670.
[3]. Karimi, M., et.al. . (1997), Modelling Simul. Mater. Sci. Eng. 5, 337-346.
[4]. Mishin, Y., et.al. (1999), Phys. Rev.B59, 3393-3407.
[5]. Anderson, T. L. (1991), Fracture Mechanics, CRC Press, Boca Raton, Florida.
[6] Swanson, G.R. and Arakere, N. K. (2000), NASA/TP, 210074; Stouffer, D.C. and Dame, L.T. (1996), Inelastic Deformation of Metals, John Wiley& Sons.

2001

NASA/ASEE SUMMER FELLOWSHIP PROGRAM

MARSHALL SPACE FLIGHT CENTER

THE UNIVERSITY OF ALABAMA IN HUNTSVILLE

HOLOGRAPHIC GRATINGS FOR OPTICAL PROCESSING

Prepared by:	Nickolai Kukhtarev
Academic Rank:	Research Professor
Institution and Department:	The Alabama A&M University Physical Department
NASA/MSFC Directorate:	Space Optics Manufacturing
MSFC Colleague:	Joseph Grant

Introduction

Investigation of astronomical objects and tracking of man-made space objects lead to generation of huge amount of information for optical processing. Traditional big-size optical elements (such as optical telescopes) have a tendency for increasing aperture size in order to improve sensitivity. This tendency leads to increasing of weight and costs of optical systems and stimulate search for the new, more adequate technologies.

One approach to meet these demands is based on developing of holographic optical elements using new polymeric materials. We have investigated possibility to use new material PQ-PMMA (phenantrenequinone-doped PMMA) for fabrication of highly selective optical filters and fast spatial-temporal light modulators. This material was originally developed in Russia [1] and later was tested in CalTech [2] as a candidate material for an optical storage. Our theoretical investigation predict possibility of realization of fast spatial and temporal light modulation, using volume reflection-type spectral filter. We have developed also model of holographic-grating recording in PQ-PMMA material, based on diffusional amplification. This mechanism of recording allow to receive high diffraction efficiency during recording of reflection-type volume holographic grating (holographic mirror).

We also investigated recording of dynamic gratings in the photorefractive crystals LiNbO3 (LN) for space-based spectroscopy and for adaptive correction of aberrations in the telescope's mirrors. We have shown, that specific 'photogalvanic' mechanism of holographic grating recording in LN allow to realize recording of blazed gratings for volume and surface gratings. Possible applications of dynamic gratings in LN for amplification of images, transmitted through an imaging fiber guide was also demonstrated.

Holographic Recording in Polymeric Materials with Diffusional Amplification

Thick holographic gratings combine high diffraction efficiency with high spectral selectivity and may be used for optical filtering, date transmission and storage. Important applications are in solar astronomy, optical communications (as satellite detection and ranging [1]), Raman Spectroscopy for detection of small concentration of heavy metal [1], for wavelength division multiplexing [2].

Recently it was suggested to use volume reflection grating for the new type of all-optical time-space modulator with fast response [3,4]. Recording of the efficient volume reflection holographic grating in real-time media (like traditional photopolymers) is hindered by the constant phase-shift of interference pattern during recording caused by self-diffraction [4]. To overcome this fundamental problem, new materials with diffusional enhancement were suggested [5]. In these materials during the hologram recording two out-of-phase gratings are formed. Initial diffraction efficiency is small, so selfdiffraction effect does not spoil recording process. Post expose annealing at moderate temperature ($T \sim 50^0$ C) leads to the diffusional enhancement of the recorded grating. We will discuss the model of diffusional enhancement, suggested in [5] for different modes of recording:

1) fast recording with post expose annealing;
2) slow recording (with simultaneous annealing, real-time gratings).

We consider photochemical reactions in the material, containing initial product with concentration A during the formation of molecules with concentration B:

$$A \xrightarrow{h\upsilon} B$$

Later molecules B are chemically connected to the polymer micromolecules with reaction constant K leading to creation of immobilized molecules C with the rate

$$\frac{\partial C}{\partial t} = KB \tag{1}$$

During the photochemical reactions refractive index n will be changed

$$n = n_o + \alpha_A A + \alpha_B B + \alpha_C C \tag{2}$$

At the initial stage, during recording, refractive index changes $\Delta n = n(t) - n(t=0)$ are due to difference of polarisabilities α_A and α_B. In practically important special case (realized in polymethyl methacrylate with phenantrenequinone PQ=PMMA) α_A and α_B are equal, but have different signs:

$$\alpha_A + \alpha_B \approx 0 \tag{3}$$

It means, that during illumination of such material with spatially modulated intensity

$$I = I_0(1 + m\cos qx) \tag{4}$$

Two holographic gratings of refractive index modulation are formed, which compensate each other. Two of components A and B are mobile, and are diffusing in space, tending to homogeneous distribution. Phenanthrene chromophores chemically attached to F macromolecules are practically immobilized. After diffusion at elevated temperature (annealing) final modulation of refractive index will be due to the spatial modulation of concentration of the chromophores F. Complementary gratings of A and B components will be washed out by diffusion. For detailed description of holographic recording, we will consider system of equations, modeling photoinduced reactions and diffusion.

Basic Model

Basic equations, describing rate of concentration changes due to photoexcitation, photochemical reaction and diffusion will be:

$$\begin{aligned} \frac{\partial A}{\partial t} &= -sIA + D_A \frac{\partial^2 A}{\partial x^2} \\ \frac{\partial B}{\partial t} &= sIA + D_B \frac{\partial^2 B}{\partial^2 x^2} - KB \\ \frac{\partial C}{\partial t} &= KB \end{aligned} \tag{5}$$

here s is cross-section of photon absorption, K is the rate constant of photochemical reaction, $D_{A,B}$ are diffusion coefficient for A and B components.

For harmonic intensity modulation, given by (4) we may expect also harmonic solution for the concentrations for small modulation ratio m≤ 1. Note, that for general case, for high contrast (m ≅ 1) we can get additional spatial harmonics of concentration as follows from (5).

Solution for a small contrast (m<1)

For a small modulation ratio (m<1) we will seek the solution of Eq. (5) in the form

$$A = A_0 + A_1 \cos kx \tag{6}$$

For A and other concentration (B and C) considering that $A_1 << A_0$. We will get from Eq.(4) for the amplitudes A_1, B_1, C_1

$$\begin{aligned} \frac{\partial A_1}{\partial t} &= -(sI_0 + q^2 D_A)A_1 - sI_1 A_0 \\ \frac{\partial B_1}{\partial t} &= -(K + q^2 D_B)B_1 + sI_1 A_0 + sI_0 A_1 \\ \frac{\partial C_1}{\partial t} &= KB_1 \end{aligned} \tag{7}$$

here $I_1 \equiv mI_0$

Grating recording

For the spatially averaged components of concentration A_0, B_0, C_0 we have

$$\begin{aligned} \frac{\partial A_0}{\partial t} &= -sI_0 A_0 \\ \frac{\partial B_0}{\partial t} &= sI_0 A_0 - KB_0 \\ \frac{\partial C_0}{\partial t} &= KB_0 \end{aligned} \tag{8}$$

that directly gives solution:

$$\begin{aligned} A_0 &= A_0(0)e^{-sI_o t} \\ B_0 &= B_0(0)e^{-Kt} + \frac{A_0(0)sI_0}{(K - sI_0)}(e^{-sI_0 t} - e^{-Kt}) \\ C_0 &= C_0(0) + B_0(0)(1 - e^{-Kt}) + \frac{KA_0(0)sI_0}{(K - sI_0)}\left\{\frac{(1 - e^{-sI_0 t}}{SI_0} - \frac{(1 - e^{-Kt})}{K}\right\} \end{aligned} \tag{9}$$

It can be checked, that conservation law for total concentration hold (for $A_0+B_0+C_0 = A_0(0) + B_0(0) + C_0(0)$. In the steady-state $A_0(\infty) = B_1(\infty) = 0$; $C_0(\infty) = A_0(0) + B_0(0) + C_0(0)$. For the initial homogeneous distribution and $A_0(0) = C_0(0) = 0$ we will get

$$A_1 = -\frac{sI_1A_0(0)}{D_Aq^2}(1-e^{-D_Aq^2t})e^{-sI_0t}$$

$$B_1 = \frac{sI_1A_0(1-\frac{sI_0}{D_Aq^2})}{K+D_Bq^2}(e^{-sI_0t} - e^{-(K+D_Bq^2)t} +$$

$$+\frac{s^2I_1I_0A_0(0)}{D_Aq^2(K+(D_B-D_A)q^2-sI_0}(e^{-(D_Aq^2+sI_0)t} - e^{-(K+D_Bq^2)t}) \qquad (10)$$

$$C_1 = \frac{Ksh_1A_0(1-\frac{sI_0}{D_Aq^2})}{K+D_Bq^2-sI_0}(\frac{1-e^{-(sI_0t}}{sI_0} - \frac{(1-e^{-(K+D_Bq^2)t})}{K+D_Bq^2}) +$$

$$+\frac{S^2I_1I_0A_0(0)}{D_Aq^2(K+(D_B-D_A)q^2-sI_0)}\{\frac{1-e^{-(D_Aq^2+sI_0)t}}{(D_Aq^2+sI_0)} - \frac{(1-e^{-(K+D_Bq^2)t})}{K+D_Bq^2}\}$$

On the initial stage of recording (in the approximation linear on t, case considered by A.Veniaminov et al[5])

for $B_0(0) = C_0(0) = 0$

$A_0 = A_0(0)(1-sI_0t)$; $A_1 = -sI_1tA_0(0)$

$B_0 = A_0(0)sI_0t$; $B_1 = sI_1tA_0(0)$

$C_0 = 0$ $C_1 = 0$

or (11)

$A(t) = A_0(0)[1-sI_0t(1+m\cos qx)] = C - C_1^0(1+m\cos qx)$

$B(t) = C_1^0(1+m\cos qx)$; $C_1^0 \equiv A_0(0)sI_0t$

in Veniaminov's notation $C \equiv A_0(0)$

In the steady-state ($t \to \infty$)

$A_0 = B_0 = 0$

$A_1 = B_1 = 0$

$$C_1|_\infty = \frac{I_1KA_0(0)q^2D_A}{I_0(K+D_Bq^2)(sI_0+q^2D_A)} \qquad (12)$$

For the large steady-state modulation of C we need:

1) large diffusion coefficient D_A ($D_Aq^2 >> I_0$)
2) large holographic grating vector q (small period)

3) small diffusion coefficient D_B ($D_B q^2 << K$)
4) large K (rate of phototransformation).

Diffusional enhancement of grating

Kinetic of holographic grating enhancement during annealing in the dark is described by equations:

$$\frac{\partial A_1}{\partial t} = -D_A q^2 A_1$$
$$\frac{\partial B_1}{\partial t} = -(K + D_B q^2) B_1 \qquad (13)$$
$$\frac{\partial C_1}{\partial t} = K B_1$$

with obvious solution

$$A_1 = A_1(0) e^{-D_A q^2 t}$$
$$B_1 = B_1(0) e^{-(K + D_B q^2)} \qquad (14)$$
$$C_1 = K B_1(0)(1 - e^{-(K + D_B q^2)t}) + C_1(0)$$

and amplitude of the refractive index grating

$$n_1 = \alpha_A A_1 + \alpha_B B_1 + \alpha_C C_1$$

Comparing refractive index changes from initial value (for $sI_0 t$, $q^2 D_{A,B} t << 1$)

$$n_1(t \to 0) \cong A_1(\alpha_B - \alpha_A) = S I_1 A_0(0) t(\alpha_B - \alpha_A) \qquad (15)$$

with the value after annealing (from Eq. (14) $t \to \infty$

$$n_1(t \to \infty) \cong \alpha_C \frac{K B_1(0)}{K + D_B q^2} \qquad (16)$$

we can find coefficient of diffusional enhancement:

$$\frac{n_1(t \to \infty)}{n_1(t \to 0)} = \frac{K \alpha_C}{(\alpha_B - \alpha_A)(K + D_B q^2)} \qquad (17)$$

obtained by A.Veniaminov et al in [5]. In the case, when steady-state is reached under constant illumination (recording and annealing are simultaneous) , the modulation of refractive index (using Eqs. (12) and (2) will be:

$$n_1(\infty, I_0) = \alpha_C \frac{mKA_0(0)D_A q^2}{(K + D_B q^2)(sI_0 + D_A q^2)} \qquad (18)$$

$$m = \frac{I_1}{I_0}$$

We may compare now amplitudes of refractive index modulation for two cases:

a) when initial recording was interrupted at the time $sI_0t.D_{A,B}q^2t << 1$ and sample was annealed $(t \to \infty)$; n (∞); (fast recording)

b) when recording and annealing were simultaneously, n_1 (∞, I_0) (real-time grating)

$$\frac{n_1(\infty, I_0)}{n_1(\infty)} = \frac{mA_0 q_2 D_A}{B_1(0)(sI_0 + q^2 D_A)} = \frac{q^2 D_A}{I_0 st(sI_0 + q^2 D_A)}$$

We can see, that in the second case (for annealing during recording) amplitude may be further enhanced especially for grating with small periods (when $q^2D_A >> SI_0$).

Holographic filter for spatial – temporal light modulator

We have tested the holographic filter based on recording of reflection volume gratings for modulation of light [3,4]. For convenience, we summarize mail theoretical results following [3,4].

Initial coupled-wave equations for the amplitude of incident C_1 and diffracted waves C_2 will be for reflection geometry

$$\pm \frac{\partial C_{1,2}}{\partial z} = i\gamma_0 C_{1,2} + i\gamma C_2 \qquad (19)$$

here $\gamma_0 = k_0 \Delta n_0$ is coupling coefficient due to change of the average of refractive index Δn, k_0 is the wave number. In the similar wave $\gamma \equiv k_0 \Delta n$, where Δn is the amplitude of refractive index grating. For $\gamma \geq \gamma_0$ solution of Eq. (19) gives for diffraction efficiency

$$\eta = \left|\frac{C_2(0)}{C_1(0)}\right|^2 = \frac{\gamma^2 \tanh^2 gl}{\gamma_0^2 \tanh^2 gl + g^2} \qquad (20)$$

here $g \equiv (\gamma^2 - \gamma_0^2)^{1/2}$, l is the grating thickness. For the large changes in homogeneous average refractive index Δn_0 (when $\gamma_0 > \gamma$) instead of (20) we get

$$\eta = \frac{\gamma^2 \sin^2 |g| l}{\gamma_0 \sin^2 |g| l + |g| \cos^2 |g| l} \qquad (21$$

For a relatively small diffraction efficiency $\eta \sim 0.21$ (for $\gamma l = 0.5$ and $\gamma_0 = 0$), changes in γ_0 from 0 to $\gamma_0 = \gamma$ give diffraction efficiency $\eta \sim 0.20$. In this case of small diffraction efficiency η , relative changes is $\Delta\eta/\eta = 5\%$. For larger η ($\eta_0 \sim 0.58$ for $\gamma l = 1$, and $\gamma_0 = 0$), changes in γ_0 from 0 to $\gamma_0 = \gamma$ results is $\eta = 0.5$, that means for relative changes $\Delta\eta/\eta_0 = 14\%$. For the same case ($\gamma l = 1$) changing in γ_0 to 2γ gives $\eta \sim 0.245$, that gives $\Delta\eta/\eta_0 = 50\%$. We may conclude that holographic filter with high diffraction efficiency are preferential for SLM. For large change of average refraction index (when $\gamma_0 >> \gamma$) diffraction efficiency becomes oscillating (Eq.20), as illustrated by Fig.1. On fig.1 we show spatial modulation observed in Bragg reflected HeNe ($\lambda = 633$nm) laser beam with simultaneous illumination by focused Ar-laser beam ($\lambda = 514$ nm, P=200mW)

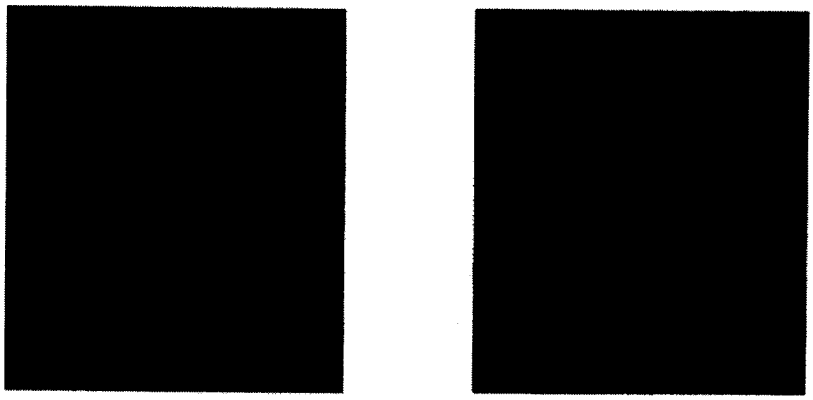

Figure 1. Spatial Modulation By Holographic Filter (left and right pictures were made with time delay of 2 min).

Holographic Blazed Gratings in LiNbO3

Now it is renewed interest to the nonsymmetrical (blazed gratings) for applications in space-based spectroscopy and for optical correction of the telescope's mirrors aberrations. Traditional methods of blazed-gratings formation require special gray-scale masks, or need time-consuming processing with particle beams or mechanical ruling.

We have suggested and tested new method of blazed grating formation, that is based on nonlinearity of mechanism of holographic recording in LN crystal. This nonlinearity is due to photogalvanic (or photovoltaic) effect, that is main mechanism of recording in the Fe-doped crystals of LN. In this crystal holographic grating recording is due to the photoinduced grating of electric field, formed by photo-excitation of Fe-impurity and redistribution of the photoexcited charge carriers by diffusion, drift and photogalvanic current. Photoinduced electric field mimic light interference pattern and create refractive index grating via linear electro-optic effect. Our theoretical estimations and preliminary experimental results, show. feasibility of this new holographic method of blazed grating formation in Fe-doped crystals of LiNbO3.

Conclusions

We have described theoretical model for the diffusional enhanced recording of holograms in the materials with photochemical reactions. As example, we consider perspective novel polymer material with phenantrenequinone (PQ). Good results were reported in [1] for polymethyl metacrylate (PMMA) with PQ dissolved in it. Both transmission and reflection diffraction gratings were recorded in this material [1], that were tested as narrow-band holographic filters. We suggest new application of reflection-type holographic filters as a basic element for all-optical light modulators with a fast response. Second mode of diffraction "slow recording" with simultaneous annealing may give larger efficiency for holographic grating. It may be applied for the recording of transmission type gratings. Note, that for recording of reflection gratings with high efficiency, real-time effects (selfdiffraction) may prevent effective recording in the second mode of recording. To avoid destructive influence of selfdiffraction, recording in real-time mode should be done in transmission geometry. Recorded holographic filter may be used in reflection geometry for longer wavelength, provided Bragg-conditions are satisfied.

The volume holographic gratings in polymer materials are promising candidates for spectrally selective optical elements, dense data storage, optical communication, and spectral selective imaging. Recently new application of volume reflection-type grating for fast all-optical temporal/spatial light modulators was suggested.

Spatial modulation of diffracted red beam by green laser was demonstrated. We also suggest and analyze theoretical model for material with diffusional amplification for different modes of recording:

1) Fast recording with following annealing;
2) Slow recording (real–time grating).

We also have tested feasibility of holographic approach for the blazed grating formation in LN-crystals , using nonlinearity of recording mechanisms due to photogalvanic response.

Preliminary results with imaging fiber guide demonstrate possibility of image enhancements by dynamic holographic gratings in LN crystals.

Acknowledgements

We acknowledge help of T. Kukhtareva, H. Abdeldayem, W. Witherow, B. Penn, D. Frazier, A. Veniaminov in part of this research efforts, related to PQ-PMMA and V. Edwards and T. Kukhtareva in participation in experiments with blazed gratings in LiNbO3 crystals.

References

1. A. Popov, I.Novikov, K.Lapushka, I.Zyuzin, Yu. Popov, A.Ashcheulov, A.Veniaminov, (Appl. Optics , 2, 494-499, 2000).

2. I Novikov, Tech. Phys. Lett., 24, 76, 1998.

3. N. Kukhtarev, T. Kukhtareva at al, Technical Digest, CLEO'2000.

4. N.Kukhtarev, T.Kukhtareva , R. Jones, D. Frazier, B.Penn, H.Abdeldayem, Fast All Optical Spatial-Temporal Light Modulator," SPIE Proc.. Vol. **4042,** 140-145, 2000.

5. A.Veniaminov, V.Goncharov, A.Popov, Optics and Spectr., V.70, 505-508, 1991.

2001

NASA/ASEE SUMMER FACULTY FELLOWSHIP PROGRAM

MARSHALL SPACE FLIGHT CENTER
THE UNIVERSITY OF ALABAMA IN HUNTSVILLE

3D VISUALIZATION IN SUPPORT OF ADVANCED PROPULSION

Prepared By:	Jan P. Kyzar
Academic Rank:	Assistant Professor
Institution and Department:	East Tennessee State University Department of Technology
NASA/MSFC Directorate:	Transportation
MSFC Colleague:	Dr. George Schmidt

Introduction

Young computer graphics enthusiasts today might think they are pioneers of new technology. On the contrary—computer graphics experimentation began in the 1940s. A rich and eventful history exists in a short time frame of six decades. The first graphics software was developed as "a tool for scientists and engineers in government and corporate research centers such as Bell Labs and Boeing."[4] Computer graphics software today includes anything from vector-based page layout packages to extremely sophisticated three-dimensional design and animation software and *everything* in-between. The realm of this summer faculty fellowship project required three-dimensional (3D) digital capabilities. Therefore, the remainder of the paper will focus only on this facet of the graphics industry.

What is three-dimensional digital animation? Some define animation as the art in movement, while others call it the illusion of movement [3]. It is both: animation is art and it is definitely an illusion. 3D animators create the illusion of movement with digital objects and many images- or frames- played in sequence. Any of these objects can literally be tumbled around in space to reveal every side and detail. A digital "camera" can even be created and moved around the objects. This capability is extremely helpful in any training environment. 3D visualization helps the audience to better understand the subject matter by giving them a sense of size, perspective and placement of objects.

Much of the public today may only see 3D digital imagery used in the entertainment industry for films or gaming. However, digital animation is a critical support structure, or backbone, to a wide variety of fields. Some other fields that depend on some form of digital visual support for survival include web design, advertising, product design, medical education and architectural visualization. The world of science, forerunner of computer graphics, continues to utilize this technology in many aspects of research and education.

What could all of these varied fields have in common? Why do they all rely on 3D digital technology? The answer is visual communication. A message is always being delivered—and a visual presentation is the tool with which to deliver it. The message being conveyed might be anything from the life and process of a certain star, the latest surgical technique or simply unadulterated entertainment. This message can be communicated to students, scientists, families, the general public—to anyone. Careful attention must be paid to the intended audience. Once the exact target audience determined, the level at which content must be delivered is designed.

The audience for this project is multi-tiered. The first and most important level is the Propulsion Research Center. They must be satisfied and enthusiastic about the animations and believe that they will help in their efforts to educate and gain support. When approved by the PRC, other possible audiences for the animations are NASA Headquarters, other scientists, the general public, or students in a classroom. Due to the wide range of audience members, the animations must be designed to appeal to all levels of interest and knowledge.

3D digital animation for the Propulsion Research Center

One of the Propulsion Research Center's (PRC) present goals is to gain approval and support to design and launch an orbiter powered by Fission Electric Propulsion within the decade (see Figure 1). Nuclear power is and always has been a controversial subject. There are many skeptics who believe only negative scenarios exist and that it is simply unsafe. The PRC team of scientists is trying to prove the opposite. The general public needs to be informed of the realities and benefits made possible by Fission Electric Propulsion (FEP).

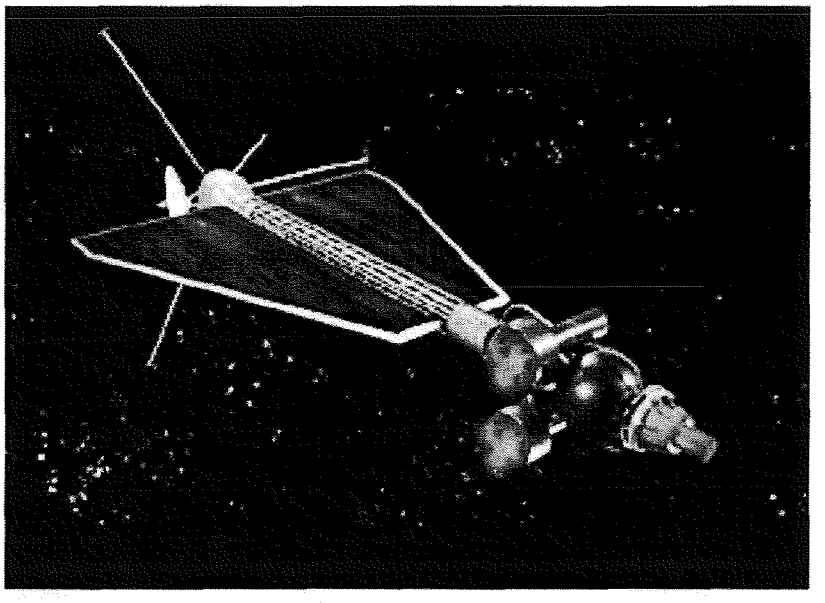

Figure 1: Proposed orbiter using Fission Electric Propulsion

So how do Fission Electric Propulsion and three-dimensional animation connect? Why should scientists use this visual technology to support their efforts? The audience does not have to read data- they watch it. With the help of animation, scientists can show how these systems work and a broad range of scenarios made possible by FEP. Audience members of any knowledge-level become involved and possibly more enthusiastic about the content of presentations. An astrophotographer, David Malin explains his take on using visuals to aid in the scientific education process. "Images can reach an audience which knows nothing about astronomy. Then a scientist can come along and explain what it means."[1] The same is true for many images played consecutively at an extremely fast rate, or simply— animation.

The propulsion research scientists will also be able to use these animations to literally point at objects on the proposed orbiter and describe them. The orbiter will include unique features, such as deployable radiators, presently being designed by the propulsion team. The proposed orbiter will be able to relay visual and scientific data from the smallest and least understood planet in the furthest reaches of this solar system, Pluto. The estimated time in orbit for this mission using FEP is 12-18 months. Previously proposed fly-by missions using chemical propulsion would offer one mere hour of data acquisition. Chemical systems simply cannot sustain the energy output needed to travel to deep space and remain for long periods of time.

Results

Content delivered to the Propulsion Research Center includes the completed model, fully textured, of a proposed orbiter using FEP. Textures for all planets, satellites and backgrounds were also created for placement in space scenes. Animations created during the course of this project include the orbiter sailing around the author's interpretation of Pluto and Charon (see figure 2) and into the untouched Kuiper Belt region. Other animations created include visuals of the orbiter leaving from earth, traveling through deep space passing the beautiful gas giants, and others showing the orbiter eventually encountering the last planet yet to be studied at close range: Pluto. Ten final animations have been completed to date.

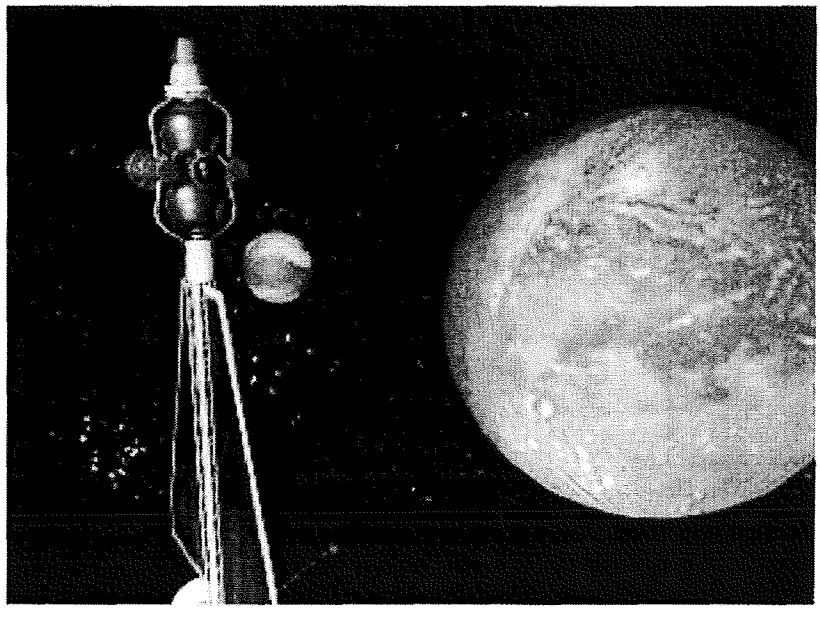

Figure 2: Orbiter leaving orbit of Charon

Future Applications for the PRC

The next logical step should be to create an animation showing how Fission Electric Propulsion will work on the latest system design. An FEP expert can educate the public on what this process is, how it works, and the benefits of using it while showing an animation to aid in his or her explanation. Future possible applications for animation in the Propulsion Research Center are endless. Any subject matter that is either difficult to explain or understand can always become clearer with supplementary animation.

Resources

This project required the use of many software tools. The main software chosen for the project was Aliaslwavefront Maya. This is a high-end 3D design and animation software used throughout the scientific and entertainment community. All modeling, lighting and animation were completed with Maya. Most textures were created in Adobe Photoshop and the remaining with Maya's procedural texturing. All post-production was completed in either Adobe Premiere or After Effects. This is the final step where animation, transitions, text, etc. are compiled into one file that can be viewed through a media player on the computer or transferred to videotape or CD.

Conclusion

"...The tools and techniques of three-dimensional computer imaging and animation are more than just a new bag of tricks. They have the power...to communicate, inspire and move the minds of people." [2] Through these animations, it is the intent of the author to help the Propulsion Research Center educate and inspire the public about the vast possibilities of space exploration using Fission Electric Propulsion systems.

Acknowledgements

The author would like to thank the entire team of scientists in the propulsion research area of the Marshall Space Flight Center's Transportation Directorate. George Schmidt, Mike Houts, Suman Chakrabarti, Melissa Vandyke, Kirk Sorensen, Sandy Kirkindall, Ivana Hrbud and Charles Schafer: thank you for the opportunity to create visual support for your cause.

References

[1] Hayden, T. (2001), "Exploration and Discovery: Shooting the Moon and Stars," U.S. News and World Report Special Issue.

[2] Kerlow, I. V. (1996), *The Art of Three Dimensional Imaging and Animation*, Van Nostrand Reinhold, pp. 12.

[3] Laybourne, K. (1998), *The Animation Book*, Three Rivers Media, pp.12.

[4] Masson, T. (1999), *CG 101: A computer Graphics Industry Reference*, New Riders, pp. 388-402.

2001

NASA/ASEE SUMMER FACULTY FELLOWSHIP PROGRAM

MARSHALL SPACE FLIGHT CENTER
THE UNIVERSITY OF ALABAMA AT HUNTSVILLE

SCIENCE OUTREACH AT NASA'S MARSHALL SPACE FLIGHT CENTER

Prepare By:	George Lebo
Academic Rank:	Associate Professor
Institution and Department:	The University of Florida Department of Astronomy
NASA/MSFC Directorate:	Science
MSFC Colleague	Ron Koczor

Background

At the end of World War II Duane Deming, an internationally known economist enunciated what later came to be called "Total Quality Management" (TQM). The basic thrust of this economic theory called for companies and governments to identify their customers and to do whatever was necessary to meet their demands and to keep them satisfied. It also called for companies to compete internally. That is, they were to build products that competed with their own so that they were always improving. Unfortunately most U.S. corporations failed to heed this advice. Consequently, the Japanese who actively sought Deming's advice and instituted it in their corporate planning, built an economy that outstripped that of the U.S. for the next three to four decades. Only after U.S. corporations reorganized and fashioned joint ventures which incorporated the tenets of TQM with their Japanese competitors did they start to catch up.

Other institutions such as the U.S. government and its agencies and schools face the same problem. While the power of the U.S. government is in no danger of being usurped, its agencies and schools face real problems which can be traced back to not heeding Deming's advice. For example, the public schools are facing real pressure from private schools and home school families because they are not meeting the needs of the general public. Likewise, NASA and other government agencies find themselves shortchanged in funding because they have failed to convince the general public that their missions are important. In an attempt to convince the general public that its science mission is both interesting and important, in 1998 the Science Directorate at NASA's Marshall Space Flight Center (MSFC) instituted a new outreach effort using the internet to reach the general public as well as the students. They have called it "Science@NASA.

History

In 1995 NASA's MSFC strayed from tradition by inviting several professors from the University of Florida's School of Journalism to become part of their Summer Faculty Fellowship Program (SFFP). One, Dr. Debbie Triese, was assigned to analyze how the Science Directorate could better communicate the excitement of its discoveries to the public. Among other things she suggested that they form a collaborative weekly meeting which they called the "Science Communications Roundtable" and that they institute an aggressive marketing effort using the Internet. Dr. John Horack retained Dr. Tony Phillips, a brilliant young astrophysicist and writer, of Bishop Webworks to help improve the content of their science website. The science communications effort was called Science@NASA and the URL of the website became science.nasa.gov. Beginning in 1998 Dr. Phillips applied a novel technique which he called "Search Engineering" to the website. As a consequence, the traffic to the site increased about one hundred fold during 1998 and 1999 and, at the end of 1999, the website was awarded a "Webby Award" as the best science site on the internet worldwide.

After an internal reorganization at MSFC in early 2000 Mr. Ron Koczor became the director of the Science@NASA effort. He increased the number of stories being published each week on the science.nasa.gov website and broadened its appeal by increasing the emphasis on other websites in the Science@NASA family: thursdaysclassroom.com, spaceweather.com, liftoff.msfc.nasa.gov, ciencia.nasa.gov, and kids.msfc.nasa.gov. The Thursday's Classroom site includes lesson plans crafted around the science of the latest stories on the home page; the Space Weather page is an up-to-date compilation of activity in the interplanetary medium, on the sun,

the aurorae, magnetic storms, etc; Liftoff is a page for students of high school age, Ciencia is a Spanish language site and NASA Kids is an entertaining page for students in the grade range K-8. The popularity of the suite of websites continues to increase and has attracted the attention of administrators at NASA Headquarters. In fact nearly half of the stories produced on the Science@NASA website are featured on the NASA Headquarters home page, nasa.gov. At the end of the year 2000 the website, science.nasa.gov again received international acclaim, winning the "Pirelli Award". The figure below supplied by Patrick Meyer at the MSFC shows the traffic to the primary site(s) as a function of time. The two spikes in November 1998 and again in November 1999 correspond to particularly active Leonid meteor showers. A major Leonid shower is anticipated again in November, 2001.

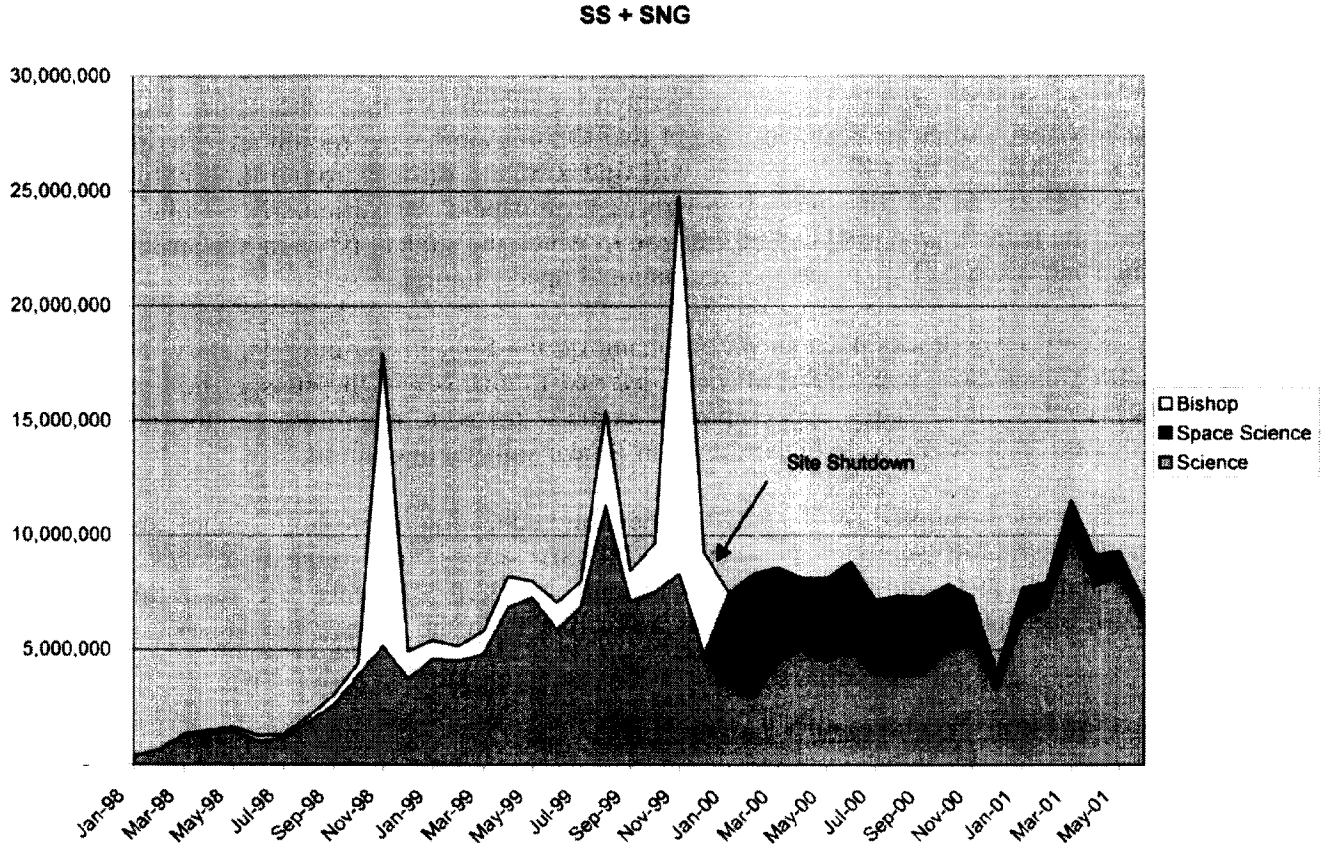

A hit is the download of a file and not an individual visitor. A given page may have as many as 10 files on it.

Current Features and Programs

When he took over management of the website, Mr. Koczor not only increased the number of active websites, he also introduced a number of new features on the primary science.nasa.gov site. As it now stands one can search the archive of approximately 400 stories from the home page. Also featured on the home page one can: subscribe to an email list which alerts you to the release of new stories and news events; link to Ciencia@NASA, a Spanish version of Science@NASA; subscribe to AvantGo, a specially edited version for wireless connections such

the Palm Pilot; download parts of the website onto your own home page; and link to the other webpages for kids, teachers and adults. Once you have linked to a story you will find links to: a streaming audio version of the story for those who are either sight impaired or who do not know how to read, an invitation to send the story to a friend by typing in their email address, and Thursday's Classroom.

Thursday's Classroom, now called Thursday's Classroom Corner, is featured with each story rather than once every several weeks as it had been earlier this year. While it currently doesn't contain the large number of lesson plans that the older, less frequent episodes did, the content is related to truly current events and has attracted even more interest. For the younger students there are reading exercises written for the second through fourth graders and for the fifth through eighth graders. Duane Hilton also prepares coloring exercises that are featured for the younger students in each episode.

The Liftoff site features stories that have been written for students of high school age. Not all of the Science@NASA stories are featured. About two to three stories per month are rewritten for the Liftoff site. Also on the Liftoff site one will find a wealth of background information that high school students can use for reference in writing term papers. A particularly popular aspect of the Liftoff site is the link to tracking information in which the student types in his/her zip code to learn when and where to look to see the International Space Station.

The Space Weather site tracks phenomena occurring on the Sun, in the interplanetary medium and the Earth's magnetosphere. Subscribers are alerted to changes in the sunspot number, the solar wind velocity, solar flares and eruptions, comets, meteors, asteroids and the aurorae. Traffic to this site is currently quite high as the Sun is near sunspot maximum.

The NASA Kids site is tailored for the entertainment and education of pre-high school students. It contains a rewrite of some of the Science@NASA stories and interesting background information and projects and games for the younger children. Parents also find this site interesting. It attracts a lot of traffic as it has a hot link from the NASA Headquarters home page.

Suggestions for Future Features on Science@NASA

Past experience has shown the "Science Communications" effort started by Dr. Debbie Treise and continued by Mr. Ron Koczor to be immensely successful. However, even though it has garnered support from NASA Headquarters, it is still relatively unknown – even at the MSFC. In no particular order I list below some suggestions to enlarge its scope:

1. **Continue efforts to activate the "Telescope Farm".** Dr. Phillips is currently working to put small but powerful telescopes on-line for use by Internet users. It should be activated as soon as possible.
2. **Add the feature "NASA Mysteries".** I have developed a side-bar feature for the website which challenges the reader to identify a NASA-related photo, movie, audio file, etc. I give hints and multiple choice questions on two levels of difficulty to help them find the answer.

3. **Re-institute "Search Engineering".** Early growth in the traffic to Science@NASA was due, in some part, to the application of a search engine sensitive redirection process called "Search Engineering. It should be reapplied as soon as possible.
4. **Expand Ciencia@NASA.** Every effort should be expended to acquire funding for Ciencia@NASA as the Spanish language website is truly unique and has a large and interested following.
5. **Create TV Quality Program Segments.** Jean Michelle Cousteau (Jacque Cousteau's son) recently challenged us to create high quality program segments for use on television. He volunteered to help. We could use people like Bill Nye "the Science Guy", Walter Cronkite et al. Successfully launching any such initiative would necessarily require a substantial amount of extra funding, hopefully from NASA HQ.
6. **Expand its Outreach to Other MSFC Directorates.** Science@NASA already produces stories for other directorates but they should increase their funding support. I have met with the Space Transportation Directorate's Dr. Row Rogacki, Mr. Steve Rodgers, and Ms. Rose Allen in an effort to get them to fund Science@NASA.
7. **Expand its Outreach to Other NASA Centers.** Science@NASA already produces stories covering efforts at other NASA Centers. I believe that we can expand our funding by continuing Mr. Koczor's efforts at NASA Headquarters. As Science@NASA increases in popularity with Headquarters and with the general public, I believe other centers, especially JPL, will want to join its effort.

My Other Summer Duties

I worked with Dr. George Khazanov, a plasma physicist in the National Space Science and Technology Center (NSSTC), to improve and update his website. I wish to thank him for his support this summer. I also gave a series of lectures explaining the Science@NASA website to about 120 secondary school teachers who attended a UAH summer workshop.

2001

NASA/ASEE SUMMER FACULTY FELLOWSHIP PROGRAM

MARSHALL SPACE FLIGHT CENTER
THE UNIVERSITY OF ALABAMA IN HUNTSVILLE

Finite Element Modeling of Deployment, and Foam Rigidization of Struts and Quarter Scale Shooting Star Experiment

Prepared By:	Larry Leigh Jr.
Academic Rank:	Masters of Science in Mechanical Engineering Student
Institution and Department:	South Dakota State University Mechanical Engineering Department
NASA/MSFC Directorate:	Engineering
MSFC Colleague:	Mike Tinker

Introduction

Inflated cylindrical struts constructed of kapton polyimide film and rigidized with foam have considerable practical application and potential for use as components of inflatable concentrator assemblies, antenna structures and space power systems. Because of their importance, it is of great interest to characterize the dynamic behavior of these components and structures both experimentally and analytically. It is very helpful to take a building-block approach to modeling and understanding inflatable assemblies by first investigating in detail the behavior of the components such as the struts. The foam material used for rigidization of such cylinders has varying modulus, which is a function of different factors, such as density of the foam. Thus, the primary motivation of the tests and analytical modeling efforts was to determine and understand the response of foam-rigidized cylinders for different densities, sizes, and construction methods.

In recent years, inflatable structures have been the subject of renewed interest for space applications such as communications antennae, solar thermal propulsion, and space solar power. A major advantage of using inflatable structures in space is that they are extremely lightweight. This makes inflatables a perfect match for solar thermal propulsion because of the low thrust levels available. An obvious second advantage is on-orbit deployability and subsequent space savings in launch configuration. A recent technology demonstrator flight for inflatable structures was the Inflatable Antenna Experiment (IAE) that was deployed on orbit from the Shuttle Orbiter. Although difficulty was encountered in the inflation/deployment phase, the flight was successful overall and provided valuable experience in the use of such structures (Ref 1).

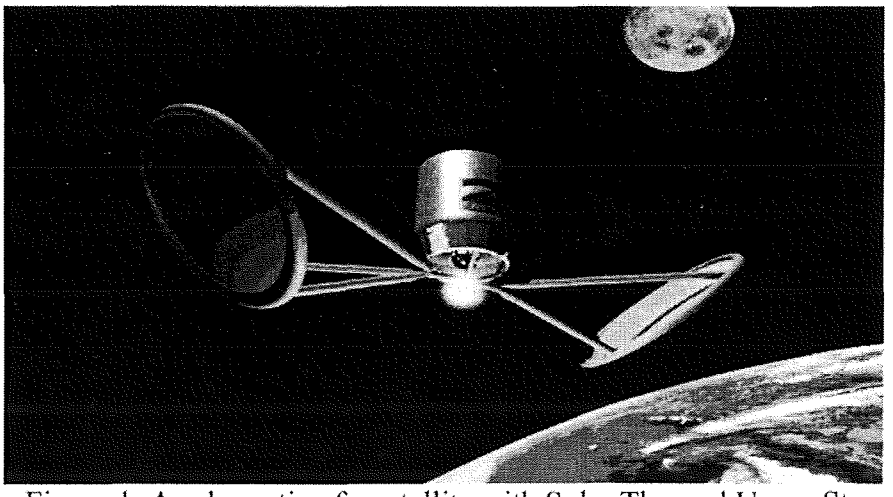

Figure 1. A schematic of a satellite with Solar Thermal Upper Stage

The Solar Orbital Transfer Vehicle (SOTV) is planned technology demonstrator flight for solar thermal propulsion. The basic concept behind solar thermal propulsion is to utilize sunlight or solar energy as a means of heating a working fluid (propellant) to provide thrust at increased specific impulse. Expanding the heated propellant through a nozzle produces thrust. No combustion occurs, and the thrust level is low. For this reason, solar thermal propulsive systems are mainly applicable for orbital transfer vehicles.

Another technology demonstration program for solar thermal propulsion is the Solar Thermal Upper Stage (STUS). The engine system envisioned for the STUS is designed to utilize hydrogen propellant to produce a thrust level of about 2 lbf. Two inflatable parabolic collectors

could be used that would be rotated and gimbaled for focusing sunlight into an absorber cavity (Fig. 1). The collectors would be inflated after separation of the upper stage from the launch vehicle.

In Fig. 2, the quarter scale foam rigidized inflatable solar concentrator finite element model (FEM) is shown that consists of a torus assembly supported by three struts. This concentrator is constructed of Kapton polyimide film, with epoxy as the primary adhesive for joints. In practical applications, the fresnel lens of such a concentrator assembly would focus sunlight into a collector near the fixed ends of the struts. Solar energy stored in the collector could be utilized to heat a propellant as described previously.

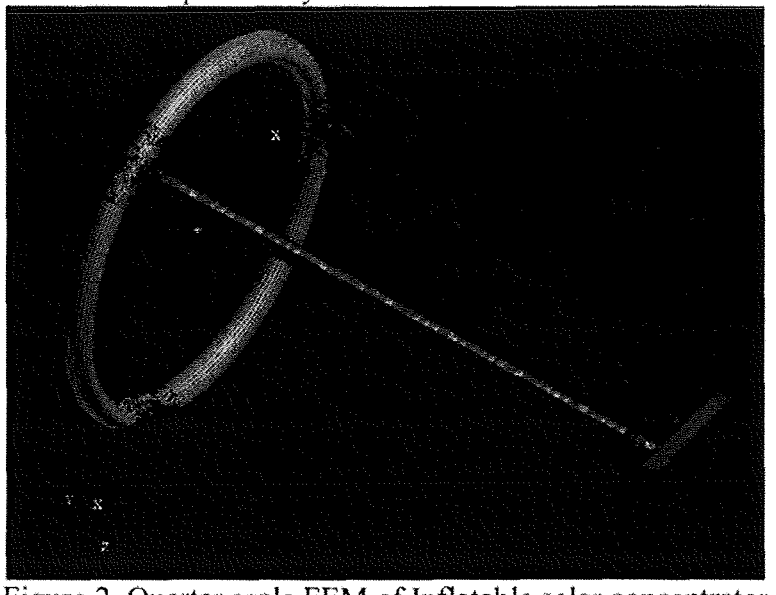

Figure 2. Quarter scale FEM of Inflatable solar concentrator

It can be seen from figure 2 that inflatable cylindrical struts and torus are critical components of structural assemblies. In view of this importance, structural dynamic and static behaviors of typical rigidized polyimide struts are investigated in this paper. The paper will focus on the finite element models that were used to model the behavior of the complete solar collector structure, and the results that they provided, as compared to test data.

Description of Problems

Rigidized Foam Struts

One problem that became apparent at a very early stage was trying to either determine the properties of the foam, or trying to find properties for the foam. The problem with trying to find properties for this foam was that it has very low-density. Properties for highly dense foam were available but not suitable for the foam that was used to rigidize our struts. Finally, after some research, it was found that most of the foam properties could be determined, if the composition of the foam was know, and it's density (Ref 2). The biggest piece of information that came out of this was that the elastic modulus followed the following equation, for low-density foam (below 4 Lb per cu ft). $E=573.5D^{1.1508}$

After this piece of information was determined, the modeling could begin, and there were many different struts that where modeled. One example of a strut modeled was a 6" diameter, 6' long foam filled strut. The foam density of this strut was 2 lb/ft^3. Based on this and the above equation, this gave us a modulus value of 1273 psi, and we had a Poisson's ratio of 0.30.

Another type of strut that was considered was annular foam filled tube. The reason for going this route, was simple, less weight, without hurting the over all strength of the structure to any great degree, because of the fact that very little strength is needed to support these structures in a zero gravity environment. The particular strut that was modeled had the following properties, length = 12", outside diameter = 3.5", inside diameter = 3", modulus = 1273 psi, density of 2 lb/ft^3, and a Poisson's ratio = 0.30.

Foam filled quarter scale Shooting Star

The next approach was to try and get a handle, on whether or not the properties of the foam we were using in the models really correlated with true results. No results could be found at the time, all this modeling began, but results for the quarter scale Shooting Star structure was at hand. So a FEM of the Shooting Star was constructed. The basic model had three struts of 1" diameter, and a length of 28", and these connected to a torus constructed of 1.5" diameter foam filled material, at 20" outside diameter. The three struts connected together at the top to a plate 6" X 6" X 1" (refer to figure 2).

Modeling of Deployment

Along with taking a look at the dynamics of the structures after they had already been inflated and rigidized, an effort was made to model the inflation process of these structures. The real effort was to see if this process could be modeled, and what it took to do such a model. The original process was to go ahead and "draw" the structures, in their deflated form. This ended up being an extremely difficult task. The first inflation model created (Fig 3) was a Z-Fold model, which was created by drawing an end cylindrical strut that flattened down to a fold after 3 inches then was folded back and forth on itself 10 times. This modeled during the inflation process showed how unstable the type of packaging was, so a new style of folding was created. This consisted of constructing the model of a strut, compacted down along the axial direction. The model in figure 3 shows a strut of 30 inches long and with a 3" diameter compressed down to 4".

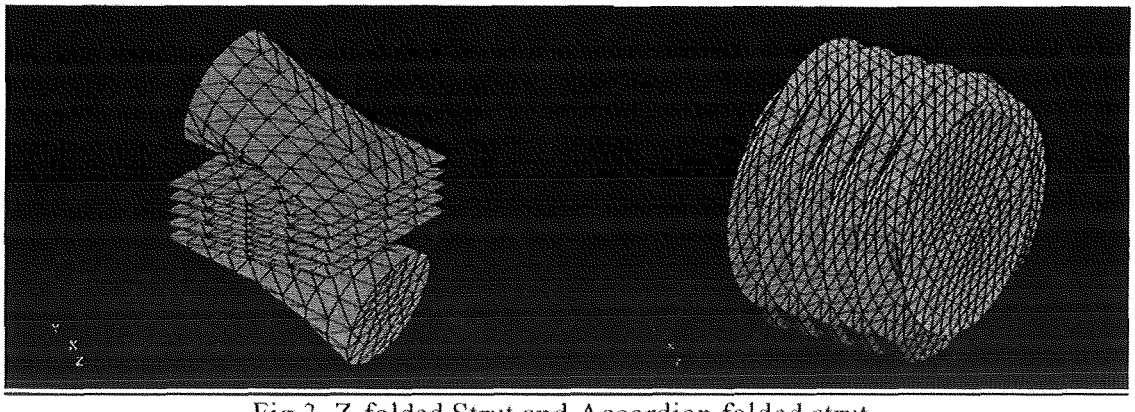

Fig 3. Z-folded Strut and Accordion folded strut.

Results

Rigidized Foam Struts

The result obtained for the rigidized struts will be compared to the results of current ongoing modal testing of struts, when the tests are complete.

Foam filled quarter scale Shooting Star

The results from a modal test of a quarter scale Shooting Star structure were compared to the FEM that was created, with very promising results. Table 1 shows the comparison of modal frequency from the test, with the results of the FEM model. Looking at the table it would seem like the results were almost dead on, but the most important detail is that the actual mode shapes were not compared, with the exception of the mode referred to as the flapping mode. Actual mode shapes where not available, and the only comparison that could be done was a comparison of mode shapes via a verbal description of what the test data were. But based on those descriptions the feeling is the model did a very good job of predicting the results. It's hoped that this data can be compared in a more analytical fashion at a later date. So with this it was assumed that the properties based on the findings in reference 2 where in fact a good way to come up with properties for this low-density foam.

Test data		FEM data		Notes
Frequency (Hz)		Frequency (Hz)		
0.28		0.27		
1.92		2.1024		
4.24		4.0066		Flapping mode
6.86		6.2109		
13.34		12.175		

Modeling of Deployment

The deployment modeling of the struts, at this time, did not lead to a lot of data to compare to existing results, but instead was an exercise to see if this process could indeed be done. Some of the things that were found was that by drawing the structure as it exists, in it's final inflated state, and then deflating the model and "folding" it, proved to be an easier way to deploy more complex structures. This approach required more computer time, to do the actual deflation process, but required a lot less cad time to draw, as compared to trying to draw the objects in an already deflated state. Other things learned were, what the ballpark of flow rates were, required to do the actual inflation, without actually popping the structure. As mentioned previously the Z-fold (unless under very low inflation rate) caused the struts to swing wildly until full inflation was achieved. When it came down to it just understanding the process required to make these simulation work, so that once the real tests are done and test articles are ready, a comparison could be done. Once the process is verified to actual small-scale prototypes, the process can simulate large structures that would be impractical or impossible to do on earth.

References

1. Main, J.A., Carlin, R.A., Garcia, E., Peterson, S.W., and Strauss, A.M., "Dynamic Analysis of Space-Based Inflated Beam Structures", Journal of the Acoustical Society of America, 97(2), pp. 1035-1045, Feb. 1995.

2. Bender, R. J., Handbook Of Foam, Lake Publishing Corporation, Libertyville, IL, 1965

2001

NASA/ASEE SUMMER FACULTY FELLOWSHIP PROGRAM

MARSHALL SPACE FLIGHT CENTER
THE UNIVERSITY OF ALABAMA IN HUNTSVILLE

THE SOLAR-SAIL LAUNCHED INTERSTELLAR PROBE : PRE-PERIHELION TRAJECTORIES AND APPLICATION OF HOLOGRAPHY

Prepared By:	Gregory L. Matloff
Academic Rank :	Lecturer
Institution and Department:	Pace University Chemistry and Physical Sciences
NASA / MSFC Directorate:	Transportation
MSFC Colleague:	Randy Baggett

Introduction

Design of missions beyond our solar system presents many challenges. Here, we consider certain aspects of the solar-sail launched interstellar probe (ISP), a spacecraft slated for launch in the 2010 time period that is planned to reach the heliopause, at 200 Astronomical Units (AU) from the Sun after a flight of about 20-years duration.

The baseline mission under consideration by NASA / JPL (Liewer et al. and Mewaldt and Liewer [5,8]) has a sail radius of 200 m, a science payload of 25 kg, a spacecraft areal mass thickness of about 2 grams per square meter and is accelerated out of the solar system at about 14 AU per year after performing a perihelion pass of about 0.25 AU. In current plans, the sail is to be dropped near Jupiter's orbit (5.2 AU from the Sun) on the outbound trajectory leg.

One aspect of this study is application of a realistic model of sail thermo-optics to sail kinematics that includes diffuse / specular reflectance and sail roughness. The effects of solar-wind degradation of sail material, based on recent measurements at the NASA / MSFC Space Environment Facility were incorporated in the kinematical model.

The interstellar-trajectory and kinematics model utilized was that of Dr. Giovanni Vulpetti [10]. After setting initial and final conditions for the spacecraft, trajectory was optimized using the provision of variable sail aspect angle. One initial conclusion of Vulpetti is the realization that there are two launch windows per year to achieve any selected interstellar cruise trajectory. One, the posigrade approach, has the sail aspect angle adjusted so that the sail's orbital energy increases and the sail's apogee approaches the orbit of Mars. Then, the aspect angle is altered and the sail "falls" towards its close perihelion. In the second retrograde approach, the sail reverses direction of the angular-momentum vector (**H**) at or near aphelion and then falls towards perihelion.

The second phase of the study included consideration of rainbow holography as a medium for a message plaque that would be carried aboard the ISP in the spirit of the message plaques aboard Pioneer 10 /11 and Voyager 1 /2. A prototype holographic message plaque was designed and created by artist C Bangs with the assistance of Ana Maria Nicholson and Dan Schweitzer of the Center for Holographic Arts in Long Island City, NY. The piece was framed by Simon Liu Inc. of Brooklyn, NY.

Concurrent to the creation of the prototype message plaque, we explored the potential of this medium to transmit large amounts of visual information to any extraterrestrial civilization that might detect and intercept ISP. It was also necessary to investigate possible degradation of holograms by the space environment. Assisting the author and C Bangs in this part of the effort were Pace University student Ryan Haggerty and the MSFC Space Environment team headed by Dr. David Edwarda and including Whitney Hubbs of MSFC and Tesia Stanaland of the University of Louisiana. We developed a new way of characterizing the optical quality of holograms and confirmed the conclusions of Golden et aL, Hotaling et al, and McKay and White [2, 3, 7] that holograms do not degrade rapidly in the space environment.

Advantages of Not Dropping the ISP Sail at Jupiter (5.2 AU)

Begin with Eq. (4.26) of Matloff [6]. Simplify this approximation by assuming that the pre-perihelion trajectory is parabolic and recalling that solar-system escape or parabolic velocity is much smaller than perihelion velocity (V_{init}). Then incorporate Eq. (4.27) of Matloff [6] to obtain the fractional velocity loss, K, if sail is dropped at 5.2 AU rather than retained to infinity (inf.):

$$K = (V_{1,inf} - V_{1,5.2au}) / V_{1,inf} = [(\eta_{sail} - 1)/(\eta_{sail})] V^2_{para,5.2au} / (2V_{init}^2), \quad (1)$$

where $V_{1,inf}$ = interstellar cruise velocity if sail is dropped at infinity, $V_{1,5.2au}$ = interstellar cruise velocity if sail is dropped at Jupiter's solar orbit (5.2 AU), $V_{para,5.2au}$ = solar – system escape velocity at 5.2 AU, and η_{sail} = sailcraft lightnes number. Sailcraft lightness number, the ratio of solar radiation-pressure force to gravitational force on the sailcraft, can be approximated using Eq. (4.19) of Matloff [6]: $\eta_{sail} = 0.000787(1+REF_{sail}) / \sigma_{s/c}$, where REF_{sail} = sail reflectivity and $\sigma_{s/c}$ = sailcraft areal mass thickness in MKS units.

Figure 1 presents parametric solutions of velocity loss factor K as a function of sailcraft lightness number and perihelion distance. Note that K increases for low-mass missions and high perihelion distances. Giovanni Vulpetti, using the software described below, has also found a kinematical advantage to retaining the sail beyond Jupiter.

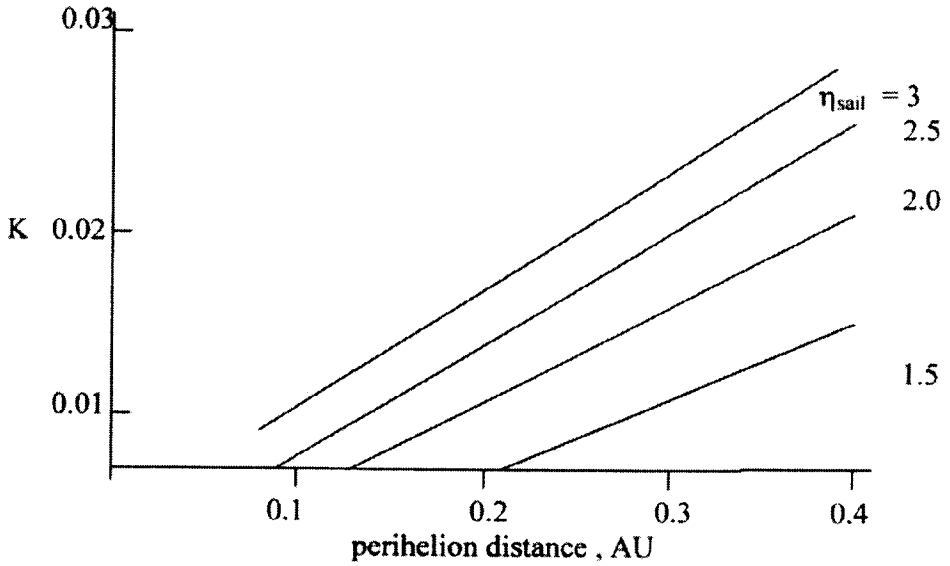

Fig. 1. Fractional Velocity Loss K as a function of perihelion and lightness number

There are non-propulsive sail applications that could be performed if the sail is retained. A properly shaped sail could function as an antenna. A more exciting application would be to form an electric circuit around the (disc) sail's outer edge, which would allow the sail to function as a magnetometer during the interstellar cruise.

Results of Trajectory Modeling

A total of 10 scenarios were investigated using the pre-perihelion trajectory optimization program. These are presented as Table 1.

Table 1. ISP Trajectory Scenarios, from G. Vulpetti's Computer Code
25 kg science payload, root-mean square Aluminum /Chromium sail roughness = 20 nm

	Scenario #									
	1	2	3	4	5	6	7	8	9	10
Inputs:										
Total s/c mass	250 kg		250 kg		350 kg		220 kg		210 kg	
s/c areal mass thickness	2 gram / meter^2				1 gm/m^2		2.2 gm/m^2		2.1 gm/m^2	
sail radius, meters	200	200	200	200	334	334	178	178	178	178
sail degradation status	on	off	off	on	off	on	off	on	off	on
Outputs :										
Aphelion, AU	1.826	1.809	1.116	1.159	1.099	1.099	2.13	2.64	1.94	2.12
Aphelion time, yr	0.723	0.716	0.274	0.259	0.201	0.200	0.931	1.283	0.806	0.922
Perihelion, AU	0.240	0.242	0.200	0.201	0.203	0.202	0.175	0.261	0.204	0.248
Peri. Velocity, AU/yr	14.60	14.67	18.61	18.58	19.03	19.17	17.16	13.41	15.89	14.18
Perihelion time, yr	1.404	1.384	0.581	0.583	0.496	0.496	1.776	2.470	1.543	1.773
Max. Peri. Sail Temp.,K	587	450	471	578	458	547	530	574	490	584
Time to 200 AU, yr	16.61	16.54	10.20	10.20	8.99	9.03	15.70	20.57	16.67	18.10
Interstellar vel, AU/yr	13.13	13.17	20.79	20.79	23.57	23.46	14.34	11.02	13.20	12.23

Notes: Solar wind sail degradation on means total solar wind fluence after 1 yr of 2 X10^{-4} Gwatts/m^2, 7 X 10^{-4} Gwatts/m^2 after two years. Maximum degradation after about 1.7 yr. All cases presented are for an H-reversal trajectory, launch in Oct. 2011. Direct (posigrade) launch also possible in June 2011. Maximum perihelion temperature is a function of time near perihelion, trajectory profile, and sailcraft attitude. Maximum permissible sail temperature for an Al/Cr sail is about 600 K, 60% of Al melting temperature. Sail is dropped at heliopause bow shock (about 200 AU).
Scenarios 7—10: hyperbolic excess at Earth/moon departure is about 1 km/sec. For other scenarios, it is 50-70 m/sec. The reason for 4 scenarios (1-4) at 2 gm/m^2 is the number of parameters optimized. Scenarios 1 & 2 are closest to JPL interstellar sailcraft.

Sail-reflectance degradation by the solar wind increases absorbation. Aphelion time and distance are increased by sail degradation. Perihelion distance is increased and perihelion velocity is decreased. Both perihelion time and maximum sail temperature at perihelion are increased by solar-wind sail degradation. As a consequence of lower sail reflectivity, solar-wind sail degradation decreases interstellar cruise velocity and increases the time required to reach 200 AU. These effects become noticeable for the more massive missions, where spacecraft areal mass thickness exceeds 2 grm/m^2. For scenarios 1-6, the Earth-departure hyperbolic excess velocity is less than 100 km/sec. In scenarios 7-10, it approaches 1 km/sec.

Holographic Message Plaques for Interstellar Probes

There are many advantages to storing the visual information for a comprehensive message plaque using the medium of rainbow holography. C Bangs prototype Holographic Message Plaque can be viewed in non-monochromatic, non-coherent light, although a laser is required to prepare it. See Caulfield [1], Kasper and Feller [4] , and Saxby [9] for details on the preparation of rainbow holograms. C Bangs' prototype message plaque consists of 6 holographic images superimposed upon an Apollo 16 phtograph of the full Earth. The piece ideally should be illuminated from a distance of 6 feet at an angle of 45 degrees above with a halogen light source. As the observer moves from left to right, he / she first notices a diagram showing our location in the galaxy and solar system. Next is a line drawing of a female figure holding the spacecraft payload for scale. The next image is the 3-dimensional sculpted female figure, followed by the sculpted male figure whose hand is raised in greeting. Next is the line drawing of the male figure. The final image presents the standard equation of solar sail acceleration.

To estimate the information capacity of a rainbow hologram, we use Dan Schweitzer's estimate that at least 30 separate images can be exposed on one holographic plate. Let's say that the dimensions of the plate are 35 X 46 centimeters, the approximate dimensions of Bangs' hologram. Since a rainbow hologram can store 3-dimensional reduced size images, assume that each stored (square) image has a dimension of 2-cm and is placed on one face of a cube. Each image stored on the hologram can accommodate 250 cubes or more than 1000 reduced-size images. Since 30 separate images can be exposed on one hologram, roughly 30,000 separate reduced-size images can be placed on one 35 X 46 cm hologram. If each of these is equivalent to one page of information, one properly designed rainbow hologram can hold the equivalent of 30,000 text pages. According to Dr. John Caulfield of Fisk University, a rainbow hologram can be as thin as a few microns.

The previously mentioned tests at the MSFC Space Environment Facility were performed by exposing commercial hologram samples supplied by Spectratek Technologies, Inc. in Los Angeles, CA to as much as 100 Mrad of simulated solar-wind radiation after the samples (each of dimension about 2 cm) were baked at 60 C to outgas impurities. One set of hologram-degradation data was generated by observing optical properties (absorption and emittance) of control and irradiated samples. We developed a new testing procedure in which control and irradiated holograms were scanned into a computer and were evaluated for image quality changes in three colors (red, green, and blue) using the hostogram option of Adobe Photoshop™. To the (6%) limit of experimental repeatability, no holographic-sample degradation was observed.

Conclusions

NASA should consider the kinematic and scientific advantages of not dropping the ISP sail at 5.2 AU. Solar-wind sail reflectivity degradation does not render the ISP mission infeasible, although it does result in closer perihelion passes, when analysis is performed using a realistic sail thermo-optics model. Rainbow holography may be a very useful medium for message plaques to be affixed to ISP and future interstellar probes. The

radiation resistance of holograms, their low mass and optical properties offer the possibility of other applications in space.

Acknowledgments

As well as thanking the people mentioned in the above text, the author is grateful to Dr. Robert Forward for suggesting rainbow holography to C Bangs. The author also appreciates the assistance of Randy Baggett, Melody Herrmann , Les Johnson, Edwin Reichmann and Shelia Nash-Stevenson of MSFC. He is also grateful for the assistance of Jeanelle Bland, Michelle Garrett, and Gerry Karr of University of Alabama at Huntsville. Literature searches would not have been possible without the assistance of the staff of the Redstone Scientific Information Service

References

[1] Caulfield, H. J., ed. (1979), *Handbook of Optical Holography*, Academic Press, NY.

[2]. Golden, J. P., Summers, G. P., and Carter, W. H. (1988), "Resistance of Holograms of Polaroid DMP128 Photopolymer to Ionizing Radiation ," *Optics Letters, 13*, 349-351.

[3] Hotaling, S. P., Manivannan, G., Changkakoti, R., and Lessard, R. A. (1993), "The Performance and Survivability of Dichromated Poly (Vinyl Alcohol) Holograms for Space Based Photonic Applications, Report AD-A270 974, RL-TR-93-131, Rome Laboratory, USAF Material Command.

[4] Kasper, J. E. and Feller, S. A (1987) ., The Complete Book of Holograms : How They Work and How to Make Them," John Wiley, NY.

[5] Liewer, P. C., Mewaldt, R. A., Ayon, J. A., Garner, C., Gavit, S. and Wallace, R. A. (2000), "Interstelar Probe using a Solar Sail : Conceptual Design and Technological Challenges," presented at Cospar Colloquiom (The Outer Heliosphere: the Next Frontier), Potsdam, Germany, July 24-28, 2000.

[6] Matloff, G. L. (2000), *Deep-Space Probes*, Springer-Praxis, Chichester, UK.

[7] McKay, A. and White, J. (1989), "Effects of Simulated Space Environment on Dichromated Galatin Holograms," *SPIE, 1044*, 269-276.

[8] Mewaldt, R. A. and Liewer, P. C. (2000), "An Interstellar Probe Mission to the Boundaries of the Heliopause and Nearby Interstellar Space," presented at Space 2000, Long Beach, CA, Sept. 19-21, 2000.

[9] Saxby, G., *Practical Holography*, Prentice-Hall, NY (1988).

[10] Vulpetti, G. and Scaglione, S., "The Aurora Project: estimation of the Optical Sail Parameters, *Acta Astronautica, 44*, 123-132 (1999). See cited references in this paper.

2001

NASA/ASEE Summer Faculty Fellowship Program

MARSHALL SPACE FLIGHT CENTER
THE UNIVERSITY OF ALABAMA IN HUNTSVILLE

THE KINETICS OF CRYSTALLIZATION OF COLLOIDS AND PROTEINS: A LIGHT SCATTERING STUDY

Prepared By:	Jim McClymer
Academic Rank:	Associate Professor
Institution and Department:	University of Maine Department of Physics and Astronomy
NASA/MSFC Directorate:	Biotechnology
MSFC Colleague:	Phil Segre

Introduction

Hard-sphere colloidal systems serve as model systems for aggregation, nucleation, crystallization and gelation as well as interesting systems in their own right. Similar colloidal systems have important technological uses such as in paints and pharmaceuticals. There is strong current interest in using colloidal systems to form photonic crystals. A number of colloidal experiments have flown on the space shuttle and a suite of experiments is currently active on the ISS.

A major scientific thrust of NASA's microgravity research is the crystallization of proteins for structural determination. The crystallization of proteins is a complicated process that requires a great deal of trial and error experimentation. In spite of a great deal of work, "better" protein crystals cannot always be grown in microgravity and conditions for crystallization are not well understood.

Crystallization of colloidal systems interacting as hard spheres and with an attractive potential induced by entropic forces have been studied in a series of static light scattering experiments. Additionally, aggregation of a protein as a function of pH has been studied using dynamic light scattering.

Colloidal Crystalization-Hard sphere interactions

The simplest possible interaction is that of a hard sphere: interactions occur only when spheres touch each other. At low volume fractions hard sphere particles interact infrequently and a "gas" of particles is formed. Static and dynamic light scattering experiments show the particles acting as freely diffusing particles with no interparticle structure. Further increasing the volume fraction results in interactions between the particles that are indicated by both a decreased diffusion constant and increased light scattering about a certain angle, resulting in a fluid peak. Increasing the volume fraction further, between 46 and 58%, results in the formation of colloidal crystals with FCC and random hexagonal closed pack structure. Microgravity studies indicate that the FCC structure is a result of the crystals settling out of solution. Further increase in volume fraction results in gel or glass formation.

For our experiments we used PMMA (polymethylmethacrylate) spherical particles interacting as hard spheres, with no attractive potential. These particles have a radius of 304 nm, a density of 1.22 gm/ml and an index of refraction of 1.52.

A PMMA colloidal sample at a volume fraction of approximately 54% was index matched in a solution of cycloheptyl bromide (CHB) and *cis*-decalin. At such high concentrations the sample would otherwise appear extremely turbid and we would be plagued with multiple scattering. The sample cannot also be density matched in this two-component system so that colloidal particles and crystals will sediment out. The sample is in a glass cylindrical vial that is placed in an ALV static and dynamic light scattering goniometer system. The vial is immersed in a toluene bath for index matching to minimize flair. Vigorous shaking melts any colloidal crystals initially present. The

sample is illuminated with diverging laser light (632.8 nm) from a 4x microscope objective placed so that the beam is approximately 1 cm in diameter at the sample location. The sample is rotated about its long axis at approximately 3.5 revolutions per minute (highest speed) as the colloidal crystal system is non-ergodic. The scattered light is detected at various angles using the ALV light detection optics, which is fed into an APD detector module and linked to a computer. The scattering angle (between 12 and 160 degrees), scattering angle step size (0.1degree minimum) and acquisition time (minimum 3 s) is set by the user.

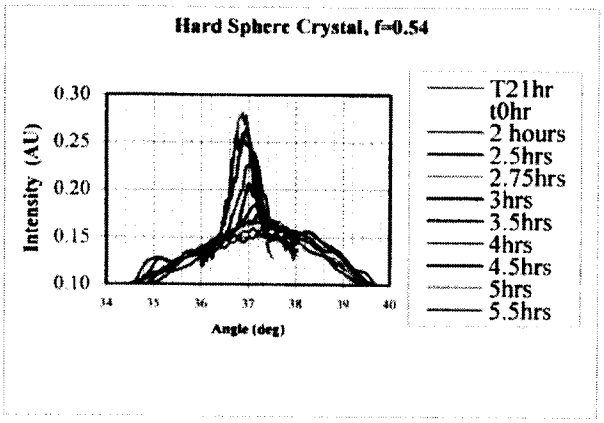

Figure 1: The growth of a Bragg scattering peak from the initial fluid peak.

Colloidal crystallization induced by entropic forces:

Under hard-sphere interactions, colloidal crystallization only occurs in a narrow concentration range. Adding an attractive potential should induce crystallization, or at least aggregation, at lower volume fractions. One surprising way to induce such attractive forces is to add smaller particles to the large colloidal particles. These small particles induce what are commonly known as "depletion or entropic forces". When no small particles are present, the large colloidal particles are able to diffuse throughout the sample, except into the excluded volume determined by the hard sphere interaction. When the numerous small particles are added they two can diffuse anywhere except into the excluded volume of the large spheres. When two large spheres touch, the excluded volume is *decreased*, resulting in an entropy *increase* for the small particles. This entropy increase lowers the free energy of the system when large particles come together, resulting in an attractive force. The interactions are characterized by the size ratio of the small particles to the large,>, and the number density of small particles. Instead of the number density, we use the more convenient measure of mass density, which we designate cp.

We studied 304 nm PMMA particles with added polystyrene particles at two size ratios, >= .13 and .21 at various small particle loadings and different volume fractions. These samples were index and density matched using a three-component mixture of CHB, decalin and tetralin.

The size of the colloidal particles is determined from static light scattering from a dilute solution. The resulting single particle form factor is used to calculate the mean size assuming a Gaussian profile, as indicated by dynamic light scattering measurements, and Mie scattering;

$P(q) \propto \int_{min}^{max} \frac{e^{\frac{-(r-\bar{r})^2}{2\sigma^2}}}{(qr)^6} * (\sin(qr) - qr * \cos(qr))^2 dr$ where q is the scattering wave number, $q = \frac{4\pi n}{\lambda} \sin(\theta/2)$. This equation provided an excellent fit to the data and indicated the particles have a mean radius of 304 nm with a standard deviation of 32nm .

Static light scattering results in peaks similar to Figure 1, but less sharp. The raw intensity data is corrected for the particle form factor, which for these low volume fraction samples is the intensity at early times before any structure forms. The area under the resulting curves is proportional to the fraction of sample converted from fluid to crystal. Figure 2 shows the fraction of crystal as a function of time in Brownian units (R^2/D_0)=.159 s. Both samples had a polymer loading of 1.11 mg/ml, >=.21 and a colloid volume fraction of 26%. The square data points represent a well density matched sample with a $\Delta\rho \approx 2 mg/cm^3$. The colloidal particles do not show any settling over the time scale of the experiment yet the crystals did slowly sediment during the experiment. The diamonds represent an improvement in density matching by approximately a factor of 5 as determined from sedimentation in a 1750g field using a concentration corrected form of the Stokes settling velocity. In both cases the crystal size remains nearly constant at about 5:m. Both samples also show $X(t) \propto t^3$ yet the induction time is significantly longer *with* sedimentation. An alternate possibility is that small differences in polymer concentration is responsible for this difference, as raising the polymer concentration to 1.22 mg/ml for the better density matched sample results in induction times approximately two orders of magnitude longer. Since the size of the crystals is constant the number of crystals also grows as t^3. This exponent indicates that nucleation is accelerated and that nucleation occurs in a burst, which suppresses crystal size. Such behavior is similar to hard sphere systems at high volume fractions. The small crystal size, about 8 particle diameters, is much smaller than the scaled crystal size (L=20) for hard spheres even at the glass transition (volume fraction of 58%).

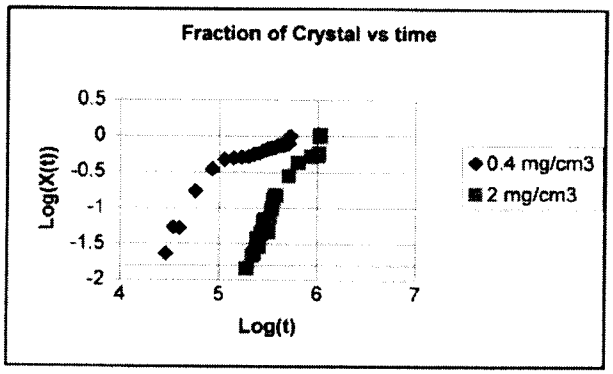

Figure 2. Log of fraction of crystal vs log of reduced time. See text for details.

A dynamic scattering study of the protein catalase in various pH buffer solutions is also ongoing. Both the monomer and aggregating proteins are easily seen. Figure 3 shows the size of aggregates as a function of time for a pH of 5.8. The solid line indicates diffusive ($t^{1/2}$) growth. Studies at longer times and at other pH values are ongoing.

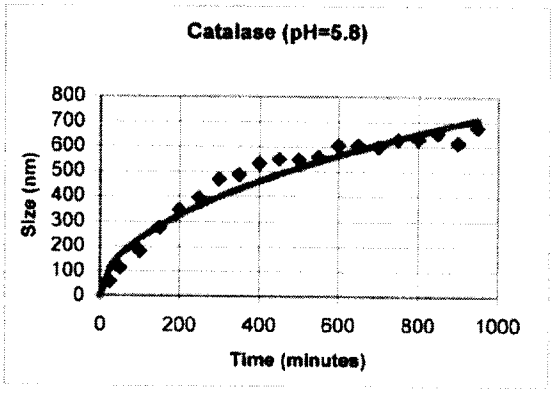

Figure 3. Size of catalase aggregates vs time.

Acknowledgments

I thank NASA and ASEE for supporting this program, the SFFP people who make us welcome and keep us in line and particularly Phil Segre for both his professional hospitality in sharing his lab and insights as well as his personal hospitality towards my family and me.

References

[1] Ilett, S.M., A. Orrock, W.C. Poon and P. N. Pusey (1995), "Phase Behavior of a model colloid-polymer mixture", Phys. Rev. E **51** 1344-1352.

Harland, J.L. and W. van Megan, (1997), "Crystallization kinetics of suspensions of hard colloidal sphere", Phys. Rev. E **55** 3054-3067.

Poon, W. and A. Donald (2001), "Soft condensed matter: where physics meets biology", Physics World May 33-38.

Pusey, P.N., W. van Megen, P. Bartlett, B.J. Ackerson, J.G. Rarity and S.M. Underwood (1989), "Structure of crystals of hard colloidal spheres", Phys. Rev. Lett. **63** 2753-2756.

Rosenbaum, D., P.C. Zamora and C.F. Zukoski (1996), "Phase behavior of small attractive colloidal particles", Phys. Rev. Lett. **76** 150-153.

Zhu, J., M. Li, R. Rogers, W. Meyer, R.H. Ottewill, STS-73 Space Shuttle Crew, W.B. Russel and P.M. Chaiken (1997), "Crystallization of hard-sphere colloids in microgravity" Nature **387** 883-885.

2001

NASA/ASEE SUMMER FACULTY FELLOWSHIP PROGRAM

MARSHALL SPACE FLIGHT CENTER
THE UNIVERSITY OF ALABAMA IN HUNTSVILLE

RDBMS DESIGN AND DEPLOYMENT METHODOLOGIES:
Using the ACTIVE approach for database project implementation

Report Not Available

Prepared By:	John V. Mohlenkamp
Academic Rank:	Adjunct Professor
Institution and Department:	Volunteer State College Computer Information Systems/Business Department
NASA/MSFC Directorate:	Shuttle Integration Office, MP71
MSFC Colleague:	Mr. Steven Glover

2001

NASA/ASEE SUMMER FACULTY FELLOWSHIP PROGRAM

MARSHALL SPACE FLIGHT CENTER
THE UNIVERITY OF ALABAMA IN HUNTSVILLE

AN OVERVIEW OF PRA WITH APPLICATIONS TO AEROSPACE SYSTEMS

Prepared by:	Sharon E. Navard
Academic Rank:	Assistant Professor
Institution and Department:	The College of New Jersey Department of Mathematics & Statistics
NASA/MSFC Program:	2nd Generation Reusable Launch Vehicle (RLV)
MSFC Colleague:	Fayssal M. Safie

Introduction

Probabilistic Risk Assessment (PRA) is a systematic process for evaluating the probabilities and consequences of undesirable events that can occur in a process or system along with providing a measure of the uncertainty associated with these probability estimates. In the past it was looked at with suspicion by many at NASA, perhaps because of bad experiences with unsuccessful quantitative methods during the Apollo era, but since the *Challenger* accident NASA has mandated that it be used, and it has been very successful. With NASA's new "faster, better, cheaper" philosophy, it is vital that a tool be in place that can help to achieve these goals in the reliability area. This paper describes the history of PRA, gives examples of its aerospace applications to date, and gives suggestions for how it can be used in the future, both for space shuttle upgrades and for totally new technologies such as the 2nd Generation Reusable Launch Vehicle.

A Brief History of PRA

NASA's earliest attempts at probabilistic risk assessment were somewhat less than successful. Early Apollo program estimates of the probability of a successful moon landing mission were as low as 0.2, whereas the observed success rate was 6 out of 7, or 0.86 (Stamatelatos, 2001). Perhaps for this reason NASA basically abandoned quantitative techniques and switched to qualitative methods, most notably the Failure Mode and Effects Analyses (FMEA) with their associated Critical Items List (CIL). The FMEA/CIL process was so successful that it became entrenched within NASA, and quantitative methods were not seriously used even during the development of the space shuttle and into the early eighties.

In the meantime, during the sixties and seventies, the nuclear power industry began to have an increasingly bad public relations problem. For a discussion of the reasons why, see Fragola (1996). The industry designed safety into the plants using a qualitative method called design basis accidents (DBAs) which was similar to NASA's FMEA/CIL process, but it provided no estimate of the probability of a plant accident. Responding to public pressure to quantify the reliability of nuclear power plants, a quantitative study was conducted and published in Rasmussen (1975). This study, which was based on a combination of fault trees and event trees, was the basis of modern probabilistic risk analysis.

Prior to the *Challenger* accident in January 1986, no significant quantitative risk assessments were done at NASA. Quantitative estimates based on expert judgment were used, giving extremely optimistic failure probabilities on the order of one in several thousand. In the aftermath of *Challenger* when NASA's risk pronouncements were studied in fine detail, both the Rogers and Slay Commissions (Rogers et. al. 1986 and Slay et. al. 1988) strongly recommended that NASA improve its quantitative approach. Two proof-of-concept studies were commissioned, one on the Shuttle Auxiliary Power System and the other on the Main Propulsion Pressurization Subsystem (Slay, et al., 1987, and Plistiras et al., 1988).

Not surprisingly, the first comprehensive PRA of the shuttle was conducted for the launch of the *Galileo* probe (Buchbinder, 1989). The spacecraft contained plutonium fuel, and there was great concern that a launch accident would be an environmental disaster. This study, which covered

only the ascent phase, estimated failure probabilities between 1/350 and 1/18, with a mean of 1/78. The *Galileo* study was updated in 1993 (SAIC 1993), and a PRA of the shuttle in all phases was completed in 1995 (Fragola, et. al., 1995). Finally, in 1996 NASA conducted its own study to develop a shuttle PRA model. The model developed uses the Quantitative Risk Assessment System (QRAS) which was developed by NASA. For a more complete history of PRA, see Fragola (1996) and Paté-Cornell & Dillon (2000).

The PRA Process

Probabilistic Risk Assessment is a process that follows a quantitative approach to determine the risk of a top undesirable event and the associated uncertainty arising from inherent causes. It is not a specific technique, but rather an adaptable process that can be modified to fit different situations. However, there are some characteristics that all PRAs have in common. It requires the identification of the top level events of interest and the initiating events that can lead to them. The system must be diagrammed, usually using event trees and fault trees, and probabilities must be determined as well as their associated uncertainties.

A PRA begins by defining the goals and objectives of the study, and the end states of interest. For example, the goal might be to determine what can go wrong, how likely these things are to happen, how uncertain the results are, and how the risks can be mitigated. For the 2nd Generation RLV, end states of interest might be Loss of Mission, Loss of Vehicle, or Loss of Crew.

Once the objectives are known, it is necessary to determine the initiating event categories. To do this, it is necessary for the analyst to be extremely familiar with the system. A preferred tool for identifying the initiating events is a Master Logic Diagram (MLD). The MLD is a top-down procedure that begins with an end state and works down, with each lower step identifying events that are necessary but not sufficient to produce the higher level event. The top levels are functional failures, and the lower levels are subsystem and component levels. The hierarchy continues until groups of initiating event categories are determined that have the same system response.

For each initiating event identified, accident scenarios are then developed. This can be done with event sequence diagrams (ESDs) or event trees. The ESD is an inductive bottom-up procedure that begins with an initiating event and is developed by asking the question "What could happen next?" It ends with the top level events. The ESD can be quantified by converting it to an event tree, where each node of the tree has an associated probability of occurrence.

The compliment to the event tree is the fault tree, which is a deductive top-down procedure. It begins with the end state and works down by asking the question "How could this event have happened?" Fault trees and event trees are used together to delineate the necessary and sufficient conditions for the top level events to occur. They form the basis of the Boolean algebraic equations used to find the probabilities and uncertainties of the top events (Maggio, 1996).

Before reliabilities and uncertainties can be calculated, it is necessary to collect data. The data can be from previous operational experience, test data, handbooks, design engineering, or expert experience. Often the data is scarce, and when this is the case, Bayesian analysis is applied. The

final reliabilities are usually expressed as the 5th, 50th, and 95th percentiles of the Bayesian posterior distributions.

Aerospace Applications of PRA

Several aerospace applications of PRA have already been mentioned—in particular, the proof-of concept studies, the *Galileo* study and its update, the PRA of the space shuttle in all phases, and the development of QRAS. There have been other aerospace applications. PRA has been used to assess the safety of wind tunnels at both Langley Research Center and Ames Research Center. An external maintenance study of Space Station *Freedom* led to design changes to reduce the predicted maintenance load (Fisher and Price et. al., 1990). The *Cassini* probe also had a nuclear fuel, but it was launched on a Titan IV rocket and hence required its own PRA prior to launch (PRC, 1994). QRAS is now being used successfully to evaluate upgrades of space shuttle propulsion elements (Safie, 1998).

PRA can also be a useful tool for a system that is in the design phase. It is being used in the Space Exploration Initiative Program (Buchbinder, 1993) as well as in the Space Launch Initiative, or 2nd Generation Reusable Launch Vehicle Program. The 2nd Gen program is trying to apply PRA in selective areas such as engines and ground operations, where enough design information is available to decompose the system. More in-depth PRA studies will be developed at later design phases of the program.

While at first glance it might seem that it is impossible to do PRA in the earliest design stages of a new system, it can actually be quite useful. The very process of systematically outlining the design options and studying the tradeoffs can be enlightening to design engineers. New design options might actually be revealed in this process, while others may be shown to be unfeasible. It can help prevent the program from being sidetracked by interesting sounding alternatives that clearly will not work.

Conclusions

PRA has proven to be a valuable tool for NASA in designing safe and reliable vehicles. Besides providing a method to calculate the reliability of an existing system, it also provides a means of doing sensitivity analyses and trade studies. The QRAS model is making it easier to do these analyses for space shuttle upgrades. Finally, the PRA thought process can be useful in helping to choose the best designs and systems for the 2nd Generation Reusable Launch Vehicle.

References

Buchbinder, Ben, "Independent Assessment of Shuttle Accident Scenario Probabilities for the Galileo Mission", Vol. 1, April 1989, NASA/HQ Code QS, Washington, D.C., 20546.

Buchbinder, Ben, "Risk Management for the Space Exploration Initiative", AIAA 93-0377, 31st Aerospace Sciences Meeting & Exhibit, Reno, Nevada, January 11-14, 1993.

Fisher, W. F., and Price, C. R., et. al., "External Maintenance Task Team", Final Report, Vol. 1, NASA/JSC, Houston, Texas, 1990.

Fragola, Joseph R., et. al., "Probabilistic Risk Assessment of the Space Shuttle: A study of the Potential of Losing the Vehicle During Nominal Operation Volume 1: Final Report", SAIC, February 28, 1995.

Fragola, Joseph R., "Space Shuttle Program Risk Management", 1996 Proceedings of the Annual Reliability and Maintainability Symposium, pp. 133-142.

Maggio, Gaspare, "Space Shuttle Probabilistic Risk Assessment: Methodology & Application", 1996 Proceedings of the Annual Reliability and Maintainability Symposium, pp. 121-132.

Paté-Cornell, Elisabeth, and Dillon, Robin, "Probabilistic Risk Analysis for the NASA Space Shuttle: A Brief History and Current Work", submitted to *Reliability Engineering and System Safety*, April 2000.

Plistiras, J. et. al., "Space Shuttle Main Propulsion Pressurization System Probabilistic Risk Assessment," Final Report, Lockheed Corp., Palo Alto, CA, 1988.

PRC, "Analysis Methodology Report: Titan IV *Cassini* RTG Safety Databook: Final", submitted to Martin Marietta Space Launch Systems, September 16, 1994.

Rasmussen, Norman C., "Reactor Safety Study—An Assessment of Accident Risks in U.S. Commercial Nuclear Power Plants", WASH-1400, U.S. Nuclear Regulatory Commission, October 1975.

Rogers, W. et. al., "Report of the Presidential Commission on the Space Shuttle *Challenger* Accident", Washington, D.C., 1986. (See especially II-F, "Personal Observations of Reliability of Shuttle, Feynman, R.)

Safie, Fayssal M., "An Overview of Quantitative Risk Assessment of Space Shuttle Propulsion Elements", PSAM4 Probabilistic Safety Assessment and Management, 1998.

SAIC, "Probabilistic Risk Assessment of the Space Shuttle Phase 1: Space Shuttle Catastrophic Failure Frequency Final Report", 1995.

Slay, et. al., "Space Shuttle Risk Assessment Proof-of-Concept Study, Auxiliary Power Unit and Hydraulic Power Unit Analysis Report," McDonnell Douglas Corp., December 18, 1987.

Slay et. al., "Post-*Challenger* Evaluation of Space Shuttle Risk Assessment and Management", National Research Council Report, National Academy of Sciences, National Academy Press, Washington, D.C., January 1988.

Stamatelatos, Michael, et. al., "Probabilistic Risk Assessment Workshop for NASA Managers and Practitioners," presented at NASA Headquarters, April 2-5, 2001.

Multi-Zone Liquid Thrust Chamber Performance Code with Domain Decomposition for Parallel Processing

MARSHALL SPACE FLIGHT CENTER
THE UNIVERSITY OF ALABAMA IN HUNTSVILLE

Prepared by: Homayun K. Navaz

Academic Rank: Associate Professor

Institution and Department: Kettering University, Flint, Michigan
Department of Mechanical Engineering

NASA/MSFC:

Office: Space Transportation Directorate
Division: Applied Fluid Dynamics Analysis

MSFC Colleagues: Mr. Robert Garcia

Report Prepared for: TD64

Date: August 8, 2001

INTRODUCTION

Computational Fluid Dynamics (CFD) has considerably evolved in the last decade. There are many computer programs that can perform computations on viscous internal or external flows with chemical reactions. CFD has become a commonly used tool in the design and analysis of gas turbines, ramjet combustors, turbo-machinery, inlet ducts, rocket engines, jet interaction, missile, and ramjet nozzles. One of the problems of interest to NASA has always been the performance prediction for rocket and air-breathing engines. Due to the complexity of flow in these engines it is necessary to resolve the flowfield into a fine mesh to capture quantities like turbulence and heat transfer. However, calculation on a high-resolution grid is associated with a prohibitively increasing computational time that can downgrade the value of the CFD for practical engineering calculations.

The Liquid Thrust Chamber Performance (LTCP)[1] code was developed for NASA/MSFC to perform liquid rocket engine performance calculations. This code is a 2D/axisymmetric full Navier-Stokes (NS) solver with fully coupled finite rate chemistry and Eulerian treatment of liquid fuel and/or oxidizer droplets. One of the advantages of this code has been the resemblance of its input file to the JANNAF standard TDK[2] code, and its automatic grid generation for JANNAF defined combustion chamber wall geometry. These options minimize the learning effort for TDK users, and make the code a good candidate for performing engineering calculations. Although the LTCP code was developed for liquid rocket engines, it is a general-purpose code and has been used for solving many engineering problems[3-6]. However, the single zone formulation of the LTCP has limited the code to be applicable to problems with complex geometry. Furthermore, the computational time becomes prohibitively large for high-resolution problems with chemistry, two-equation turbulence model, and two-phase flow.

To overcome these limitations, the LTCP code is rewritten to include the multi-zone capability with domain decomposition that makes it suitable for parallel processing, i.e., enabling the code to run every zone or sub-domain on a separate processor. This can reduce the run time by a factor of 6 to 8, depending on the problem.

MULTI-ZONE LTCP

Multi-zone geometry is basically user-defined where different zones share all, or part of a face referred to as a "zonal boundary". Figure 1 shows an example of user-defined multi-zone geometry. This type of division is sometimes necessary for proper definition of the geometry, but not necessarily for parallel processing due to an unbalanced computational load.

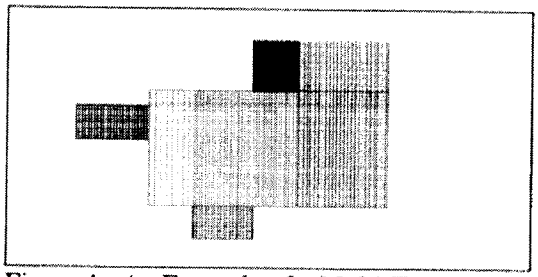

Figure 1. An Example of a Multi-Zone Domain

DOMAIN DECOMPOSITION

Domain decomposition is defined as dividing one, or more zones into smaller sections called sub-domain or sub-zone. For instance, in Figure-1 each zone can be further divided into smaller sub-domains. The load balancing is more feasible with this option for parallel processing. Figure 2 demonstrates a typical domain decomposition for the SSME. The domain is decomposed into 2,3, and 4 zones.

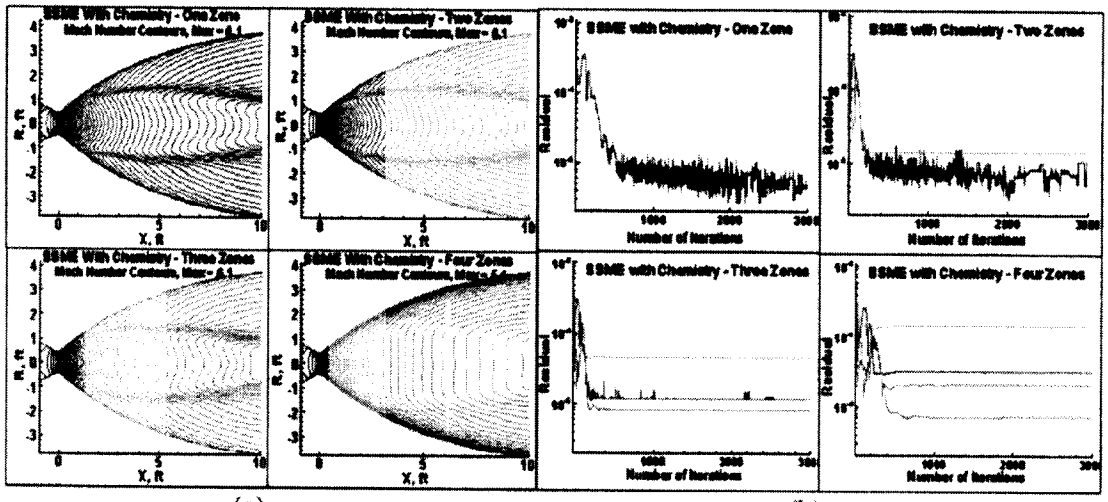

(a) (b)

Figure 2. Mach Number Contours for the Space Shuttle Main Engine (SSME) with Domain Decomposition for 1, 2, 3, and 4 Horizontally Divided Sub-Domains with their Corresponding Residual

Table 1 – ISP for SSME with Domain Decomposition

Case	Zones	Run Time*, hr, min, sec			ISP
Ideal Gas	1	0	18	58	424
	2	0	20	1	423
	3	0	22	55	421
	4	0	24	10	404
	4**	-	-	-	422
	9	0	25	36	421
Chemistry	1	1	19	51	457
	2	1	24	16	456.7
	3	1	30	5	454
	4	1	38	25	430
	9	1	46	10	454

*Run time is measured on NEXUS

** 4-Zone problem with grid sequencing

It can be seen from Table 1 that the ISP is significantly reduced for 4-zone or sub-domain problem. It was found that this was due to the fact that the zonal boundary between zone 1 and 2 (starting from the left) was exactly at the attachment point after the nozzle throat. There is a compression shock originating from this point and having a zonal boundary at this point will

smear the results. Therefore, care must be taken in the domain decomposition strategy by properly locating the zonal boundaries. Furthermore, when grid sequencing option was utilized the accuracy of the solution increased, mainly because of the increased resolution at the attachment point only and the fact that the zonal boundary was not at the attachment point. This is demonstrated for the 4-zone ideal gas case in Table 1. It is seen that after doubling the number of points in axial direction, the ISP prediction has improved considerably. It can also be seen that although the run time has somewhat increased for a multi-domain case, the convergence is achieved in fewer number of iterations, therefore, reducing the computational time. This is because of the fact that each zone has its own time and length scale. We can postulate that if the domain is vertically divided into sub-domains, the near wall region can be separated from the rest of the flow. This will make the convergence faster for the low-speed region. Figure 3 demonstrates that this could result in faster convergence for low speed flow without using pre-conditioning. This idea should be examined further in the future.

Figure 3 also depicts the accuracy of the zonal boundary conditions implemented in the LTCP code, i.e., the information across a zonal boundary is continuous. This has not been accomplished in many CFD codes.

It should be mentioned that for domain decomposition and/or grid sequencing, all the zonal boundary conditions and communication protocol is automatically set in the code and the user is expected to only define the baseline case and boundary conditions.

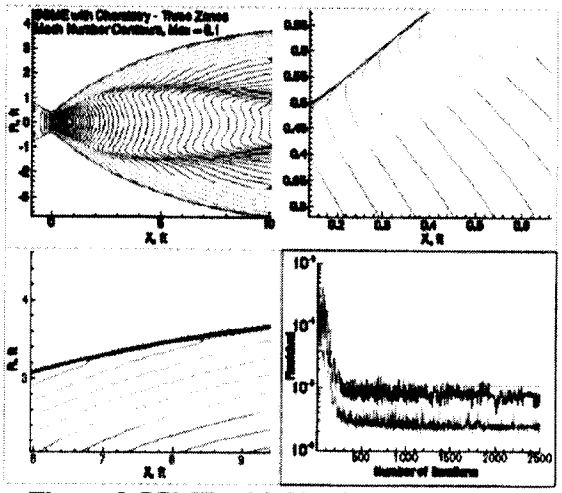

Figure 3 SSME with Vertical Zoning

PARALLEL PROCESSING

OpenMP[7] is a parallel programming model that is adopted here. This model is suitable for shared memory and distributed shared memory multiprocessors pioneered by Silicon Graphics, Inc. (SGI). OpenMP takes a directive-based approach for supporting parallelism. It consists of a set of directives that are embedded within the LTCP code. It works in conjunction with the Fortran compiler. A set of compiler directives describes the parallelism in the code along with a supporting library of subroutines. The present architecture of the LTCP code will allow for each zone or sub-domain to be processed on a separate processor. This requires a load balancing for maximum efficiency, i.e., same grid resolution for each zone or sub-domain is recommended.

Table 2 is the actual run time for the SSME nozzle contour. It can be seen that the run time compared to a one-zone problem is reduced by a factor of 7.

CONCLUSION

The added capabilities to the Liquid Thrust Chamber Performance (LTCP) code have made this application program suitable for handling more sophisticated geometries. The OpenMP directives have enabled the code to run faster by a factor of 7, thereby, making the code more of an engineering tool. It was shown that by increasing the number of zones the accuracy of the solution is compromised. However, the necessary accuracy can be achieved by increasing the grid resolution by the added grid sequencing option in the LTCP code.

Table 2 – Run Time on a 61 X 61 Mesh – SSME Ideal Gas – Single or Multiple Processors

Number of Zones/domains	Run Time* – One Processor Min: Sec	Run Time - # of Processors = # of Zones	MP/SP** MP/SP (1 Zone)
1	36: 51.95	36: 51.95	1.00 – 1.00
2	36: 58.76	18: 39.37	1.98 – 1.97
4	38: 24.55	9: 59.50	3.88 – 3.69
9	42: 50.07	5: 49.83	7.35 – 6.32
12	44: 36.12	5: 04.98	8.77 – 7.25

* Run time is for Silicon Graphics with R-10000 chip at 194 MHz

** Multiple Processors/Single Processor

REFERENCES

1. Navaz, H. K., and A. D. Dang, The Development of the Liquid Thrust Chamber Performance (LTCP) Code for Turbulent Two-Phase Flow Combustion of Dense Sprays, Final Report Prepared for NASA/MSFC, Contract No. NAS8-38798, January 1994.
2. Nickerson, G. R., Dang, A. L., Coats, D. E., Dunn, S. S., and H. K. Navaz, Two Dimensional Kinetic (TDK) Nozzle Performance Program, Final Report prepared for NASA/MSFC, Contract No. NAS8-36863, September, 1988.
3. Navaz, H. K., and S. S. Dunn, A Computer Model for Gun Barrel Flow Analysis: The Gun Tube Boundary Layer Code (GTBL), Final Report prepared for Software and Engineering Associates (SEA), Inc., June 1999.
4. Navaz, H. K., and R. M. Berg, "Formulation of Navier-Stokes Equations for Moving Grid and Boundary," *Journal of Propulsion and Power*, Vol. 15, No. 1, January – February 1999.
5. Navaz, H. K., and R. M. Berg, "Numerical Treatment of Multi-Phase Flow Equations with Chemistry and Stiff Source Terms," *J. of Aerospace Science and Technology*, Vol. 2, No. 3, pp. 219 – 229, March – April, 1998.
6. Navaz, H. K., Henderson, B. S., and R. M. Berg, "A New Approach to Teaching Undergraduate Thermal/Fluid Sciences - Courses in Applied Computational Fluid Dynamics and Compressible Flow," To be appeared in *the International Journal of Mechanical Engineering Education*, September 2001.
7. Chandra, R. Dagum, L., Kohr, D., Maydan, D., McDonald, J., and R. Menon, Parallel Programming in OpenMP, Academic Press, 2001.

2001

NASA/ASEE SUMMER FACULTY FELLOWSHIP PROGRAM

MARSHALL SPACE FLIGHT CENTER
THE UNIVERSITY OF ALABAMA IN HUNTSVILLE

IMAGE DIS-INTEGRATION FOR IMPROVED PLASMASPHERE VISUALIZATION

Prepared by:	Timothy S. Newman, Ph.D.
Academic Rank:	Associate Professor
Affiliation:	Department of Computer Science University of Alabama in Huntsville
NASA/MSFC Organization:	SD50
MSFC Colleague:	Dr. Paul Craven

IMAGE DIS-INTEGRATION FOR IMPROVED PLASMASPHERE VISUALIZATION

Introduction

Traditionally, study of the plasmasphere has involved terrestrial observation of local characteristics. Global modeling of the plasmasphere in such an observation regime made use of an ensemble of (sparse) local measurements. Recently, sensors aboard the IMAGE (Imager for Magnetopause-to-Aurora Global Exploration) satellite (in particular, the EUV (Extreme Ultra Violet) Imager) have created the potential for truly global study of the plasmasphere.

IMAGE was launched in spring of 2000 in an orbit with apogee altitude 7.2 R_E (Earth radii) and perigee altitude 1000 km [3]. IMAGE's EUV sensor allows an external view of the distribution of cold plasma in the plasmasphere to be acquired. EUV is designed to image light emission at 30.4 nm [3], which is the emission wavelength of the He^+ ion in the presence of solar radiation. He^+ makes up approximately 15-20% of the plasma in the plasmasphere [3], thus imaging of He^+ enables determination of plasma distribution. The EUV instrument provides a 90^o by 84^o field of view which is imaged as an equally spaced 150x140 pixel array on a spherical imaging surface. The EUV produces an image approximately every 10 minutes when the sensor is operating. An example EUV image is shown in Fig. 1.

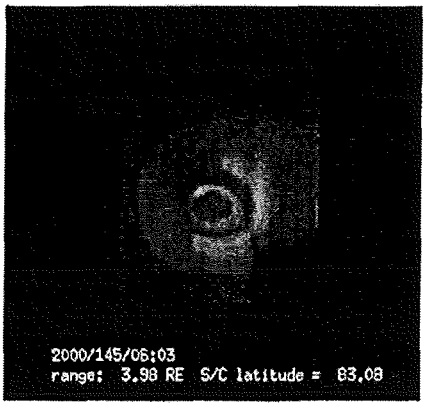

Figure 1: Example EUV Image

Since EUV images contain line-of-sight integrations of plasma distributions, they do not directly express equatorial plane density (which would enable comparison of observed plasma distributions with predictions from models). Furthermore, the plasma density at any point in 3-space is not known. The goal of our work was development of a technique that can enable plasma density to be determined throughout three-space.

Approach

Our approach to creation of a 3-space representation of the plasma distribution involves dis-integrating the EUV lines of sight to form a volumetric map of plasma densities. Eventually, we will exploit physical models of plasma distribution, although we expect to exploit only conservative (i.e., "safe") assumptions. To date, we have not implemented the physical model exploitation mechanisms, although certain mechanisms have been considered and formulated.

Previously, a few methods have been suggested for deconvolving integrated line-of-sight satellite imagery in a way that allows equatorial plane plasma distributions—but not the distribution in 3-space—to be determined. One class of approaches seeks to avoid search for the best deconvolution (which is computationally challenging) and instead seeks a plausible equatorial plane distribution that could give rise to the image. For example, Taylor [4] has outlined a genetic-algorithm based approach for equatorial plane plasma distribution determination from EUV images. Roelof and Skinner [2] have presented a suite of techniques that use variations on gradient descent to find a plausible equatorial plane plasma distribution. Their approach was designed for neutral atom (ENA) data, although they only had simulated ENA data available for

testing. Roelof and Skinner suggested their approach may also be adaptable to EUV data. Roelof and Skinner's paper [2] also presented the Edge Algorithm method for finding the extent of the plasmapause in the equatorial plane by projecting an envelope of edges from the EUV image into the equatorial plane. The Edge Algorithm has been applied to simulated EUV images. One disadvantage of the Edge Algorithm is that the plasma's distribution is not determined. In addition, there may be positional inaccuracy in edge locations.

Our approach is novel in that it will enable determination of the plasma distribution throughout 3-space. The approach is motivated from approaches in tomographic reconstruction, especially limited-angle reconstructions. Traditional Radon-transform-based reconstruction is not applicable to the EUV image inversion problem, however, due to the very limited number of view angles at which the plasmasphere is sampled by EUV.

Figure 2 illustrates one step of a typical tomographic imaging procedure. In the figure, a radiation source emits "lines" of particles that are attenuated as they pass through a subject object causing a pattern of response on a detector array opposite the emitter(s). In contrast, for an EUV image, the lines of sight are cone-shaped and collected from a single viewpoint. An illustration of a portion of two lines of sight is shown in Fig. 3. In the figure, two rays, P_1 and P_2, pass through many grid cells. The intensity V observed at the pixel associated with a ray contains the integrated sum of samplings from the cells the ray intersected. For example, the intensity $V(P_1)$ of pixel P_1 is shown in the formula at the bottom of the figure.

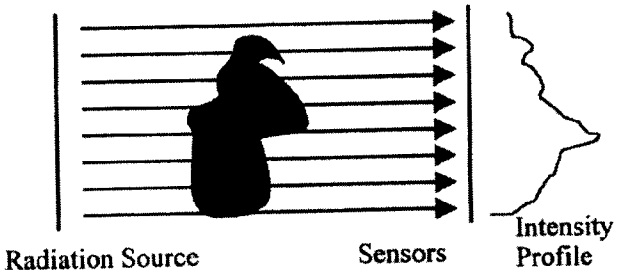

Figure 2. One step of a tomographic imaging procedure

The plasma distribution in each cell in 3-space can be determined by singular value decomposition (SVD) if the cell sizes are formulated such that adjacent rays do not sample equal sub-volumes of the same sequence of cells and if each cell (for which the plasma distribution is desired) is sampled along at least one line of sight. Care must also be taken to avoid formulation of a problem which is too under-constrained. (I.e., the number of cells for which the plasma distribution is desired should be less than the number of rays that sample the plasmasphere. In addition, cell cross-sections must be larger than line (beam) of sight cross-sections.)

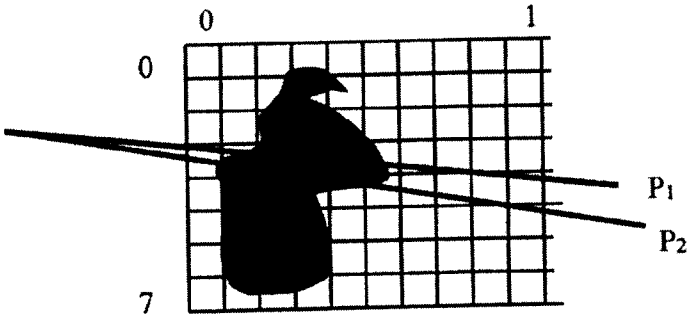

$$V(P_1) = a_1V_{20} + a_2V_{21} + a_3V_{32} + \cdots + a_{10}V_{10,2}$$

Figure 3. Illustration of two lines of sight in EUV

Thus, the first step of our approach is to build the 3D grid. We have conducted several experiments that have guided our determination of an appropriate grid size and placement.

These experiments included development of a greedy algorithm that appears to demonstrate that it is always possible, considering EUV positional geometries, to arrange the grid in a manner that no two adjacent beams sample the same sequence of cells.

We have also considered the impact of the Earth's shadow and ionospheric plasma on the images, however we have not yet included those factors in the physical implementation of our approach. Our calculations indicate that the highest-resolution volume likely to be resolvable, considering these factors, will be of size 68 x 62 x 34 (i.e., of approximate resolution 0.47 R_E).

The second step of our approach is to trace the lines of sight through the volume. Each line of sight can be considered to be a pyramidal-shaped beam that originates at the focal point and passes through a square pixel on a spherical imaging surface. As each beam is traced, a record of the cells it intersects is built and the volume of each cell-beam intersection is recorded. Currently, the intersection volume is approximated. (The approximation assumes that, for a given beam at a given slice, each intersected cell is equally sampled by the beam.) As time allows, we will correct our method to use the actual sub-volume. The sub-volume within each slice can be calculated using the general polyhedral volume formulation. In particular, we have used the general polyhedra volume formulation of Goldman [1] which expresses the volume V as a function of the surface areas of the polyhedron's faces:

$$V = \frac{1}{3}\left|\sum_j \left(Q_j \bullet N_j \, Area(S_j)\right)\right|$$

where N_j is the outward pointing normal of a face S_j and Q_j is one point on S_j.

The records of intersected cells are used to construct a system of equations where the vector of unknowns contains the plasma distributions in the cells and the matrix of coefficients are the sub-volumes of the cells. The image pixel values form the vector of right-hand side quantities. The system is solved using SVD (singular value decomposition) code (from *Numerical Recipes*).

Results

Simulated results are shown in Figs. 4 and 5. In Fig. 4, the left image shows a 150x140 EUV image, the middle image shows a possible equatorial plane plasma distribution for the image, and the right image shows a filtered (sharpened) version of the equatorial plane distribution. The rightmost image is the type of output we anticipate being able to provide from our approach. In Fig. 5, the left image shows one cross-section in 3-space of plasma distribution in the plasmasphere. The right image in Fig. 5 displays a 3D rendering of isosurfaces at two isothresholds on the plasma distribution in 3-space.

The approach has been applied to two small images (i.e., 15x14 sampled versions of 150x140 EUV images) and to one larger image (i.e., a 75x70 sampled version of an EUV image). Volumes can be constructed from small images in, on average, about 2 seconds on a Pentium III/833. The larger image required 14 hours of wall clock time on a 1.7 GHz Pentium IV. Over 95% of the total processing time involved computation of the SVD. A side view of an isosurface extracted from the computed plasma distribution in 3-space for the larger image is shown in Fig. 6. Additional experimentation is needed to determine a more optimal cell size and placement

and to consider the effects of arithmetic precision on computations; the image dis-integration approach involves applying SVD to a large, sparse matrix that is nearly singular.

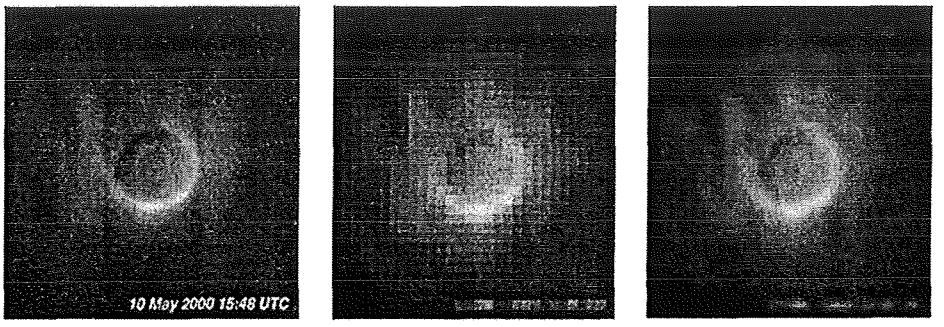

Figure 4. EUV image, simulated equatorial distribution of plasma, and sharpened equatorial plane plasma distribution

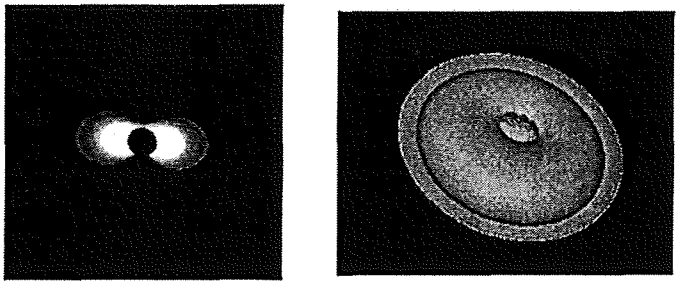

Figure 5. Cross-section of plasma distribution, dipole field model (left) and nested isosurfaces of plasma distribution (right)

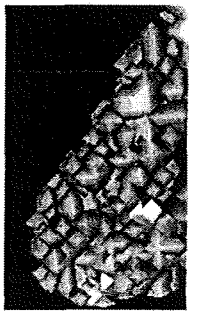

Figure 6. Isosurface extracted from computed 3-space distribution of plasma

Conclusion

A new method for determining plasma distribution in 3-space about the Earth from a single satellite image has been presented.

References

[1] Ronald N. Goldman, "Area of Planar Polygons and Volume of Polyhedra," *Graphics Gems II*, edited by J. Arvo, Academic Press: New York, 1991, pp. 170-171.

[2] Edmund C. Roelof and Andrew J. Skinner, "Extraction of Ion Distributions From Magnetospheric ENA and EUV Images," *Space Science Reviews* 91:437-459, 2000.

[3] B. R. Sandel, A. L. Broadfoot, C. C. Curtis, R. A. King, T. C. Stone, R. H. Hill, J. Chen, O. H. W. Siegmund, R. Raffanti, D. D. Allred, R. S. Turley, and D. L. Gallagher, "The Extreme Ultraviolet Imager Investigation for the Image Mission," *Space Science Reviews* 91: 197-242, 2000.

[4] J. Taylor, personal conversation, July 2001.

2001

NASA/ASEE SUMMER FACULTY FELLOWSHIP PROGRAM

MARSHALL SPACE FLIGHT CENTER
THE UNIVERSITY OF ALABAMA IN HUNTSVILLE

Crystallization And X-Ray Analysis Of Canavalin Mutants

Report Not Available

Prepared By:	Joseph D. Ng
Academic Rank:	Assistant Professor
Institution and Department:	University of Alabama in Huntsville Laboratory for Structural Biology
NASA/MSFC Directorate:	SD 48 - Biophysics
MSFC Colleague:	Marc Pusey

2001

NASA/ASEE SUMMER FACULTY FELLOWSHIP PROGRAM

MARSHALL SACE FLIGHT CENTER
THE UNIVERSITY OF ALABAMA AT HUNTSVILLE

EXPERIMENTAL VALIDATION OF A NEURO-FUZZY APPROACH TO PHASING THE SIBOA SEGMENTED MIRROR TESTBED

Prepared By:	Philip D. Olivier, Ph.D., P.E.
Academic Rank:	Professor
Institution and Department:	Mercer University Electrical and Computer Engineering Department
NASA/MSFC Directorate:	Science
MSFC Colleague:	Edward E. (Sandy) Montgomery, IV

Introduction

NASA is preparing to launch the Next Generation Space Telescope (NGST). This telescope will be larger than the Hubble Space Telescope, be launched on an Atlas missile rather than the Space Shuttle, have a segmented primary mirror, and be placed in a higher orbit. All these differences pose significant challenges. This effort addresses the challenge of aligning the segments of the primary mirror during the initial deployment. The segments need to piston values aligned to within one tenth of a wavelength. The present study considers using a neuro-fuzzy model of the Fraunhoffer diffraction theory. The intention of the current study was to experimentally verify the algorithm derived earlier. The experimental study was to be performed on the SIBOA test bed. Unfortunately the hardware/software for SIBOA was not ready by the end of the study period. We did succeed in capturing several images of two stacked segments with various relative phases. These images can be used to calibrate the algorithm for future implementation.

This effort is a continuation of prior work [1]. The basic effort involves developing a closed loop control algorithm to phase a segmented mirror test bed (SIBOA) [4]. The control algorithm is based on a neuro-fuzzy model of SIBOA and incorporates nonlinear observers built from observer banks. This effort involves implementing the algorithm on the SIBOA test bed.

Algorithm

Image Quality: Sharpness vs. Masked-Intensity

One change in the algorithm is the replacement of the masked-intensity with the sharpness (see equation 1) as the measure of image quality. Two factors motivated the change. The first factor is that ***sharpness*** is a standard quantity, [3]

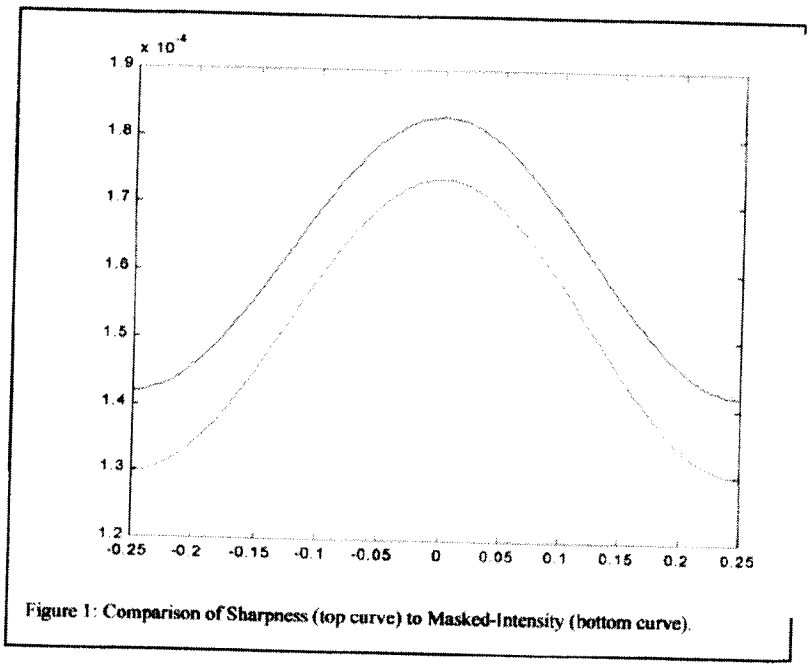

Figure 1: Comparison of Sharpness (top curve) to Masked-Intensity (bottom curve).

$$S = \int [I(x,y)]^2 dxdy / S_{\max} \qquad (1)$$

The second factor is that it is more robust since it does not require having the image precisely centered. Figure 1 provides a plot comparing these two measures of image quality. As can be seen from this figure, the two measures are qualitatively the same, and quantitatively very similar. This curve was produced by assuming that segments 1, 2, 4, and 6 were illuminated and letting the piston of segment 2 move from $-.25\lambda$ to $.25\lambda$.

Model Accuracy

The accuracy of the model is verified by comparing the sharpness computed from the Frauhnhoffer model to that computed by the fuzzy logic model. The plots are shown in Figure 2.

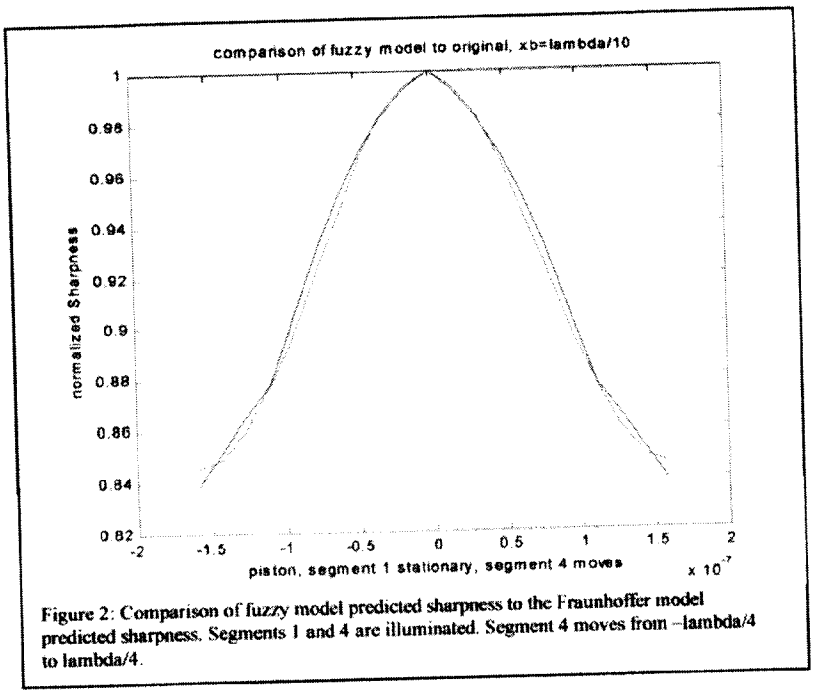

Figure 2: Comparison of fuzzy model predicted sharpness to the Fraunhoffer model predicted sharpness. Segments 1 and 4 are illuminated. Segment 4 moves from –lambda/4 to lambda/4.

Observability

From the point of view of state-space control theory, the model of segmented mirror telescopes with rigid mirrors and without edge sensors is

$$p_{n+1} = Ap_n + Bdp_n$$
$$y_n = f(p_n) \qquad (2)$$
$$A = B = I$$

where y_n is the vector of measurements that are extracted from the intensity distribution produced by the segmented mirrors, and I denotes the identity matrix. The y_n could be the entire image, i.e. one piece of information for each pixel. Alternatively, the y_n could be some data extracted from the image, in the case of this study, we use the image sharpness, the x and y centroids and perhaps higher order image moments. With A=I this system is observable only if the function f(p) is invertible. Hence to observe 6 piston values requires 6 independent outputs. This situation would be different if the "A" matrix were not the identity matrix. Including piston adjustments that are based on the relative piston values of other segments would cause the "A" matrix to deviate from the identity matrix, thereby, potentially, allowing the system to be observable with fewer measurements using a traditional linearized Luenerberger observer. However, if the system is unobservable, we need f(p) to be invertible. In this case we need to solve for the piston value, p, using some numerical technique such as Newton-Raphson. In this study the function f(p) that is comes from the Fraunhoffer diffraction theory is replaced by an approximation that is constructed from fuzzy logic.

SIBOA

SIBOA is an acronym for *Systematic Image Based Optical Alignment*. It is a ground based test bed that will allow evaluation of various phasing and alignment algorithms. SIBOA consists of 7 rigid mirrors; one in the middle that is assumed to be stationary and which is surrounded by 6 movable mirrors, a helium-neon laser ($\lambda \approx 638nm$), a digital camera and associated optics.

Enclosure: An enclosure was built to shield SIBOA from air currents and ambient light. The enclosure, which rests on the floor, is constructed from angle irons and 4 by 8 sheets of black foam core. This appears to solve the problems due to air currents and ambient light.

Simulation Results

The phasing algorithm was verified by simulation. Figure 3 shows typical simulation results. The initial piston value was $p_0 = -1.433*10^{-6}[0\ 0\ 0\ 1\ 0\ 0\ 0]$m. The horizontal lines indicate +/- 0.1 λ. The curve at the top of the graph is normalized sharpness multiplied by 10^{-7}. The remaining two curves are the actual piston values (the smooth curve) and the estimated piston values (the more jagged curve). The jaggedness of the right third of the estimated piston curve results from the estimated piston values moving from one region to another, whereas the actual piston values stay in the same region. The simulation is stopped when the sharpness decreases. The final piston value is

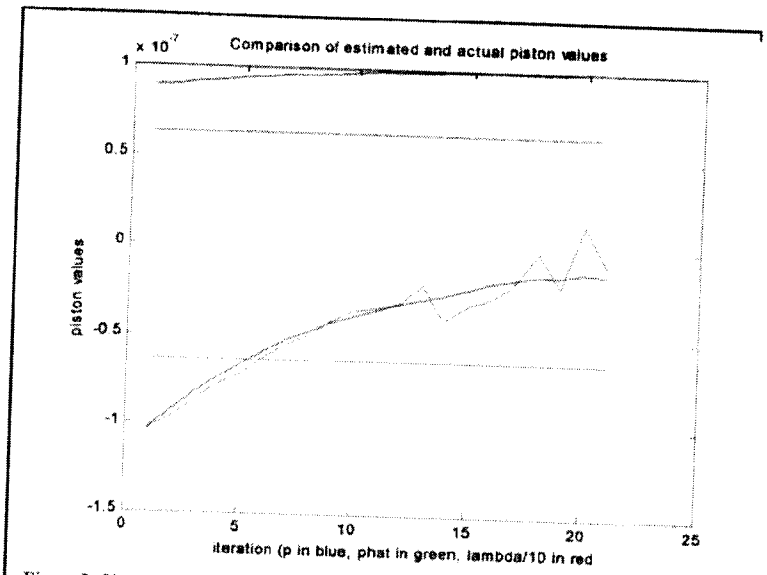

Figure 3. Simulation results.

$$p_f = [0\ 0\ 0\ -.0217\ 0\ 0\ 0]\,\lambda,$$

whereas the best piston occurred one iteration earlier and is

$$p_{opt} = [0\ 0\ 0\ -.0194\ 0\ 0\ 0]\,\lambda.$$

The algorithm stops when any of three conditions occur, a) the normalized sharpness exceeds .999 (1 is the theoretical maximum); b) there were 50 iterations; c) the sharpness is reduced from its previous value after 2 or more iterations. The logic behind option a) is that the system is aligned as well as possible. Option b) was put in to avoid infinite loops. Option c) was installed when it was noticed that when the piston values became small, the estimators jumped from region to region (one region for each estimator in the observer bank), and this erratic behavior was evidence of a well-aligned system.

Experiment

Camera Initialization: The camera has four settings that affect the experiment: 1) shutter speed; 2) gain; 3) V_{HI}; and 4) V_{LOW}. Failure to set these correctly will result in underutilization of the cameras dynamic range and consequent poor phasing. The last three are associated with a amplifier stage. Solid state amplifiers typically have low and high reference voltages that determine where the amplifier saturates and hence is no longer linear. With this in mind: V_{LOW} needs to be set just above the noise level to zero out the noise; V_{HI} needs to be set high enough to avoid amplifier saturation; the gain needs to be set to the maximum value that avoids camera saturation. The camera is a 10bit CCD camera, this means that the intensity levels range from 0 to 1023. The camera has a "shutter speed" which is really an "integration time". This speed can be set to avoid camera saturation. By judiciously setting the "shutter speed", the "gain" and the

voltage references it is possible to optimally use the cameras dynamic range. The maximum intensity that occurs when all the images are stacked and phased is n^2 times the maximum intensity due to the image from a single mirror. To avoid saturation, the maximum intensity of the image due to a single mirror should be $1023/n^2$. The gain and shutter speed should be set achieve this. (See [2]). When the maximum intensity of the mirrors is not identical, then the maximum intensity of the stacked and phased apertures is

$$I_{max} = \left(\sqrt{I_1} + \cdots + \sqrt{I_n}\right)^2 \tag{3}$$

Once the camera has been initialized, the maximum intensity that will occur needs to be noted and is used in the algorithm (it will be close to 1023).

In this experiment, as in the real implementation of this algorithm, the initial piston values are unknown, and unknowable. The

Conclusions

This study demonstrates that segmented mirror systems can be phased using approximate fuzzy models. The experimental work needs to continue to include more moving mirrors. We did succeed in generating a series of images that incorporate the real world imperfections that are inevitable. These images will help fine tune the algorithm until a full experimental validation can be performed.

Acknowledgments

The author gratefully acknowledges and thanks NASA/MSFC/SOMTC for its hospitality. Special thanks go to Sandy Montgomery, Glenn Zeiders and John Rakoczy for their technical help and support. In addition the author would like to thank Witt Brantley, Mike Stalcup, and Roy Young for stimulating conversations. Finally thanks go to Rita McDole for her help and support.

References

1. Olivier, P. D. (2000), Neuro-Fuzzy Phasing of the SIBOA segmented mirror test bed, report.
2. Partridge, James D. (2001),
3. Tyson, R. K. (1998), *Principles of Adaptive Optics*, Academic Press, San Diego.
4. Zeiders, G. W., Diffraction Effects with Segmented Apertures, Proc. SPIE Vol. 3356, p. 799-809.

Glossary

A segmented aperture is said to be ***phased*** if all segments are aligned to within a tenth of a wavelength.

A segmented aperture is said to be ***stacked*** if the images due to each sub aperture are all centered on the same point.

2001

NASA/ASEE FACULTY FELLOWSHIP PROGRAM

MARSHALL SPACE FLIGHT CENTER
THE UNIVERSITY OF ALABAMA

MONITORING OF STRUCTURAL INTEGRITY OF COMPOSITE STRUCTURES BY EMBEDDED OPTICAL FIBER SENSORS

Prepared By:	Albert J. Osei
Academic Rank:	Associate Professor
Institution and Department:	Oakwood College Mathematics and Physics Department
NASA/MSFC Directorate:	Science
MSFC Colleague:	Joseph Grant

Introduction

Real time monitoring of the mechanical integrity and stresses on key aerospace composite structures like aircraft wings, walls of pressure vessels and fuel tanks or any other structurally extended components and panels as in space telescopes is very important to NASA. Future military and commercial aircraft as well as NASA space systems such as Space Based Radar and International Space Station will incorporate a monitoring system to sense any degradation to the structure. In the extreme flight conditions of an aerospace vehicle it might be desirable to measure the strain every ten centimeters and thus fully map out the strain field of a composite component. A series of missions and vehicle health management requirements call for these measurements. At the moment thousands of people support a few vehicle launches per year. This number can be significantly reduced by implementing intelligent vehicles with integral nervous systems (smart structures). This would require maintenance to be performed only as needed. Military and commercial aircrafts have an equally compelling case. Maintenance yearly costs are currently reaching astronomical heights. Monitoring techniques are therefore required that allow for maintenance to be performed only when needed. This would allow improved safety by insuring that necessary tasks are performed while reducing costs by eliminating procedures that are costly and not needed.

The advantages fiber optical sensors have over conventional electro-mechanical systems like strain gauges have been widely extolled in the research literature. These advantages include their small size, low weight, immunity to electrical resistance, corrosion resistance, compatibility with composite materials and process conditions, and multiplexing capabilities. One fiber optic device which is suitable for distributed sensing is the fiber Bragg grating (FBG).

Researchers at NASA MSFC are currently developing techniques for using FBGs for monitoring the integrity of advanced structural materials expected to become the mainstay of the current and future generation space structures. Since carbon-epoxy composites are the materials of choice for the current space structures, the initial study is concentrated on this type of composite. The goals of this activity are to use embedded FBG sensors for measuring strain and temperature of composite structures, and to investigate the effects of various parameters such as composite fiber orientation with respect to the optical sensor, unidirectional fiber composite, fabrication process etc., on the optical performance of the sensor.

This paper describes an experiment to demonstrate the use of an embedded FBG for measuring strain in a composite material. The performance of the fiber optic sensor is determined by direct comparison with results from more conventional instrumentation.

Fiber Bragg Grating Sensors

Bragg gratings can be written into Germaniun doped optical fiber by exposing the fiber to an UV interference signal generated either holographically via two beam interferometry (Meltz

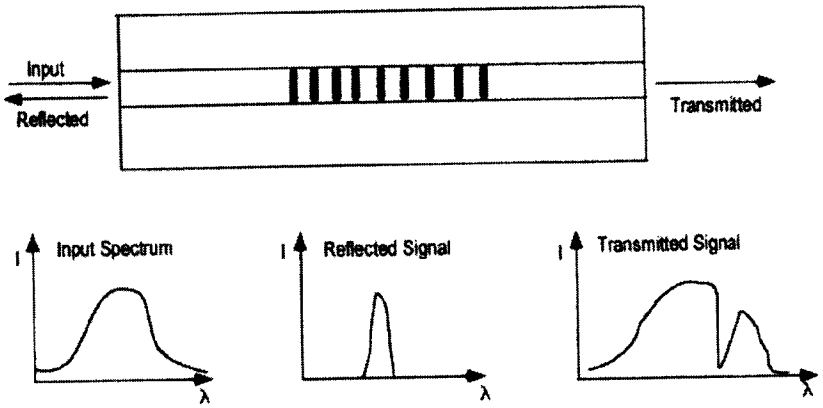

Figure 1: Reflected and transmitted Bragg grating signal with a broadband source

et al. 1989) or by using a diffraction mask (Hill et al. 1993). The absorption of the UV light in the fiber changes the chemical bonds in the glass (producing defect centers) thus giving rise to a change in the complex refractive index of the glass. The resulting spatial modulation in the index of the fiber produces the Bragg grating. This structure is permanent for temperatures up to 350 degrees Celsius, and acts as a very narrow- band in-line filter. In reflection, the grating reflects strongly at the wavelength, λB for which the Bragg resonance given by equation (1) is satisfied,

$$\lambda_B = 2n\Lambda \tag{1}$$

where Λ is the grating pitch and n is the effective index of the core. With such a device, injecting spectrally broadband source of light into the fiber, a narrowband spectral component at the Bragg wavelength is reflected by the grating. In the transmitted light, this spectral component is missing, as depicted in Fig. 1. The bandwidth of the reflected signal depends on several parameters, particularly the grating length, but typically is ~ 0.05 to 0.3 nm in most sensor applications. A strain applied to the grating results in a shift in the Bragg wavelength of the device which can be detected in either the reflected or transmitted spectrum as shown. By measuring the shift in Bragg wavelength, one can easily determine the applied strain according to equation (2):

$$\frac{\Delta\lambda_B}{\lambda} = (1 - P)\frac{\Delta L}{L} \tag{2}$$

Where L is the length of the sensor and P is the optical strain coefficient which has a typical value of 0.22 for axial strain (Davis et al. 1997). The nature of the output of Bragg gratings provides these sensors with built-in self-referencing capability. As the sensed information is encoded directly into wavelength, which is an absolute parameter, the output does not depend directly on the total light levels, loses in the connecting fibers and couplers, or source power. This is widely acknowledged as one of the most important advantages of these sensors. The wavelength encoded nature of the output, however, also facilitates wavelength division multiplexing (Kersey et al. 1997) by allowing each sensor to be assigned to a different portion of the available source spectrum. The upper limit to the number of gratings which can be addressed

in this way is a function of the source profile width and the operational wavelength bandwidth required for each grating element.

Fabrication of Bragg Gratings

High reflectivity Bragg gratings were produced into the core of single mode, Germanium doped optical fibers using the phase mask method described earlier. The optical fibers were hydrogen loaded (Lemaire et al.) under high pressure to increase photosensitivity prior to writing the grating. A continuous wave argon ion laser operating at 244 nm (second harmonic of the blue line) was used as the source for writing the gratings at Bragg wavelengths around 1300 nm. Real-time monitoring of grating growth was carried out during the writing process by illuminating the grating with broadband source (a laser diode) covering the grating reflection spectrum. Transmission and reflection spectra were measured with the aid of a monochromator and a recorder.

Embedded Optical Fibers

Carbon /epoxy composite panels, with embedded optical fiber sensors were fabricated using the NASA-MSFC composite fabrication facilities. The carbon/epoxy prepreg used for the panel fabrication was provided by NASA. The fabrication technique focused on the hand lay-up and autoclave cure. The optical fiber was arranged to lie parallel with adjacent structural carbon fibers during fabrication. The study concentrated on fabric based composites.

Experimental Set—Up

Shown in Figure 2 is a schematic of the set-up used for performing physical tests on the composite panels fabricated with the embedded optical sensor. The composite was tested under axial tension. It was gripped on either end in a special hydraulic wedge grips. Approximately one inch of the composite was gripped by each of the two wedge grips. A compact tunable diode laser was used to couple light into the optical fiber. The transmission spectrum of the grating was recorded with the aid of a detector and a lock-in amplifier. The composite was loaded to approximately 20,000 psi and unloaded. At each load level the shift in Bragg wavelength was obtained from the transmission spectrum. The unstrained Bragg wavelength was 1292.1 nm. The corresponding strain, defined as the change in length divided by the original length, was also recorded at each load level.

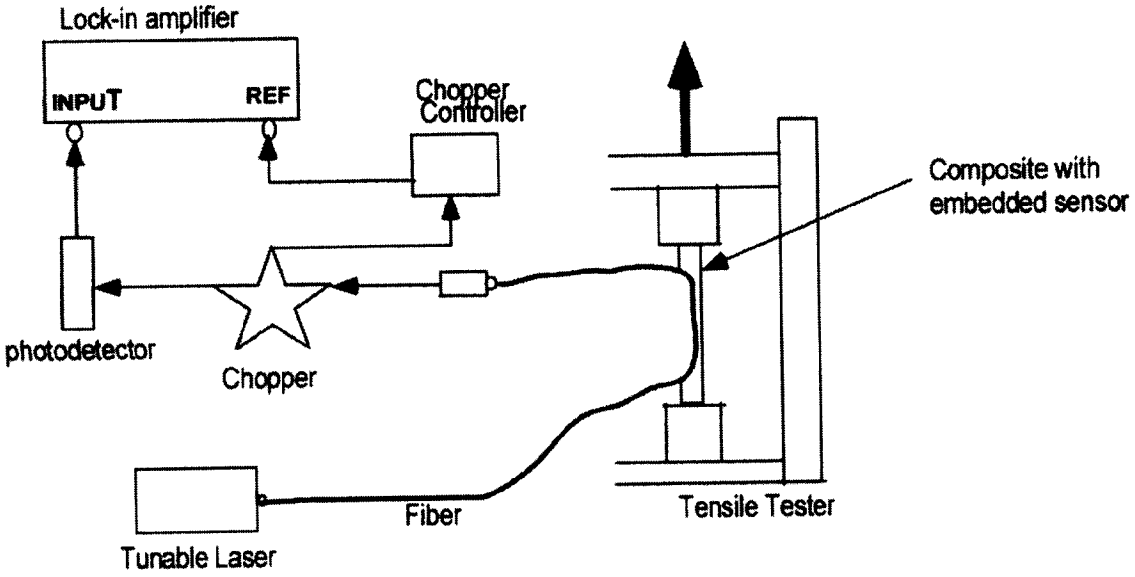

Figure 2: The Experimental Set-Up

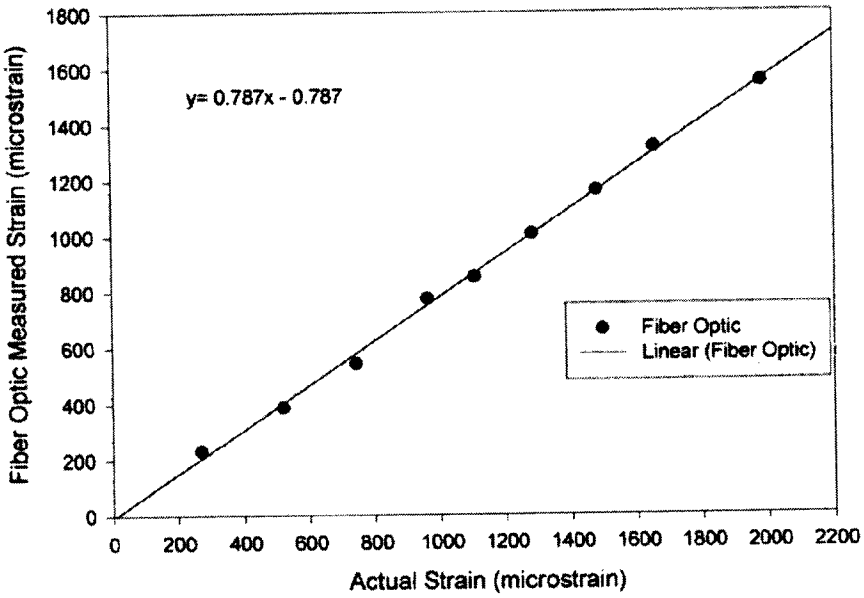

Figure 3. Fiber Optic Measured Strain versus Actual Strain

2001

NASA/ASEE SUMMER FACULTY FELLOWSHIP PROGRAM

MARSHALL SPACE FLIGHT CENTER
THE UNIVERSITY OF ALABAMA IN HUNTSVILLE

LOW-ENERGY STUDY OF GAMMA-RAY BURSTS USING TWO BATSE SPECTROSCOPY DETECTORS

Prepared By:	Michael J. Pangia
Academic Rank:	Associate Professor
Institution and Department:	Georgia College & State University Department of Chemistry & Physics
NASA/MSFC Directorate:	Science
MSFC Colleagues:	Gerald J. Fishman Robert D. Preece (UAH)

Introduction

Gamma-ray bursts (GRBs) are energetic, short-duration emissions of gamma-rays from astronomical sources typically well beyond our galaxy. The Burst and Transient Source Experiment (BATSE) that was onboard NASA's Compton Gamma-Ray Observatory (CGRO) had detected an unprecedented 2704 GRBs during CGRO's nine-year mission. BATSE consisted of 8 detector assemblies located at the corners of CGRO to give full sky coverage. Each assembly consisted of two detectors, a Large Area Detector (LAD) and a Spectroscopy Detector (SD) as shown in Figure 1.

In determining the detail features of GRBs, the degree to which they possess a low-energy component (~10 keV) is of interest. Preece et al. (1996) have developed a method (see below) to study the low-energy characteristics and concluded that 14% of the 86 bright GRBs they studied had a definite low-energy component, referred to as a low-energy excess. Their study, and for the present study as well, needed to use SD data, because it extends down to the low-energy range when operating in a high-gain mode. For their study, low-energy data was used from just one SD. To better quantify the low-energy behavior, this study will consider bursts for which two SDs satisfy the same criteria (listed below) as used by Preece et al (1996).

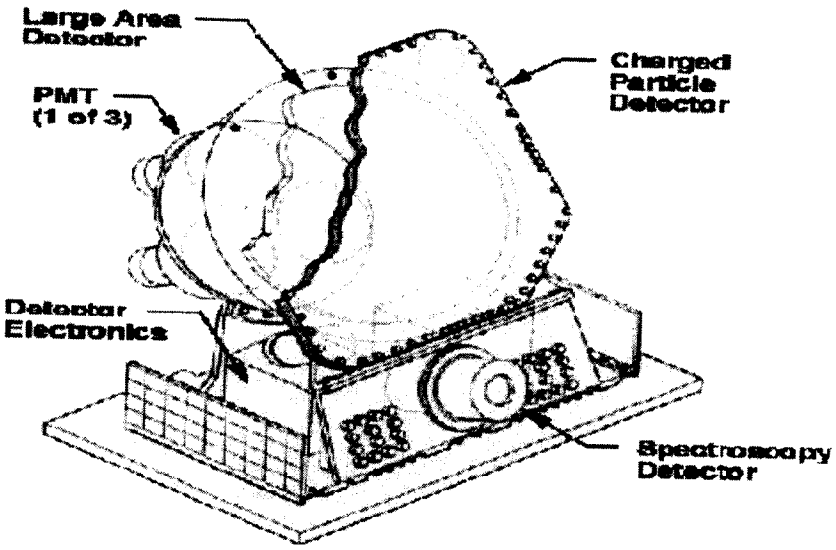

Figure 1. BATSE Detector Assembly (cut-away view).

Data Types

BATSE data was acquired and recorded in a number of formats. The properties of the data types vary in resolution and coverage in both time and energy. Of particular interest are the continuous sampling mode (2.048 s resolution) and the burst-triggered higher temporal resolution mode with the finest resolution used in our study of 0.128 s. The continuous type used is the low-energy channel of the DISCSP data type, and the burst-triggered type is SHERB. The data type SHER is

the corresponding background data that is needed to determine the uncertainties in the data and the model, and to determine the signal-to-noise ratio.

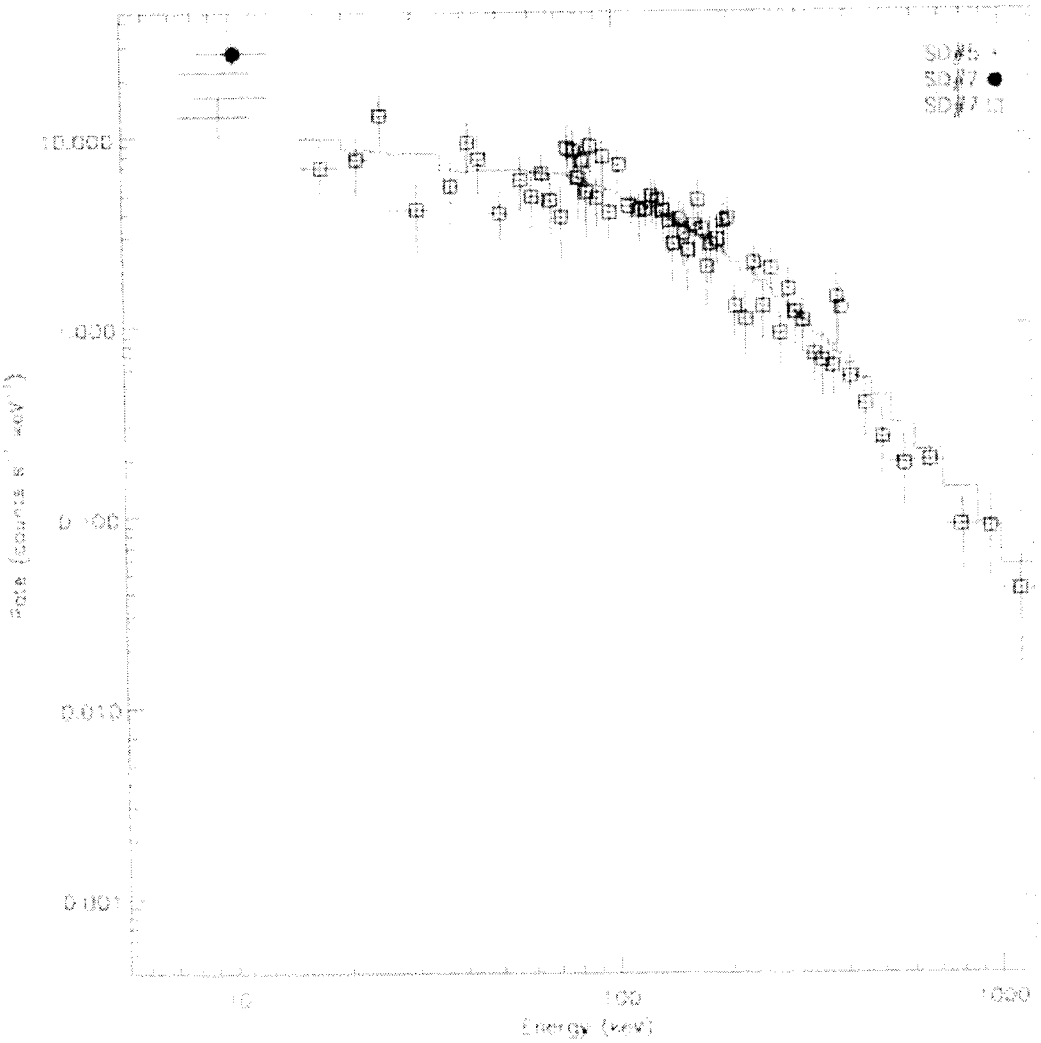

Figure 2: Spectral fit of Trig 2852 from 2.4 to 3.2 s.

Method and Criteria

The procedure developed by Preece et al. (1996) to study the low-energy aspects of GRBs with BATSE data is to fit the data to a representative spectral function. In particular, two components are used, one corresponding to the low-energy component, and another representing the main part of the spectrum. The low-energy function used is the optically thin thermal bremsstrahlung (OTTB) model, which has the following form

$$f_{OTTB} = A \frac{E_P}{E} e^{-(E-E_P)/kT} \quad (1)$$

where A is the amplitude, T is the temperature , and E_p is a peak energy parameter constrained to 10 keV for the fits. The main part of the spectrum is typically fit by the Band GRB model (two smoothly-joined power-laws), or, if that doesn't converge, a model known as the Comptonized Spectral Model (see Preece et al. (2000) for the formulae).

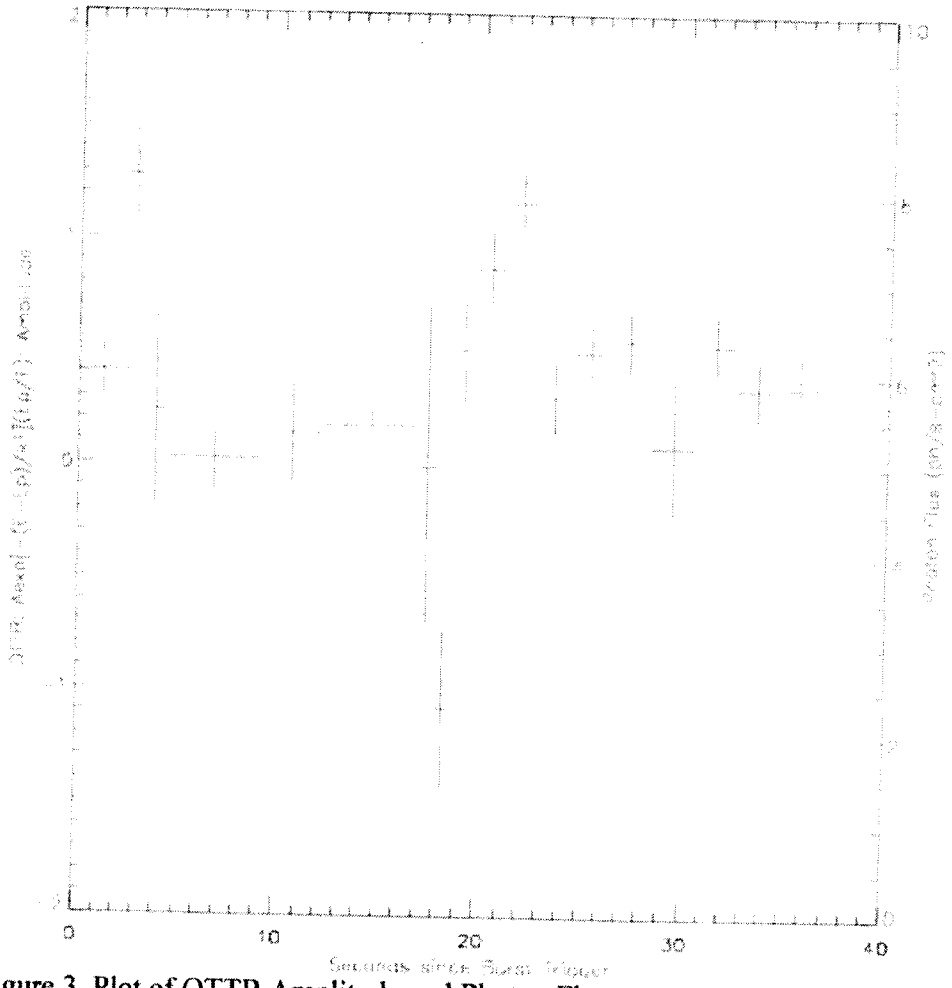

Figure 3. Plot of OTTB Amplitude and Photon Flux versus time for Trig 2852.

To increase upon the low-energy coverage used by Preece et al. (1996), we restrict the study to bursts for which DISCSP, SHER, and SHERB data are available from the two most significant SDs satisfying the following criteria: their azimuthal angles to the source are less than 70° to avoid obstruction caused by the LADs, and their gain settings are either 4× or 8×. These data are

rebinned in time by imposing a signal-to-noise level criterion of 15 to the DISCSP data of the SD with the second most significant signal to improve on the accuracy of the fit.

Results and Conclusions

Three bursts satisfying the criteria were studied. Identifying them by their BATSE trigger numbers, they are 1609, 2431, and 2852. As an example of a spectral fit, Figure 2 is for the time interval corresponding to the first peak (2.4 to 3.2 s following the trigger) of Trig 2852. For display purposes, a signal-to-noise level criterion of 2 was used to rebin the energy channels in this figure. The spectral fit is shown with a solid line. Its reduced chi-squared value is 1.03, and the OTTB amplitude and temperature values are 1.3 ± 0.2 photons/cm^2·keV and 4.6 ± 1.7 keV, respectively. The data values are also shown in the figure with their uncertainties in photon count rate (vertical span). The four horizontal lines to the left of the figure correspond to two data points and two spectral fit values for the lowest energy ranges of SDs 5 and 7 as indicated by their widths. Note that although the low-energy datum for SD 5 is below the spectral fit, the one for SD 7 exceeds the spectral fit by a greater statistical amount; thus the conclusion that the low-energy excess is more significant.

Correlations between the OTTB parameters and the photon flux were investigated. Trigs 1609 and 2431 did not exhibit any obvious correlation, but one did exist for the OTTB amplitude for Trig 2852. Figure 3 is a plot of the OTTB amplitude (on left axis) and photon flux (on right axis) as a function of time since the start of Trig 2852. The vertical span of each amplitude value indicates the uncertainty in the results. Notice the value at ~3 s is the corresponding OTTB amplitude for the fit of Figure 2. The correlation observable in Figure 3 is that the rise and fall in OTTB amplitude coincide with the two peaks in flux activity at ~3 and 22 s. In regard to the OTTB temperature values, the fractional uncertainties, which range from 30 to 100% are too large to either identify or refute any correlation. It is worth noting that the OTTB temperature fractional uncertainties were significantly greater for Trigs 1609 and 2431 than for Trig 2852. This suggests that the reason no OTTB amplitude versus photon flux correlation is identifiable for the former group is because the huge temperature uncertainties render the OTTB amplitude values more suspect than their uncertainties suggest, hence possibly masking a correlation. In fact, this could explain why a correlation in Figure 3 is only apparent at the peaks in photon flux, because it is during these periods that the fractional uncertainties in OTTB temperature values are least. Although this study suggests the existence of a correlation, clearly more GRBs must be analyzed using the present criteria before anything definite can be stated.

References

Preece, R. D., et al. (1996), "BATSE Observations of Gamma-Ray Burst Spectra. III. Low-Energy Behavior of Time-Averaged Spectra," *The Astrophysical Journal*, v. 473, 310.

Preece, R. D., et al. (2000), "The BATSE Gamma-Ray Burst Spectral Catalog. I. High Time Resolution Spectroscopy of Bright Burst using High Energy Resolution Data," *The Astrophysical Journal Supplement Series*, v.126, 19.

2001

NASA/ASEE SUMMER FACULTY FELLOWSHIP PROGRAM

MARSHALL SPACE FLIGHT CENTER
THE UNIVERSITY OF ALABAMA IN HUNTSVILLE

LABVIEW IMPLIMENTATION OF IMAGE PROCESSING AND PHASING CONTOL FOR THE SIBOA SEGMENTED MIRROR TESTBED

Prepared By:	James D. Partridge, EIT
Academic Rank:	Accompanying Student
Institution and Department:	Mercer University Mathematics and Mechanical Engineering
NASA/MSFC Directorate:	Science
MSFC Colleague:	Edward E. (Sandy) Montgomery, IV

Introduction

"NASA is preparing to launch the Next Generation Space Telescope (NGST). This telescope will be larger than the Hubble Space Telescope, be launched on an Atlas missile rather than the Space Shuttle, have a segmented primary mirror, and be placed in a higher orbit. All these differences pose significant challenges." This effort addresses the challenge of implementing an algorithm for aligning the segments of the primary mirror during the initial deployment that was designed by Philip Olivier and members of SOMTC. The implementation was to be performed on the SIBOA test bed. Unfortunately, hardware/software aspect concerning SIBOA and an extended time period for algorithm development prevented testing before the end of the study period. Properties of the digital camera were studied and understood, resulting in the current ability of selecting optimal settings regarding saturation. The study was successful in manually capturing several images of two stacked segments with various relative phases. These images can be used to calibrate the algorithm for future implementation. Currently the system is ready for testing. [1]

LabVIEW Code

Controller Implementation:

In order to phase the SIBOA (**S**ystematic **I**mage-**B**ased **O**ptical **A**lignment) testbed with the Neuro-Fuzzy controller developed by Philip Olivier, images taken by the segmented telescope testbed (See #1 Figure 1) are processed to produce new piston values for each of the seven reflective elements. Initially, an acquired image is converted in LabVIEW from a Portable

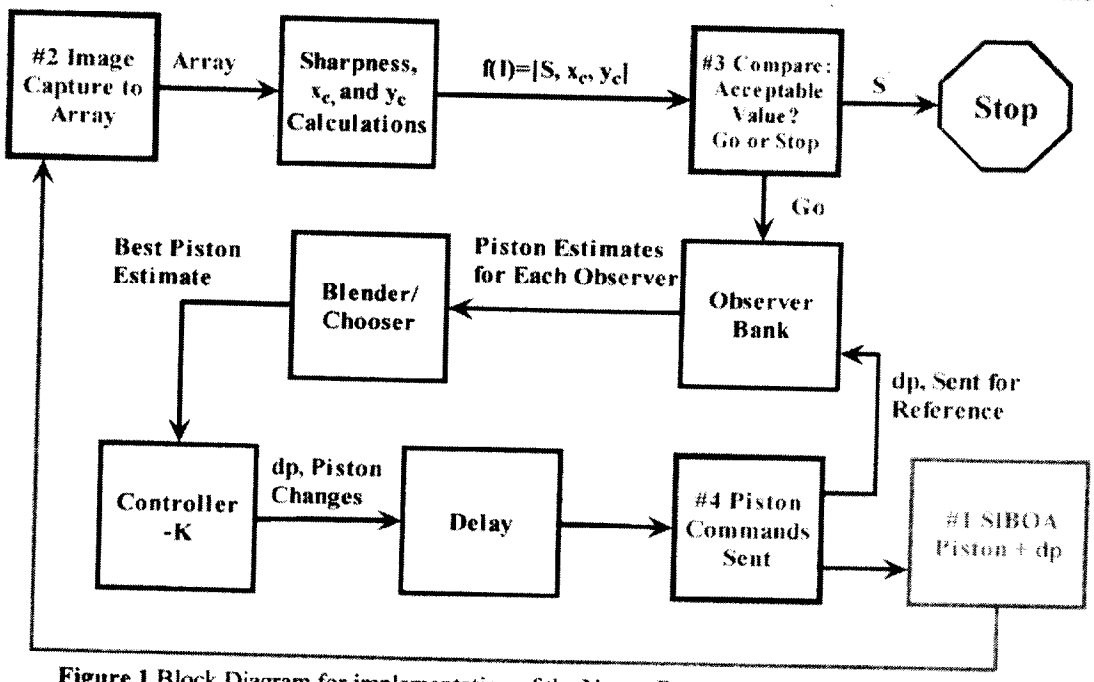

Figure 1 Block Diagram for implementation of the Neuro-Fuzzy controller.

Network Graphic format into a 2-D array (#2) that is readable by the MATLAB controller code. The MATLAB code initially processes the converted image and produces values, such as

sharpness, that are used to compare with theoretical result. Based on this output, the control loop continues or phasing is complete, resulting in the stop command (#3). The blocks between #3 and #4 find the optimum piston values that should result in a sharper image and then produces piston adjustment commands. LabVIEW code takes these commands and sends them via voltage signals to actuators that change the piston position (#4). Finally, if needed, a new image is taken, and the process is continued until the sharpest possible image is attained or the controller times out. In Figure 1, all elements with numbers apart from #1 were developed in LabVIEW, and all un-numbered blocks represent algorithm code housed within LabVIEW MatLab formula nodes.

Piston Commands:

Figure 2 shows the flow path necessary for taking piston values, given by MatLab, calibrating each mirror's actuators, and finally sending the signals to the picomotors (Block #4 in Figure 1). A MatLab algorithm working inside LabView outputs a 1 by 7 matrix of piston values that are predicted to improve image sharpness. (Each mirror lies on three actuators that, when

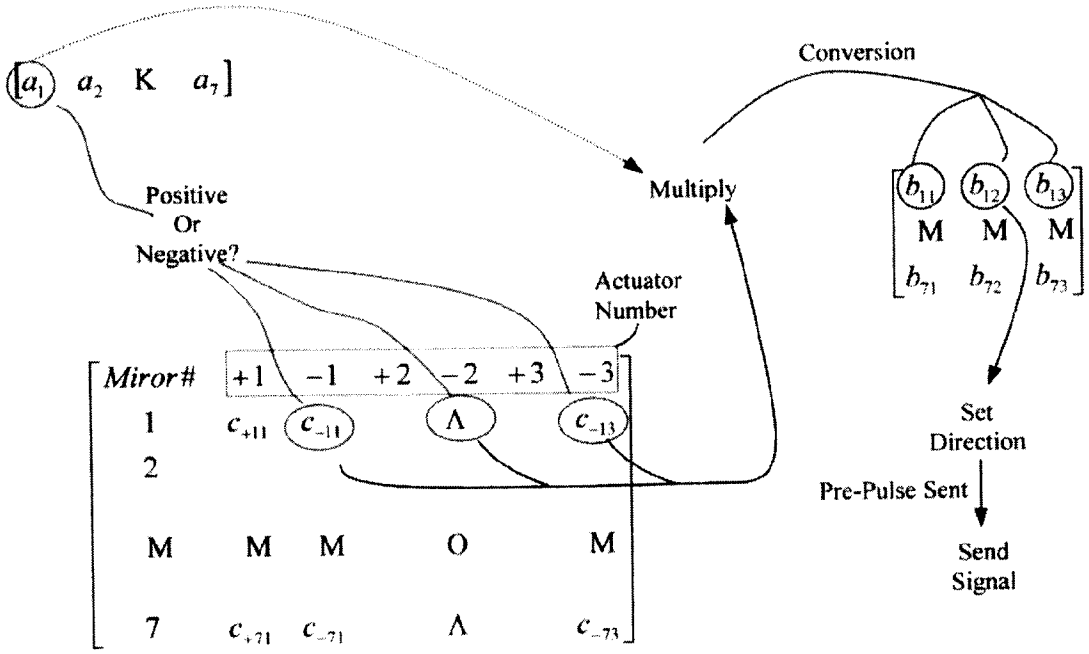

Figure 2 Data flow for readying piston values for picomotor communication.

commanded in sequence, change the piston value, z-direction only without changing the tip and tilt.) The seven values are extracted individually from the vector/matrix (a_i) in order to calibrate the commands, since each picomotor moves differently from the others and differently in both the positive and negative directions. Therefore, it is necessary to determine the direction of the command, extract a calibration constant, and then multiply the calibration by the piston value for the mirror. For example if mirror one needs to move down, the piston for mirror one, a_1, is multiplied by the constants c_{-11}, c_{-12}, and c_{-13} corresponding to the calibration values for mirror one, negative motion, picomotors one, two, and three respectively. After multiplication, these values are converted to number of pulse counts and then stored as in the final matrix. Now, even

though each of the three picomotors for any mirror will be sent differing pulse count values, each actuator should move the same physical distance downward.

Camera Discussion

Saturation:

During the processing of the phasing algorithm, the sharpness of the image is used to estimate future piston values. Sharpness involves summing all the elements of the image array after the pixel intensity values have been squared [1]. Thus, as a result of the squaring, it is essential that no higher end information is lost or the sharpness value will be greatly affected. The 10-bit Pulnix camera being used needs to be set in such a fashion that no pixel value exceeds an intensity value of 1022. (A value of 1023 indicates saturation.)

Shutter Speed and Gain:

Originally it was thought that the Pulnix camera contained only one variable, integration time or shutter speed, which controlled the range of recordable intensities. Page 11 of the Pulnix Operations Manual (TM-1300) shows the 10 shutter settings and exposes that the largest time difference between any two speeds is one setting being a quarter of the length of the previous setting. Since intensity is directly proportional to the shutter speed, a slight saturation at this longer setting would mandate the use of the shorter time period, but would reduce the 10-bit camera's resolution to just above 256, eliminating resolution between 256 and 1023. Thus, it is highly beneficial that a second variable, gain, can greatly increases the dynamic range of the camera. Figure 3 shows how gain, over a range of 120 to 210, changes the natural log of the measured intensity in a practically linear fashion (the shutter speed and reference voltages are held constant). Based on a needed intensity value, it now possible to select shutter and gain settings that provide maximum 10-bit resolution. For instance, when stacking then phasing two mirrors, the finial pistons result in a theoretical intensity four times that of an of an individual mirror. Thus, it is optimal to have an individual mirror's intensity to be just below 256 before the procedure begins so that the final intensity will be as close as possible to, with out exceeding, 1022. For this specific case, with the default unity gain settings, no shutter speed meets the requirement, but with slight gain adaptations an optimal camera setting for phasing exists. [2]

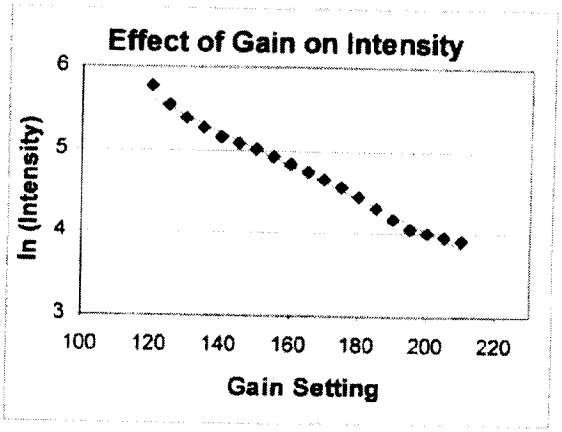

Figure 3 Experimental Gain Results

Reference Voltages:

The Pulnix camera contains another control, reference voltage, which limits the output voltages from the camera. Originally, images taken by SIBOA showed background noise of magnitude

around 450, about 44% of the resolution, a highly unacceptable value. Changing the low voltage reference, Vref low, can greatly reduce this portion of the noise. A setting of 130 results in a truncation of noisy voltages that reduces the background to a maximum value of 15 or 1.5% of the total resolution. Hence, $V_{ref\ low}$ reduces the noise by setting the zero point of the camera's resolution. Likewise, $V_{ref\ high}$ sets the upper limit of the voltage output that gives the 1023 ceiling for resolution. It is possible to set $V_{ref\ high}$ so that saturation occurs in the physical system at a value lower than 1023, thus, it is necessary to set the voltage below the saturation point (found to be 222). As well, if only a small output voltage range is needed, the two reference voltages can be set close in order to have the total resolution in this small range. For SIBOA purposed, values of 222 and 130 for $V_{ref\ high}$ and $V_{ref\ low}$ respectively are ideal. [2]

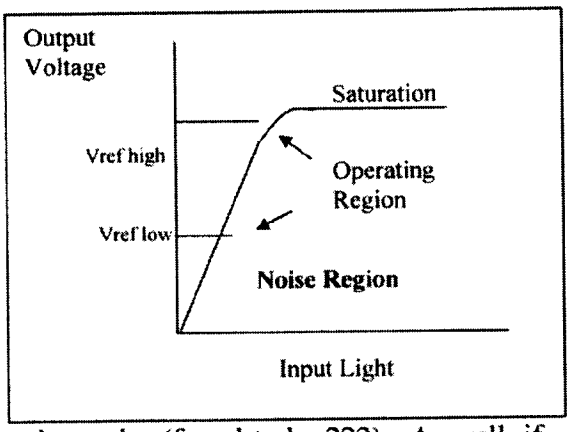

Figure 4 Reference Voltage Selections

Camera Stability:

After all camera settings are selected, it is important to know the stability of the recorded intensity results. To quantify this, multiple images were recorded at second intervals, the maximum intensity values were recorded, and a Root Mean Square was calculated. For instance, one trial consisted of 210 images that had an average maximum intensity value of 487 and a RMS value of 30. Other trials were conducted, but no direct relation between average maximum intensity and RMS was developed. At this point, the experiments have shown that data captured with the camera is quite inconsistent. It is therefore necessary to account for this instability through normalization or correcting the physical system. [2]

Conclusions

The summer's efforts resulted in a mirror phasing control system that is ready for testing. Optimal settings for the digital camera are understood, and saturation should be avoided at the time of testing. Images were captured that will help fine-tune the algorithm until a full experimental validation can be performed.

Acknowledgments

The author would like to thank NASA/MSFC/SOMTC for its hospitality. Special thanks go to Sandy Montgomery, Glenn Zeiders, and Philip Olivier for their technical assistance.

References

1. Olivier, Philip D., Experimental Validation of a Neuro-Fuzzy Approach to Phasing the SIBOA Segmented Mirror Testbed, SFFP Report, 2001
2. Zeiders, Glenn W. (2001)

2001

NASA/ASEE SUMMER FACULTY FELLOWSHIP PROGRAM

MARSHALL SPACE FLIGHT CENTER
THE UNIVERSITY OF ALABAMA

THE EFFECT OF FRICTION ON PENETRATION IN FRICTION STIR WELDING

Prepared by:	Steve Rapp
Academic Rank:	Assistant Professor
Institution and Department:	Southwest Virginia Higher Education Center University of Virginia, Department of Physics
NASA/MSFC Directorate:	Engineering, ED 33
MSFC Colleague:	Arthur Nunes, Jr.

Introduction

"Friction stir butt welding," as it was originally termed by Wayne Thomas and Christopher Dawes, in the early 1990s, but now commonly called "friction stir welding," has made great progress as a new welding technique (Thomas, et al., 1995). Commercially, friction stir welding (FSW) is finding many applications. Marine Aluminum of Norway is using the process for welding 20-meter aluminum sheets for ferry construction. Japan is using the technique in development work on bullet trains. Sapa of Sweden utilizes FSW in the building of refrigeration units for cargo ships. In the United States, Boeing is using the technique in the production of Delta rockets (Wilks, 1999). Eclipse Aviation Corporation plans to use FSW to produce a business jet available in August, 2003 (Velocci, 2000).

Marshall Space Flight Center has been investigating the use of FSW for assembly of the Shuttle's external fuel tank since the late 1990s and hopes to have the process in use by the summer of 2002 (Lawless, private communication). Currently, a modified 15-foot vertical weld tool is being utilized to produce friction stir welds on full-scale hardware. In building 4711, a modified Kearney & Trecker milling machine, as shown in Figure 1, is being used to produce FSW. A retractable pin tool (RPT), invented at the Marshall Space Flight Center, is being used to produce friction stir welds without the usual hole at the end of the weld (Figure 2). Figure 3 shows the retractable pin tool making a friction stir weld in aluminum alloy 2219.

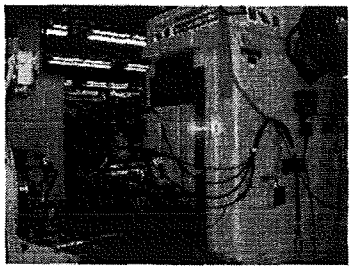

Figure 1: Milling Machine

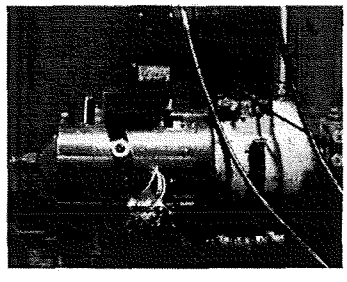

Figure 2: The RPT

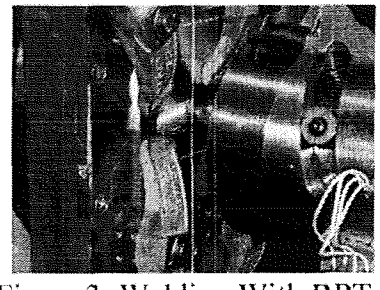

Figure 3: Welding With RPT

Friction stir welding has many advantages over soft plasma arc welding that is presently being used on the Al-Li external tank. Since FSW is a solid-state process, the problems associated with phase changes are eliminated. The mechanical properties of friction stir welds have been shown to be, in most cases, even better than fusion welded joints. The fracture strength and elongation at fracture of friction stir welded joints are improved as compared with fusion welded joints. The welding process is energy efficient and eliminates the need for filler metals and weld pool shielding gas (Dawes and Thomas, 1996). The main disadvantage of FSW is that substantial force has to be produced constantly on the pin tool. Fusion welds require no loads between the welding tool and the weldment.

In FSW, a cylindrical pin tool of hardened steel, is rotated and plunged into the abutting edges of the parts to be joined. The tool is plunged into the weldment to within about .050" of the bottom to assure full penetration. As the tool moves along the joint, the tool shoulder helps produce frictional heating, causing the material to plasticize. The metal of the two abutting plates flows

from the front of the tool to the back where it cools and coalesces to form a weld in the solid phase (see Figure 4).

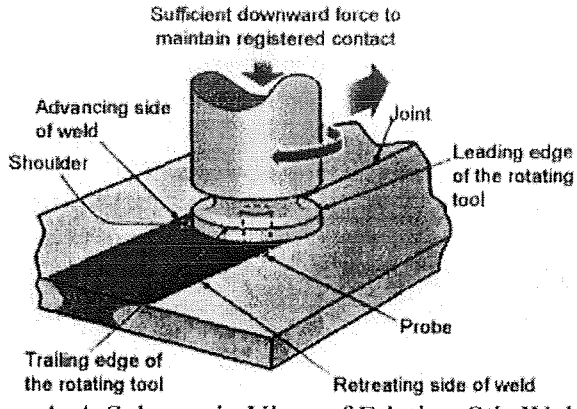

Figure 4: A Schematic View of Friction Stir Welding

Procedure

One quarter inch thick plates of aluminum alloy 2219 were used in this study. Two samples, each consisting of two 4" x 12" plates, were friction stir welded. The anvil for one sample was coated with molybdenum disulfide (plate # 1), while for the other sample a sheet of roughened stainless steel was placed between the anvil and the sample (plate # 2). The welds were made using a retractable pin tool developed by Ding and Oelgoetz (1999). The tool was mounted on a Kearney and Trecker five-axis milling machine modified for friction stir welding. The maximum pin tool length was set at .250". Other parameters were as follows: shoulder diameter, .937"; pin tool diameter, .375"; lead angle, 2.5^0; pin tool rotary speed, 220 rev/min; pin tool linear speed, 3.5 in/min; shoulder plunge depth (including deflection), .043"

The retractable pin tool was used so that the depth of the pin tool penetration could be varied. Initially, penetration of the pin tool was set at .050". As welding proceeded, the length of the pin tool was gradually increased to .25" at 3" from the starting point. For the next 2.5", the pin tool was at a constant .25" penetration. During the next 3", the pin tool was tapered back to .05" (see Figure 5). After welding, root-side die-penetrated tests were performed on the specimens. Root-side chemical etchings, using Keller's reagent, were also done. The welded panels were then cut and machined into microstructure analysis specimens.

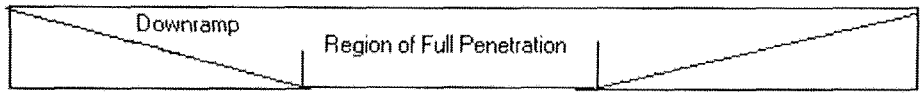

Figure 5: Illustration of Down-ramp and Full Pin tool Extension

The purpose of this investigation is to find out at what point, in the down-ramp, penetration occurs. Differences in root structure of the friction stir weld due to differences in anvil friction will be observed. These observations will be analyzed using friction stir weld theory.

Results and Discussion

The dye-penetrated tests and subsequent etching with Keller's reagent show that full weld penetration occurred in both panels for a distance of 2.5" in the area where the RPT was in full extension. Full penetration did not occur in the areas where the RPT was tapered in and out. It also appears that the vortex created by the rotating pin tool pumps material up from the bottom surface because no "tool marks" are seen until about .050" from the bottom of the root side of the plates. Figure 6 shows a side view in which swirl marks are seen .050" from the bottom of the specimen.

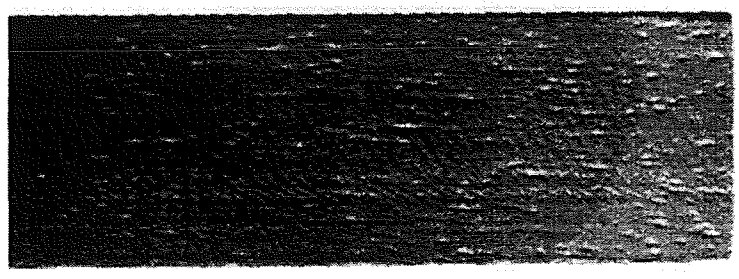

Figure 6: "Tool Marks" Are Seen .050" From the Bottom of the Weldment in Side View

From the limited data in this study, the plates welded on the lubricated anvil show a steeper slope during tapering in toward full penetration and tapering out away from the full penetration area compared to the other specimen. This indicates that the friction coefficient of the anvil may promote penetration as proposed by Nunes (2001). Theoretical and measured slopes are shown in Table 1.

Table 1. Theoretical and Measured Slopes

Type of Anvil	Theoretical	Taper In	Taper Out
Lubricated Anvil (MoS_2) (#1)	.07	.13	.15
Unlubricated Anvil (#2)	.11	.11	.13

In the late 1990's Nunes (2001) discovered that the flow around a friction stir pin-tool could be represented by the superposition of three flow fields: a uniform translation, the rotation of a radially symmetric solid plug of metal surrounding the pin-tool, and a ring vortex flow (like a smoke ring) around the tool. If the metal sticks to the tool, the plug surface extends down into the metal from the outer edge of the tool shoulder, decreases in diameter like a funnel, and closes up beneath the pin.

In this model most of the shearing action takes place on the surface of the rotating plug surrounding the tool. It is to be expected that the hottest, softest part of the metal flow is located on the shear interface at the plug surface because here the principal mechanical work of the tool is transformed to heat, which always flows away from its source down a temperature gradient to colder metal.

Nunes has conjectured that the hottest, softest part of the flow, i.e. the plug surface, acts as a channel through which the asymmetrical rotating pin threads pump an oscillating flow with the period of rotation of the tool. He has proposed this oscillating flow as the origin of "tool marks" that not only rise and fall on the weld bead surface in the wake of the tool but also extend deep into the interior of the weld.

It is apparent from this study that the tool marks do not extend all the way to the anvil upon which the bottom of the workpiece rests (see Figure 6). This is to be expected because here there is no free surface which could accommodate variations in metal volume, as is the case at the top surface outside the tool shoulder. The periodic flow oscillations must move toward and away from the upper free surface.

Although tool marks, once looked for to indicate contact of the plug interface with anvil (full penetration), are not present on the weld root, the distinct, white-etching microstructure acquired by the metal through the huge shear strain upon passage into and out of the rotating plug rotational field remains as a visible indication of full penetration.

Nunes has also conjectured that the slip surface around the rotating plug takes that shape which minimizes the torque required to rotate the tool. If the anvil/weld-metal interface is more slippery than the weld-metal/weld-metal interface, slip at the anvil will be favored over slip above the anvil. However, an extra cylindrical ring of slip surface is needed for the extension of the slip surface from its position directly under the pin down to the anvil. Less extra slip surface is required as the pin approaches the anvil.

A simple model representing the above situation estimates that full penetration occurs when the distance between the pin bottom and the anvil is less than $\frac{R}{3}\left(1-\mu\frac{\sigma_N}{\tau}\right)$ where R is the radius of the slip surface at the bottom of the pin, about the radius of the pin; μ is the coefficient of friction at the anvil/weld-metal interface; σ_N is the normal stress acting on the pin bottom; and τ is the shear stress under the pin bottom. The smaller the anvil friction coefficient, the larger the pin/anvil separation at which full penetration occurs! This implies that reduction of anvil friction promotes earlier penetration.

The above implies that the rate at which the lower edge of tool penetration approaches the anvil, should be greater (close to the anvil) in instances of reduced anvil friction. Measured slopes, both down-ramping and up-ramping, were about 15% greater on an anvil lubricated with MoS_2, than on an unlubricated anvil, even when the programmed tool rate of descent for the lubricated tool was only 64% of that for the unlubricated tool.

Acknowledgements

The author would like to thank Dr. Arthur Nunes, Jr. for his guidance and direction during this study and for providing a stimulating work environment, , Bob Carter for securing materials and doing the friction stir welds, and Kirby Lawless for having a computer readily available.

Conclusions and Recommendations

- "Tool marks" are not visible on the root side of the weld, but are visible when .050" is removed indicating that material is being "pumped" up from the bottom of the weldment.
- The extremely limited data implies that that anvil lubrication does promote penetration in accordance with theory.

Further study is needed to confirm the effect and to determine if the effect can be made large enough to be of commercial use. In contrast to the simple theory, no discrete jumps in penetration were observed. A revised theory is required to compute a continuous slope.

References

1. Dawes, C.J. and Thomas, W.M. (March, 1996). Friction stir process welds aluminum alloys. *Welding Journal,* Vol. 75, no. 3, pp. 41-45.
2. Ding, J.R. and Oelgoetz, P.A. Auto-adjustable pin tool for friction stir welding. *United States Patent 5,893,507,* April 13, 1999.
3. Lawless, K. (June 26, 2001). Private communication.
4. Nunes, A. Wiping metal Transfer in Friction Stir Welding. TMS 130th Annual International Meeting, New Orleans, LA., February 11-15, 2001.
5. Thomas, W.M., Nicholas, D., Needham, J.C., Murch, M.G., Temple-Smith, P. and Dawes, C.J. Friction welding. *United States Patent 5,460,317,* October 24, 1995.
6. Velocci, Jr., A.L. (Oct. 16, 2000). Eclipse Presses Amid Wide Skepticism. *Aviation Week & Space Technology.*
7. Wilks, N. (Nov.3, 1999). A Stir in the Joint, *Professional Engineering,* vol. 12, no. 20, p. 18.

2001

NASA/ASEE SUMMER FACULTY FELLOWSHIP PROGRAM

MARSHALL SPACE FLIGHT CENTER
THE UNIVERSITY OF ALABAMA IN HUNTSVILLE

APPLICATION OF RISK ASSESSMENT TOOLS IN THE CONTINUOUS RISK MANAGEMENT (CRM) PROCESS.

Prepared By:	Paul S. Ray
Academic Rank:	Associate Professor
Institution and Department:	The University of Alabama Department of Industrial Engineering.
NASA/MSFC Directorate:	Safety and Mission Assurance Office
MSFC COlleague:	Mike Galuska.

APPLICATION OF RISK ASSESSMENT TOOLS IN THE CONTINUOUS RISK MANAGEMENT (CRM) PROCESS.

Introduction

Marshall Space Flight Center (MSFC) of the National Aeronautics and Space Administration (NASA) currently implementing the Continuous Risk Management (CRM) Program developed by the Carnegie Mellon University and recommended by NASA as the Risk Management (RM) implementation approach. The four most frequently used risk assessment tools in the center are: (a) Failure Modes and Effects Analysis (FMEA), Hazard Analysis (HA), Fault Tree Analysis (FTA), and Probabilistic Risk Analysis (PRA). There are some guidelines for selecting the type of risk assessment tools during the project formulation phase (MWI 7120.6-Rev.A–May15, 2001) of a project. But there is not enough guidance as to how to apply these tools in the Continuous Risk Management Process (CRM). But the ways the safety and risk assessment tools are used make a significant difference in the effectiveness in the risk management function. Decisions regarding, what events are to be included in the analysis, to what level of details should the analysis be continued, make significant difference in the effectiveness of risk management program. Tools of risk analysis also depends on the phase of a project e.g. at the initial phase of a project, when not much data are available on hardware, standard FMEA cannot be applied; instead a functional FMEA may be appropriate. This study attempted to provide some directives to alleviate the difficulty in applying FTA, PRA, and FMEA in the CRM process. Hazard Analysis was not included in the scope of the study due to the short duration of the summer research project.

Fault Tree Analysis

FTA in Risk Identification;

Risk identification starts with the determination of the mission objectives. The top-level FTA is developed at this stage. This may be derived from :(a) brainstorming, (b) lessons learned from the past projects, and (c) hazard analysis.

Determining level of details:

The level of details to include will depend on the objectives of a project. If a branch on the tree is in the area that is well understood and the history of failures is low, the fault tree development in this area should be minimal and resources should be dedicated into areas where technologies are new and where there is a history of failures and problems. One simple rule is to develop the tree to a manageable level of details at which it is possible to exert a reasonable amount of control (Long.2001).

An example of a fault tree presenting the sequence of events leading to a rupture of pressure tank is given in Figure 1 (Greenfield). In this simple system, an air compressor pumps up an air receiver tank, when the operator closes the switch. The air horn is used as a backup in the event the timer fails or the operator forgets to open the switch. Once the horn is sounded it is the operator's responsibility to manually open the switch. A potential risk statement for the air-pumping example would be: The controls to prevent rupture of the air-receiving tank are overly dependent on operator intervention. If a single

system failure were to occur, tank rupture would result in a loss of the system availability and a potential loss of human life.

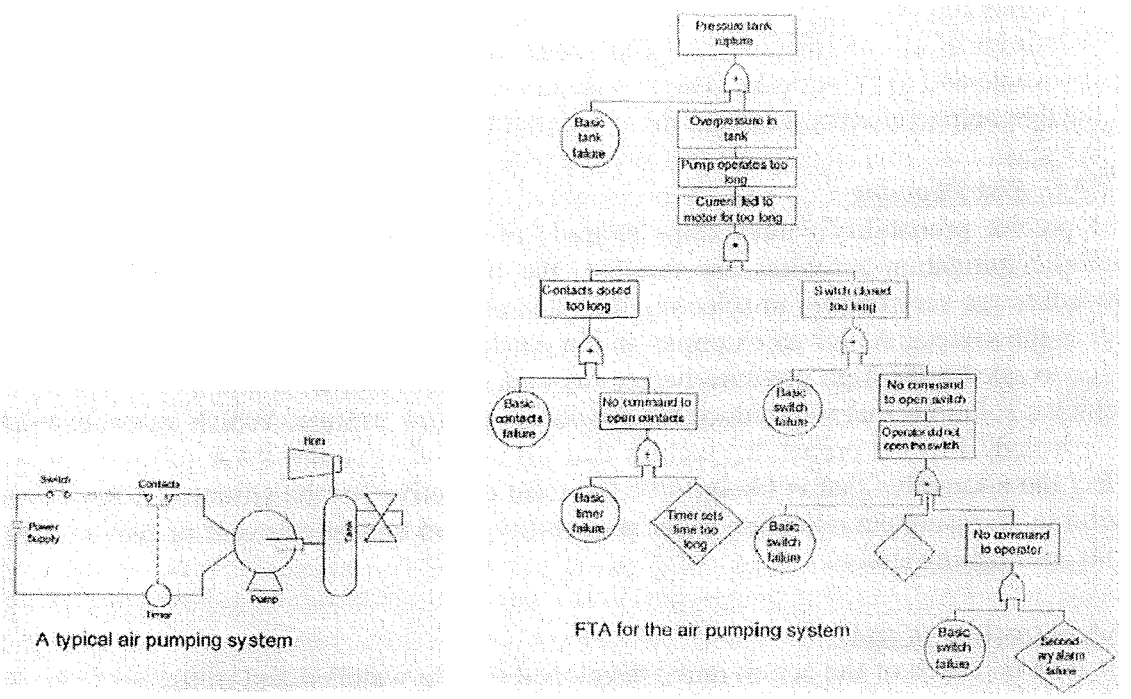

Figure 1. Fault Tree for the Air Pumping System.

Qualitative fault tree may be adequate for many cases. In these cases the level that permits evaluation of significant contributions to the top event may be adequate. If a Quantitative probabilistic risk assessment is needed, the development of fault tree should continue to the level for which reliable data are available.

In Figure 1.the fault tree analysis of the Air Pump System indicates that the instruments controlling the air pump are the most vulnerable component of the system. The tank design is understood so the risk analyst has decided not to develop this fault tree any further.

FTA in Risk Analysis:

Analyzing risks consists of determining which are the most significant regarding mission impact, timeframe of risk exposure, and probability of occurrence of an undesirable event. The calculation is based on determining the probability of the sub-level events in a fault tree.

The hardest element of risk analysis is to establish the probability of occurrence of the basic events. The usual source of probability data is: handbooks, data banks, field reports, and flight data, or laboratory tests.

FTA in Tracking and Control:

FTA does not have any significant role in tracking unless probabilities are available. However, FTA has to be updated to reflect any change in the original plan due to deviation resulting from incorporation of mitigation activities.

Probabilistic Risk Analysis (PRA).

PRA in Risk Analysis:
Probabilities of all intermediate and end-state events are based on the probability of the basic events and logic network. The precise quantitative values of the event-probabilities in the tree help to analyze a system more accurately.

PRA in Risk Planning:
The precise probability values helps to trade off risk and mitigation activities. Where multiple mitigation activities are feasible, the precise probability values in the PRA procedure are very helpful in selecting the most effective alternative action to reduce the risk in the system. As for an example: in the Air Pump example, the provision of a relief valve to release the high pressure before the tank ruptures or a redundant timer are both technical solutions that will reduce the possibility of tank rupture. Which alternative is to be selected? Precise probability values that are available in the PRA process helps to select the alternative that is likely to be the most effective for the situation. PRA is very useful in assessing the reduction in the probability of an undesired event or risk, resulting from a mitigating action.

PRA in tracking of risks:
The data on status of the action items developed for the watched and mitigated items are collected, compared with the plan, and reported as per CRM format. PRA can trend any changes in the probability of occurrence of the risk during the execution of the mitigation plan.

PRA in Risk Control
In the control phase of the CRM paradigm, PRA provides numerical results on the trend and the reduction of probability of occurrence for the risk as a result of a mitigation action taken.

Failure Mode and Effect Analysis (FMEA)

Functional and Hardware FMEA:
FMEA may be performed by either of two methods: (1) functions or (2) hardware.
A functional FMEA/CIL is normally performed early in the design definition phase, when design of systems and components are still incomplete and under development.
A hardware FMEA/CIL is normally performed after the design has matured past the definition phase. In this method, the component is divided into lower sub-assemblies, modules, and piece parts, and then each is analyzed separately.

FMEA/CIL in Risk Identification and Analysis:
While performing FMEA/ CIL each item is analyzed for each possible failure mode and for the "worst case" effect. The analysis begins with defining the system, function, and its performance requirements. Assumptions and ground rules to use in the analysis are specified, block diagrams are constructed to identify each component analyzed in the

FMEA/CIL. For critical failure modes, the CIL contains specific rational, which justifies the retention of the critical item in the system. CIL influences operations planning, and reports failure history. An example of FMEA (Table 1.), that is part of the air pump assembly illustrates a typical bottom-up approach of FMEA .

Table 1.Typical FMEA Worksheet

FAILURE MODE AND EFFECTS ANALYSIS

SYSTEM--Air Pump PAGE-----OF ----- DATE----
COMPONENT--Timer Contact PREPARED BY---------
DRAWING---XYZ APPROVED BY----------

Item code	Component/ Part No.	Function/ Description/ Reference	Failure Mode/ Cause	Failure Cause	Failure Effect	Criti calit y	Failure Detectio n
APS-3	Timer contacts. No. TMR-1	Closes electrical circuit bet. Power source and Pump	Contacts fail closed	Timer fails when contacts are closed; contacts weld together.	Air Pump continues filling air tank, air tank ruptures	1	none

As an example in the air-pump case given in Table 1, the failure mode "contact fail closed" of the part "Timer contacts" has been identified as having a criticality of "1" in FMEA. This being of the highest category risk must have some mitigation action and will be recorded in the CIL. An early action to improve the design of the part will reduce the risk at economic cost, if done before the design is finalized. An alternative may be a provision of a redundant component to reduce the risk. In case of our air-pump example a provision of a relief valve will reduce the risk, and now the "Timer contacts" will be assigned a criticality of "1R" instead of "1" which indicates a lower risk. Alternatively additional test may be conducted to determine if the risk is within the acceptable limits. If it is, then retention rational has to be recorded in the CIL document, for approval of the project management. FMEA and CIL are to be applied in making the trade-off decision.

FMEA/CIL in Risk Tracking and Control:
FMEA/CIL has no significant role in risk tracking and control. The major contribution of this tool is in risk identifying, analyzing and mitigation action planning.

Conclusion:

Application of FTA, PRA, and FMEA, the most frequently used risk assessment tools, were reviewed and Guidance in applying, these tools in the context of CRM process have been presented. These directives are not explicitly mentioned either in NASA Procedures and Guidelines (NPG), or in Marshall Work Instruction (MWI) for risk management. The guidelines tailored in this report will facilitate in applying these tools in the CRM process.

Acknowledgments:

The author would like to thank Dr. Amanda H. Goodson, director of the Safety and Mission Assurance office, for providing a stimulating environment and support needed for a successful summer research project. I am thankful to Mr. Michael Galuska for providing guidance to relevant literatures, and for several hours of productive discussions that made this study feasible within this short summer research program.

References:

Crosetti, P.A.,(1982). Reliability and Fault Tree Analysis Guide. UNC Nuclear Industries, Inc. Richland, Washington 99352.

Dorofee, A. J., Walker, J. A., Alberts, C.S., Higuera, R. P., Murphy, R. L., and Williams, R.C. (1996). Continuous Risk Management Guidebook, Software Engineering Institute (SEI), Carnegie Mellon University, MA: Hanscom AFB.

Ericson II, C. A., Fault Tree Analysis-A History, In the Proceedings of the 17th.International System Safety Conference in 1999

Greenfield, M. A., Risk Management Tools (2000,March 21-22). Paper presented at the Risk Management Colloquium, Ames Research Center, California
Haimes, Y. Y.(1998). Risk Modeling, Assessment, and Management. John Wiley, New York.

Long, A. Allen. Beauty and The Beast- Use and Abuse of The Fault Tree As a Tool (2001). In the Proceedings of the International System Safety Conference in 2001 (in press).

Marshall Space Flight Center/NASA, Organizational Issuance (1999). Failure Mode and Effects Analysis and Critical Items List. Organizational Issuance-QS10-R-001, Revision-C, released on July 1,1999.

Marshall Space Flight Center/NASA. (2000). Procedures and Guidelines, DA 01, Program/ Project Planning, MPG. 7120.1, Revision-B released on October 3, 2000

National Aeronautics and Space Administration-NASA. (1993). Requirements for Preparation and approval of Failure Modes and Effects Analysis (FMEA) and Critical Items List (CIL), NSTS 22206, Revision-D. December 10, 1993

National Aeronautics and Space Administration-NASA. (1999). International Space Station Program. JSC. Contract No.NAS15-10000. Failure Modes and Effects Analysis and Critical Items Requirements for Space Station, SSP 30234 Revision E, 1999.

National Aeronautics and Space Administration-NASA. (2000). Continuous Risk Management Course Manual. NASA SATC, Rev. 4, 5/00.

2001

NASA/ASEE SUMMER FACULTY FELLOWSHIP PROGRAM

MARSHALL SPACE FLIGHT CENTER
THE UNIVERSITY OF ALABAMA IN HUNTSVILLE

An Optical Direction Finder for Cloud-to-Ground Lightning Strikes

Report Not Available

Prepared by:	Paul M. Rybski
Academic Rank:	Associate Professor
Institution and Department:	The University of WI-Whitewater Department of Physics
NASA/MSFC Directorate:	Science
MSFC Colleague:	William Koshak

2001

NASA/ASEE SUMMER FACULTY FELLOWSHIP PROGRAM

MARSHALL SPACE FLIGHT CENTER
THE UNIVERSITY OF ALABAMA IN HUNTSVILLE

OPERATIONS ANALYSIS OF SPACE SHUTTLE SYSTEM

Prepared By:	Bhaba R. Sarker
Academic Rank:	Professor
Institution and Department:	Louisiana State University Industrial & Manufacturing Systems Engineering
NASA/MSFC Directorate:	Systems Management Office (VS20)
MSFC Colleague:	Eric J. Shaw

Introduction

The space science program at NASA since 1950's has gone through stages of development and implementation in rocketry and scientific advancement. It has become the nation's largest scientific institution of research and innovation for space exploration and military research, and overall a pride of the nation at an exorbitant cost.

After placing man on moon, space shuttle program at NASA is an on-going project with a high success rate at an average cost of about $450m per flight. A future endeavor from both government and private sectors needs to be undertaken for commercialization of this expensive mission. In order to attract private enterprises, it needs to boost up its operations with better technology at lower cost to cope with rapid changes in scientific advancement and economic competition. Thus, a *second-generation reusable launch vehicle (2GRLV)* will play a major role in future operation of NASA centers.

Envisioning this potential way of saving the program by reducing the cost, NASA is currently managing an innovative program called the Space Launch Initiative (SLI) to develop key technologies that will support the development of second-generation reusable launch vehicles (RLV) which will be more economical and safer and reliable than the existing space shuttle system. The selection of which technologies to fund for further development is being based on their likelihood to contribute to providing cost reduction or safety improvements. It is envisioned that in the 2006 timeframe, NASA will make a decision as to whether or not to commit to the replacement of the current space shuttle system with a new RLV. The decision to proceed with a new RLV will be partly based on the likelihood that the new system will be better than the existing space shuttle.

Government and private entrepreneurs are currently considering four different types of RLV projects: commercial programs, government programs, international concepts, and X Prize competitors. NASA has already commissioned a series of X-programs to study the future RLV program. Today, NASA decision makers need analytical tools to help determine which technologies to fund the development of this technology. In the 2006 timeframe, these same decision makers will need analytical tools to evaluate and compare various RLV architectures, including the existing space shuttle so as to make the best decision for whether or not to proceed with the development of a new RLV, and if so, then which one.

The Objectives:

Three major missions that cover all objectives of the RLV program are that the flights should be cheaper, safer and reliable. To be commercially and economically most cost-effective the flights must be cheaper, and the enhancement of flight rate will generate continuous improvement in RLV program. Therefore, to enhance the thrust values of the vector 'cheaper, safer and reliable' knowledge from the heritage data of the space shuttle program will provide a platform for such an undertaking. A study is conducted here to establish ground level knowledge from the historical data and expertise experiences of the field personnel. Such Information is compiled in the form of mission statement, goals, space shuttle operations, payloads and cargo constraints, resource constraints, and bottlenecks to the enhancement vector.

Preliminary Study

At the beginning, preliminary information on the economic cost models to assess the cost of the RLVs for cheaper, safer and reliable flights was studied. Obviously, this study calls for thorough understanding and analysis of the current space shuttle program (SSP) and its orbiter processing facilities (OPF). So a fast-paced plant tour was conducted to the summer faculty fellow (Bhaba Sarker) at the KSC/OPF under the supervision of Grant Cates, Manager of Orbiter Integration Process to understand the general workflow of the entire shuttle processing system such as vehicle assembly base, orbiter processing facilities, liftoff/launching systems, boosters recovery process, and their maintenance and refurbishment systems. This visit was complemented with supplemental data, a series of discussions and a run-through of ARENA simulation model of the OPF demonstrated at the University of Central Florida (UCF).

One tool that may be of use to NASA, both for choosing technologies and RLV architectures, is discrete event simulation modeling. NASA and UCF, under a Space Act Agreement, have developed at the Kennedy Space Center a macro-level simulation model of space shuttle flight hardware processing, to understand and identify bottlenecks in the process. This model was built using the commercially available ARENA discrete event simulation software. After NASA developed a project plan and provided the raw data, the UCF research group developed an ARENA based simulation model and has obtained some preliminary results. As a result of conducting this project, today NASA-KSC has information on at least five general aspects of data: (a) macro-level flow diagram of the SSP model, (b) general information on flight hardware processing, (c) EXCEL data files containing historical/heritage data from over 75 shuttle flows, (d) fitted distributions for various sets of data, and (e) ARENA simulation model. Under the current shuttle simulation project, work is undergoing to ascertain the bottleneck constraints that possibly hinder the enhancement of shuttle flight rate and other related performance measures.

NASA is currently working to evolve further, and to develop spin-off models to support the Space Launch Initiative for the near future. Part of this effort will ascertain the utility of using the existing space shuttle heritage data to identify potential area where new technologies and system improvements are needed. Also of interest is how the shuttle historical data and simulation results can be used to obtain information useful to future RLVS in terms of performance of different processing operations, identification of bottleneck problems that hinders the enhancement of system performance measures. Identification of these problems and causes may help envision the conceptualization, planning, design, build-up and operations of the second-generation model.

General Findings and Recommendations

On-site visit to KSC set the groundwork effectively for thorough understanding of the space flight process. Information on the background of the space shuttle project, mission and goals of the second-generation space launch initiatives, critical issues on payload system, general observations, and constraints on the physical limitations and processing capabilities have been gathered as a basis for future study to address, explore and solve some critical problems that may dominate the decision-making of second-generation RLVs. Some general finding and recommendations are listed below.

(a) The system is not designed for business and commercial market. The undertaking needs safer, cheaper and reliable flights. Transferability of NASA's space operations to private sectors and NASA'a concentration on scientific research, technical development, space exploration is of prime concern. The mission of the next generation is to have a full-scale development that will be commercially competitive, privately owned and operated, ten times cheaper, and 100 times safer. It must have a coordinated approach between NASA and industry with unique hardware to have commercial capabilities and purchase of cargo re-supply services for International Space Station.

(b) The initial goals comprises of two major primary objectives: (i) defining the detailed requirements (ii) identifying and initiating the initial risk reduction options (technology maturation), both of which call for further definition of system requirements for 2GRLV program before business and technical risk reduction effort. National Space Transportation Policy (1997) recognized these problems faced by NASA for which the currently used RLV technologies call for leap-ahead technologies, new business opportunities in space, and launch cost reduction (currently 25% of the total budget).

(c) Risk reduction in main engine, solid rocket boosters, and thermal protection system by assessment from past data is a direct approach to a safer flight. Unfortunately cost grew with all of these risk reduction undertakings and advancements. Hence, cautious proposition must be undertaken.

(d) The development of a second-generation launch vehicle (non-existing) is still in the conceptual and experimental phases. There could be many propositions and subsequent pursuits. One could be creating a dynamic model to incorporate the interactive concurrent phases of the 2GRLV life-cycle, and predict/advise on the on-going process of development such that a dynamic simulation model can correct the deficiencies in design phase as it progress, before it goes for the expensive build-up/fabrication operations (see Figure 1). In fact, parts of such a concept is already in place in X-series of tests. This phase could be extended to future operation of the 2GRLVs when they will be operational.

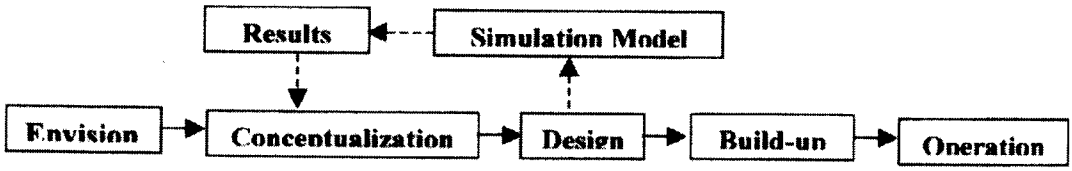

Figure 1. Interfacing simulation into the RLV life cycle model concurrently

(e) Major lookouts should concentrate on business development and planning, technological planning, advancement of development action, and flight and ground experiment.

(f) The payload should consider the shuttle volume utilization, propellant use, and bin-packing approach to load the shuttle.

Conclusions

In addition to above findings and general recommendations, the investigator has gathered many other important information the use of which will reveal many avenues for further study and open new frontiers for innovative research and development in space transportation. Detailed address of these problems and their solution approaches under different scenarios will generate a better understanding of the system life-cycle problems, and eventually open a roadmap for decision-making at different phases of operations.

Acknowledgements

The author is thankful to Eric J. Shaw and Joe Hamaker of NASA Marshal Space Flight Center for facilitating this research. He is also thankful to Grant Cates for extending his time and effort in showing the KSC/OPF and generously proving with numerous data for this study. The author has also benefited from fruitful discussions with Martin Steele of KSC, and Monsooreh Mollaghasemi and Ghaith Rabadi of UCF. This research was funded by the NASA-ASEE Summer Faculty Program's Contract *#NAG8-1786.*

References

[1] Cates, G., "The space shuttle flight rate and discrete event simulation modeling: a Term paper," IE Dept., University of Central Florida, Orlando, FL 32765, April 10, 2001.

[2] Cates, G., Mollaghasemi, M., Rabadi, G., and Steele, M., " Macro-level simulation model of space shuttle processing," *Symposium on Military, Government and Aerospace Simulation*, sponsored by the Society for Computer Simulation International, Seattle, WA, April 22-26, 2001.

[3] Cates, G., Mollaghasemi, M., Rabadi, G., and Steele, M., ARENA model for shuttle processing, University of Central Florida, Orlando, FL; June 18, 2001.

[4] Fragola, J. and Maggio, G., "Using heritage to forecast: future vehicle risk," Science Application International (SCI) Corporation, presented to KSC, August 19, 1999.

[5] *Information Summaries*: *Countdown! NASA Launch Vehicles and Facilities*, IS-2000-09-31-*KSC*, Kennedy Space Center, Cape Canaveral, FL 32899, September 2000.

[6] Space shuttle main engine (SSME) enhancements, *NASA Facts*, *FS-2000-07-159-MSFC*, Marshall Space Flight Center, Huntsville, AL 35812, August 2000.

[7] *Space Shuttle Program*, Website materials at http://shuttlepayloads.jsc.nasa.gov/ collected at Marshall Space Flight Center, Huntsville, AL 35812; June 5, 2001.

[8] The Space Launch Initiative: Technology to pioneer the space frontier, *NASA Facts*, *FS-2001-06-122-MSFC*, Marshall Space Flight Center, Huntsville, AL 35812, June 2001.

[9] The payload Operations Center: Integration and Management of Space Station Science Operations at NASA's MSFC, *NASA Facts*, *FS-2001-03-65-MSFC*, April 2001.

2001

NASA/ASEE SUMMER FACULTY FELLOWSHIP PROGRAM

MARSHALL SPACE FLIGHT CENTER
THE UNIVERSITY OF ALABAMA IN HUNTSVILLE

COMPARISONS OF KINEMATICS AND DYNAMICS SIMULATION SOFTWARE TOOLS

Prepared By:	Yeu-Sheng Paul Shiue
Academic Rank:	Associate Professor
Institution and Department:	Christian Brothers University Mechanical Engineering Department
NASA/MSFC Directorate:	Engineering Directorate
MSFC Colleague:	Geoffrey Beech

Introduction

Kinematic and dynamic analyses for moving bodies are essential to system engineers and designers in the process of design and validations. 3D visualization and motion simulation plus finite element analysis (FEA) give engineers a better way to present ideas and results. Marshall Space Flight Center (MSFC) system engineering researchers are currently using IGRIP from DELMIA Inc. as a kinematic simulation tool for discrete bodies motion simulations. Although IGRIP is an excellent tool for kinematic simulation with some dynamic analysis capabilities in robotic control, explorations of other alternatives with more powerful dynamic analysis and FEA capabilities are necessary. Kinematics analysis will only examine the displacement, velocity, and acceleration of the mechanism without considering effects from masses of components. With dynamic analysis and FEA, effects such as the forces or torques at the joint due to mass and inertia of components can be identified.

With keen market competition, ALGOR Mechanical Event Simulation (MES), MSC visualNastran 4D, Unigraphics Motion+, and Pro/MECHANICA were chosen for explorations. In this study, comparisons between software tools were presented in terms of following categories: graphical user interface (GUI), import capability, tutorial availability, ease of use, kinematic simulation capability, dynamic simulation capability, FEA capability, graphical output, technical support, and cost. Propulsion Test Article (PTA) with Fastrac engine model exported from IGRIP and an office chair mechanism were used as examples for simulations.

The Evaluations Behind the Ratings

Evaluation of all software tools were conducted on the same computer equipped with Pentium III 993 MHz processor and 512 MB memory under Windows NT environment. The **GUI** is based on user-friendly interface of the software. **Import Capability** is the evaluation of handling different file format such as IGES, STL, and STEP. **Tutorial Availability** is based on the tutorial available on the software CD or company website. **Ease of Use** focuses on file conversion, model building, setup simulation parameters, and run simulations. **Kinematics and Dynamics Simulation Capabilities** are based on the relative process time, the motion simulation output, and the ability to export force, torque, acceleration, and other data. **FEA Capability** is an assessment of FEA capability including transferring from dynamic results to FEA environment. **Graphical Output** reflects the capability of producing video clips, image files, data chart, and simulation report. **Technical Support** is an assessment of company's customer services during test period. **Cost** is the approximate price for professional edition of the software on current market. **Overall Score** is the average of all categories. Test results are shown in Table 1 below.

Table 1: Rating of Software Tools

Excellent★★★★★ Very Good ★★★★ Good★★★ Fair ★★ Poor ★

Item	Category	ALGOR Mechanical Event Simulation	MSC visualNastran 4D	Unigraphics Motion+ (ADAMS solver)	Pro/MECHANICA

1	GUI (Graphical User Interface)	★★★★	★★★★	★★★★	★★★★
2	Import Capability (IGES, STL, STEP, ...)	★★★	★★★★★	★★★★	★★★★★
3	Tutorial Availability	★★★★	★★★★	★★★★★	★★
4	Ease of Use	★★	★★★★★	★★★	★★★
5	Kinematics and Dynamics Simulation Capabilities	★★★	★★★★	★★★★	★★★★
6	FEA Capability	★★★★	★★★★	★★	★★★
7	Graphical Output Capability	★★★★	★★★★★	★★★★	★★★★
8	Technical Support	★★★★	★★★★	★★★★	★★★★
9	Cost	$18,130	$8000	$15,000	$19,990
10	Overall Score	★★★	★★★★★	★★★★	★★★★

Evaluation Notes

Graphical User Interface -- All software evaluated are compatible to Windows NT environment with Windows GUI. However, each of them has different background color and style. ALGOR/MES needs to switch back and forth from CAD interface/FEA environment to its SUPERDRAW III, which is a separate program. Rests of the software are all running within the same window.

Import Capability -- All software tested are able to import IGES, STL, DXF, and other file formats. However, ALGOR/MES does not support STEP format in the tested version. It is not able to retrieve STL files generated from IGRIP and Pro/E. After importing STL file format into Pro/ENGINEER or Unigraphics, surface and line selection become unavailable to the imported features. Only visualNastran 4D can select surfaces of STL imported features. IGES file format is much larger than STL and STEP in terms of file size. Pro/ENGINEER handle large size file better than Unigraphics in terms of refreshing time. ALGOR and visualNastran handle large IGES file pretty well and both have direct interface with Pro/ENGINEER.

Tutorial Availability -- ALGOR/MES and visualNastran both have step-by-step tutorial on CD and on-line help. Unigraphics also has on-line step-by-step tutorial and documentation. Pro/ENGINEER has good on-line documentation. However, step-by-step tutorials are not available on-line or on the web. Purchase is available through another publisher (e.g. Schroff Development Corporation).

Ease of Use -- MSC visualNastran 4D is the most easy to use among all. It is because visualNastran 4D will be able to import both STL and IGES format and snap on surface to create coordinates for assembly and joints. Based on directions of coordinates to create joints and loads

make it easy to align and build the model. After finishing tutorial excises, all necessary functions are pretty much covered. Simulations were performed in no time.

On the other hand, ALGOR/MES needs to mesh every part after import. If the STL or IGES file misses some lines or surfaces during export or import, it will not be able to get an error-free mesh. Mesh size and method are also a factor of success. After meshing the part after import, it cannot be remeshed in SUPERDRAW as described in the documentation. Connections between parts (groups) are based on the mesh grids. Therefore, it makes it difficult to get the assembly correctly. It is hardly to get the job done without previous experiences or proper training from ALGOR. Due to this reason, sales representative at ALGOR was hesitated to give out evaluation software at the beginning of evaluation period.

Unigraphics Motion+ and Pro/MECHANICA require more keystroke and steps to get the assembly, joints, and all other parameters done. Both packages are separate embedded modules of Unigraphics and Pro/ENGINEER respectively. Simulations were carried out after seeking help from technical support. It needs extensive previous experiences with Unigraphics or Pro/ENGINEER to do an effective job. Therefore, it will be better to have proper training before trying to build and run the simulations.

Kinematic and Dynamic Simulation Capability -- Kinematic and dynamic simulations were performed using MSC visualNastran 4D, Unigraphics Motion+, and Pro/MECHANICA. All three of them will be able to out force, acceleration, torque, and other data. However, visualNastran 4D output its graphs as a child-window in the main-window and the other two output their data to external software (e.g. EXCEL). Assembly was not successful in ALGOR/MES due to mesh and connection problems. Therefore, simulation was not able to perform using ALGOR/MES. It is believed that the task can be done with proper training from ALGOR.

MSC visualNastran 4D uses MSC.Nastran solver for analysis. Unigraphics Motion+ used ADAMS solver, which implement Newton's law of motion and the system of Euler-Lagrange equations of motion. It is the faster solver comparing to other three packages. ALGOR Mechanical Event Simulation combines static equilibrium and Newton's law of motion for dynamic analysis. Pro/MECHANICA implements Kane's method for dynamic analysis.

FEA Capability -- MSC visualNastran 4D uses Nastran Solver for FEA. However, it will only handle linear analysis. For nonlinear analysis, model has to be exported to MSC Nastran for analysis. Real-time motion simulations and FEA can be performed simultaneously. ALGOR/MES is basically a FEA package with motion simulation capability. It has both linear and nonlinear analysis capabilities. Unigraphics does not have its own FEA solver. Unigraphics v16 supports Nastran and ANSYS while v17 add another support of Structures PE. Since Unigraphics does not have its own FEA solver, either Nastran or ANSYS solver has to be installed on the system. Pro/MECHANICA use its own FEA solver for structure and thermal analysis. Unigraphics and Pro/MECHANICA both need to transfer results from motion analysis to structure module before performing FEA.

Graphical Output -- All packages tested will export video clips, images, and graphs. MSC visualNastran 4D can include one graph output in the video clip and perform real-time demonstration that makes the package more attractive. Photo rendering will only render sheet surfaces and solid bodies. Pro/MECHANICA and Unigraphics have the capability to output MPEG file instead of AVI format. ALGOR and Pro/MECHANICA will able to output its results in HTML format with images.

Technical Support -- Customer service or technical support from all software companies mentioned above were friendly and courteous. MSC visualNastran 4D and ALGOR/MES tested were 2-week evaluation version. It took 5 weeks to get the MSC visualNastran 4D evaluation software due to communication and process issues. ALGOR has evaluation software available on their website. However, it requires password to install the software. ALGOR sales representative was anxious and helpful but hesitated to give out the password at the beginning. ALGOR also has on-line live demo available through website.

Cost -- Both prices for MSC visualNastran 4D and ALGOR are one time fee with upgrade available. Pro/MECHANICA and Unigraphics Motion+ are yearly license and renewable. Price for Pro/MECHANICA includes structure/vibration and motion simulation without thermal analysis. Price for Unigraphics Motion+ does not include Nastran or ANSYS solvers. Price may be different in another time frame.

Conclusions and Recommendations

Considering all factors above, all packages tested have capabilities in kinematics, dynamics, and finite element analysis. However, the author would recommend MSC visualNastran 4D because of ease of use, excellent graphical outputs, combinations of kinematics, dynamics, and FEA in the same Windows environment. Unigraphics Motion+ will perform kinematics and dynamics analysis faster than MSC visualNastran. However, Unigraphics needs external FEA solver to implement structure analysis. Pro/MECHANICA has good kinematic and dynamics analysis solver but its FEA capability is limited to linear and small deformation problems. For large deformation or nonlinear problems, Pro/MECHANICA does not handle well compared with ANSYS or NASTRAN. ALGOR has very attractive on-line live demonstration for customer through their website. Nevertheless, it needs previous FEA background and proper training of the software to run simulations.

Regarding hardware for simulations, the author would recommend a machine with at least 1 GB memory and 1 GHz processor or above. Faster and larger capacities hard drive and OPENGL supported video card will be a must.

Evaluation results obtained in this study might be different depending on preferences and previous experiences of the evaluator.

Acknowledgements

The author would like to thank Mr. Geoffrey Beech, Mr. Tim Walton, and all personnel in Engineering Directorate for providing a quiet but stimulating work environment and support.

2001

NASA/ASEE SUMMER FACULTY FELLOWSHIP PROGRAM

MARSHALL SPACE FLIGHT CENTER

CONSEQUENCES OF COUPLED ELECTROMAGNETIC-GRAVITATIONAL FIELDS

Prepared By:	Larry Smalley
Academic Rank:	Professor
Institution and Department Physics Department	The University of Alabama in Huntsville
NASA/MSFC Directorate:	Flight Projects
MSFC Colleague:	Jonathon Campbell

Introduction

In the late 1980s there was a flurry of activities involving the newly discovered high Tc superconductors in the development of new devices such as more efficient current transmission, transformers, generators, and motors. One such developmental project by Podkletnov in 1992 [1] noted some small, anomalous gravitational behaviorS. A following paper by Podkletnov 1995 (unpublished) [2] provided data with larger effects using a larger (~ 25 cm) Superconducting disk. Unfortunately this disk was extremely fragile and was broken beyond repair. To date, these experiments have not been successfully repeated because of the difficulties of producing stable, durable (and fired) superconducting disks. This problem with firing these disks has been solved by Li [3] (see: www.supergemlab.com). What remains is to install the disk in "motor", at superconducting temperatures in the presence of appropriately tailored magnetic fields.

Theory

There are prior and parallel, independent theoretical investigations to the work of Podkletnov by Li and Torr [4] [5], Smalley and Kirsch [6], and Torr and Li [7] that discuss the mechanism for electromagnetic coupling to the gravitational field. These works either assume [4] [5] [7] or predict [6] from first principles an unknown coupling constant between the electromagnetic field and the gravitational field inside matter. It is the works of Li and Torr that has identified the macro quantum state of superconducting of superconductors as the most likely system in which these effect might be observed; whereas Smalley and Krisch have given the theoretical underpinning for the coupling using a fundamental variational calculation of the electromagnetic and the gravitational field in RC spacetime. The use of (RC) geometry is crucial because of the torsion contributions to the connection since it is well known that Riemannian geometry has no constructs either through the metric or the connection $\left\{{}^{k}_{ij}\right\}$ (which is called the Christoffel connection) that could couple directly to the electromagnetic field.[1] An early extension of general relativity was due to Weyl in which he introduces a scalar potential, which acted as a conformal transformation of the connection. This led only to a trivial rescaling of the metric with an undetermined gauge. Thus the extension of the spacetime manifold to RC spacetime seems to be a worthwhile investigation.

The second aspect centers on the type of matter that must be considered. In particular, there must be charge in some form—bound or free. The theory of this particular type of charged matter in a RC spacetime has been considered by Smalley & Krisch [6] in a "first principles," variational coupling of geometry and matter containing a charged spin fluid in which the torsion tensor $S_{ij}{}^{k} \equiv \Gamma_{[ij]}{}^{k}$ is the antisymmetric components[2] of the RC connection $\Gamma_{ij}{}^{k} = \left\{{}^{k}_{ij}\right\} + S_{ij}{}^{k} - S_{j}{}^{k}{}_{i} + S^{k}{}_{ij}$. Note that the connection is not a tensor but the torsion is a tensor. The torsion tensor can be decomposed into two irreducible pieces: the torsion vector $\mathbf{S}_i = S_{ix}{}^{x}$ and a proper (trace-free) torsion $\square_{ij}{}^{k} = S_{ij}{}^{k} - (3/2)\delta^{k}_{[i} S_{j]x}{}^{x}$ where δ^{k}_{j} is the Kronecker delta function. This decomposition

[1] Note that this tensor will be used extensively in this work.

[2] Square brackets $[jk]$ surrounding indices implies antisymmetrization, and curly brackets, $\{jk\}$ imply symmetrization. Do not confuse symmetrization of indices with the Christoffel connection.

will be important in understanding the interaction of the spin fluid with the electromagnetic *and* the gravitational field quantities.

Theoretical Rationale

The use of a Lagrangian based variational principle for a gravitationally based, charged perfect[3] spin fluid [8] provides a precise, fundamental (as opposed to an ad hoc) formulation for the field equations. The solutions to the field equations then give a sound basis for predictions and subsequently definitive, experimental comparison.

This procedure gives individual field equations for the spacetime metric, torsion tensor plus a set of constraint equations, which insure that the spin fluid maintains various continuity relations and constraints. One particularly interesting constraint includes the possibility of both external and internal fields. This means that thermodynamics of the perfect fluid also includes the internal and external contribution from both spin and electromagnetic energy (See ref. 6 for details). [4]

The heart of this calculation rests on the strict observance of the minimal coupling of the electromagnetic field to the geometry. The electromagnetic field is given in Minkowski geometry by a field tensor $F_{jk} = A_{k,j} - A_{j,k}$ where A_k is the electromagnetic, vector potential. This equations is then "lifted" into the more extensive RC geometry by "minimal coupling" to $F_{jk} = A_{k;j} - A_{j;k}$.[5] The minimal coupling leads directly to the most interesting constraint

$$S_k = bA_k \qquad (1)$$

which predicts a direct relationship between the torsion (vector) and the electromagnetic field (vector potential) in the arena of RC geometry. Also the charged, spin fluid interacts with the geometry of spacetime through the proper torsion such that $\square_{jk}{}^{l} = \frac{\kappa}{2}\rho s_{jk}u^{l}$ where $\kappa = 4\pi G$, G is the gravitational constant, ρ is the density, s_{jk}, is the spin (per particle), and u^l is the four-velocity.

The Field Equations

The variation of the Lagrangian gives the gravitational field equation

$$G^{(ij)} - \overset{\bullet}{\nabla}_k(T^{kij} + T^{kji}) = \kappa T^{ij} \qquad (2)$$

where G^{ij} is the Einstein Tensor *in* RC spacetime, $T_{ij}{}^{k} = S_{ij}{}^{k} + 2\delta^{k}_{[i}S_{j]}$, and T^{ij} is the energy-momentum tensor where

$$T^{ij} = T^{ij}{}_{M} + T^{ij}{}_{S} + T^{ij}{}_{EM} + T^{ij}{}_{GF} \qquad (3)$$

where

$$T^{ij}{}_{M} = \rho[(1 + \varepsilon + \frac{p}{\rho}) - \frac{1}{2}m^{ik}F_{kl}]u^{i}u^{l} + pg^{ij} \qquad (4)$$

---

[3] Here, "perfect" means that the fluid obeys certain conservation law such as continuity, charge conservation, and metric constraints, which insure that the parameterization of spin fluid is consistent with the metric.

[4] In quantum mechanics, it is necessary to include the interactions of internal spin with the external magnetic fields as well as the internal magnetic fields of the of the spin fluid itself. In particular, this is necessary for correctly describing the thermodynamics of the system.

[5] The semicolon ";" refers to the covariant derivative "4_k" in RC spacetime, and minimal coupling refers to the simplest extension of Riemannian geometry to RC spacetime based upon the concept of minimal coupling by Einstein.

is the matter energy-momentum of a perfect fluid in the presence of the electromagnetic field, where ε is the energy, p is the pressure, and $m^{kl} = \chi s^{kl}$ is the magnetic dipole moment and χ is the susceptibility; the spin energy-momentum

$$T^{ij}{}_S = 2\rho u^{(i}s^{j)k}\omega_k + \overset{*}{\nabla}_k \rho u^{(i}s^{j)}{}_k] - \rho\omega_k{}^{(i}s^{j)k} \tag{5}$$

where $\omega_k{}^i$ is the frame angular velocity; the energy-momentum tensor of the electromagnetic field

$$T^{ij}{}_{EM} = -[F^{ki}F^j{}_k + \frac{1}{4}g^{ij}F^{kl}F_{kl} + M^{k(i}B_k^{j)}] \tag{6}$$

and

$$T^{ij}{}_{GF} = -(\frac{8}{3\kappa})(S^iS^j - \frac{1}{2}g^{ij}S^kS_k) \tag{7}$$

is the gauge fixing term that insures the overall gauge invariance of the Lagrangian.

It is instructive to write the Einstein tensor into its metric, proper torsion, and torsion vector parts so that

$$\begin{aligned} G^{(ij)} - \overset{*}{\nabla}_k(T^{ki} + T^{kj}) &= G^{ij}(\{\}) + 2\hat{S}^{(i}{}_{lx}\hat{S}^{j)lx} + \hat{S}^{(i}{}_{lx}\hat{S}^{j)xl} - \hat{S}^{xli}\hat{S}_{xl}{}^{j)} \\ - g^{ij}(\hat{S}^{lmx}\hat{S}_{lmx} + 2\hat{S}^{lmx}\hat{S}_{lmx}) - \frac{3}{8}(S^iS^j - \frac{1}{2}g^{ij}S_kS^k). \end{aligned} \tag{8}$$

Note that the gauge fixing term in Eq. (7) cancels the same term in Eq. (8). This is the typical case that the gauge cannot influence the physics described by the field equation no matter how it's displayed.

Some Consequences

1. Spin energy momentum

The driving "power" of this system is the constraint between the electromagnetic vector potential and the torsion vector (Eq. 1), which occurs in the spin energy momentum tensor (Eq. 5). If the spin energy-momentum tensor is rewritten in terms of the RC covariant derivatives that only contain the proper torsion $\overset{*}{\nabla}_k$ plus a remainder term that involves only the torsion vector, then this gives

$$T^{ij}{}_S = \hat{T}^{ij}{}_S - \frac{4}{3}b\kappa u^{(i}s^{j)k}S_k = \hat{T}^{ij}{}_S - \frac{4}{3}b\kappa u^{(i}s^{j)k}A_k \tag{9}$$

where the torsion constraint was used in the last step. To check the validity of this equation, set $A_k = 0$. It follows that there is no electromagnetic field and consequently the torsion vector $S_k = 0$, $\hat{T}^{ij}{}_S$ is just the usual spin energy momentum of a perfect fluid with spin density when there is no electromagnetic field, and the magnetic $T^{ij}{}_M$ and the gauge fixing $T^{ij}{}_{GF}$ terms disappear.

The above results directly prove that the assumption of Li & Torr [4][5] is justified for the spin fluids, and in particular, bound spin fluid inside superconductors. If this isn't worth a Nobel Prize, nothing is!

2. Post-Newtonian analysis of the charged, spin fluid, field equations

One of the overriding problems with investigating the field equation in the post-Newtonian approximations is in the treatment of spin/angular momentum. The prevailing wisdom concludes that the effects of spin occurred at the order $\eta(v^6)$ (v is the velocity) that is far beyond the $\eta(v^2)$- $\eta(v^3)$ level of PPN approximation.[6] By inference of that wisdom, the torsion (or spin density in this work) would be of relatively little important in neutron star structure [10] [11]. However, later work of Castagnino, et al [12] showed that if the structure of the source is known to $\eta(v)$, then the presence of spin can be detected, and that the theory can be verified to $\eta(v^2)$. Unfortunately they did not apply their results to any models. Thus this implication implies that the effect of spin and therefore the torsion (noted here) are detectable. The proof of this assertion lies in the work of Brown [9] who noted, that in carrying out the calculations for the spin fluid, and in redoing the PPN approximation with the appropriate assumptions for spin, it is necessary to introduce a *new* potential Σ_k into the time-space component, g^{0k} of the Metric where Σ_k is the solution of the differential equation

$$\nabla^2\Sigma_k = -2\pi(\rho \overset{1}{s_k}^m)_{,m} \approx \vartheta(v^3) \qquad (10)$$

where the density $\rho \approx \eta(v^2)$ and the spin (per particle) $\approx \eta(v)$. this implies that the third order correction to g^{0k} becomes

$$\overset{3}{g}_{0k} = \overset{PPN}{g}_{0k} - 4\overset{3}{\Sigma}_k \qquad (11)$$

and all other PPN parameterization of the metric remains the same. This means that is now possible to obtain effects of charged spin fluids to the level of the PPN approximation looking at field equation for the spin fluid, Eq. (2), minus the effects of the "gauge fixing" term which cancels.

3. Consequences for the Local Lorentz Frame

From the torsion vector Eq. (1), it is then evident that electromagnetic vector potential A_k couples the electromagnetic field directly to the gravitational field G^{ij} through Eq. (1), and subsequently, the spin energy momentum tensor Eq. (9) to the metric as shown by Brown [9].

Since the spin interacts with the metric at least at $\eta(v^3)$ or greater, it is obvious that the electromagnetic field *can* **shape** the gravitational.

In this work we have referred to the charged spin fluid, but it should be remembered that this works for *both* **free** or **bound** charge spin fluids. The macroscopic quantum state of the ion rotation in superconductors [4] is such a state. This means that we can, given the appropriate energy sources, alter the local gravitational field, or in other words, manipulate the local Lorentz frame. Now all that is necessary is to figure out how to open up a wormhole and develop the energy sources that will, though the spin fluid, *drive* the gravitational field.

References

[1] E. Podkletnov and R. Nieminen, *Physica C*, **203**, 441 (1992).

[6] Recall that in the PPN approximation, the time g_{00} and spatial g_{xy} components are to order $\eta(v^2)$; and the space-time components, to $\eta(v^3)$.

[2] Eugene Podkletnov, "Weak gravitation shielding properties of composite bulk YBCO superconductor below 70K under e.m. field." See the LANL database number cond-mat/9701074, v. 3, 16 Sep 1997; unpublished.

[3] J. Wilson, "Taming Gravity," Pop. Mechanics, Oct., 2000.

[4] N. Li & D. Torr, Phys. Rev. D, **43**, 457 (1991).

[5] N. Li & D. Torr, Phys. Rev. B, **46**, 5489 (1992).

[6] L. Smalley, J. Math. Phys., **33**, 1073 (1992).

[7] D. Torr & N. Li, Found. Phy. Lett., **6**, 371 (1993).

[8] J. R. Ray and L. L. Smalley, Phys. Rev D 27, 1381 (1983); Phys. Rev. Lett. **49**, 1059 (1982); **50**, 626E (1983).

[9] J. P. Brown, "The Post-Newtonian Approximation for Self-consistent Perfect Fluids with Spin Density," Ph.D. Thesis, The University of Alabama in Huntsville, (1989).

[10] F. W. Hehl, P. von der Heyde, G. D. Kerlick, and J. M. Nester, Rev. Mod. Phys. **48**, 393 (1976).

[11] F. W. Hehl, P. von der Heyde, and J. M. Nester, Phys. Rev D. **10** (1066).

[12] M.Castagnino, M. L. Levinas, and N. Umerez, Gen. Rel. Grav. **17**, 683 (1985).

2001

NASA/ASEE SUMMER FACULTY FELLOWSHIP PROGRAM

MARSHALL SPACE FLIGHT CETNER
THE UNIVERSITY OF ALABAMA IN HUNTSVILLE

Database Reports Over the Internet

Prepared By:	Dean Lance Smith
Academic Rank:	Assistant Professor
Institution and Department:	The University of Memphis Department of Engineering Technology
NASA/MSFC Directorate:	Engineering
MSFC Colleague:	Rich Wegrich

Introduction

Most of the summer was spent developing software that would permit existing test report forms to be printed over the web on a printer that is supported by Adobe Acrobat Reader. The data is stored in a DBMS (Data Base Management System). The client asks for the information from the database using an HTML (Hyper Text Markup Language) form in a web browser. JavaScirpt is used with the forms to assist the user and verify the integrity of the entered data. Queries to a database are made in SQL (Sequential Query Language), a widely supported standard for making queries to databases. Java servlets, programs written in the Java programming language running under the control of network server software, interrogate the database and complete a PDF form template kept in a file. The completed report is sent to the browser requesting the report. Some errors are sent to the browser in an HTML web page, others are reported to the server.

Access to the databases was restricted since the data are being transported to new DBMS software that will run on new hardware. However, the SQL queries were made to Microsoft Access, a DBMS that is available on most PCs (Personal Computers). Access does support the SQL commands that were used, and a database was created with Access that contained typical data for the report forms.

Some of the problems and features are discussed below.

Problems and Features

Since PDF is text markup language, it would seem appropriate to generate PDF dynamically, much as is done with HTML. However, Adobe licensing agreements preclude this approach, and PDF is considered a proprietary markup language.

An approach permitted by Adobe is to generate a form template in an extension to PDF called FDF and dynamically insert the data [1-4]. Adobe supplies FDF access software for C/C++, Visual Basic, Perl, and Java compilers that will open template files, insert data into blank fields, and perform other tasks associated with using FDF documents such as data entry and report forms.

Another approach is to create an intermediate text file that contains the field data [5]. Acrobat Reader reads the intermediate file, extracts the field data, uses a reference in the file to read the form file, inserts the data in the form, and displays the result. This was the approach used to generate the data base forms. Both the Java and Perl interfaces were tried, but the interfaces were not compatible with the Windows 98 system used for development.

The template for the test reports was created with Microsoft Word 2000 and saved in the Word's (.doc) format. The Word document was converted to PFD with Adobe Acrobat. Version 4.0 of Acrobat permits fields (groups of data) in PDF files to be tagged (given an identifier or name) so that the tag can be used to retrieve or insert data in the form, converting the PDF document to an FDF document.

Java servlets [6-9] were used on the server to read the data from the database and inset it in the FDF forms. Java is a very popular programming language for web software even though it is not an industry standard. It is object oriented and strong typing [6]. Compilers are available for free over the web directly from Sun Microsystems [10].

Java should not be confused with JavaScript. JavaScript is a weak typing, interpreted language supported by Microsoft Internet Explorer and Netscape Navigator web browsers [7].

An attempt was made to scan the existing paper forms and convert them to text with OCR (Optical Character Recognition) software built-in to Acrobat. The conversion was successful, although a lot of errors needed to be corrected manually. Unfortunately, Acrobat's OCR software failed to correctly identify all of the fields in the recovered text, and that limited the success of this approach. The only way to correct the errors was to generate a reasonable facsimile of the original form in a word processor, then convert the document to a PDF form with Acrobat.

Several peculiarities were observed when using Java 1.3.1 to compile the servlets. The complier could not correctly interpret the PATH command in MS-DOS in Windows 98 and locate the servlet.jar archive file that contains the parent class for the servlets. The MS-DOS SET command apparently works. However, the classpath option for the compiler is recommended [11]. A typical example invoking the compiler using the classpath option is

javac –classpath c:/jdk1.3.1/lib/servlet.jar source.java

where javac is the name of the executable form of the Java complier, /jdk1.3.1/lib/ is the path through the directories or folders in MS-DOS to servlet.jar, the Java archive file containing the parent for the servlet class, and source.java is the source code for the servlet. Note that the compiler expects forward slashes as separators between directory or folder names, not back slashes, which is the convention in Microsoft operating systems. The complier, javac, can be located by Windows 98 if the MS-DOS path is set correctly in the autoexec.bat file, by issuing the path command prior to calling the compiler, or by preceding the compiler name with the correct path.

Allaire's Jrun was used as a local web server for the servlets. A free developer's version is available over the web [12]. It is supplied in machine code and will run under Windows 98. However, the developer's version is limited to three concurrent connections.

Servlets can be tested by copying them to the directory

c:\Program Files\Allaire\JRun\servers\default\default-app\WEB-INF\classes

where the directory, Program Files, is the directory where Jrun is installed in Windows 98. The servlets are invoked by issuing the URL

http://localhost:8100/servlet/MyFirstServlet

where MyFirstServlet is the name of the servlet being run. It isn't necessary to change the configuration of the default server in Jrun to view the servlets, although some sets of installation instructions indicate otherwise.

Tomcat will also support servlet development and is also available over the web in both binary and Java virtual machine code [13]. Unfortunately, the binary code is for a Windows NT and not a Windows 98 system. The BAT files for Microsoft operating systems that come with the Java virtual machine version would not work on Windows 98. While they could have been modified so that they would work, the time required to make the modifications was excessive.

Micosoft Access was used to supply the data that tested the forms. SQL (Sequential Query Language) is used to extract the data from the Access. SQL is an industry standard data base access language that will work with most popular databases. It is quite easy to call up new interface drivers to a different vendor's DBMS software. It is also quite easy to change the field names in the software to accommodate new or revised forms.

The report request form uses an HTML form to get the data from the user. JavaScript is embedded in the form to assist the user in entering the data correctly and do some error checking at the browser. Care was taken to use HTML tags and JavaScript common to both Internet Explorer and Netscape Navigator. (E.g. The tag INPUT of TYPE=BUTTON, common to both Explorer and Navigator, was used rather than the tag BUTTON, which is supported only by Internet Explorer.) Most users of the web use one of these two browsers. The forms were tested with both Navigator and Explorer to insure that the forms would work with both browsers.

Conclusions and Recommendations

The approach works well even though there were several unexpected difficulties developing the software. The type fonts on the new forms are close to the hand lettered type fonts on the forms they replace. Using a computer to generate the forms is both faster and cheaper, particularly since the data is already in the database. Generating the reports is convenient since they can be generated on any computer connected to the web that has access to Adobe Reader, and most desk top computers have that access.

The software was not tested over the web, only on a local server. It is possible that the software may have difficulty locating the template file over the web. If this is the case, the template file will have to be downloaded along with the intermediate file that calls the template file.

It is recommended that work continue on the project to covert all of the report forms to the new format.

Acknowledgments

A special thanks to Rich Wegrich, MSFC Colleague, for his vision and guidance. Ginger Pierce of CSC helped set up Acrobat, did the scanning of the forms, and gave much useful advice on Acrobat. Linda Huber, also of CSC, gave much helpful advice on DBMSs, and SQL.

References

[1] Anon., "Adobe Solutions Network: Developer Program, Acrobat Toolkit-Version 5", Adobe Systems, Inc., San Jose, CA, http://partners.adobe.com/asn/developer/acrosdk/forms.html.

[2] Anon., "Adobe Solutions Network: Developer Program, Acrobat FDF Toolkit – Version 4.05," Adobe Systems, Inc., San Jose, CA, http://partners.adobe.com/asn/developer/acrosdk/forms405.html.

[12] Anon., "Allaire Jrun,", Allaire-Macromedia, Inc., http://www.allaire.com/products/jrun/.

[3] Anon., "FDF Data Format Toolkit Overview," Version 5.0, Technical Note 5191, Adobe Systems, Inc., San Jose, CA, June, 2001. (Available at http://partners.adobe.com/asn/developer/acrosdk/docs/fdftk/FDFToolkitOverview.pdf.)

[4] Anon., "Forms Data Format Toolkit Reference", Technical Note 5194, Version: Acrobat 5.0, Adobe Systems, Inc., San Jose, CA, June, 2001. (Available at http://partners.adobe.com/asn/developer/acrosdk/docs/fdftk/FDFToolkitReference.pdf.)

[5] Anon., "Forms Data Format," Appendix H, "Portable Document Format Reference Manual, Version 1.3," Adobe Systems, Inc, San Jose, Ca, March 11, 1999, pp. 485-494 (Available at http://partners.adobe.com/asn/developer/acrosdk/docs/pdfspec.pdf)

[10] Anon., "Java 2, Standard Platform, Version 1.3", Sun Microsystems, Inc., Palo Alto, CA, http://java.sun.com/j2se/1.3/.

[11] Anon, "Setting the class path," Sun Microsystems, Palo Alto, CA, http://java.sun.com/j2se/1.3/docs/tooldocs/win32/classpath.html..

[13] Anon., "The Jakarta Project," Apache Software Foundation, Forest Hills, MD, http://jakarta.apache.org/.

[9] Avila, John, *Server-Side Java Programming for Web Developers*. El Granada, CA: Scott/Jones, Inc., 2001. (ISBN 1-57676-042-1)

[8] Callaway, Dustin R., *Inside Servlets, Server-Side Programming for the Java Platform*, 2nd ed. Boston: Addison-Wesley, 2001. (ISBN 0-201-70906-6)

[6] Dietel, Harvey M. and Paul J. Dietel, *Java, How to Program*, 3rd ed. Upper Saddle River, NJ: Prentice Hall, 1999. (ISBN 0-13-012507-5)

[7] Hall, Marty and Larry Brown, Core Web Programming, 2nd ed. Upper Saddle River, NJ: Prentice-Hall, 2001. (ISBN 0-13-089793-0)

2001

NASA/ASEE SUMMER FACULTY FELLOWSHIP PROGRAM

MARSHALL SPACE FLIGHT CENTER
THE UNIVERSITY OF ALABAMA IN HUNTSVILLE

GENETIC OPTIMIZATION OF A TENSEGRITY STRUCTURE

Prepared By:	Jaime R. Taylor
Academic Rank:	Associate Professor
Institution and Department:	Austin Peay State University Physics
NASA/MSFC Directorate:	Engineering
MSFC Colleague:	Jim Steincamp

Introduction

Marshall Space Flight Center (MSFC) is charged with developing advanced technologies for space telescopes. The next generation of space optics will be very large and lightweight. Tensegrity structures are built of compressive members (bars), and tensile members (strings). For most materials, the tensile strength of a longitudinal member is larger than its buckling strength; therefore a large stiffness to mass ratio can be achieved by increasing the use of tensile members[8]. Tensegrities are the epitome of lightweight structures, since they take advantage of the larger tensile strength of materials.

The compressive members of tensegrity structures are disjoint allowing compact storage of the structure. The structure has the potential to eliminate the requirement for assembly by man in space; it can be deployed by adjustments in its cable tension. A tensegrity structure can be more reliably modeled since none of the individual members experience bending moments. (Members that experience deformation in more than one dimension are much harder to model.) Structures that can be more precisely modeled can be more precisely controlled[8].

Furthermore, an astoundingly wide variety of natural systems, including carbon atoms, water molecules, proteins, viruses, cells, tissues and even human and other living creatures are tensegrity structures[2]. Through the process of evolution, nature continually improves the design of living creatures for the environment they live in. Since tensegrities are nature's structure of choice, it is conceivable that they have other benefits we are unaware of.

A. Keane and S. Brown designed a satellite boom truss system with an enhanced vibration performance. They started with a standard truss system, Figure 1, then used a genetic algorithm to alter the design, Figure 2, while optimizing the vibration performance. An improvement of over 20,000% in frequency-averaged energy levels was obtained using this approach[3].

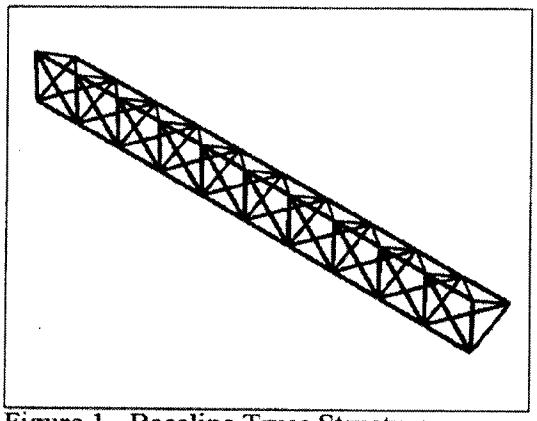

Figure 1. Baseline Truss Structure.

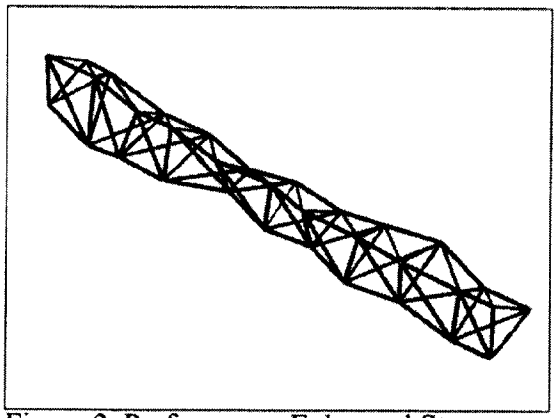

Figure 2. Performance Enhanced Structure.

In this report an introduction to tensegrity structures is given, along with a description of how to generate the nodal coordinates and connectivity of a multiple stage cylindrical tensegrity structure. A description of how finite elements can be used to develop a stiffness and mass matrix so that the modes of vibration can be determined from the eigenvalue problem is shown. A brief description of a micro genetic algorithm are then presented.

What is a Tensegrity Structure?

According to Pugh, a tensegrity (tension and integrity) structure consists of discontinuous compression members suspended by a continuous network of pure tension members all of which are pin-jointed[7]. Figure 3 shows a 2D tensegrity structure that fits this definition. C2T4 stands for 2 compressive members, bars, and 4 tension members, cables. Skelton defines Class k Tensegrity structures, where k is the maximum number of compressive members connected at the nodes. Figure 3 is a class 1 structure and Figure 4, a C4T2 structure, as a class 2 tensegrity structure[8].

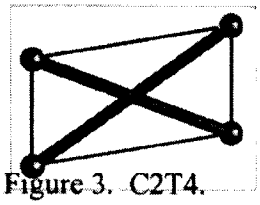

Figure 3. C2T4.

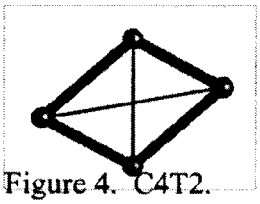

Figure 4. C4T2.

A detailed description on how to find the shape of a multi-stage cyclic-right-cylindrical-tensegrity is presented by Murakami and Nishimura[6]. Figure 5 shows a 4 stage, 6 bar tensegrity structure.

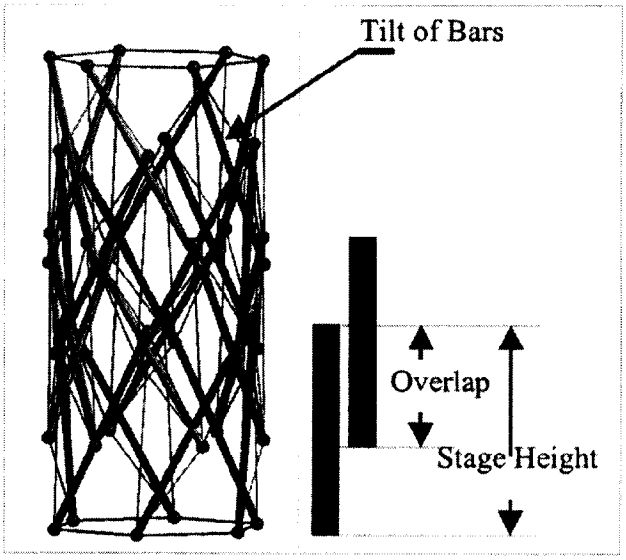

Figure 5. A 4 Stage, 6 Bar Tensegrity Structure.

A tensegrity structure can be modeled in the same fashion as a truss structure using finite elements. The difference between modeling a truss and tensegrity structure is that the tension members cannot undergo compression. Figure 6a shows the forces, $\boldsymbol{F}$, and displacements, $\boldsymbol{u}$, for a bar or tension member. A member, either bar or tension, is modeled as a spring with lumped masses on each end, Figure 6b. In Figure 6a xy are the global coordinates and $\overline{xy}$ are the local coordinates. The relationship between the local and global coordinates are given in Equation Set 1. $\{q\}$ is the vector representation of the displacements $\{u_1, v_1, u_2, v_2\}$. [T] is the transformation matrix composed of $\cos(\phi)$ and $\sin(\phi)$[5].

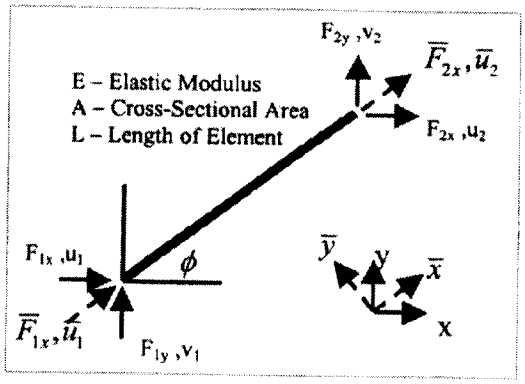

Figure 6a. Finite Element Model.

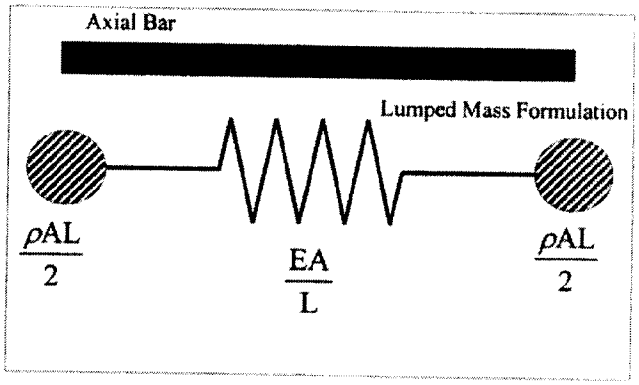

Figure 6b. Physical Model of Elements.

$$\begin{Bmatrix} \overline{u}_1 \\ \overline{v}_1 \\ \overline{u}_2 \\ \overline{v}_2 \end{Bmatrix} = \begin{bmatrix} c & s & 0 & 0 \\ -s & c & 0 & 0 \\ 0 & 0 & c & s \\ 0 & 0 & -s & c \end{bmatrix} \begin{Bmatrix} u_1 \\ v_1 \\ u_2 \\ v_2 \end{Bmatrix} \qquad \begin{matrix} c = \cos(\phi) \\ s = \sin(\phi) \end{matrix} \qquad \begin{matrix} \{\overline{q}\} = [T]\{q\} \\ \{\overline{F}\} = [T]\{F\} \end{matrix} \qquad (1)$$

The stiffness matrix is given in Equation Set 2.

$$\begin{Bmatrix} \overline{F}_{1x} \\ \overline{F}_{1y} \\ \overline{F}_{2x} \\ \overline{F}_{2y} \end{Bmatrix} = \frac{EA}{L} \begin{bmatrix} 1 & 0 & -1 & 0 \\ 0 & 0 & 0 & 0 \\ -1 & 0 & 1 & 0 \\ 0 & 0 & 0 & 0 \end{bmatrix} \begin{Bmatrix} \overline{u}_1 \\ \overline{v}_1 \\ \overline{u}_2 \\ \overline{v}_2 \end{Bmatrix} \qquad \begin{matrix} \{\overline{F}\} = [\overline{k}]\{\overline{q}\} \\ [k] = [T]^T[\overline{k}][T] \end{matrix} \qquad (2)$$

Once the global stiffness matrix is constructed for an individual element, all the stiffness matrices can be assembled into the total stiffness matrix for the structure. The global mass matrix is constructed in a similar fashion, as shown in the first two columns of Equation Set 3. The last column of equations shows the eigenvalue problem, where ω is the angular frequency of the modes of vibration of the structure.

$$[\overline{m}] = \frac{\rho AL}{2} \begin{bmatrix} 1 & 0 & 0 & 0 \\ 0 & 0 & 0 & 0 \\ 0 & 0 & 1 & 0 \\ 0 & 0 & 0 & 0 \end{bmatrix}; \qquad \begin{matrix} [m] = [T]^T[\overline{m}][T]; \\ \{q\} = \{Q\}\sin\omega t; \end{matrix} \qquad \begin{matrix} \{F\} = [k]\{q\} + [m]\{\ddot{q}\} \\ \{F\} = ([k] - \omega^2[m])\{q\} \\ [0] = ([k] - \omega^2[m])\{q\} \end{matrix} \qquad (3)$$

Micro-Genetic-Algorithm

The goal is now to design a tensegrity structure while minimizing mass, increasing the lowest mode of vibration and maintaining the structural integrity of the tensegrity. The design parameters are n-number of stages, m-bars per stage, s-scale of pre-stress, the overlap between stages and the tilt of the bars (see Figure 5), and the radii of the top and bottom of each stage. A micro-genetic-algorithm is an ideal method for optimizing the structure[4]. (A classic book on genetic algorithm's is Goldberg[1].)

The micro-GA starts with a baseline solution similar to that for the truss system Figure 1. Four new individuals are randomly generated and centered about the baseline solution. The five individuals, four new ones and original "best of breed", are paired up for mating. The "Best" pair is chosen to mate and generate four new individuals; the "best of breed" is kept. This process is repeated, see last column in Figure 7, until the best fit no longer improves, a Restart is then performed. The flowchart for the micro-GA is given in Figure 7.

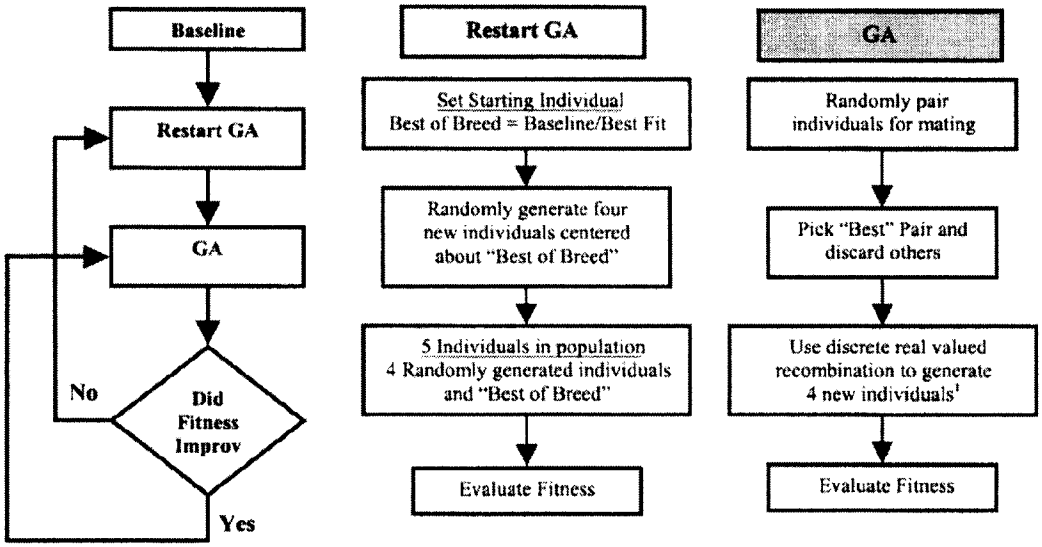

Figure 7. Flow Chart Describing a Micro-Genetic-Algorithm.

Acknoledgements

The author would like to thank Dr. Jim Steincamp for providing the problem and many suggestions for research direction. The author would also like to thank Mr. Mike Stallcup and Mr. John Rakoczy for there contributions to understanding tensegrity strucutres.

References

[1] Goldberg D., *Genetic Algorithms in Search, Optimization and Machine Learning*,Reading, MA, Addison Wesley Longman, Inc.; 1989.

[2] Ingber D. E., "The Architecture of Life," Scientific American: Feature Article, January 1998, pp 48-57.

[3] Keane A. and Brown S., "The Design of a Satellite Boom with enhanced Vibration Performance using Genetic Algorithm Techniques," pp. 107-113 in Proceedings of the Conference on Adaptive Computing in Engineering Design and Control 1996, ed. I. C. Parmee, P.E.D.C., ISBN 0-905227 61 1, Plymouth.

[4] Krishnakumar K., "Micro-Genetic Algorithms for Stationary and Non-Stationary Function Optimization," SPIE Vol. 1196, 1989, pp. 289-296.

[5] Kwon Y. W. and Bang H., *The Finite Element Method using MatLab,"* CRC Press LLC 2000 Corporate Blvd. NW Boca Raton, FL 33431.

[6] Murakami H. and Nishimura Y., "Initial Shape Finding and Modal Analysis of Cyclic Right-Cylindrical Tensegrity Modules," Computers and Structures, 79, 2001, pp. 891-917.

[7] Pugh A., *An Introduction to Tensegrity.* Berkeley, CA: University of California Press; 1976.

[8] Skelton R., Helton J.,Adhikari R., Pinaud J., and Chan W., "An Introduction to the Mechanics of Tensegrity Structure," A Book Chapter in Handbook on Mechanical Systems Design: CRC Press LLC 2000 Corporate Blvd. NW Boca Raton, FL 33431.

2001

NASA/ASEE SUMMER FACULTY FELLOWSHIP PROGRAM

MARSHALL SPACE FLIGHT CENTER
THE UNIVERSITY OF ALABAMA IN HUNTSVILLE

AN EVALUATION OF THE ROSE SYSTEM

Prepared By:	John M. Usher, P.E.
Academic Rank:	Professor
Institution and Department:	Mississippi State University Department of Industrial Engineering
NASA/MSFC Directorate:	Flight Projects
MSFC Colleague:	John Jaap

Introduction

A request-oriented scheduling engine, better known as ROSE, is under development within the Flight Projects Directorate for the purpose of planning and scheduling of the activities and resources associated with the science experiments to be performed aboard the International Space Station (ISS). ROSE is being designed to incrementally process requests from payload developers (PDs) to model and schedule the execution of their science experiments on the ISS. The novelty of the approach comes from its web-based interface permitting the PDs to define their request via the construction of a graphical model to represent their requirements. Additional information on the specifics of ROSE can be found in [1, 2]. Based on an examination of the current ROSE implementation, this paper proposes several recommendations for changes to the modeling component and makes mention of other potential applications of the ROSE system.

Activity and Sequence Modeling

The strength of the current implementation of ROSE is its modeling capability. ROSE provides a robust method of graphically representing the operational requirements of a user's payload. To gain a better understanding of the modeling capabilities of ROSE and the needs of the users in defining their models, this study evaluated the models posed by several PDs, as well as initiated discussions with both PDs and Payload Activity Requirements Coordinators (PARCs). From this study, several recommendations are proposed and listed in Table 1. Each of these is addressed in the discussion that follows.

Table 1. Recommendations for ROSE Modeling Language.

- Add new construct to represent *preemptive* tasks
- Add ability to define a task as *optional*
- Add ability to specifically represent the *disjoint* relation
- Delete the *either* option associated with the *during* relation
- Delete the *advanced* relation
- Use additional visual cues to express relations between graphical entities
- Use shape to supplement use of color for distinguishing between graphical entities
- Add ability to define a power source as either a *source* or *sink*

The nature of some activities permits that their execution may be preempted and later restarted with no penalty. An ability to preempt an activity becomes an important option for activities of long durations that are difficult to handle within a single work cycle. Identifying an activity as preemptive would be an option specified by the user, permitting a scheduler to divide the activity into a set of sub-activities thereby enhancing its flexibility in scheduling the activity. Modeling a preemptive activity would require that the user specify it as an option for an activity and provide some indication of how the activity could be subdivided into a subset of activities (i.e., minimum durations, maximum suspension times, etc.). Modeling a preemptive activity would also require that resource constraints be annotated to indicate that either they are needed only during activity execution and not during the suspended periods between sub-activities, or during the entire span from first to last sub-activity, including suspended periods.

There appears to currently be two indirect methods a user may try to use to model an optional activity. One would be to define an activity of a variable duration with a minimum duration of zero. This would not work properly, in that if an optional activity actually had a minimum time (i.e., 10 minutes), then given the minimum of zero, the scheduler would be permitted to schedule it for less than 10 minutes. Another approach one might use would be to specify an activity with a minimum repetition of zero and a maximum repetition of one. Although theoretically correct it would result in a model that is more difficult to interpret than an activity directly labeled as optional. It would be better to add an option that specifically identifies an activity as optional and then eliminate the ability to specify an activity with zero repetitions to enhance the uniqueness of the modeling language. This approach would enhance the readability of the modeling language and reduce the chance of error.

It seems a bit confusing to indirectly define a *disjoint* relation as an option of the *sequential* relation by specifying the choice of "either" for its precedence. It would be best to add a new relation to the list of possibilities that permits the direct definition of a disjoint relation between activities. Another problem is the capability of the user to specify the relation between two activities as *during* and then further define the precedence between these activities as either. This also seems confusing if not unlikely of ever occurring. It may make more sense for a user to model these activities as overlapping with the either option indicating that either one could start with a simultaneous start identified by a zero separation time. The availability of the *advanced* option for the specification of a relation permits a user to define relations that are redundant with some of the others already defined. The result is a modeling language that yields non-unique models in that it is possible to define the same model multiple ways. The *advanced* option should be deleted or constrained to eliminate the possibility of using it to define relations that are already available using other modeling primitives.

To enhance the readability of the resulting graphical models, more visual cues should be added to more clearly express the relationships between the graphical entities. Some possibilities include placing arrows on arcs to define *sequential* precedence, using a dotted line to represent a *disjoint* relation, and placing arrows on arcs to show the *during* relation. Two of the four sequences I evaluated had errors that would have been eliminated with the addition of such visual cues. Also, to enhance readability of the models, particularly when using grayscale printers, alternative shapes should be used to supplement the use of color for distinguishing between the graphical entities representing activities, sequences, and public services.

Based on an examination of one model it was difficult to distinguish whether a resource associated with an activity was acting as a sink or source for the energy specified in the model. This confusion could be overcome if there was a better understanding of the science, but such a distinction in the model will become important particularly if the modeling language is extended to representing system level activities on-board the ISS.

One last interesting issue arose in the review of a model where an activity in a sequence resulted in a condition that had the potential to impact activities in other unidentified sequences. For example, activity *A* states in its description that one feature of a resource should not be disturbed during the procedure or for 3 hours after its completion. Therefore, the result is that even though

the activity is finished with the resource, the use of the resource is restricted to activities that do not alter this feature of the resource. Modeling of such requirements should be considered.

Enhancing the Modeling Process

Given the powerful modeling language that ROSE provides it is possible for a user to easily create intricate models composed of nested sequences and activities with an abundant number of relations between them. Given the complex nature of the resulting models, it is not unusual for a PD to go through several iterations of their model based on subsequent evaluations of the models by their assigned PARC. The only feedback currently provided by the ROSE system to the PD during development is the graphical model itself and a text based report stating the requirements defined for the sequence and each activity. One of the major problems with is that much of the temporal nature of the model is embedded within the modeling primitive and not visible in the graphical model.

The usefulness of the feedback information would be enhanced if users were provided with a visual means that would allow them to check their models to ensure that the temporal relations represent their actual intended requirements. One possibility is to generate a generic graphical timeline from the model and display it for validation purposes. This timeline would be created against a blank schedule and display the temporal relationships defined within the model. Figure 1 shows one example of such a sequence.

If the PD is able to more easily check their model's expression of their requirements it would reduce the amount of interaction between them and the PARC, the number of iterations, as well as the time required to develop a valid model. Such a mechanism has the potential to also enhance the PD's understanding of the construction of models and use of relations through the availability of timely feedback provided in a familiar representation, the common Gannt chart.

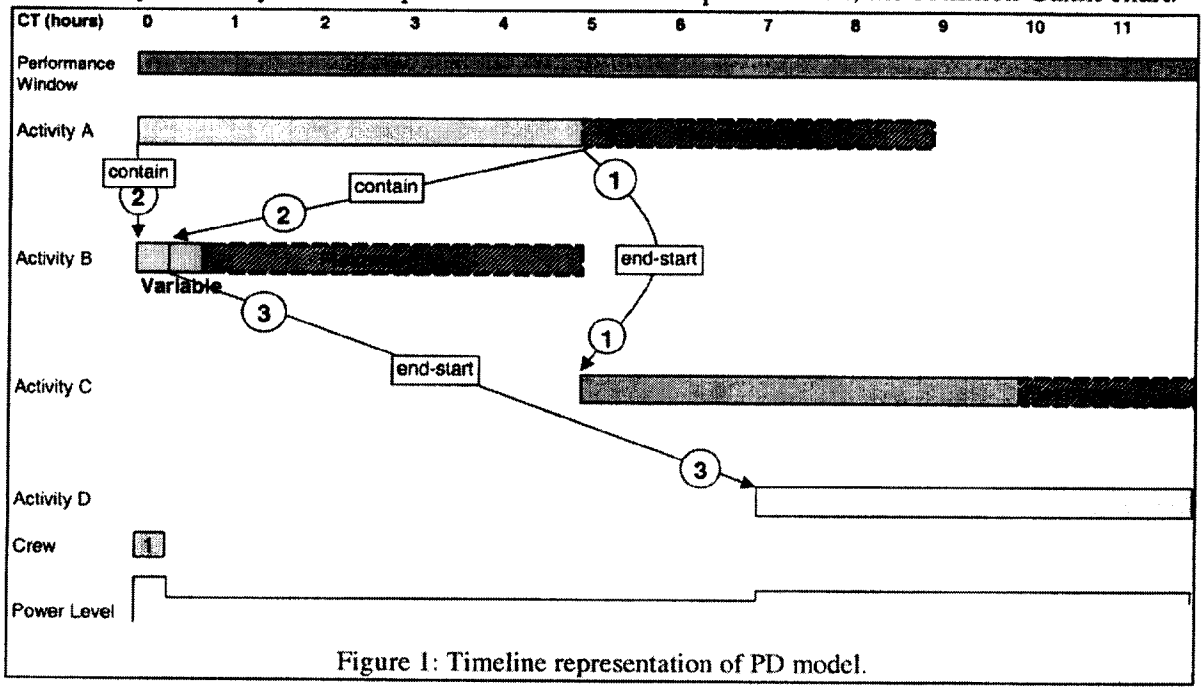

Figure 1: Timeline representation of PD model.

Alternative Applications of ROSE

Given the robust modeling provided by ROSE to express activities and sequences and its future ability to generate schedules from these models, there was an interest in determining what other potential applications would benefit from this tool. Preliminary considerations gave rise to the identification of several potential applications worth further examination. These are the scheduling of hospital operating rooms, airline scheduling, new product development planning, construction planning, and manufacturing scheduling. A focused report on each of these can be found in [3] and [4]. Although similarity exist between each of the applications and that of space activity planning and scheduling, it is believed that the best match would be with new product development planning and construction planning. Exploration of the algorithms used in operating room scheduling may provide some additional insight as well.

Conclusions

The ROSE system has the potential to provide a robust modeling environment with an ability to capture complex payload activity and requirements. Several changes are recommended to further enhance its capabilities and usability. Additional studies are needed to evaluate the user's understanding and use of the modeling tool for the purpose of assessing the need for further changes, as well as to determine what mechanisms are best to enhance the feedback the system provides to users for validation of their requirements. The space activity planning and scheduling domain is quite similar to that of other planning and scheduling problems. It is believed that the availability of the ROSE modeling and scheduling tool may benefit these applications as well.

References

[1] Jaap, J., and Davis, E. (2000), "Can Customers Schedule Their Own Payload Activities?," Proc. of the 2nd Int. NASA Workshop on Planning and Scheduling for Space, (Online: http://payloads.msfc.nasa.gov/ROSE/publications/welcome.asp#workshop).

[2] Jaap, J. and Muery, K. (2000), "Putting ROSE To Work: A Proposed Application of a Request-Oriented Scheduling Engine for Space Station Operations," Proc. of the Sixth Inter. Symposium on Space Mission Operations and Ground Data Systems (SpaceOps 2000), Toulouse France, (Online: http://payloads.msfc.nasa.gov/ROSE/publications/welcome.asp#spaceops).

[3] Usher, J.M. (2001), "Other Potential Applications for the ROSE Technology," Technical Report, 7 pp. (Online: http://payloads.msfc.nasa.gov/ROSE/publications/usher/other.html).

[4] Usher, J.M. (2001), "Preliminary Review of the Airline Scheduling Domain," Technical Report, 4 pp. (Online: http://payloads.msfc.nasa.gov/ROSE/publications/usher/airline.html).

2001

NASA/ASEE SUMMER FACULTY FELLOWSHIP PROGRAM

MARSHALL SPACE FLIGHT CENTER
THE UNIVERSITY OF ALABAMA IN HUNTSVILLE

MEASURING ROCKET ENGINE TEMPERATURES WITH HYDROGEN RAMAN SPECTROSCOPY

Prepared By:	Joseph A. Wehrmeyer
Academic Rank:	Research Associate Professor
Institution and Department:	Vanderbilt University Mechanical Engineering Department
NASA/MSFC Directorate:	Space Transportation
MSFC Colleague:	Huu P. Trinh

Introduction

Laser-based combustion diagnostics, such as single-pulse UV Raman spectroscopy (Wehrmeyer et al. 2001) and visible Raman spectroscopy (Yeralan et al. 2001), have been successfully applied to optically-accessible rocket-like test articles. If an independent pressure measurement is available, Raman major species concentration measurements can also provide a temperature measurement. However it is desirable to obtain a Raman-derived temperature measurement without the need for simultaneous pressure measurement, especially when chamber pressure may vary spatially. This report describes Raman temperature measurements obtained by exploiting the variation in shape of the H_2 Raman spectrum. Hydrogen is advantageous since it is ubiquitous in H_2-O_2 systems and its Raman spectrum is simpler than for other diatomics. However the influence of high pressure on the H_2 Raman spectrum must be investigated. At moderate pressures, well below those of rocket engines, the Raman spectra of O_2 and N_2 are known to become featureless due to collisional broadening (Eckbreth 1988).

Theoretical H_2 Raman Spectra: Wavelength, Line Strength, and Linewidth

Hydrogen is a centrifugally-stretched rotor with rotational energy, E_r, given by (Eckbreth 1988):

$$E_r = hc[BJ(J+1) - DJ^2(J+1)^2 + \ldots] \qquad (1)$$

where h is Planck's constant (6.6 x 10^{-34} joule-sec), c is speed of light (3 x 10^{10} cm/sec), B is the rotational term value, in cm^{-1}(wavenumbers), D is a centrifugal stretch correction term value, and J is rotational quantum number (0, 1, etc.) Assuming H_2 is also an anharmonic oscillator, its vibrational energy can be modeled as a function of vibrational quantum number, v (0, 1, etc.), by:

$$E_v = hc[\omega_e(v+\tfrac{1}{2}) - \omega_e x_e(v+\tfrac{1}{2})^2 + \ldots] \qquad (2)$$

where ω_e is the fundamental vibrational term value and x_e is an anharmonicity correction factor. Both B and D are functions of v through vibration-rotation interaction and are given v subscripts:

$$B_v = B_e - \alpha_e(v+\tfrac{1}{2}) + \ldots \qquad D_v = D_e + \beta_e(v+\tfrac{1}{2}) + \ldots \qquad (3,4)$$

where B_e, D_e, α_e, and β_e, are constants. Values are in Jennings et al. (1985) and Weber (1973).

Spontaneous Raman scattering is the inelastic scattering of light by a molecule. For Stokes vibrational Q-branch Raman transitions, the molecular internal energy change obeys $\Delta v = +1$, $\Delta J = 0$. The increase in the scattering molecule's final energy, E' from its initial energy, E'', is:

$$E' - E'' = hc[\omega_e - 2\omega_e x_e(v''+1) - \alpha_e J(J+1) - \beta_e J^2(J+1)^2 + \ldots] \qquad (5)$$

where v'' is v for the initial energy state. Equation 5 gives the energy lost by the interacting photons, and since their wavelengths are related to their energies, the wavelength of the Raman scattered light, λ_R, will depend upon the incident photon's wavelength, λ_L, and v'' and J through:

$$\lambda_R = \{\lambda_L^{-1} - [\omega_e - 2\omega_e x_e(v''+1) - \alpha_e J(J+1) - \beta_e J^2(J+1)^2 + \ldots]\}^{-1} \qquad (6)$$

Since $\omega_e >> \omega_e x_e >> \alpha_e >> \beta_e$, ω_e approximately determines the λ_R's; next in importance is $\omega_e x_e$, which groups together Raman lines according to v''; and within each v'' group the J value determines a line's exact λ_R. Actually, E'-E'' also depends upon temperature, T, and density, ρ, through vibrational perturbations, which can either reduce or increase E'-E'' through the relative importance of short-range repulsive forces compared to long-range attractive forces (May et al. 1964). A correction term, $\Delta E/hc$, can be added to Eq. 6 for the ρ-, T-, J-, and collision partner-dependent shift of λ_R . Values for $\Delta E/hc$ are available for H_2 in H_2 (May et al. 1964), H_2 in H_2, Ar, He, N_2, or CH_4 (Lallemand and Simova 1968), and H_2 in N_2 (Sinclair et al. 1996).

Each Raman line's intensity is related to its v'', J level population and its transition probability (cross section). Calculated cross sections, $\sigma_{v''=0,J}$, for H_2's $v''=0$, $J=0$ to $J=3$ levels are available (Ford and Browne 1973) and higher vibrational level cross sections scale as $(v''+1)$ (Placzek 1932). Assuming a Boltzmann distribution, each Raman line's intensity, I_R, is related to T by:

$$I_R \propto \sigma_{v''=0,J}(v''+1)Q^{-1}g''(2J+1)\exp(-E''/kT) \qquad (7)$$

where Q is the T-dependent ro-vib-nuc partition function, k is Boltzmann's constant (1.38×10^{-23} joule/K), and g'' is relative degeneracy for ro-nuclear spin coupling (for H_2: 1 odd J, 3 even J).

Figures 1 and 2 show Stokes vibrational Q-branch Raman spectra (for 248.623 nm excitation) at two T's, 700 K and 3400 K, and use the lineshift data of Sinclair et al. (1996) for H_2 diluted in N_2. At 700 K only the first seven rotational levels for $v''=0$ are significantly populated. At 3400 K more rotational levels in the ground and excited vibrational states become populated due to the T dependence of the Boltzmann fraction factor in Eq. 7.

A Raman line's width, Γ (in cm^{-1}), is not zero, as in Figs. 1 and 2, but is finite and depends upon molecular velocities and collisions, hence is a function of T, ρ, collision partner, and collection geometry. At low ρ a Doppler-broadened gaussian lineshape occurs with a linewidth, Γ_{Do}, dependent upon angle, θ, between incident and scattered photon directions (Weber 1973):

$$\Gamma_{Dopp} = 2\left[2\ln(2)\,kT/m\right]^{1/2}\left[4\left(\lambda_L^{-2}+\lambda_L^{-1}\frac{E''-E'}{hc}\right)\sin^2\theta/2+\left(\frac{E''-E'}{hc}\right)^2\right]^{1/2} \qquad (8)$$

where m is the molecular mass. Thus Γ_{Do} is a minimum for forward scattering (θ=0°) and a maximum for backward scattering (θ=180°) and intermediate for θ=90°.

Because of the Uncertainty Principle, a Doppler shifted photon gives velocity information for a molecule that is averaged across a distance it travels, given by $\lambda_R/2\pi$ (Murray and Javan 1972). For increasing number of velocity changing collisions experienced through this travel length, the molecule's average velocity and Doppler shift will approach zero. This Dicke (or collisional) narrowing and can be thought of as a viscous drag, exerted on the scattered photon, that increases with ρ. If the mean free path $< \lambda_R/2\pi$, a Dicke-narrowed linewidth (Γ_{Dicke}) can be modeled as:

$$\Gamma_{Dicke} = \left[4\pi D_0/c\rho\right]\left[4\left(\lambda_L^{-2}+\lambda_L^{-1}\frac{E''-E'}{hc}\right)\sin^2\theta/2+\left(\frac{E''-E'}{hc}\right)^2\right]^{1/2} \qquad (9)$$

where D_0, in cm^2/(sec amagat), is an "optical" diffusion coefficient $\approx 1.13 \times$ molecular diffusion coefficient (Rahn et al. 1991; Bergmann and Stricker 1995). One amagat = ρ at 1 atm, 273 K. For large ρ collisional broadening occurs due to collisions that terminate, rather than perturb, the scattering process. The resulting finite-lived wavetrain has a frequency, or wavenumber, spread inversely proportional to its duration. The collisionally-broadened linewidth can be modeled as:

$$\Gamma_{Coll.Broad} = 2\gamma^0_J\rho \qquad (10)$$

where γ^0_J is a broadening coefficient dependent on J, collision partner, and T, and γ^0_J has been modeled by Hussong et al. (2000) for H_2-H_2 and H_2-N_2 collisions. Thus Γ is composed of a combination of three terms, each term dominating within a ρ range: $\Gamma = \Gamma_{Dopp}$ at low ρ, $\Gamma = \Gamma_{Dicke}$ at medium ρ, and $\Gamma = \Gamma_{Coll.\,Broad}$ at high ρ. Figure 3 shows the first two rotational lines of the H_2 Stokes vibrational Q-branch spectrum at 300 K, for dilute H_2 in N_2. At 1 atm (0.911 amagat) and

10 atm (9.14 amagat) Dicke narrowing dominates, with Γ less at 10 atm than 1 atm. At 100 atm (91.9 amagat from Redlich-Kwong data) collisional broadening dominates, but the lines are fully resolved and remain so even at 370 atm, a pressure expected in advanced preburners.

Experimental Raman Spectrum

Using the experimental system, shown in Fig. 4, of Wehrmeyer et al. (2001), a demonstration of high resolution H_2 Raman spectroscopy is performed in an atmospheric pressure H_2-air flame. A tunable krypton-fluoride excimer laser with a laser linewidth, $\Delta\lambda_L$, of 0.003 nm, is used along with an 0.3 m imaging spectrograph with an imaging resolution, $\Delta\lambda_S$, of 0.2 nm. Both $\Delta\lambda_S$ and $\Delta\lambda_L$ cause the measured linewidth of each Raman line, $\Delta\lambda_R$, to be greater than Γ/λ_R^2, (the "natural" linewidth expressed in wavelength units rather than wavenumbers). Assuming gaussian lineshapes, $\Delta\lambda_S$ and $\Delta\lambda_L$ can be convoluted together to form a gaussian "instrumental" lineshape with a FWHM of $(\Delta\lambda_S^2 + \Delta\lambda_L^2)^{1/2}$. In addition the 100 μm spectrograph slit also broadens the instrumental linewidth through its further convolution with a rectangular lineshape of 0.07 nm, from the 0.1mm slit width x 0.7 nm/mm dispersion (for a 3600 groove/mm grating).

Figure 5 shows Raman spectra for five atmospheric pressure H_2-air flames at varying equivalence ratio, ϕ. As ϕ decreases, T increases which lowers ρ (reducing the overall Raman signal strength) but also increases the population fractions of the higher rotational and vibrational levels ("spreading out" the H_2 and H_2O Raman signals). Figure 6 shows the H_2 Raman signal for the ϕ = 1.6 flame compared to theoretical Raman spectra at three T values. A manual best fit gives 2400 K, compared to an expected adiabatic T (T_{ad}) of 2220 K. Measured T's for all flames are high compared to T_{ad}'s: ϕ=2.0, T=2350K, T_{ad}=2060; ϕ=2.9, T=2200K, T_{ad}=1780; and ϕ=4.0, T=1900K, T_{ad}=1560. This could be due the noninclusion of the the O and S rotational wings around the Q-branch or a systematic error in ϕ measurement.

Conclusions and Future Work

Using the collisional broadening data of Hussong et al. (2000) the H_2 Stokes Raman Q-branch is modeled and shows no significant overlap of individual ro-vibrational lines, even up to 370 atm (from 300 to 3400 K). Thus a Raman temperature measurement based on spectral shape can be implemented even in high pressure advanced preburners. Atmospheric pressure H_2-air flames show systematic errors in temperature measurement of ~300 K. Better spectrograph resolution would clarify the error source. A high resolution 0.5 m spectrograph is available for future work.

References

Bergmann, V., and W. Stricker. 1995. *Appl. Phys. B* **61**, 49.
Eckbreth, A. 1988. *Laser Diagnostics for Combustion Temperature and Species*. Abacus Press: Cambridge, MA.
Ford, A. L., and J. C. Browne. 1973. *Atomic Data* **5**, 305.
Hussong, J., W Stricker, X Bruet, P Joubert, J Bonamy, D Robert, X Michaut, T Gabard, H Berger. 2000. *Appl. Phys. B* **70**, 447.
Jennings, D. E., L. A. Rahn, and A. Owyoung. 1985. *The Astrophys. Journ.* **291**, L15.
Lallemand, P., and P. Simova. 1968. *J. Molecular Spectroscopy*. **26**, 262.
May, A. D., G. Varghese, J. C. Stryland, and H. L. Welsh. 1964. *Canadian J. Physics* **42**, 1058.
Murray, J. R., and A. Javan. 1972. *J. Molecular Spectroscopy* **42**, 1.
Placzek, G. 1934. in *Handbuch der Radiologie*, H. 6 T. 2 ed. E. Marx. Leipzig: Akademische Verlag. NTIS UCRL-Trans-526(L).
Rahn, L. A., R. L. Farrow, and G. J. Rosasco. 1991. *Phys. Rev.* **43**, 6075.
Sinclair, P., J. Berger, X. Michaut, R. Saint-Loup, R. Chaux, H. Berger, J. Bonamy, and D. Robert. 1996. *Phys. Rev. A* **54**, 402.
Weber, A. 1973. in *The Raman Effect, Vol. 2: Applications*. ed. A. Anderson. Marcel Dekker: New York.
Wehrmeyer , J. A., J. M. Cramer, R. H. Eskridge, and C. C. Dobson. 2001. *J. Prop. Power* **17**, 27.
Yeralan , S., S. Pal, and R. J. Santoro. 2001. *J. Prop. Power* **17**, 788.

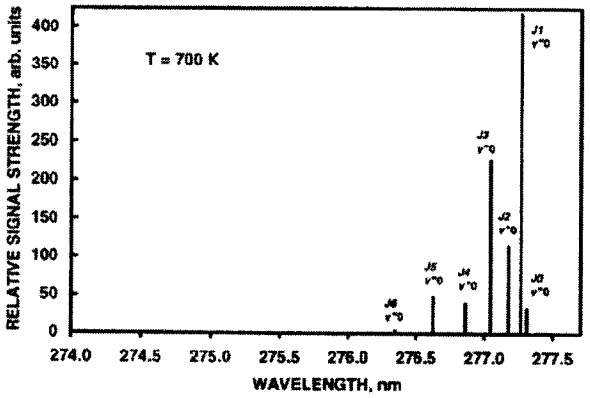

Fig. 1. H_2 Stokes vibrational Q-branch Raman spectrum for 700 K, assuming zero natural linewidth. 248.623 nm monochromatic laser.

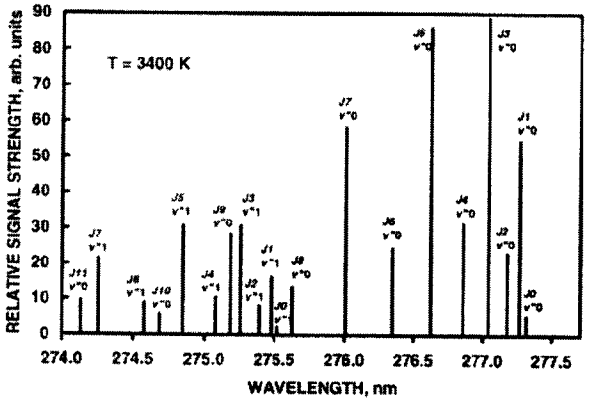

Fig. 2. H_2 Stokes vibrational Q-branch Raman spectrum for 3400 K, assuming zero natural linewidth. 248.623 nm monochromatic laser.

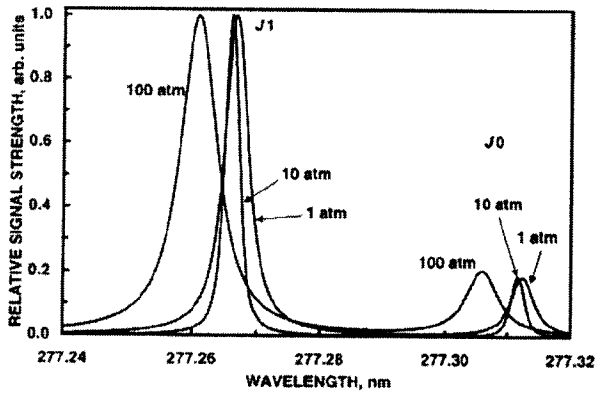

Fig. 3. First two rotational lines of H_2 Stokes vibrational Q-branch spectrum for 300 K including natural linewidth for three pressures. Assuming dilute H_2 in N_2.

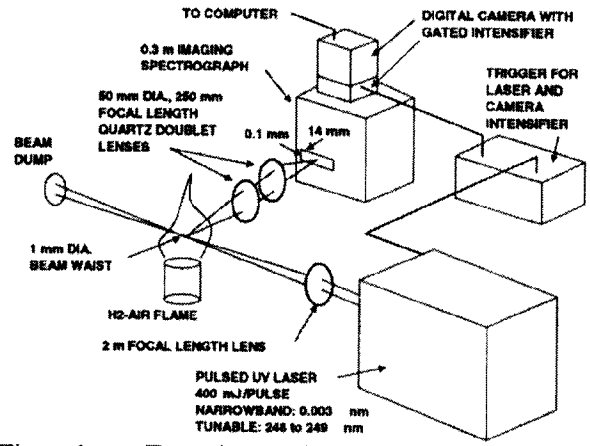

Fig. 4. Experimental system schematic.

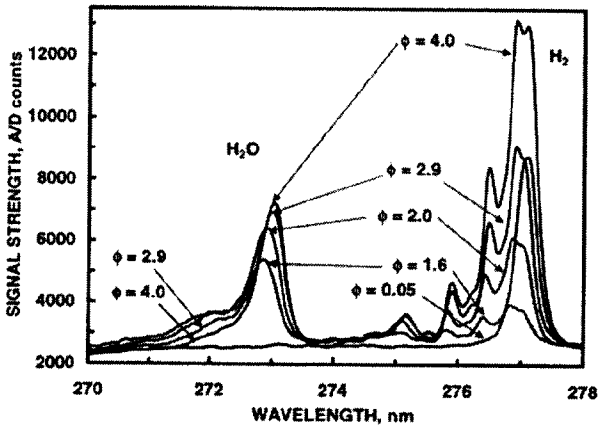

Fig. 5. Experimental Raman spectra for 1 atm H_2-air flames at various equivalence ratios (ϕ), using 248.623 nm laser (0.003 nm linewidth) and imaging spectrograph (0.2 nm resolution).

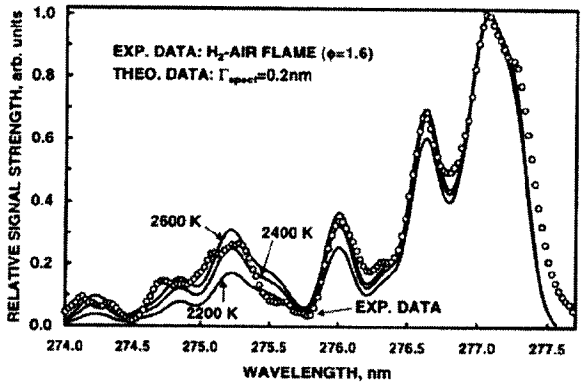

Fig. 6. Experimental H_2 Stokes vibrational Q-branch Raman spectrum (for ϕ=1.6 H_2-air flame) compared to theoretical spectra modeled with 0.2 nm spectrometer resolution.

2001

NASA/ASEE SUMMER FACULTY FELLOWSHIP PROGRAM

MARSHALL SPACE FLIGHT CENTER
THE UNIVERSITY OF ALABAMA IN HUNTSVILLE

ORBITAL PROPAGATION OF MOMENTUM EXCHANGE TETHER SYSTEMS

Prepared By:	John Westerhoff
Academic Rank:	Graduate Student
Institution and Department:	University of Illinois at Urbana/Champaign Aeronautical and Astronautical Engineering
NASA/MSFC Directorate:	Transportation
MSFC Colleague:	Kirk Sorensen

Introduction

An advanced concept in in-space transportation currently being studied is the Momentum-Exchange/Electrodynamic Reboost Tether System (MXER). The system acts as a large momentum wheel, imparting a Δv to a payload in low earth orbit (LEO) at the expense of its own orbital energy. After throwing a payload, the system reboosts itself using an electrodynamic tether to push against Earth's magnetic field and brings itself back up to an operational orbit to prepare for the next payload. The ability to reboost itself allows for continued reuse of the system without the expenditure of propellants. Considering the cost of lifting propellant from the ground to LEO to do the same Δv boost at $10000 per pound, the system cuts the launch cost of the payload dramatically, and subsequently, the MXER system pays for itself after a small number of missions.[1]

One of the technical hurdles to be overcome with the MXER concept is the rendezvous maneuver. The rendezvous window for the capture of the payload is on the order of a few seconds, as opposed to traditional docking maneuvers, which can take as long as necessary to complete a precise docking. The payload, therefore, must be able to match its orbit to meet up with the capture device on the end of the tether at a specific time and location in the future. In order to be able to determine that location, the MXER system must be numerically propagated forward in time to predict where the capture device will be at that instant. It should be kept in mind that the propagation computation must be done faster than real-time. This study focuses on the efforts to find and/or build the tools necessary to numerically propagate the motion of the MXER system as accurately as possible.

MXER Simulation

To simulate the motion of the MXER system, a software package called GTOSS was used. Created by David Lang, this software was originally developed for the shuttle TSS missions, and has subsequently been used in a wide variety of tether studies and has been validated as a robust simulation tool for space tethers.

Simulation Configuration

The table below shows the configuration of MXER that was run in the simulations.

Ballast Mass	10 MT	Capture Device Mass	1 MT
Initial Angular Velocity	.0156 rad/s	Tether Material	Spectra 2000
Tether Length	100 km	Tether Mass	3.5 MT
Tether Diameter	0.00678 m	Tether Young's Modulus	170 GPa

Results of Simulation

[1] See the references for detailed descriptions of the MXER system. It is assumed throughout the rest of this paper that the reader has a working knowledge of the concepts behind it.

The first item of note in the resultant motion of the MXER system is that the tether length and angular velocity oscillate in the steady state. This is due to the fact that the gravity gradient force varies sinusoidally as the tether rotates, imparting a continually varying force on the system. This causes longitudinal oscillations, as well as transverse oscillations due to the coriolis effect. These oscillations are more prominent near perigee, where gravity gradient effects are stronger.

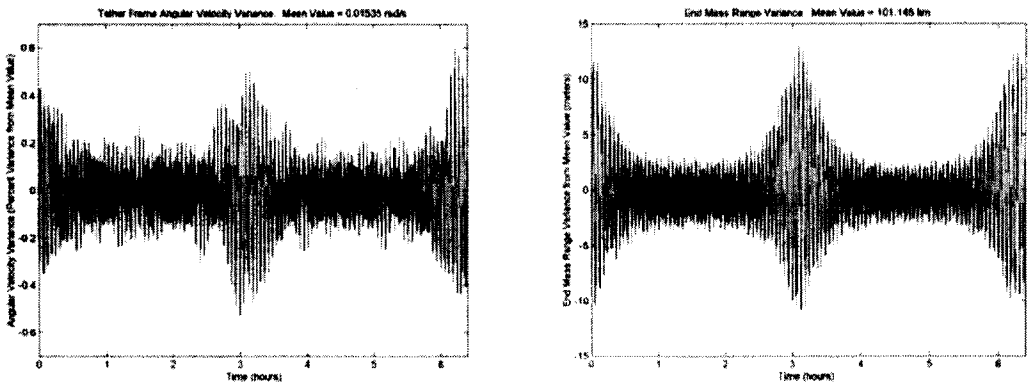

The left plot shows the percent variance in the tether frame angular velocity from its mean value over a period of 2 orbits. The plot starts and ends at perigee. The angular rate is shown to remain within ±0.6% of its nominal value, which is calculated to be 0.01535 rad/s. On closer examination, 2 discernible frequencies can be seen in the oscillation of the angular rate: 0.0046 Hz and 0.019 Hz. Note that the mean rotational frequency of tether is: 0.00244 Hz, approximately half of the first frequency.

The right plot shows the variance in the distance between the end masses over the period of 2 orbits. Again, the stronger variance occurs near perigee. At perigee, the length of the tether is shown to vary by approximately ±12 meters from its nominal value of 101.145 km. It is noted that the effects of centripetal forces on the stretch of the system studied were an order of magnitude greater than the stretch due to the gravity gradient effects. There are 2 frequencies that can be seen on closer examination: 0.0043 Hz and .029 Hz.

The following plots show the transverse motion (in the tether frame) of 2 of the bead points. Bead 1 is the closest to the capture device, and bead 5 is toward the middle of the tether. It was observed that the strongest transverse oscillations occur near the capture device, and then taper down toward the ballast mass. In this study, the end masses were treated as point masses, so the full motion of the end masses was not examined. Due to the stronger oscillations at the capture device end, this has implications for induced pendulum motion and stability criteria, which may impact the design of the capture device. Two discernible frequencies can be observed in the transverse motion of the tether: .0041 Hz and 0.015 Hz.

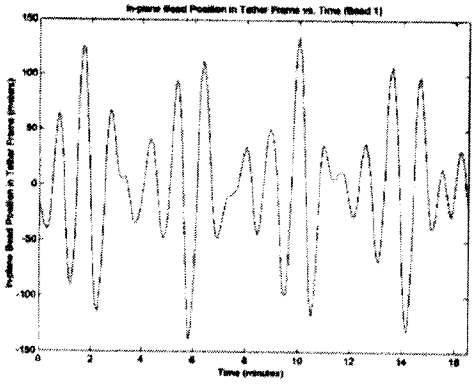

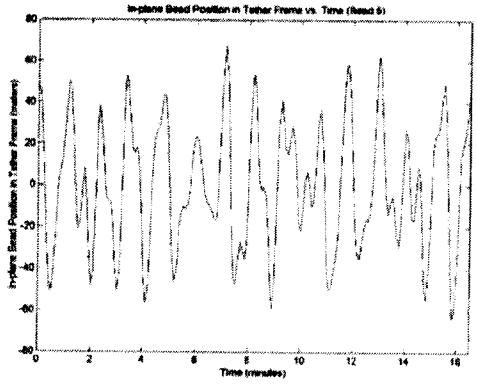

Another effect that was noticed was the presence of initial transients in the simulation. As stated before, this is partially due to the inaccuracies of the initial conditions. In addition, the bead model initialization in GTOSS adds to this initial transient, due to the fact that the tether is initialized with homogeneous strain. In the steady state (for a uniform tether), strain is strongest at the CM, and declines out toward the end masses. A side effect of these inaccuracies is to produce slightly different steady state values for tether length, angular rate, and apogee radius than predicted by the analytical equations. These differ only by a few percent in each case, and can be compensated for, if desired, by tweaking the IC's to get the desired steady state value.

After running a number of simulations, it was discovered that very short integration timesteps are necessary to converge to a final solution in GTOSS for the MXER system. Longer timesteps presented the effect of inducing artificial damping into the solution. After running the simulation for 5 orbits with a 0.1 second timestep, for example, the angular velocity of the tether had decreased by about 30%. Shorter timesteps were used in an effort to remove this effect, but the damping was still significant until using timesteps on the order of 50 microseconds. At this point, the simulation runs run slower than real-time. Also, the final position of the capture device had still not converged. Simulations using shorter timesteps were attempted to obtain convergence, but they failed to complete. A couple of simulation options were tried in order to remove this damping effect: constraining the tether to homogenous strain, and utilizing a late-start option to remove initial transients, but both were ineffectual. Artificial damping remains the principle difficulty in convergence of the solution with GTOSS. Also, note that in this study, only experiments with convergence with respect to variation of the timestep were performed. Time did not permit an analysis of using varying numbers of elements in the tether model, to determine what is the required number for convergence.

Conclusions

Although GTOSS did not converge to a solution with the accuracy desired, the simulations were able to provide several valuable observations of the general motion of the MXER system. An analysis of this motion brought to light a number of the issues involved in the propagation of the system and in the rendezvous maneuver. The convergence problem, however, may require the use of an alternate software solution in

order to be able to run the simulation in a reasonable amount of time, so that parametric studies and error analyses can be performed.

Future Work Planned

The artificial damping effect in the propagation of the MXER system may be tied to the integration method and/or tether model used in the propagation software, or may be an inherent property of the system. In order to determine this, an analysis of alternate propagation methods is will be performed. One such alternative is the JTether simulation being developed by Kirk Sorensen. Work is currently underway to incorporate the finite element model created by Dr. Canfield and Dave Johnson into JTether, to analyze the performance and convergence in comparison to GTOSS. In a paper by Robert Hoyt of Tethers Unlimited, it was proposed that a finite element model for the tether is a more efficient way to simulate the system, and converges to a solution with a timestep an order of magnitude or two longer than that required by discrete modeled tether systems. The use of this model, as well as a higher order integrator, may prove to be useful in the analysis of the MXER system. Other alternatives include TSSIM, developed by the ESA and refined by John Glaese, and TetherSim, developed by Tethers Unlimited Inc.

Once the tools are in place to propagate the motion of the MXER system, studies can be performed to look into the effects of environmental uncertainty and initial condition error on the final prediction of the simulation. This analysis will provide a more realistic error space within which the final position of the capture device for rendezvous can be predicted. This error space will drive the constraints of the terminal guidance system, which will be responsible for autonomously performing the final adjustments to the trajectories of the payload and/or the capture device to achieve rendezvous.

Acknowledgements

I would like to thank Kirk Sorensen and Randy Baggett for putting forth the effort in getting me into the Summer Faculty Fellowship Program. My thanks also go out to John Glaese, Ken Welzyn, and David Lang for help in learning and analyzing with the GTOSS system.

References

1. Bangham, M.E., Lorenzini, E. Vestal, L., *Tether Transportation System Study*, NASA TP-1998-206959, 1998
2. Hoyt, R., and Uphoff, C., *Cislunar Tether Transport System*. AIAA 99-2690
3. Hoyt, R., et al., *Stabilization of Electrodynamic Tethers*, Tethers Unlimited, Inc. Final Report on NASA/MSFC Phase I Contract NAS8-01013, August 2001
4. Lang, David, *TOSS Software Manuals Version F.9* (1992), David Lang Associates
5. Prussing, John and Conway, Bruce (1993), *Orbital Mechanics*, Oxford University Press, New York
6. Sorensen, Kirk, *Conceptual Design and Analysis of an MXER Tether Boost Station*. AIAA 2001-3915

2001

NASA/ ASEE SUMMER FACULTY FELLOWSHIP PROGRAM

MARSHALL SPACE FLIGHT CENTER
THE UNIVERSITY OF ALABAMA IN HUNTSVILLE

Deformation During Friction Stir Welding

Prepared By:	Henry J. White
Academic Rank:	Assistant Professor
Institution and Department:	The State University of New York at Stony Brook Department of Materials Science and Engineering
NASA/ MSFC Directorate:	Engineering
MSFC Colleague:	Arthur Nunes

Introduction

Friction Stir Welding (FSW) is a solid state welding process that exhibits characteristics similar to traditional metal cutting processes. The plastic deformation that occurs during friction stir welding is due to the superposition of three flow fields: a primary rotation of a radially symmetric solid plug of metal surrounding the pin tool, a secondary uniform translation, and a tertiary ring vortex flow (smoke rings) surrounding the tool (see figure 1). If the metal sticks to the tool, the plug surface extends down into the metal from the outer edge of the tool shoulder, decreases in diameter like a funnel, and closes up beneath the pin.

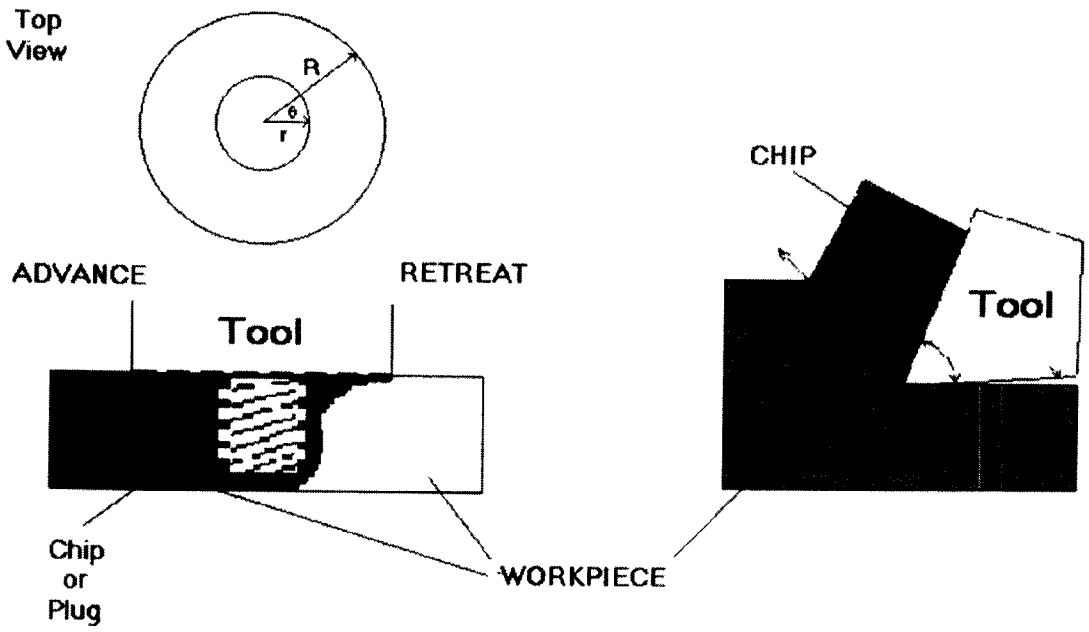

Figure 1: Schematic illustrating the similarities between friction stir welding (left) and metal cutting operations (right). The friction stir welding transverse section (left) shows base plates (gray and white), weld tool (shoulder and threaded pin), and rotating plug (black area surrounding weld pin beneath shoulder).

Since its invention, ten years have gone by and still very little is know about the physics of the friction stir welding process. Recently, (Nunes et al. 2000) engineers at the George Marshall Space Flight Center proposed the "Rotating Plug Model" to fill this void. In the model, the large plastic strain and high strain rates present during friction stir welding are compared to those experienced during metal cutting operations. As Nunes et al. (2000) states: "The incoming stream of metal resembles the cut to be made; the sliver rotated around the threaded pin, the chip or plug; and the plug interface, the shear zone". Dong et al. (1999) provides a more vivid explanation:

> "Along this narrow band, the plastic flow velocity becomes asymptotically discontinuous as elastic strains become negligible, forming a separation surface (or slip line) between the stir-induced flow zone and stationary region. The stresses acting on such a slip line can be characterized by rigid plasticity theory in terms of shear yield stress and hydrostatic stress. Under friction stir welding conditions the shear yield stresses should be considered as a function of temperature and strain rate. If the yield strength as a function of both temperature and strain rate is known, the required rotational torque and translation forces can be estimated."

Nunes et al. (2000) proceeded to estimate these values from the geometry of the weld zone shown in figure 1.

$$M = \frac{2\pi R^3}{3}\left(1 + 3\frac{r^2 t}{R^3}\right)\tau \tag{1}$$

$$F_p = 6\pi R^2 \tau \tag{2}$$

$$F_L \sim \int_0^{2\pi} \tau \frac{Vr}{2\alpha}\cos\theta\left[(rtd\theta)\cos\theta\right] \sim \tau(\pi rt)\left(\frac{Vr}{2\alpha}\right) \tag{3}$$

$$F_T \sim \int_0^{2\pi} \sigma \frac{Vr}{2\alpha}\cos\theta\left[(rtd\theta)\cos\theta\right] \sim \sigma(\pi rt)\left(\frac{Vr}{2\alpha}\right) \tag{4}$$

In the equations above, the shear yield stress (τ) is temperature dependent. It is currently unclear how strain rate fits into the Rotating Plug Model.

Since the friction stir welding process is similar to metal cutting, it is expected that very high and variable strain rates exist within the plastic flow region. The strain rate present during metal cutting is usually estimated by equation 5, where V is the cutting speed and d is the thickness of the shear band determined by electron microscopy techniques (Black 1989).

$$\frac{d\gamma}{dt} = \frac{V}{d} \tag{5}$$

A similar equation was proposed in the Rotating Plug Model, where V is taken as ωr and d as V/ω. The value of d can also be obtained by measuring the distance between weld tracks produced in the wake of the rotating pin by metallographically preparing a plan view mid section of the weldment.

Frigaard et al. (1999) proposed using analytical electron microscopy and the Zener-Holloman (1944) parameter (based on polygonization and the formation of subgrain structures) to estimate the shear strains within the plastic region. Uncharacteristically low strain rates were obtained using this technique and these values were attributed to the presence of a liquid layer at the tool/ matrix interface. Although postulated, such evidence has never been observed in friction stir weldments and the basis of this study is to invalidate these claims.

Experimental Methodology

An H13 steel weld tool (shoulder diameter, 0.797"; pin diameter, 0.312"; and pin length, 0.2506") was used to weld three 0.255" thick plates (weld parameter are listed in table 1).

Table 1. Welding Geometry and Conditions

Material	Joint Configuration	Travel Speed (ipm)	RPM	Rotation Direction
2219*	Bead on Plate	3.5	230	Clockwise
5456**	Bead on Plate	3.5	230	Clockwise
2219/ 5456***	Butt Weld	3.5	230	Clockwise

* T87
** O
*** 5456 advancing

The deformation behavior during friction stir welding was investigated by metallographically preparing a plan view sections of the weldment and taking Vickers hardness test in the key- hole region see figure 2. The proposed homogeneous technique is similar to the heterogeneous tracer, shot, and dissimilar metal joining experiments of Reynolds (2000), Colligan (1999), and McClure (1999) respectively.

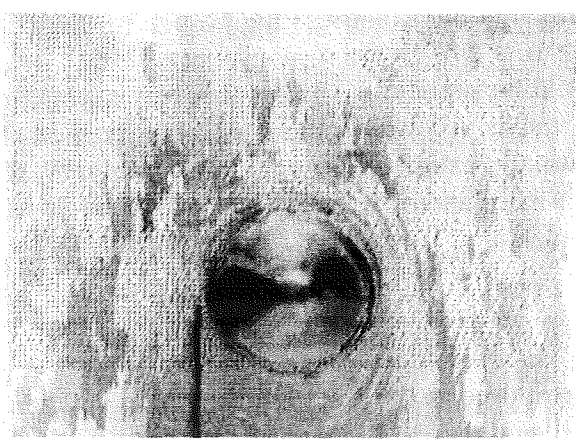

Figure 2: Vickers Hardness readings (5243) taken in the vicinity of the key- hole of the weldment.

Conclusions

Hardness is a measure of the resistance of a material to deformation. The hardness distribution surrounding the key- hole region of the 2219 bead on plate weld (figure 3) suggest variable strain and strain rates probably due to the thermal events (colder metal at the leading edge and hot metal in the wake) superimposed over the deformation profile. Frigaard's (1999) low strain rates were not due to local melting, but seem to be due to softening of material in the wake of the pin tool. Future work in this area should be directed towards obtaining deformation data throughout the specimen thickness and investigating the effects of preheat and other welding variables on the deformation profile.

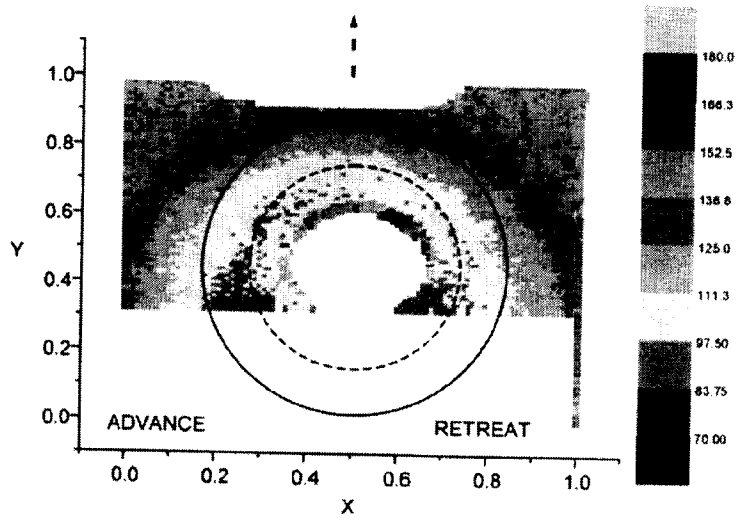

Figure 3: (a) Hardness in the vicinity of the key- hole.

Acknowledgements

The author would like to thank, Dr. Arthur Nunes for his interesting discussions on the Rotating Plug Model for friction stir welding; Jeff Ding and Robert Carter for their discussions on the friction stir welding process and Greg Steele for his metallography expertise.

References

[1] Black, J. T. (1989), "Mechanics of Chip Formation", Metals Handbook, Machining, 9th edition, ASM International, Vol. 16, 7.

[2] Colligan, K. (1999), "Material Flow Behavior During Friction Stir Welding of Aluminum", Welding Journal, 7, 229s-237s.

[3] Dong P., Lu F., Hong J. K. and Cao Z.(1999), "Analysis of Weld Formation Process in Friction Stir Welding", 1st International Symposium on Friction Stir Welding, Rockwell Science Center, Thousand Oaks, California.

[4] Frigaard, O., Grong, O., Hjelen J., Gulbrandsen-Dahl S. and Midling O. T. (1999), "Characterization of the Subgrain Structure in Friction Stir Welded Aluminum Alloys Using the SEM-EBSD Technique", 1st International Symposium on Friction Stir Welding, Rockwell Science Center, Thousand Oaks, California.

[5] Li, Y., Murr, L. E., McClure, J. C. (1999), "Solid State Flow Visualization in the Friction Stir Welding of 2024 Al to 6061 Al", Scripta Materialia, 40(9), 1041-1046.

[6] Nunes, A. C., Bernstein, E. L. and McClure J. C. (2000), "A Rotating Plug Model for Friction Stir Welding", 81st American Welding Society Annual Convention, Chicago, Illinois.

[7] Reynolds A. P. (2000), "Visualization of Material Flow in Autogenous Friction Stir Welds", Science and Technology of Welding and Joining, 5(2), 120-124.

[8] Zener C. and Hollomon J. H. (1944), "Effect of Strain Upon Plastic Flow of Steel", Journal of Applied Physics, 15(1), 22-32.

2001

NASA/ASEE SUMMER FACULTY FELLOWSHIP PROGRAM

MARSHALL SPACE FLIGHT CENTER
UNIVERSITY OF ALABAMA IN HUNTSVILLE

TORQUE LIMITS FOR FASTENERS IN COMPOSITES

Prepared By:	Yi Zhao
Academic Rank:	Assistant Professor
Institution and Department:	Michigan Technological University Department of Mechanical Engineering – Engineering Mechanics
NASA/MSFC Directorate:	Engineering
MSFC Colleague(s):	Donald Ford Stephen Richardson

Introduction

The two major classes of laminate joints are bonded and bolted. Often the two classes are combined as bonded-bolted joints. Several characteristics of fiber reinforced composite materials render them more susceptible to joint problems than conventional metals. These characteristics include weakness in in-plane shear, transverse tension/compression, interlaminar shear, and bearing strength relative to the strength and stiffness in the fiber direction.

Studies on bolted joints of composite materials have been focused on joining assembly subject to in-plane loads. Modes of failure under these loading conditions are net-tension failure, cleavage-tension failure, shear-out failure, bearing failure, etc. Although the studies of torque load can be found in literature, they mainly discussed the effect of the torque load on in-plane strength.

Existing methods for calculating torque limit for a mechanical fastener do not consider connecting members. The concern that a composite member could be crushed by a preload inspired the initiation of this study. The purpose is to develop a fundamental knowledge base on how to determine a torque limit when a composite member is taken into account. Two simplified analytical models were used: a stress failure analysis model based on maximum stress criterion, and a strain failure analysis model based on maximum strain criterion.

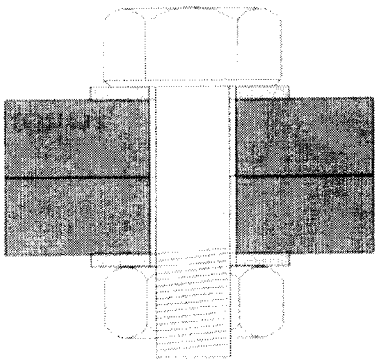

Figure 1. Mechanical Fastener Assemb.

Torque Limit Based on Stress Failure Criterion

Theoretically, a torque load can be determined from the normal force in a bolt through a static analysis. This normal force usually consists of clamping force (preload) and work load. For a joint assembly, the critical case is the superposition of preload and work load. But in this preliminary investigation, only preload in the assembly process is considered. For simplicity, consider a bolt with square thread first. From static equilibrium conditions, the relation between the torque force P and clamping force F can be obtained:

$$P = \frac{\sin\lambda + \mu\cos\lambda}{\cos\lambda - \mu\sin\lambda} F \tag{1}$$

where N is the normal reaction, and μN is the friction force due to the normal force. The maximum value of F for a composite member is the clamping force that results in compressive failure (crushing) in its transverse direction $F_{max} = \sigma_T A_W$, where σ_T is the compressive strength of the composite material in transverse direction, A_w is the face area of a washer, $A_w = \pi(r_o^2 - r_i^2)$, where r_o and r_i are the outside radius and inside radius of the washer, respectively. Since $T = P(d_m/2)$, the maximum torque can be obtained as

$$T_{\max} = \frac{\pi}{2} d_m \left(r_o^2 - r_i^2\right)\left(\frac{\sin\lambda + \mu\cos\lambda}{\cos\lambda - \mu\sin\lambda}\right)\sigma_T \tag{2}$$

A similar expression can be obtained if the effect of thread angle α is considered in the analysis.

$$T_{\max} = \frac{\pi}{2} d_m \left(r_o^2 - r_i^2\right)\left(\frac{\cos\alpha \sin\lambda + \mu\cos\lambda}{\cos\alpha\cos\lambda - \mu\sin\lambda}\right)\sigma_T \tag{3}$$

Torque Limit Based on Strain Failure Criterion

An alternative approach to determine the torque limit would be a strain-based analysis. Since strain is the ratio of change of dimension to the original dimension, and the change of dimension is related to the stiffness of the member, we need to calculate the stiffness of the composite members in a mechanical fastener assembly.

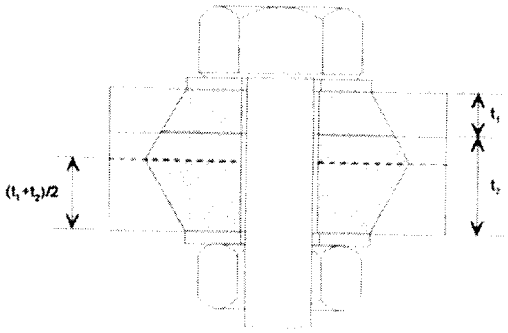

Figure 2. Transverse Pressure Zone

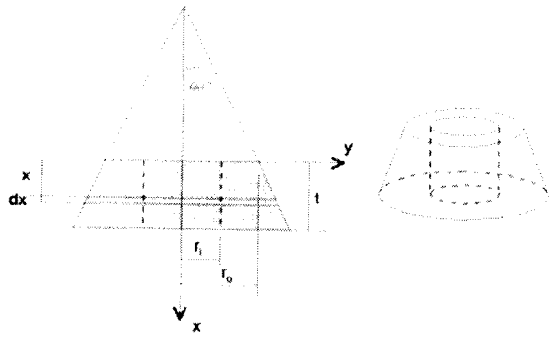

Figure 3. Pressure Cone Model

The case of a composite laminate subjected to transverse compressive force in a washer-face annulus area on top and bottom surfaces is a very complicated problem. There is no close-form solution available even for isotropic plates. A simplified approach is to use the so-called "pressure-cone" method. It is assumed that the pressure applied to the two members is primarily taken by the materials within the pressure cone; therefore, the stiffness of each member in the bolt connection can be determined by considering only this cone. If a half-apex angle β is used to describe the cone geometry, obviously the use of an appropriate angle plays an important role in the calculation of the member's stiffness. In general, a larger angle β will result in a greater stiffness. For isotropic materials, the normal range is $25° \le \beta \le 33°$ for most combinations. No information has been found for composite materials regarding this cone angle.

Consider the case of two composite members with different thickness t_1 and t_2, as shown in Fig. 2. The total change of thickness will be

$$\Delta = \frac{F}{2\pi r_i \tan\beta}\left[\frac{1}{E_{T1}}\ln\frac{(t_1\tan\beta + r_o - r_i)(r_o + r_i)}{(t_1\tan\beta + r_o + r_i)(r_o - r_i)} + \frac{1}{E_{T2}}\ln\frac{(t_2\tan\beta + r_o - r_i)(r_o + r_i)}{(t_2\tan\beta + r_o + r_i)(r_o - r_i)}\right.$$
$$\left. + \frac{1}{E_{T2}}\ln\frac{[(1/2)(t_1+t_2)\tan\beta + r_o - r_i](t_1\tan\beta + r_o + r_i)}{[(1/2)(t_1+t_2)\tan\beta + r_o + r_i](t_1\tan\beta + r_o - r_i)}\right] \tag{4}$$

where E_{T1} and E_{T2} are the transverse Young's modulus of the two composite members, and t_1 and t_2 are the thickness of the two members. In the special case that the two composite members are identical ($E_{T1} = E_{T2} = E_T$ and $t_1 = t_2 = t$), the last term of the above expression becomes zero. This relation will be reduced to

$$\Delta = \frac{F}{\pi E_T r_i \tan\beta} \ln \frac{(t\tan\beta + r_o - r_i)(r_o + r_i)}{(t\tan\beta + r_o + r_i)(r_o - r_i)} \tag{5}$$

The torque limit T_{max} can be found as:

$$T_{\max} = \left(\frac{d_m}{2}\right)\frac{\cos\alpha\sin\lambda + \mu\cos\lambda}{\cos\alpha\cos\lambda - \mu\sin\lambda} F_{\max} = \frac{\pi d_m r_i t E_T \varepsilon_{allowable} \tan\beta \left(\dfrac{\cos\alpha\sin\lambda + \mu\cos\lambda}{\cos\alpha\cos\lambda - \mu\sin\lambda}\right)}{\left[\ln \dfrac{(t\tan\beta + r_o - r_i)(r_o + r_i)}{(t\tan\beta + r_o + r_i)(r_o - r_i)}\right]} \tag{6}$$

It can be seen that the parameters contained in this expression are either material properties or geometrical parameters of the joint assembly, expect the cone angle β.

Determination of Pressure Cone Angle β

It is noted that the change of thickness of the two composite members, Δ, is not exactly the same as the bolt elongation, δ. The difference is the change of thickness of the two washers, Δ_W.

$$\delta = \Delta + \Delta_W$$

$$\frac{Fl_B}{\pi r_B^2 E_B} = \frac{F}{\pi E_T r_i \tan\beta} \ln \frac{(t\tan\beta + r_o - r_i)(r_o + r_i)}{(t\tan\beta + r_o + r_i)(r_o - r_i)} + \frac{2Ft_W}{\pi E_W (r_o^2 - r_i^2)} \tag{7}$$

Rearranging this relation results in the following non-dimensional form:

$$\left[\frac{r_i l_B}{r_B^2}\left(\frac{E_T}{E_B}\right) - \frac{2t_W r_i}{r_o^2 - r_i^2}\left(\frac{E_T}{E_W}\right)\right]\tan\beta = \ln \frac{(t\tan\beta + r_o - r_i)(r_o + r_i)}{(t\tan\beta + r_o + r_i)(r_o - r_i)} \tag{8}$$

Since $l_B = 2(t + t_W)$, this equation can be further written as

$$Z\tan\beta = \ln\left[\frac{(t/r_i)\tan\beta + \eta - 1}{(t/r_i)\tan\beta + \eta + 1}\left(\frac{\eta+1}{\eta-1}\right)\right] \tag{9}$$

where $\eta = r_o/r_i$, and

$$Z = \left[2\left(\frac{r_i}{r_B}\right)\left(\frac{t}{r_B}\right) + 2\left(\frac{r_i}{r_B}\right)\left(\frac{t_W}{r_B}\right)\right]\left(\frac{E_T}{E_B}\right) - \frac{2}{\eta^2 - 1}\left(\frac{t_W}{r_i}\right)\left(\frac{E_T}{E_W}\right) \tag{10}$$

This expression can be expended to the following polynomial form:

$$a_1 \tan\beta + a_2(\tan\beta)^2 + a_3(\tan\beta)^3 + a_4(\tan\beta)^4 + \ldots\ldots = 0 \qquad (11)$$

where

$$a_1 = (\eta+1)Z - \frac{2}{\mu-1}, \quad a_n = \frac{Z^{n-1}}{(n-1)!}\left[(\eta+1)Z + \left(\frac{t}{r_i}\right)\right], \qquad n = 2,3,4,\Lambda \qquad (12)$$

Thus a nonlinear equation about tanβ has been changed to an n-th order polynomial series and it can be solved numerically. It can be seen from this equation that the value of cone angle β is related to many variables, including Young's moduli of bolt and washer, transverse modulus of elasticity of composite member, size and thickness of washer, and the thickness of composite member.

Discussion and Conclusions

Two simplified analytical models were used: a stress failure analysis model based on maximum stress criterion, and a strain failure analysis model based on maximum strain criterion. A cone pressure model is used in obtaining stiffness of composite members. In this model, the transverse normal stress within a member is assumed to be limited to the region of a cone and distributed uniformly. The angle of the core can be determined numerically from the developed models. These models can be used in a bolt joint assembly with a single member, two identical or different members, or, in general, multiple members with different thickness and material properties. The results show that the torque limit is a function of bolt parameters (including thread profile), size of washers, thickness and material properties of each composite member involved.

Acknowledgment

The investigator would like to express his sincere gratitude to NASA and ASEE in general, MSFC and UAH in particular, for providing him a summer faculty fellowship to conduct this and two other projects. The investigator would like to thank his NASA colleagues, Mr. Donald Ford and Mr. Stephen Richardson, for their collaborations during the course of this study. Many of the concepts that the investigator used in this work were directly from the numerous discussions with his NASA colleagues. A great appreciation will also be extended to Mr. Sidney Rowe and Mr. Rod Stallworth for their support.

References

[1] "Criteria for Preloaded Bolts," NASA/JSC, NSTS 08307, Revision A, July 1998.

[2] D.E. Fox and K.W. Swaim, "Static Strength Characteristics of Mechanically Fastened Composite Joints," MSFC CDDF report, project No. 95-07, NASA/TM-1999-209735.

[3] T.G. Gutowski (editor), *Advanced Composites Manufacturing*, John Wiley & Sons, New York, 1997.

[4] R.M. Jones, *Mechanics of Composite Materials*, 2nd edition, Taylor & Francis, Philadelphia, 1999.

[5] Torque Limits for Standard, Threaded Fasteners, MSFC-STD-486B, November 1992.

REPORT DOCUMENTATION PAGE

Form Approved
OMB No. 0704-0188

1. AGENCY USE ONLY *(Leave Blank)*	2. REPORT DATE	3. REPORT TYPE AND DATES COVERED
	July 2002	Contractor Report (Final)

4. TITLE AND SUBTITLE
Research Reports—2001 NASA/ASEE Summer Faculty Fellowship Program

5. FUNDING NUMBERS
NAG8–1786

6. AUTHORS
J. Bland, Compiler; G. Karr,* J. Pruitt, S. Nash-Stevenson, L.M. Freeman,** and C.L. Karr,** Editors

7. PERFORMING ORGANIZATION NAMES(S) AND ADDRESS(ES)
The University of Alabama in Huntsville, Huntsville, AL
The University of Alabama, Tuscaloosa, AL

8. PERFORMING ORGANIZATION REPORT NUMBER
M–1054

9. SPONSORING/MONITORING AGENCY NAME(S) AND ADDRESS(ES)
National Aeronautics and Space Administration
Washington, DC 20546

10. SPONSORING/MONITORING AGENCY REPORT NUMBER
NASA/CR—2002–211840

11. SUPPLEMENTARY NOTES
*The University of Alabama in Huntsville, Huntsville, AL
**The University of Alabama, Tuscaloosa, AL
Prepared for Education Programs Department, Customer and Employee Relations Directorate

12a. DISTRIBUTION/AVAILABILITY STATEMENT
Unclassified-Unlimited
Subject Category 99
Nonstandard Distribution

12b. DISTRIBUTION CODE

13. ABSTRACT *(Maximum 200 words)*

For the thirty-seventh consecutive year, a NASA/ASEE Summer Faculty Fellowship Program was conducted at Marshall Space Flight Center (MSFC). The program was conducted by The University of Alabama in Huntsville and MSFC during the period May 29–August 3, 2001. Operated under the auspices of the American Society for Engineering Education, the MSFC program, as well as those at other NASA Centers, was sponsored by the University Affairs Office, NASA Headquarters, Washington, DC. The basic objectives of the programs, which are in the thirty-seventh year of operation nationally, are (1) to further the professional knowledge of qualified engineering and science faculty members; (2) to stimulate an exchange of ideas between participants and NASA; (3) to enrich and refresh the research and teaching activities of the participants' institutions; and (4) to contribute to the research objectives of the NASA Centers. The Faculty Fellows spent ten weeks at MSFC engaged in a research project compatible with their interests and background and worked in collaboration with a NASA MSFC colleague. This document is a compilation of Fellows' reports on their research during the summer of 2001.

14. SUBJECT TERMS
avionics; structures; mechanics; materials, processes, and manufacturing; flight projects; safety, reliability, and quality assurance; space science; optics; propulsion; vehicles development

15. NUMBER OF PAGES
327

16. PRICE CODE

17. SECURITY CLASSIFICATION OF REPORT	18. SECURITY CLASSIFICATION OF THIS PAGE	19. SECURITY CLASSIFICATION OF ABSTRACT	20. LIMITATION OF ABSTRACT
Unclassified	Unclassified	Unclassified	Unlimited

National Aeronautics and
Space Administration
AD33
George C. Marshall Space Flight Center
Marshall Space Flight Center, Alabama
35812